

**THÈSE DE DOCTORAT**  
**DE L'UNIVERSITÉ PSL**

Préparée à Chimie ParisTech / École Nationale Supérieure de  
Chimie de Paris (ENSCP)

**Use of perovskite growth additives and chemical  
composition and interfacial engineerings for high  
performance and stable solar cells**

Soutenue par

**Daming ZHENG**

Le 28 septembre 2021

Ecole doctorale n° 388

**Chimie Physique et Chimie  
Analytique de Paris Centre**

Spécialité

**Chimie Physique**



**Composition du jury :**

Nicolas, MERCIER Professeur, Université d'Angers	<i>Rapporteur</i>
Yvan, BONNASSIEUX Professeur, Ecole Polytechnique	<i>Rapporteur</i>
Iaria, CIOFINI Directrice de Recherche CNRS Chimie ParisTech, ENSCP	<i>Examinatrice</i>
Solenn, BERSON Ingénieure CEA, Commissariat à l'énergie atomique et aux énergies alternatives	<i>Examinatrice</i>
Thierry PAUPORTÉ Directeur de Recherche CNRS Chimie ParisTech, ENSCP	<i>Directeur de thèse</i>

## Table of Contents

<b>General Introduction .....</b>	<b>1</b>
<b>Chapter I. Context .....</b>	<b>3</b>
I.1 Solar energy .....	3
I.1.1 Characteristics of the solar resource .....	3
I.1.2 Solar radiation .....	4
I.1.3 Solar spectrum .....	6
I.2 Hybrid halide perovskite material .....	7
I.2.1 Types and properties of perovskite materials .....	7
I.2.2 Types and properties of perovskite materials .....	10
I.3 Perovskite Solar Cells .....	13
I.3.1 Solar Cells .....	13
I.3.2 Basic introduction to perovskite solar cells .....	23
I.3.3 The working principle of perovskite solar cells .....	25
I.4 Conclusions .....	26
References .....	27
<b>Chapter II. Exploring perovskite solar cells: From the cation composition to the cell structure.....</b>	<b>32</b>
II.1 Mono- to Triple-Cation Hybrid Perovskites for High Efficiency Solar Cells .....	32
II.1.1 Introduction .....	32
II.1.2 Experimental .....	34
II.1.3 Characterizations of Perovskite Films .....	37
II.1.4 Characterizations of PSCs .....	44
II.1.5 Conclusions .....	50
II.2 Effects of 5-Ammonium Valeric Acid Iodide as Additive on two different structure of Perovskite solar cells .....	51

II.2.1 Introduction .....	51
II.2.2 Experimental .....	53
II.2.3 Characterizations of Perovskite Films.....	54
II.2.4 Characterizations of PSCs.....	60
II.2.5 Conclusion.....	64
References.....	64
<b>Chapter III. Effects of gold nanoparticles on the growth and performances of MAPbI<sub>3</sub> perovskite solar cells. ....</b>	<b>70</b>
III.1 Introduction.....	70
III.2 Experimental .....	71
III.2.1 Preparation of Pristine and Composite Perovskite Films .....	71
III.2.2 Characterizations Method .....	72
III.3 Characterizations of perovskite Films .....	73
III.3.1 TEM, SEM and AFM .....	73
III.3.2 XRD .....	77
III.3.3 DSC.....	77
III.3.4 GD-OES.....	78
III.3.5 EDX .....	83
III.3.6 Absorbance .....	84
III.3.7 Steady-state PL and TRPL.....	86
III.4 Simulations of gold nanoparticles optical effect.....	87
III.5 Characterizations of PAI Treated perovskite Films.....	92
III.5.1 SEM and AFM.....	93
III.5.2 XRD .....	94
III.5.3 Absorbance and Steady-state PL .....	96
III.6 Characterizations of PSCs.....	97

III.7 Conclusions.....	100
References.....	101
<b>Chapter IV. Synergistic Effects of Ammonium Chloride and Potassium Chloride Additives on the Growth of Methylammonium-Free Perovskite Films for Efficient, Hysteresis-Free, Highly Stable Solar Cells.....</b>	<b>103</b>
IV.1 Introduction.....	103
IV.2 Experimental.....	104
IV.2.1 Preparation of Films and powder adducts .....	104
IV.2.2 Characterizations Method.....	106
IV.3 Characterizations of perovskite Films .....	106
IV.3.1 SEM and AFM.....	106
IV.3.2 XRD.....	108
IV.3.3 DSC .....	110
IV.3.4 GD-OES.....	112
IV.3.5 TRPL.....	115
IV.3.6 Absorbance .....	116
IV.4 Characterizations of PSCs .....	116
IV.4.1 $J-V$ curves and EQE.....	116
IV.4.2 GD-OES.....	119
IV.4.3 Stability.....	123
IV.5 Conclusions.....	126
References.....	128
<b>Chapter V. From Mono- to Tri-Alkali Metal Cations: The Mechanism of how Ammonium Chloride effect on Film Formation Process of MA-Free Halide Perovskite .....</b>	<b>131</b>
V.1 Introduction.....	131
V.2 Experimental .....	133

V.2.1 Preparation of Perovskite Films .....	133
V.2.2 Characterization Methods .....	135
V.3 Characterizations of perovskite Films.....	135
V.3.1 SEM .....	136
V.3.2 XRD .....	138
V.3.3 DSC.....	145
V.3.4 GD-OES .....	147
V.3.5 Absorbance and Steady PL .....	154
V.4 Characterizations of PSCs.....	155
V.4.1 <i>J-V</i> curves and EQE .....	155
V.4.2 Stability .....	158
V.5 Conclusions .....	159
References.....	160
<b>Chapter VI. The Effect of PAI post-treatment on Perovskite layer.....</b>	<b>162</b>
VI.1 Introduction.....	162
VI.2 Experimental.....	162
VI.2.1 Preparation of Perovskite Films.....	163
VI.2.2 Post-treatment Method.....	163
VI.2.3 Characterizations Method.....	163
VI.3 Characterizations of perovskite Films .....	163
VI.3.1 SEM.....	163
VI.3.2 XRD.....	164
VI.3.3 Absorbance and Steady-state PL .....	165
VI.3.4 TRPL.....	165
VI.4 Characterizations of PSCs .....	167

VI.4.1 <i>J-V</i> curves and EQE.....	167
VI.4.2 Stability.....	170
VI.5 Conclusions.....	172
References.....	173
<b>General Conclusion and Perspectives .....</b>	<b>174</b>
Annex I-Chapter I .....	178
Annex II-Chapter II.....	180
A.II.1. Mono- to Triple-Cation Hybrid Perovskites for High Efficiency Solar Cells .....	180
A.II.2. Effects of 5-Ammonium Valeric Acid Iodide as Additive on two different structure of Perovskite solar cells.....	191
Annex III-Chapter III.....	200
Annex IV-Chapter IV .....	205
Annex V-Chapter V .....	214
Annex VI-Chapter VI .....	223
List of publications .....	225

## General Introduction

From the perspective of energy strategy, fossil energies as non-renewable energy sources, are quickly exhausting with reserves which significantly reduce with time and costs which go up sharply. Moreover, fossil fuels cause the increase of the earth average temperature due to the released CO<sub>2</sub> gas which produces a greenhouse effect. To slow down this effect, the use of renewable energy will reduce CO<sub>2</sub> emissions, which will play a key role in many ways. Among all renewable energy sources, solar PV occupies an important part.

In Chapter I, we will start with solar energy and focus on the application of solar energy. With the continuous expansion and improvement of the application scale and R&D level of solar cells, the third-generation solar cells have the advantages of high conversion efficiency, low production cost and environmental friendliness. However, it is limited by the material structure or the immature preparation process. The current conversion efficiency of third-generation solar cells is relatively low. However, the advent of perovskite solar cells has injected a new vitality into third-generation solar cells research and has become one of the most interesting and promising emerging technology. Due to the short development time, the structural design, assembly process and working mechanism of perovskite solar cells are still under exploration. Especially in the construction of various solar cell structures, such research is of great significance for the selection and optimization of key components.

In part one of Chapter II, we fully investigate the effect of the number of monovalent cations on the electrical response of PCSs with high efficiency in their category. More precisely, the compared perovskites are: MAPbI<sub>3</sub>, FA<sub>0.94</sub>MA<sub>0.06</sub>PbI<sub>3</sub> and Cs<sub>0.08</sub>FA<sub>0.80</sub>MA<sub>0.12</sub>Pb(I<sub>0.88</sub>Br<sub>0.12</sub>)<sub>3</sub>. I have made a thorough optimization work of these cells upon my PhD in collaboration with Tao Zhu, another PhD student of Pauporté's group. In part two of Chapter II, we focus on 5-ammonium valeric acid iodide (5-AVAI or AVA) as additive. By combining scanning electron microscopy (SEM), x-ray diffraction (XRD), time-resolved photoluminescence (TRPL), current-voltage measurements, ideality factor determination and electrical impedance spectroscopy (EIS) measurements on various layers stacks structures, we have discriminated the effects of mesoscopic embedding scaffold and AVA additive.

In Chapter III, we comprehensively analyze the effect of Au\_NPs inclusion in the PVK (MAPbI<sub>3</sub>) film through the combination of absorption simulation and experiments. Our results show that the effect of Au\_NPs on the improvement of the quality of the perovskite layer is far greater than that of the increase in light harvesting. In order to further boost the performance of perovskite solar cells, we introduced a post-treatment technique, leading to the formation of a 2D capping layer on the top-surface of MAPbI<sub>3</sub> perovskite layer.

In Chapter IV, we report on the use of ammonium chloride (NH<sub>4</sub>Cl) and potassium chloride (KCl) mixed additives to control Cs<sub>0.1</sub>FA<sub>0.9</sub>PbI<sub>3</sub> crystallization and get the desirable lateral growth of the perovskite films. By using DSC and GD-OES techniques, we highlight the formation mechanism of the film upon annealing. We have also employed the GD-OES technique to investigate the mobility of I in the PVK layers, to demonstrate that K blocks the ionic mobility and to correlate iodide displacement with the *J-V* curve hysteresis.

In Chapter V, we mainly reveal the following three issues at the same time and link them together: 1) The role of ammonium chloride in perovskite containing multi-alkali metal cations; 2) How multiple metal ions move during the film formation process; 3) The effect of additives on film forming direction and distribution of multi metal cations in perovskite films.

In Chapter VI, through the application of PAI post-treatment to Cs<sub>0.1</sub>FA<sub>0.9</sub>PbI<sub>3</sub> and K<sub>0.05</sub>Rb<sub>0.05</sub>Cs<sub>0.10</sub>FA<sub>0.80</sub>PbI<sub>3</sub> systems, we found a great improvement of the performance of the solar cells, not only in their efficiency, but also in their stability.

In the end of this thesis, a general conclusion and perspectives are provided.

## Chapter I. Context

### I.1 Solar energy

The world energy pattern and the needs of renewable energy are introduced in the **Annex I**, where we highlight the importance of energy transition. Among all renewable energy sources, solar PV occupies an important part. In this part, we will start with solar energy and focus on the application of solar energy.

As we all know, the sun continuously releases of a colossal energy due to the fusion reaction and this energy reaches the earth as radiations. Familiar renewable energy sources such as wind energy, hydropower, biomass energy, etc. are indirectly related to the sun energy from the viewpoint of energy conservation. Traditional petrochemical energy is also formed by ancient living organisms which absorbed solar energy and converted it into chemical energy and stored it in their body. After death, they were buried underground for a long geological age. According to the earth's equatorial circumference (about 40,000 kilometers) and the radiation intensity in the orbit of the sun (average 1369 W/m<sup>2</sup>), it can be calculated that the energy received by the earth is as high as 173,000 TW. [1] Although it is a small part of solar radiation energy (approximately  $3.75 \times 10^{26}$ W), it has already met all the needs of the earth, including human activities. According to estimates, only 0.1% of the earth's surface area needs to be covered with solar cells with a conversion efficiency of 10% to meet current humanity energy demand [1].

#### I.1.1 Characteristics of the solar resource

Compared to traditional energy sources such as coal, oil, natural gas, and nuclear energy, solar energy has the following obvious advantages:

(1) Less geographical restrictions: Except for a few cloud-filled areas and the north and south poles, it is distributed both on land and on the oceans, and it can be developed and used on-site without transportation.

(2) Clean and pollution-free: Solar energy does not produce greenhouse gases, various pollutants, or radiation pollution during the use of solar energy. It is one of the cleanest energy sources available in the world.

(3) Huge reserves: The sun itself can continue to burn for more than 5 billion years, so it can be said that solar energy is inexhaustible.

(4) Convenient use: Solar energy can be directly converted into heat or electric energy (photovoltaics) and used by people, and unlike tremendous hydropower, thermal power, and nuclear power facilities, solar cells can be employed in large-scale power stations, as well as applied to power watches, calculators, airplanes, satellites, space stations and so on.

Although there are many advantages in developing and utilizing solar energy, the following shortcomings remain to be overcome:

(1) Low energy density: Although the total amount of solar radiation is large, the energy density is relatively low. In the case of limited conversion efficiency, the only way to obtain more energy is to increase the radiation-receiving surface area.

(2) Poor stability: Restricted by natural conditions such as day and night, seasons, and weather, the solar radiation arriving at a fixed location fluctuates widely.

(3) Low efficiency and high cost: Although the operation and maintenance costs are meager, the conversion efficiency of current solar energy utilization devices are generally low, and the construction cost is rather high.

### **I.1.2 Solar radiation**

In the process of solar radiation passing through the earth's atmosphere and reaching its surface, due to the reflection, absorption, and scattering of the solar radiation by particles, water vapor, and air molecules in the atmosphere, the intensity, direction, and spectral division of the radiation change. Therefore, the solar radiation received by the ground is generally divided into two parts: scattered radiation and direct radiation. Among them, direct radiation refers to the radiation arriving directly from the sun and whose direction does not change. It is the central part of the investigation in practical

applications. Scattered radiation is the solar radiation whose direction changes after being reflected and scattered by the atmosphere and it has a wide range of changes. When the weather is clear and cloudless, the scattered radiation is about 10% of the total radiation.

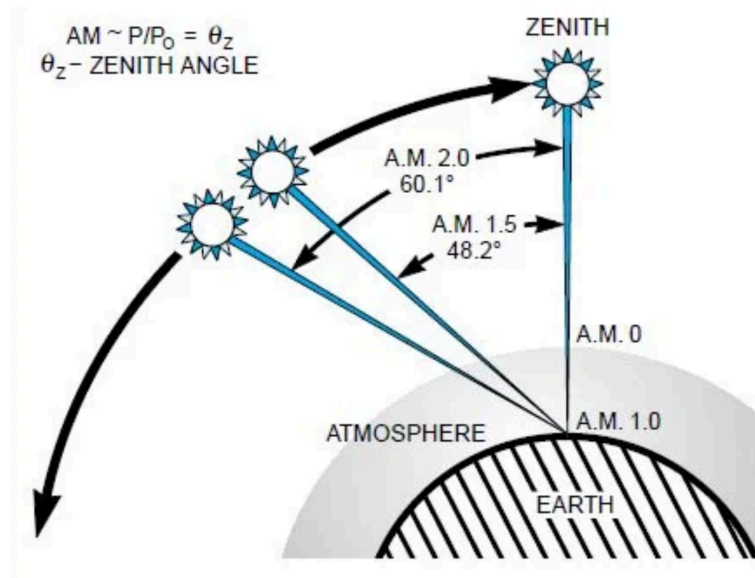


**Figure I.1 Path length, in units of Air Mass (AM), changes with the zenith angle.**

The influence of the atmosphere on the sunlight received by the surface of the earth is generally described by the atmospheric optical quality (Air Mass, AM), which is defined as the ratio of the actual path through which solar radiation passes and the path when the sun is perpendicular to the zenith direction. The air mass of zero (AM0) corresponds to sunlight received outside the atmosphere and is suitable for space application scenarios such as artificial satellites and space stations. The air mass coefficient defines “1” as the path length light travels through when the Sun is directly overhead at sea level. The spectrum of light after travelling through this path length of one atmosphere is what we call Air Mass 1 or AM1. In this case, the sun’s direct radiation passes vertically through the atmosphere in the shortest possible path. The difference between the two lies in the sun's absorption and scattering by ozone, water vapor, dust, and suspended matter in the atmosphere. In most cases, the incident sunlight is not perpendicular but forms an angle  $\theta$  with the ground normal. At this time, the optical quality of the atmosphere is  $AM=1/\cos \theta$ . When  $\theta=48.2^\circ$ , the atmosphere's optical quality is AM1.5 (Figure I.1), and the total radiation power density is  $1000 \text{ W/m}^2$ , which is in line with the typical

situation of sunlight hitting the ground on a sunny day at European latitudes. AM1.5 is generally selected as solar energy in practical applications and is the standard for solar cells efficiency testing.

### I.1.3 Solar spectrum

The solar radiation approximately meets the blackbody radiation model. As the sun's surface temperature is as high as 5778 K, the solar spectrum is close to the blackbody one and can be roughly divided into three regions. The ultraviolet wavelength region lies below 400 nm, the infrared region is above 760 nm, and the visible light ranges between 400-760 nm. They account for 7%, 43%, and 50% of the total solar radiation energy, respectively. The highest energy peak is at 475 nm. **Figure I.2** (left) shows the solar radiation spectrum under different conditions. Due to the influence of the reflection, absorption, and scattering of ozone, water vapor, carbon dioxide, and other gas molecules and dust when the solar radiation crosses the earth atmosphere (AM1.5) presents absorption bands, compared with the outer space (AM0) (**Figure I.2**, right). The spectrum range that can be converted by solar cells depends on the light absorption materials used. It is speculated that if the AM1.5 solar radiation spectrum with a wavelength less than 800 nm can be converted entirely into electric energy, the short-circuit current of 26 mA/cm<sup>2</sup> can be obtained [2].

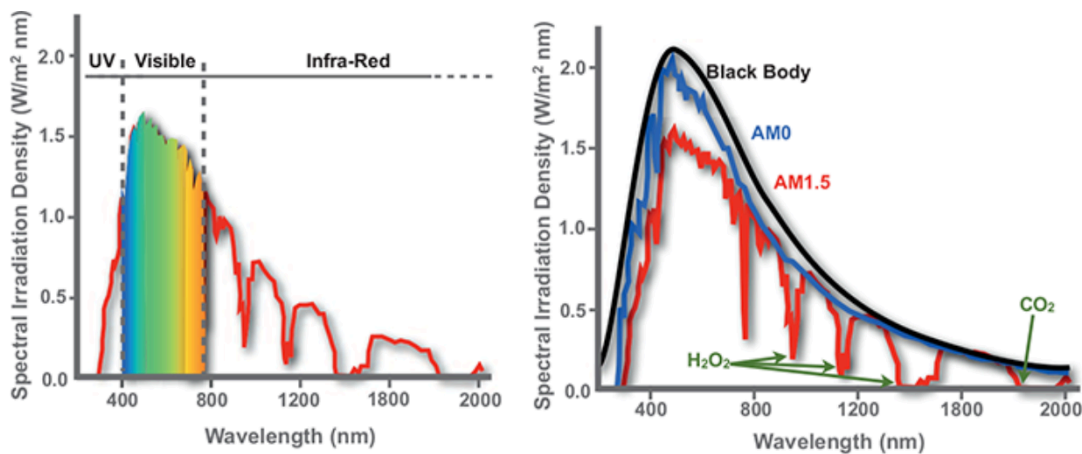


**Figure I.2** Left: spectral irradiation density at AM1.5 versus different wavelengths, showing the UV, visible and infrared wavelength region. Right: spectral irradiation density versus different wavelengths for AM0 and AM1.5, and for a black body with a temperature of 5760 K.

## I.2 Hybrid halide perovskite material

### I.2.1 Types and properties of perovskite materials

Perovskite is a kind of natural mineral with an  $ABX_3$  structure. In 1839, scientist Gustav Rose first discovered a natural mineral with a perovskite structure ( $CaTiO_3$ ) in the Ural mountain in Russia. He named it perovskite in honor of the Russian mineral scientist L.A.Perovski.

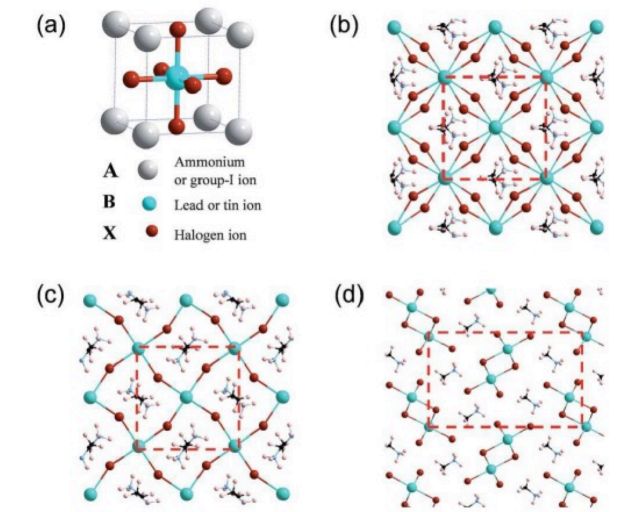


**Figure I.3** The atomic structure of Organic and inorganic hybrid perovskite materials: (a)  $\alpha$ -Phase, (b)  $\beta$ -Phase, (c)  $\gamma$ -Phase and (d)  $\delta$ -Phase. [3]

3D halide perovskites have the  $ABX_3$  general chemical formula, where A is a monovalent cation (classically  $Cs^+$ , methylammonium (noted  $MA^+$ ) or formamidinium ( $FA^+$ )), B is a divalent metal cation, usually lead, and X is a halide anion (typically  $Cl^-$ ,  $Br^-$ ,  $I^-$  or their mixtures). The crystal structure of the chemical formula  $ABX_3$  is generally divided into three categories: cubic structures ( $\alpha$ -Phase, **Figure I.3a**), tetragonal ( $\beta$ -Phase, **Figure I.3b**) and orthorhombic ( $\gamma$ -Phase, **Figure I.3c**). It is composed of a  $BX_6$  octahedron with an X position as the connection point to form its crystal structure's skeleton. The A position is filled in the octahedral gap to maintain the electrical neutrality of the overall structure. When  $FA^+$  and  $Cs^+$  are used as cations, it is possible to produce  $\delta$ -Phase (**Figure I.3d**) which is not perovskite crystal structure.[3] When the temperature is different, the three structures will be transformed into each other. Take  $CH_3NH_3PbI_3$  perovskite material as an example, after the temperature rises to 330K, the crystal structure begins to transform from phase  $\alpha$  to  $\beta$ -Phase [4]. When

the temperature drops below 160k,  $\beta$ -Phase will be transformed into  $\gamma$ -Phase. This kind of phase transition can explain the poor high-temperature stability of some perovskite materials.

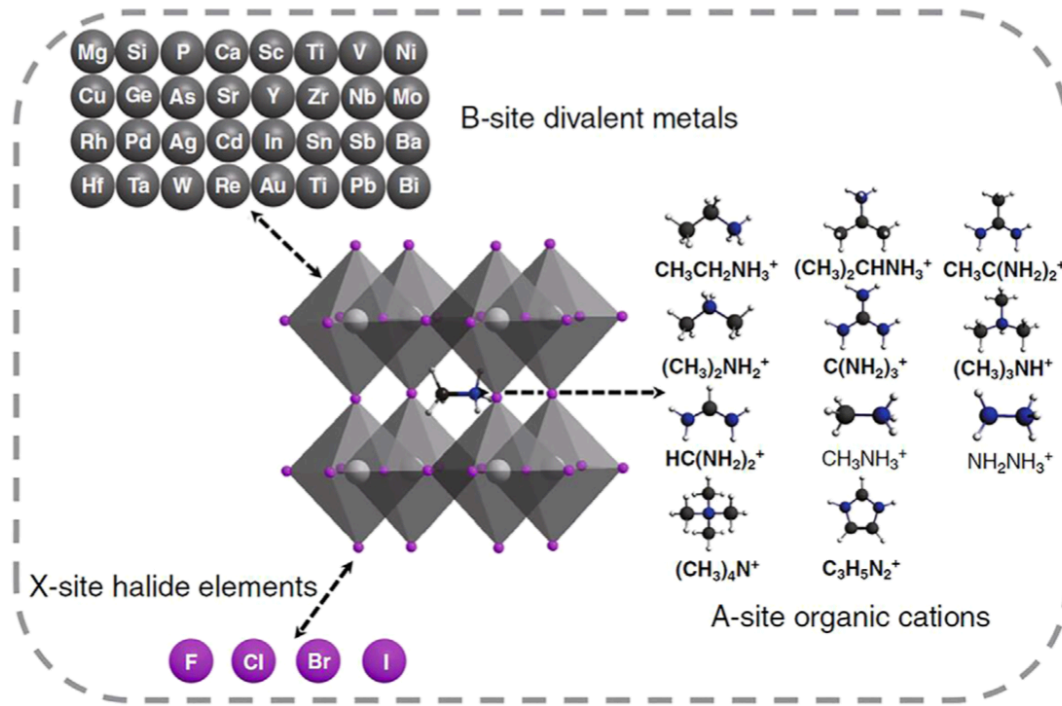


**Figure I.4 Schematic diagram of ABX<sub>3</sub> and the corresponding possible components. [5]**

In all-inorganic perovskites, the A site is a positive monovalent alkali metal ion (K<sup>+</sup>, Rb<sup>+</sup>, Cs<sup>+</sup>, etc) (**Figure I.4**). Due to the different ionic radii of different elements, all ions are usually regarded as rigid spheres in the process of ion combination. One defines the tolerance factor ( $t$ ) of the combined structure and the size of the octahedral factor  $u$ . They are given by the following formulas [6]:

$$t = \frac{r_A + r_X}{\sqrt{2}(r_B + r_X)}$$

$$u = \frac{R_B}{R_X}$$

where,  $r_A$ ,  $r_B$ ,  $r_X$  represent the radius of A, B, and X, respectively. The most suitable perovskite material as the active layer is the  $\alpha$ -phase, and the tolerance factor of the ideal  $\alpha$ -phase structure is  $t=1$ . When  $0.81 < t < 1.11$ , the perovskite crystal structure can form a relatively stable  $\alpha$ -phase[7]. When the tolerance factor  $t > 0.89$ , the crystal structure is easily transformed from phase  $\alpha$  to  $\beta$ -phase and  $\gamma$ -phase [8]. When  $t > 1.11$ , the crystal structure transforms into an unstable two-dimensional structure[9]. However, even if the tolerance factor is in the range of  $0.81 < t < 1.11$ , sometimes the perovskite crystal

structure may not maintain the  $\alpha$ -phase. At this time, the octahedral factor ( $u$ ) must be considered at the same time. It is generally believed that the octahedral factor should be in the range of  $0.44 < u < 0.9$ [10].

The energy bandgap of a perovskite material is closely related to its composition. Due to the difference in ionic radius of different components, this will cause the lattice to expand or to shrink. For example: if the ion radius of the A-site increases, the lattice will expand, and the bandgap will decrease. If the X-site is doped with a halogen element with a larger ion radius, the bandgap will decrease. This is a primary method to adjust the energy bandgap of halogen perovskites [11].

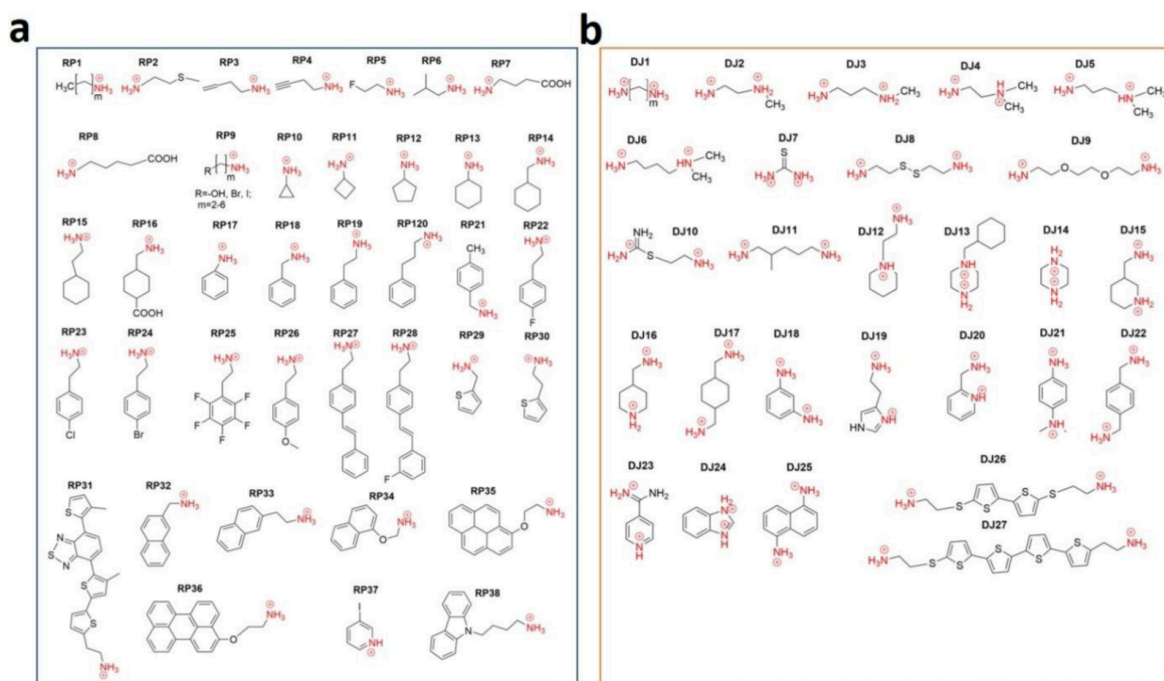


**Figure I.5 Summary of different bulky cations for 2D perovskites. [12]**

However, when a long-chain monovalent organic cation with an enlarged ionic radius (such as PEA, PMA, BA, etc. **Figure I.5** defined as A), the A-site cannot be restricted to the interstitial position of  $BX_6$ , thereby destroying the cubic crystal structure of the perovskite and forming a blocking layer. The Ruddlesden-Popper layered perovskite structure separated by groups at the A position has the general structural formula:  $(A')_2A_{n-1}b_nX_{3n+1}$  (**Figure I.6**). The three-dimensional perovskite structure corresponds to  $n=\infty$  while for quasi-two-dimensional structure,  $n$  is an integer.

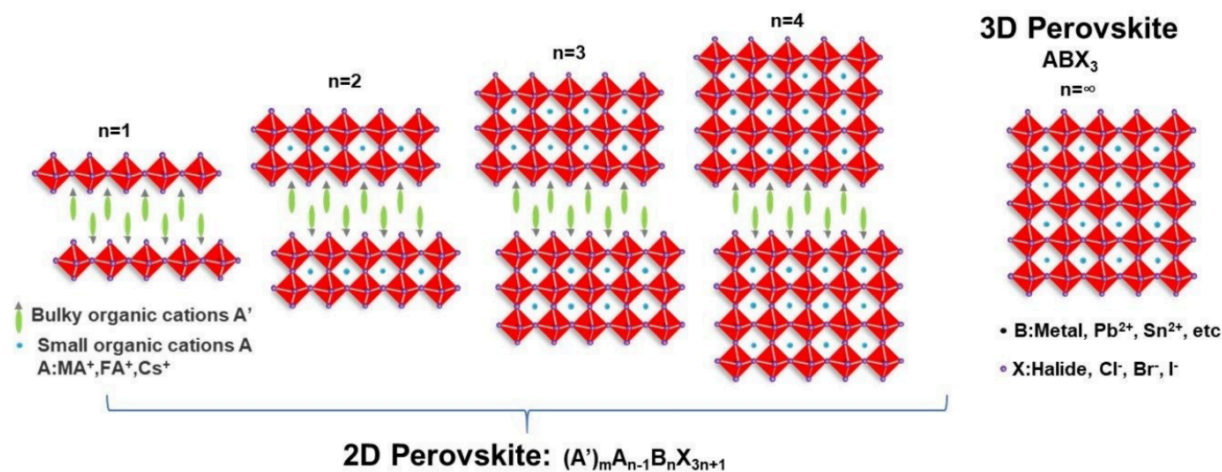


**Figure I.6 Schematic comparing 2D and 3D perovskite structures. [12]**

Two-dimensional structure corresponds to  $n=1$ . When the value of  $n$  decreases, the bandgap increases [13]. The exciton binding energy in low-dimensional perovskites increases with  $n$  decrease and can be relatively large (up to 300 meV), so after light excitation or carrier injection, the formed excitons are stable in combination, which will help improve the quantum yield and efficiency of the film for light emission but is detrimental for solar cells [14, 15].

## **I.2.2 Types and properties of perovskite materials**

### ***I.2.2.1 Solar Cells***

At present, perovskite solar cell (PSC) structures mainly include non-planar structure, planar structure, and flexible structure. Among them, planar perovskite solar cells' technology is relatively simple which is a positive point for industrial production. The cost of flexible perovskite solar cells is relatively high [16], and their rather low photoelectric conversion efficiency [16], requires more research and improvement. At present, the area of research perovskite solar cells prepared in laboratories is rather small [17, 18], and cannot meet practical application needs. The preparation of large areas and high-efficiency perovskite solar cells is the key research direction for the future. For the application of perovskite in solar cells, I will give a detailed introduction in the following **Section I.3**.

### ***I.2.2.2 Quantum dots and luminescence applications***

The application of lead halide-based perovskite thin-film materials and their quantum dots in LED and photodetection fields has also received extensive attention [19-21]. Because lead halide-based

perovskite materials have high luminescence efficiency [22, 23] and continuously adjustable light emission wavelengths [24-26], they have good application potential in the field of light-emitting diodes (LEDs) [27, 28]. At present, the most widely used LED devices are organic-inorganic hybrid lead halide perovskite  $\text{CH}_3\text{NH}_3\text{PbX}_3$  ( $X = \text{Cl, Br, I}$ ) materials, and the light-emitting bands of these devices include blue light [29], green light [28], infrared and so on [30-31]. Compared to organic-inorganic hybrid lead-halogen-based perovskite materials, there are relatively few reports on the preparation of LED devices using all-inorganic  $\text{CsPbX}_3$  ( $X = \text{Cl, Br, I}$ ) perovskite materials. In October 2015, a green LED prepared with  $\text{CsPbBr}_3$  [32] was reported for the first time. Soon after, blue, green, and yellow LED devices prepared with  $\text{CsPbX}_3$  ( $X = \text{Cl, Br, I}$ ) quantum dots were reported in the literature [33]. In the past two years, white LEDs based on  $\text{CsPbX}_3$  ( $X = \text{Cl, Br, I}$ ) quantum points [34], nanocubes, nanowires [35], and  $\text{Cs}_4\text{PbBr}_6$  single crystals appeared [36]. Compared with pure  $\text{CsPbX}_3$  quantum dot LED, the device's external quantum efficiency and current efficiency are improved. Gabriele Rainò of the Federal Institute of Technology's research group in Zurich [37] realized lead halide perovskite nanocrystals ( $\text{CsPbX}_3$ ,  $X = \text{Cl, Br}$ ) self-assembled into a three-dimensional superlattice and discovered that the perovskite superlattice could emit super-fluorescence. At present, in the research of glass-ceramic materials for high-power white light LEDs, a new technical route for the preparation of white light LEDs has been developed. Light sources' emission efficiency encapsulated with glass-ceramic materials has reached or even exceeded the technical indicators of mainstream LED lighting fixtures in the current market.

Besides, lead halide perovskite is a new type of luminescent material with significant application potential in photodetection and display. With the development of nanomaterials and nanotechnology, nanoscale perovskite materials, namely perovskite quantum dots, have higher luminous efficiency. Compared with bulk materials, perovskite quantum dots have greater exciton binding energy, the surface state is easier to control, and has quantum confinement effects. These properties make perovskite quantum dots easier to be applied to optoelectronic devices. [38]. In 2016, Ramasamy et al. [39] first used all inorganic  $\text{CsPbI}_3$  quantum dots to prepare photoelectric detection devices. They also used graphene with high carrier mobility as the transport layer to fabricate the photodetector [40].

Recently, Dr. Wu Yuchen and academician Jiang Lei cooperated with Professor Fu Hongbing of Tianjin University and Professor Zhang Xiang of University of California Berkeley to prepare high-quality two-dimensional perovskite single-crystal nanowire arrays and discovered the edge state photoconductivity effect of two-dimensional perovskite nanowires and realized the world's most sensitive perovskite photodetector. [41]

### 1.2.2.3 Application of lead halide-based perovskite radiation detector

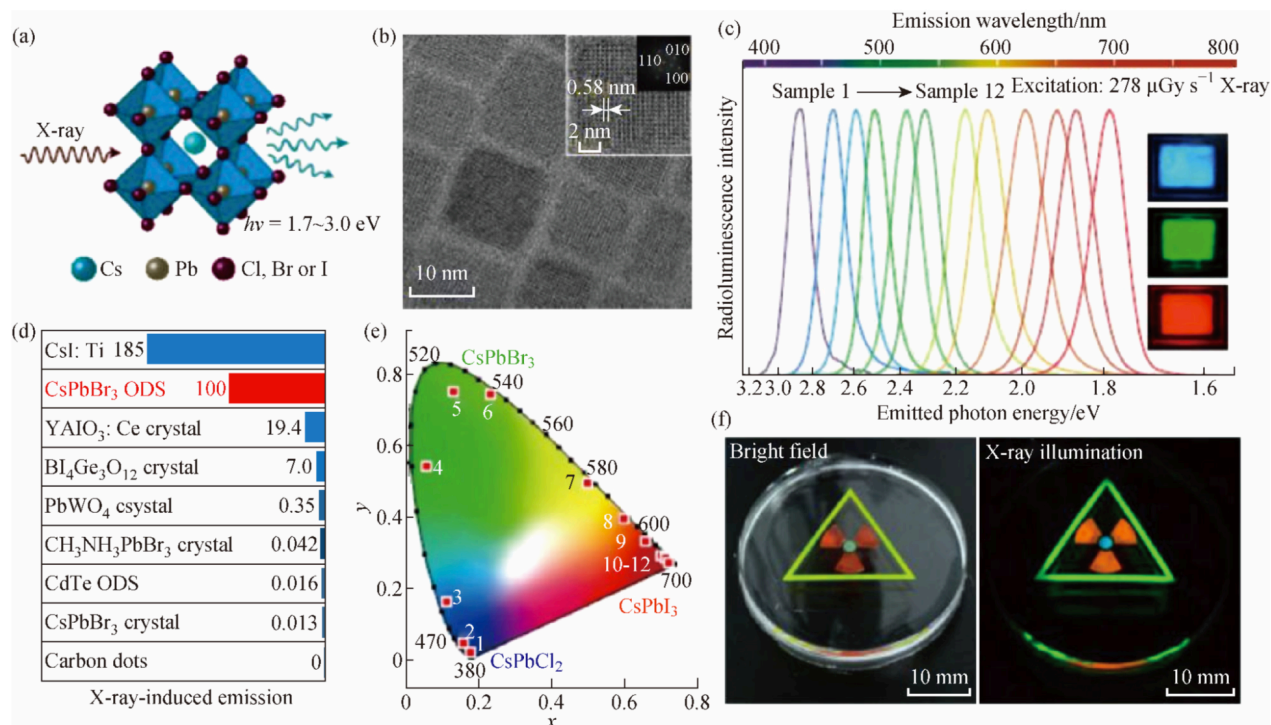


**Figure I.7 Full-color radioluminescence from perovskite nanocrystal Scintillators [12]**

With the increasing demand for radiation detection materials in various fields, scintillator materials have attracted widespread attention. Conventional scintillator materials are generally bulk materials synthesized by high-temperature crystallization, which are expensive, have limited conversion efficiency of X-ray photon energy, and which radioluminescence properties are difficult to be tuned in the visible light region. Studies have shown that the organic-inorganic hybrid lead halide perovskite material has excellent properties for indirect X-ray detection. Its X-ray absorption coefficient is significant, the carrier diffusion distance is long, and the preparation cost is low. It has received widespread attention from scientific researchers from all over the world. Compared to organic-inorganic hybrid perovskite, all-inorganic lead halide cesium perovskite (CsPbX<sub>3</sub>) has superior

stability. In 2018, academician Huang Wei from Northwestern Polytechnical University and Professor Liu Xiaogang from the National University of Singapore discovered an all-inorganic lead halide-based perovskite nanocrystalline scintillator material (**Figure I.7**) [12]. This type of nanocrystalline scintillator exhibits super-strong X-ray absorption capacity, high-efficiency triplet luminescence characteristics, adjustable electronic energy level structure, and fast radioluminescence rate. Unlike other inorganic scintillators, these perovskite nanocrystals are prepared from solutions and have a lower synthesis temperature. They can generate X-ray-induced excitation and be tuned in the visible light region by changing the anion in the synthetic precursor and exhibit stimulated radioluminescence in the visible light band. Researchers use this material to create a flexible and highly sensitive X-ray detector, the detection limit was as low as  $13 \text{ nGy}\cdot\text{s}^{-1}$ , which is 1/400 of the dose of ordinary medical imaging radiation. Besides, by changing the anions in the perovskite nanocrystal synthesis precursor, it is possible to realize its tunable luminescence in the visible light band, which provides a more straightforward visual method detection of X-rays. At the same time, it can also be integrated with commercial flat-panel imagers to detect low-dose X-ray radiation from electronic circuit boards. The emergence of such all-inorganic lead-halide-based perovskite nanocrystalline scintillators will significantly promote X-ray detection technology and imaging principles in medical imaging, national defense technology, security inspection, and high-energy physics research.

### **I.3 Perovskite Solar Cells**

#### **I.3.1 Solar Cells**

The conversion of solar energy into an usable energy is mainly divided into light/heat, light/chemistry, and light/electricity. Light and heat have a long history, mainly using solar radiation to heat other objects, and can be further converted into mechanical energy and electrical energy. Photochemical utilization is mainly the use of solar energy into chemical energy for further storage and use. The current development trend is the use of photocatalytic reactions to produce hydrogen. Photovoltaic power generation is the employment of solar cells to convert solar energy into convenient electrical energy. Its emergence and development mark a new stage of human development and utilization of solar energy.

### *1.3.1.1 The development of solar cells*

In 1839, French experimental physicist E. Becquerel put two platinum plates into a halide solution in an experiment and found that an electrical current could be detected between the two plates when they were illuminated. The voltage changed with the change of light intensity. It was the first observation of the photovoltaic phenomenon by human beings [42].

In 1877, W. G. Adams and R. E. Day studied the photovoltaic effect of selenium semiconductors and made a prototype of selenium solar cell which power conversion efficiency reached 1%.

In 1883, C. Fritts, an American inventor, prepared 30 cm<sup>2</sup> large area selenium thin-film cells and described Se solar cells' principle.

In 1904, Hallways reported the photosensitive Cu /Cu<sub>2</sub>O heterojunction.

In 1905, German physicist A. Einstein published a paper on the photoelectric effect and the Nobel Prize in Physics 1921 was awarded to Albert Einstein for his services to theoretical physics, and especially for his discovery of the law of the photoelectric effect.

In 1930, W. Schottky put forward the theory of the "photovoltaic effect" of the Cu<sub>2</sub>O barrier for the first time. The same year, B. Langer studied the Cu /Cu<sub>2</sub>O solar cell and put forward the theory for the first time that the "photovoltaic effect" can be used to manufacture solar cells.

In 1941, R. S. Ohl of Bell laboratory discovered the photovoltaic effect and prepared a semiconductor p-n junction solar cell.

In 1953, Dr. D. Trivich of Wayne State University made the first theoretical calculation of various optoelectronic materials' energy conversion efficiency with different bandgaps based on the solar spectrum.

In 1954, D.M. Chapin, C.S. Fuller, and G.L. Pearson, researchers of Bell laboratory in the United States, invented the monocrystalline silicon solar cell with a power conversion efficiency of 6%. So far, the first practical solar cell with milestone significance has officially stepped on the stage of history.

Since then, with the continuous improvement of various solar cell theories, the preparation process and conversion efficiency have been improved and applied to the satellite to achieve commercialization. CdTe, GaAs, amorphous silicon, and other materials and structures of solar cells have also emerged. After the first energy crisis in 1973, governments worldwide have launched projects such as the "sunshine plan" and "photovoltaic roof plan" to increase support to the solar photovoltaic industry.

### 1.3.1.2 Classification of solar cells

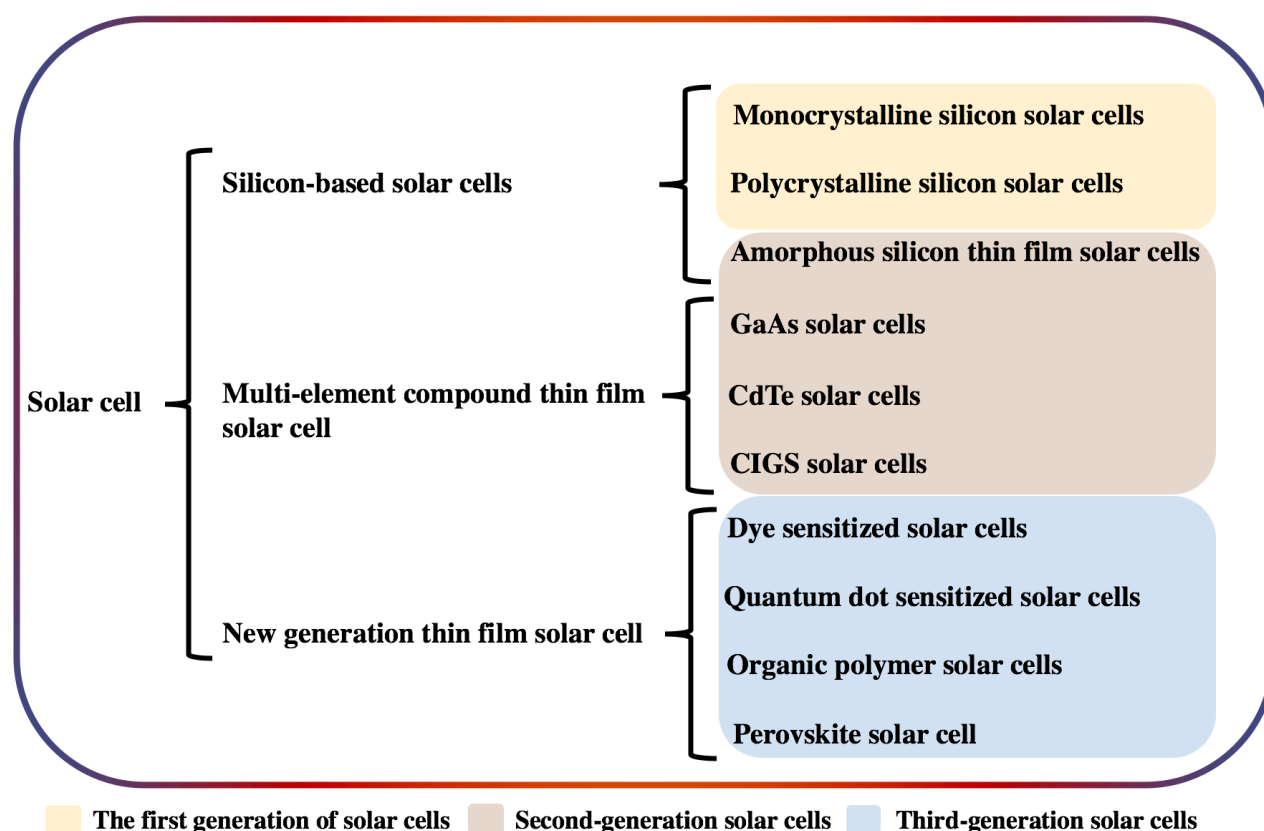


**Figure I.8** Classification of solar cells.

Various semiconductor electrical materials are employed for the production of solar cells. At present, according to the production materials and development history of solar cells, they can be divided into three generations (**Figure I.8**):

The first generation of solar cells encompasses silicon-based solar cells of single crystalline silicon [43, 44] and multicrystalline silicon [47, 48]. The certified conversion efficiency of single crystal silicon cells is 26.1% for one sun, and 26.7 % for the silicon heterostructures (see **Figure I.9**)

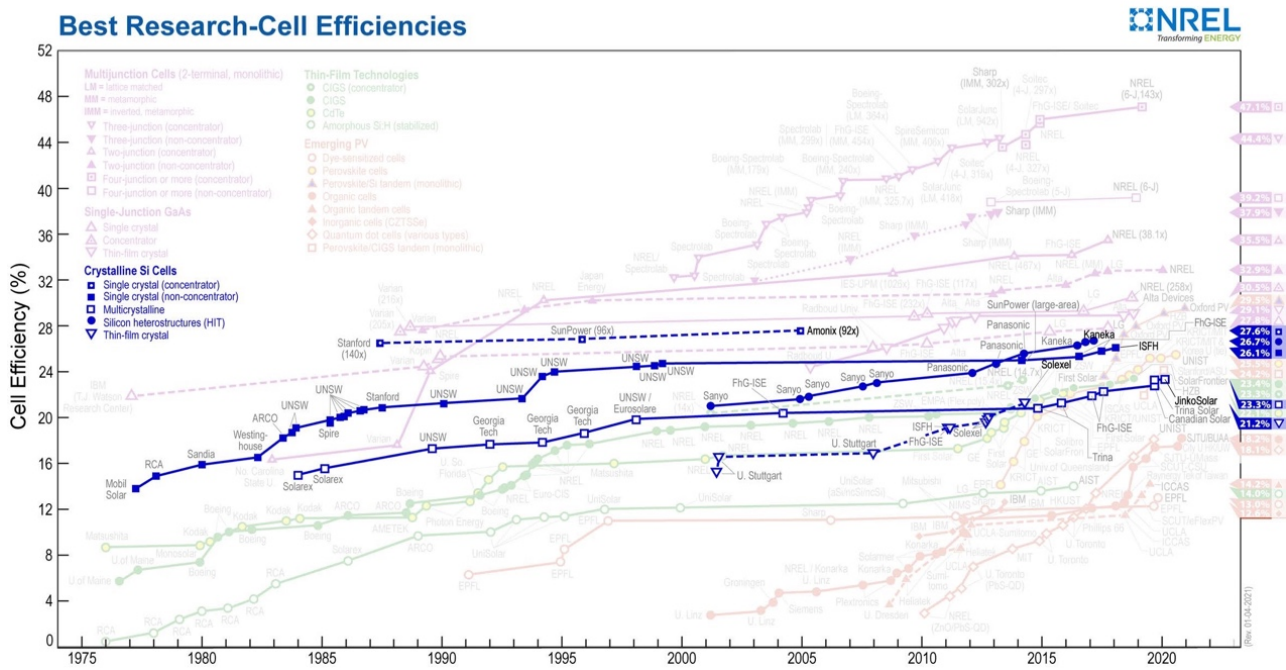


**Figure I.9 The best Research-Cell Efficiencies of Crystalline Si Cells (April, 2021).**

The second-generation solar cells encompass thin-film solar cells of amorphous silicon [47, 48] and multiple compounds including III-V compounds such as GaAs [49, 50], II-VI compounds such as CdS and CdTe [51, 52], copper indium gallium selenide (Cu-In-Ga-Se, CIGS) [53, 54] and other materials. Films prepared by chemical vapor deposition method can significantly save raw materials consumption, and their cost is significantly lower compared to the first-generation crystalline silicon solar cell. However, the shortcomings are also more prominent. The certified efficiency of amorphous silicon PV is 14.0% (**Figure I.10**) and their stability are much lower than that of crystalline silicon devices due to the Staebler-Wronski effect [55]. Multi-compound thin-film solar cells have higher efficiency (CIGS cell certified efficiency is 23.3%, CdTe cell certified efficiency is 22.1%, **Figure I.10**). However, GaAs and CdTe solar cells contain highly toxic elements such as As and Cd, which will cause damage to the environment and human health. It is a significant threat. The I-fit Se contained in CIGS batteries is a rare element with minimal reserves. Therefore, this type of solar cell is not an ideal substitute for the first generation of solar cells.

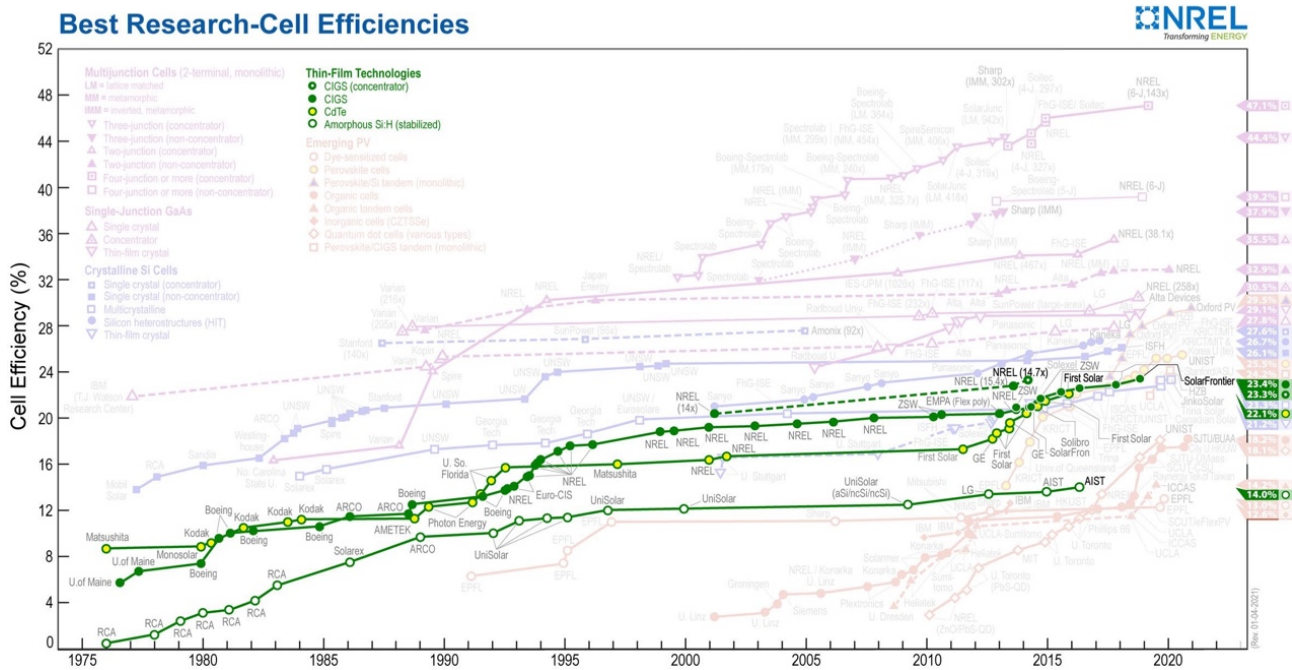


**Figure I.10 The best Research-Cell Efficiencies of Thin-films Technologies Cells (April, 2021).**

The third-generation solar cell gathers new concepts developed to solve the shortcomings of the previous two generations of solar cells. It requires the cell to be environmentally friendly, low cost, and have high conversion efficiency. It mainly includes organic solar cells [56, 57], dye-sensitized solar cells [58, 59], quantum dot sensitized solar cells [60, 61], perovskite solar cells [62, 63], etc. Organic polymer solar cells have the advantages of strong plasticity, simple preparation, no rare elements, and low cost, but their current lifetime and conversion efficiency are low. The dye-sensitized solar cells (DSSCs), invented in 1991 by Professor M. Grätzel from EPFL, Switzerland, use dye molecules adsorbed onto porous nano-titanium dioxide film, which has a high conversion efficiency meager production cost, which is only 1/3~1/5 of silicon-based solar cells. They have attracted great attention from scientists all over the world [64]. At present, the best certified efficiency is only 13.0% (Figure I.11). The structure and principle of quantum dot sensitized solar cells are similar to those of dye-sensitized solar cells. The main difference is that organic dyes are replaced by semiconductor quantum dots (QDs), including CdS, CdSe, PbS, InP, and InAs. Compared to dye molecules, semiconductor QDs have the advantages of simple and stable structure, large extinction coefficient, adjustable band gap, no rare elements such as Ru, and rich raw materials. QDs can also generate multiple excitons, and the theoretical conversion efficiency is higher than dye-sensitized solar cells.

However, quantum dot solar cells current highest certification efficiency is 18.1% (**Figure I.11**), which is higher than the highest certification efficiency achieved by DSSCs. Perovskite solar cell is a new type of solar cell that appeared in recent years. It has developed very rapidly. In just a few years, the certified efficiency has reached 25.5% (**Figure I.11**). Due to the third generation of solar cell, incompleteness, more than 90 % of the photovoltaic market is still occupied by crystalline silicon cells. However, with the continuous progress of cell preparation technology, especially the rapid improvement in various new cells' efficiency, new cells will surely compete with crystalline silicon cells in the future to achieve large-scale applications.

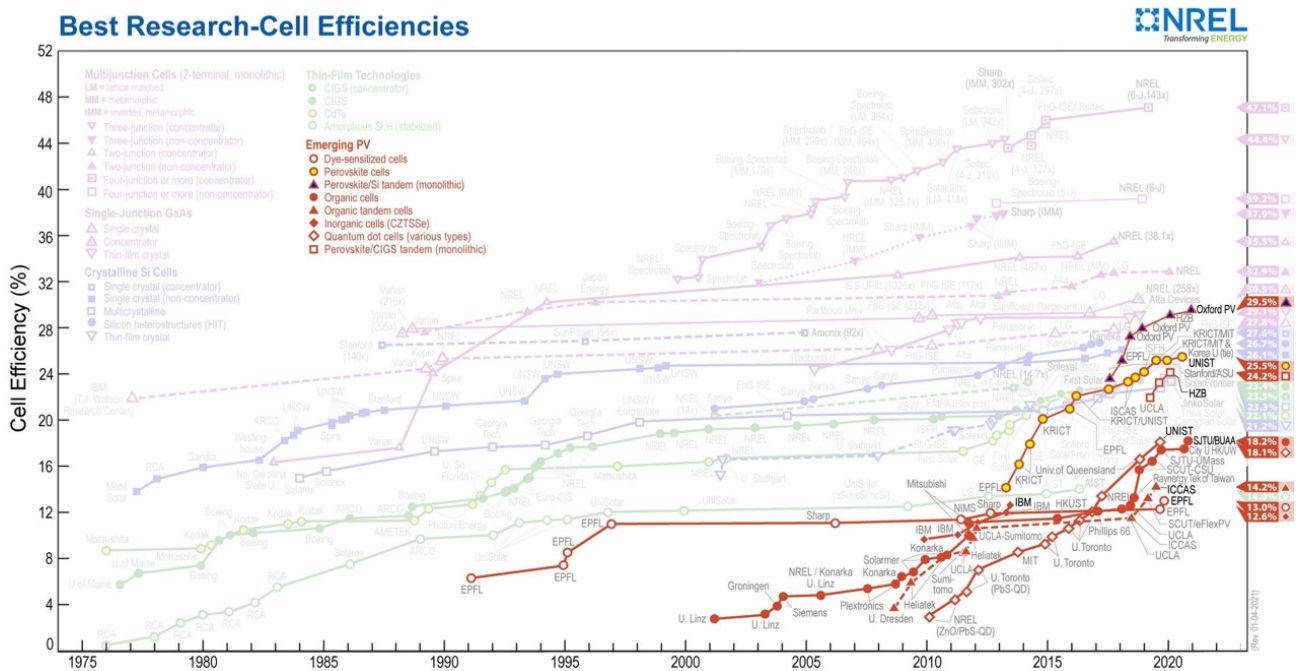


**Figure I.11 The best Research-Cell Efficiencies of Emerging PV (April, 2021).**

### 1.3.1.3 Working principle of solar cells

If the incident light energy is greater than the semiconductor bandgap, photons will promote electrons in the semiconductor conduction band (CB) and release a hole in the semiconductor valence band (VB). To generate an electrical current in an external circuit, the electron-hole pairs must be separated and collected at the two poles of the solar cell. An effective way is to establish an electric field inside the semiconductor. The most common method for most solid-state solar cells is to use a PN junction to establish this internal electric field (as shown in **Figure I.12**). Taking crystalline silicon solar cell as an example, the n-type region can be formed by doping silicon with a pentavalent element such as P

on one side. The p-type region can be formed by doping with a trivalent element such as B on the other side. A PN junction is then formed at the contact between the N-region and P-region. Due to the concentration difference of majority carriers on both sides of the PN junction, electrons of the N-type region diffuse to the P-type region and holes of the P region diffuse to the N-type region. From this charge equilibration, it results in the formation of a space charge region (SCR) and thus the establishing of an electric field. When photons of the incident light with more energy than the semiconductor bandgap are absorbed, the photoelectron and hole pairs are generated in or near the semiconductor PN junction. Then, through the diffusion motion and drift motion of the built-in electric field of the SCR, the electrons move toward the N region, and the holes toward the P region, and the photogenerated electric field in the opposite direction of the built-in electric field is formed on both sides of the PN junction. When the load is connected, the photocurrent flowing from the P-region to the N-region is generated. Moreover, the photogenerated voltage depends on the Fermi energy levels between the two sides of the PN junction when the electron and hole pair generation and recombination rates reach equilibrium.

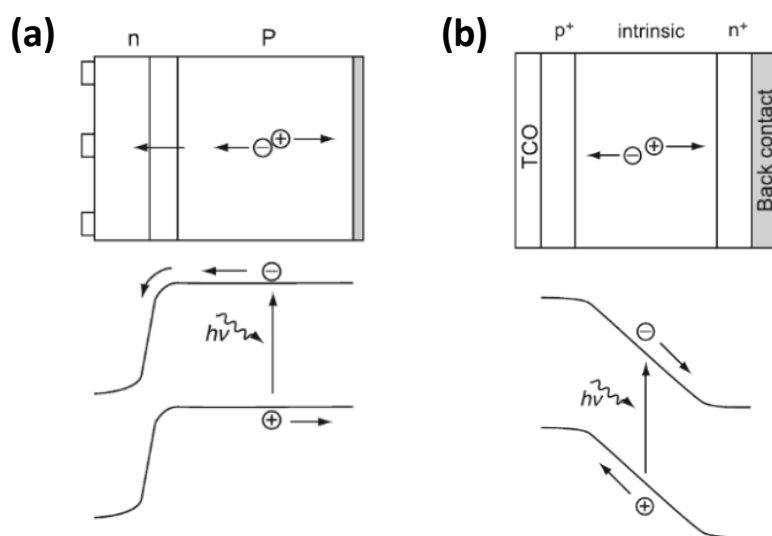


**Figure I.12** Electron-hole pair generation and separation in PN (a) and PIN (b) junctions of solid-state solar cells.

Another effective way to separate electron-hole pairs is to use the potential difference between the conduction band and valence band of semiconductors combined or not with HOMO-LUMO of organic compounds in heterostructures, as widely used in sensitized and organic solar cells. Taking DSSC as

an example (**Figure I.13**), the device is composed of a photocathode, made of the conductive glass substrate and porous titanium dioxide ( $mp\text{-TiO}_2$ ) sensitized by the adsorbed dye, a counter-electrode composed of conductive glass covered with platinum (Pt) and of an electrolyte containing redox couple (typically  $I^-/I_3^-$ ) placed between them. The dye molecules, adsorbed onto the surface of the  $TiO_2$  electrode, are excited by light, photogenerated electrons are injected into the conduction band of  $TiO_2$ , and the dye molecules are regenerated by receiving electrons from the redox shuttle. The photoelectrons are collected by  $TiO_2$  and flow to the counter electrode through the external circuit to form a loop. They regenerate the redox shuttle by reduction. In the whole cycle process, the most significant difference between PN junction solar cells and crystalline silicon solar cells is that the generation and transmission of electrons and holes are carried out separately in dye-sensitized solar cells. The bandgap of n-type semiconductor  $TiO_2$  is very wide (3.2 eV) and does not absorb visible light. It is only responsible for collecting and transmitting photogenerated electrons from dye molecules, and it blocks the recombination between electrons and holes. However, at the same time, a small number of photogenerated electrons injected into the  $TiO_2$  conduction band will combine with the oxidized component ( $I_3^-$ ) or the oxidized dye molecules in the electrolyte, as parasitic reactions which reduce the device photoconversion performances. They are very unfavorable for the energy conversion efficiency.

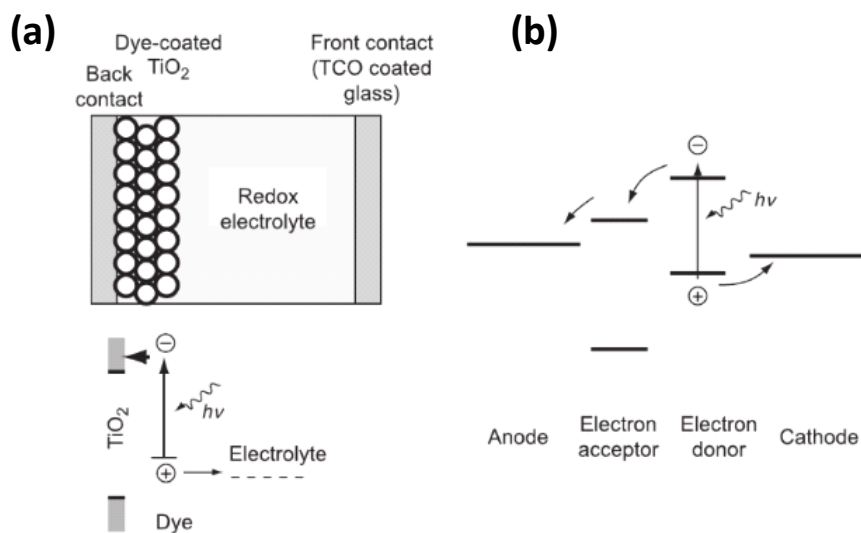


**Figure I.13** Functioning principle diagrams of (a) dye-sensitized solar cells and (b) excitonic solar cells.

#### 1.3.1.4 Important parameters of solar cells

##### (1) Photocurrent density-photovoltage curve

The most crucial comprehensive evaluation method to investigate solar cells' photoelectric conversion performance is to measure the photocurrent density versus the current-voltage curve ( $J$ - $V$ ) under a certain light intensity. The  $J$ - $V$  curve of a solar cell measured by the two-electrode method can be equivalent to the circuit diagram shown in **Figure I.14**, including a DC amperometer, a voltmeter, and an adjustable load connected at both ends of the solar cell. The light source used in the test is generally a solar simulator composed of a xenon lamp and filter, simulating the solar spectrum under AM 1.5 normal state and calibrated at a power density of  $1000 \text{ W/m}^2$ . Under the illumination of the incident light, by continuously changing the load's resistance, one measures the different current and voltage values to get the relationship curve between them, namely the  $J$ - $V$  curve. In the actual test, applying a bias voltage to the two poles of the cell is generally used to measure the current value in a specific range of voltage variation to determine the  $J$ - $V$  curve.

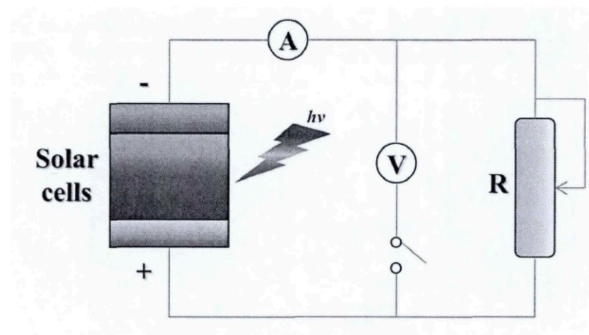


**Figure I.14** Diagram of the  $J$ - $V$  characterization for solar cells

A typical  $J$ - $V$  curve is displayed in **Figure I.15**. When the voltage is zero, it means that the external circuit's load is in a short circuit state, and the photocurrent density is short circuit current density ( $J_{SC}$ ). When the external circuit's load is infinite, it means that the circuit is in the open-circuit state, the measured current is zero, and the photovoltage is the open-circuit voltage ( $V_{OC}$ ). The photocurrent density and photovoltage product is the output power per unit area, i.e.,  $J \times V = P$ . The maximum value of output power is  $P_{max}$ , and the corresponding photocurrent density and photovoltage are  $J_{max}$  and  $V_{max}$ , respectively.

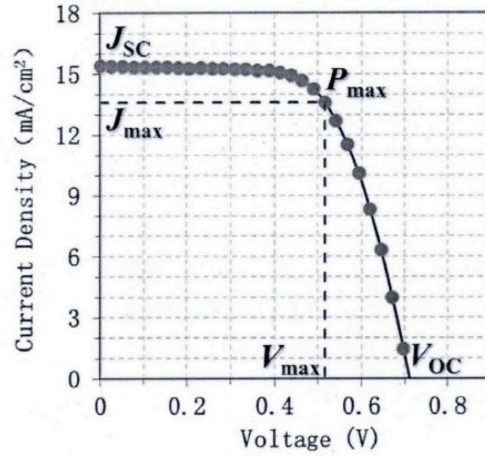


**Figure I.15 Typical  $J$ - $V$  curve of a solar cell.**

In addition to the parameters directly indicated in the figure above, we usually need to calculate the fill factor ( $FF$ ), hysteresis index ( $HI$ ) and power conversion efficiency ( $PCE$ ) to evaluate solar cells' photoelectric conversion performance.

$FF$  is defined as the ratio of  $P_{max}$  of the solar cell's maximum output power to the product of short circuit current  $J_{sc}$  and open-circuit voltage  $V_{oc}$ .

$$FF = \frac{P_{MAX}}{J_{SC} \times V_{OC}} = \frac{J_{MAX} \times V_{MAX}}{J_{SC} \times V_{OC}}$$

$FF$  can be regarded as the difference between the actual performance of the device and the ideal state. The value lies between 0 and 1. The closer the  $FF$  is to 1, the closer the  $J$ - $V$  curve is to the rectangle and the higher is the conversion performance.

The hysteresis index ( $HI$ ) measures the magnitude and type of the  $J$ - $V$  hysteresis in perovskite solar cells. In this thesis, we define the hysteresis index as:

$$HI(\%) = \frac{(PCE_{Reverse} - PCE_{Forward}) * 100}{PCE_{Reverse}}$$

$HI$  is a measure reflecting the difference between the forward and reverse scans in 0 V to  $V_{oc}$  scan range. By construction,  $HI$  is properly scaled,  $-100\% < HI < 100\%$ . The hysteresis type is identified: positive values correspond to normal hysteresis, negative values indicate inverted hysteresis. The

choice of denominator in the *HI* definition ensures a balanced evaluation of both normal and inverted hysteresis.

The definition of *PCE* is the ratio of the maximum output power of the cell  $P_{max}$  to the incident optical power  $P_{inc}$ :

$$PCE(\%) = \frac{P_{MAX} * 100}{P_{inc}} = \frac{(J_{MAX} \times V_{OC} \times FF) * 100}{P_{inc}}$$

The *PCE* is the most critical parameter that reflects the overall performance of the device. The incident light power under AM 1.5 is constant at 100 mW/cm<sup>2</sup> (1000 W/m<sup>2</sup>). *PCE* is only related to the product of short-circuit current, open-circuit voltage, and fill factor. In the case of PSC, due to the hysteresis phenomenon, both the reverse and the forward PCEs are measured. To get a better quantification of the PSC performances, the stabilized *PCE* obtained by tracking is also measured.

(2) External quantum efficiency (*EQE*) of incident monochromatic light

Incident photon-to-electron conversion efficiency (*IPCE*), also known as external quantum efficiency (*EQE*), is also an important parameter to measure the photoelectron conversion performance of solar cells. It is defined as the ratio of the number of generated electrons  $n_e$  to the number of incident monochromatic photons. *EQE* is usually expressed in % and is affected by the light absorption, the electron injection efficiency and the collection efficiency:

$$IPCE(\%) = \frac{n_e * 100}{n_p} = LHE(\lambda) \times \phi_{inj} \times \phi_c$$

$LHE(\lambda)$  is the light-harvesting efficiency,  $\phi_{inj}$  is the electron injection efficiency, and  $\phi_c$  is the electron collection efficiency. Among them,  $\phi_{inj} \times \phi_c$  is also called internal quantum efficiency (*IQE*), which examines the photoelectric conversion efficiency of light absorption.

### **I.3.2 Basic introduction to perovskite solar cells**

Although DSSCs have the advantages of simple preparation and low cost, compared to the first-generation silicon solar cells and the second-generation CdTe and CIGS cells, their current conversion efficiency is still too low. In the past few years, their PCE growth has been prolonged, while it had remained between 10% and 12% for a long time. Their further development has encountered a

significant bottleneck. In particular, most dye molecules' extinction molar coefficient is too low, and the light absorption range is relatively narrow, limiting its light absorption and utilization. Inorganic semiconductor QDs have many advantages for QD sensitized solar cells due to their high extinction coefficient, unique multi-exciton generation (MEG) effect, and hot carrier effect [65]. Their theoretical efficiency is much higher than that of DSSCs. The current research progress has been relatively slow, and the record efficiency of QDs sensitized solar cells is still below 19%.

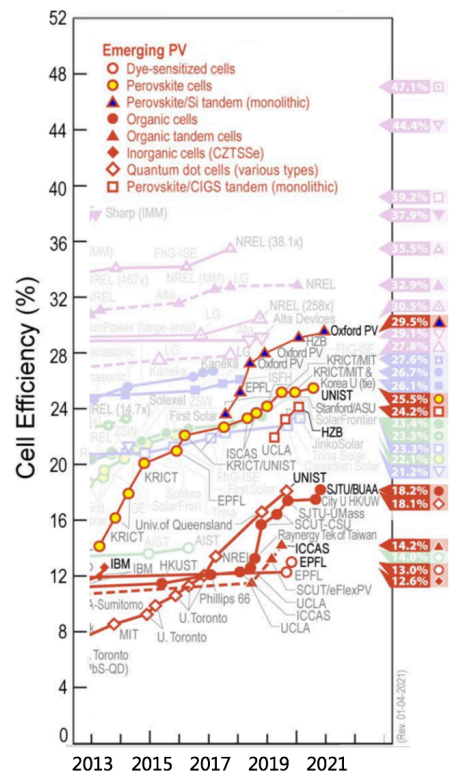


**Figure I.16 NREL chart of the best Research-Cell Efficiencies of Emerging PV (April, 2021)**

In this context, the emergence of perovskite solar cells broke the awkward situation of the third-generation solar cells that still present a lack of effectiveness. Although inorganic perovskite compounds were discovered more than a century ago [66], researchers such as Mitzi have only begun to apply organic lead halide perovskite materials to thin-film transistors and light-emitting diodes (LEDs) in the 1990s [67, 68]. The application to LEDs preliminarily indicated that this type of perovskite material can be used in solar cells. Miyasaka et al. were pioneers in the application of perovskites in solar cells. In 2006, they noticed the  $\text{CH}_3\text{NH}_3\text{PbBr}_3$  sensitized cell and formally reported a  $\text{CH}_3\text{NH}_3\text{PbI}_3$  sensitized cell with a PCE of 3.8% in 2009 [69]. After adopting the solid-state structure

in 2012, the efficiency increased to over 9%. In 2013, the Science journal evaluated the discovery of perovskite solar cells as one of the ten major scientific breakthroughs of the year. As shown in **Figure I.16**, within just a few years, the highest conversion efficiency of perovskite solar cells has continuously increased to achieve a present 25.5% record PCE [70], which exceeds the highest level of second-generation solar cells such as CdTe (22.1%) and CIGS (22.3%). Besides, because of the advantage of their simple preparation processes and mild temperature, the production cost is meager. With the continuous improvement of the theoretical mechanism and preparation process, perovskite solar cells are still hopeful for commercialization and wide application.

### **I.3.3 The working principle of perovskite solar cells**

Solar cells using various perovskite materials as light-absorber are collectively referred to as perovskite solar cells (PSCs). Most of the structures contain transparent conductive glass, electron-transporting materials (ETMs), perovskite light-absorbing materials, hole-transporting materials (HTMs), and the back-electrode. PSCs are basically composed of five layers. Among them, ETM, perovskite, and HTM can form a p-i-n like solar cell structure together. At present, the most common use conducting transparent substrate is FTO (fluorine-doped SnO<sub>2</sub>). Organic-inorganic perovskite is the light-absorbing material, TiO<sub>2</sub> the ETM, [2,2',7,7'-tetrakis-(N,N'-di-methoxyphenylamine)-9,9'-spiro-bifluorene] (spiro-MeOTAD) is typically employed as HTM and gold (Au) as the back electrode. PSC basic structure employed in Prof. Pauporté's group and working principle are shown in **Figure I.17a** (we will more detail the PSC solar cells structure in Chapter II). When the incident light enters the perovskite solar cell from the FTO side, the incident light energy (1.5~3.2 eV) that is smaller than the bandgap of TiO<sub>2</sub> and larger than the bandgap of perovskite (PVK) is absorbed by PVK and photo-generates electrons (e<sup>-</sup>) and holes (h<sup>+</sup>). After perovskite absorbs incident light, the essence of the excitation process is the transition of electrons on the 2p orbital of the anion (I<sup>-</sup>) in the valence band to the d orbital of the cation (Pb<sup>2+</sup>) at the bottom of the conduction band [71]. The carriers in the material are mainly free carrier because the exciton binding energy is small, so that the photo-generated electron-hole pair can be separated by the heterojunctions at room temperature [72]. Among them, e<sup>-</sup> diffuse to TiO<sub>2</sub>/ PVK interface and are injected into the conduction band (CB) of TiO<sub>2</sub>. After being collected by the FTO electrode, it returns to the back electrode (Au) of the cell via an external circuit.

On the other hand,  $h^+$  diffuses to the PVK/spiro-MeOTAD interface, prior to be transported to the back-electrode via the hole transport material (typically Spiro-MeOTAD), the HOMO position of which is higher than that of PVK. It forms rining a complete loop. It should be noted here that, unlike dye molecules, perovskite materials are not only used as light-absorbing materials but also HTM or ETM in some types of cells. When there is no specific material in the perovskite solar cell structure as the hole transport layer, the perovskite will serve as this structure. Since the organic-inorganic double composite perovskite material itself has p and n bipolarity, the electron and hole conductivities are extreme. It can be used for hole transport by itself [73].

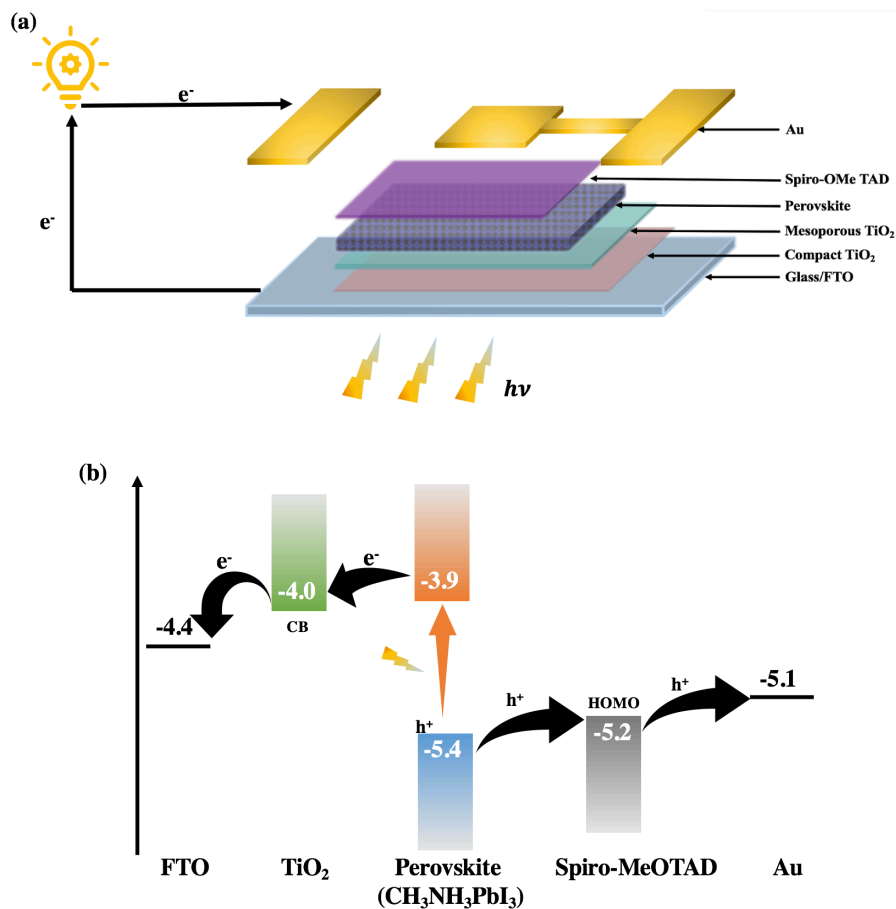


**Figure I.17 Perovskite solar cells : (a) The typical architecture employed in this thesis and (b) working principle diagram of a perovskite solar cell.**

## I.4 Conclusions

In summary, with the continuous expansion and improvement of the application scale and R&D level of solar cells, the third-generation solar cells have the advantages of high conversion efficiency, low

production cost and environmental friendliness. It could gradually replace or complete the first- and second-generation solar cells which can present high energy consumption, high pollution, or highly toxic and rare elements. This kind of iteration is inevitable in the next ten years. However, it is limited by the material structure or the immature preparation process. The current conversion efficiency of third-generation solar cells such as DSSCs, quantum dot-sensitized cells and organic polymer cells are relatively low. However, the advent of perovskite solar cells has injected a new vitality into third-generation solar cells research and has become one of the most interesting and promising emerging technology.

Moreover, PSCs also have outstanding advantages as being prepared with abundant raw materials, no rare elements, adjustable materials, by diverse preparation methods, simple processes, and extremely low production costs. Although there are still stability and scale issues that need to be resolved, with the continuous deepening and improvement of the research level and preparation process, they have the potential to occupy a place in the photovoltaic market in the future. Due to the short development time, the structural design, assembly process and working mechanism of perovskite solar cells are still under exploration. Especially in the construction of various solar cell structures (perovskite light-absorbing layer, electron/hole transporting layers and both side electrodes), such research is of great significance for the selection and optimization of key components.

In the next chapter, I will study different perovskite materials and different structures of perovskite solar cells to gain a deeper understanding into the performance and stability of PSCs.

## References

- [1] Yang, S. Dye-sensitized nanocrystalline solar cells; Zhengzhou University Press: Zhengzhou, **2007**, 1-2.
- [2] Hagfeldt, A., Boschloo, G., Sun, L. C., et al. Dye-Sensitized Solar Cells. *Chem. Rev.* **2010**, *110*, 6595-6663.
- [3] Yin, W. J., Yang, J. H., Kang, J., Yan, Y. F., Wie, S. H. Halide perovskite materials for solar cells: a theoretical review. *J. Mat. Chem. A* **2015**, *3*, 8926-8942.
- [4] Yukihiko, K., Hiroyuki, M., Katsuhiko, H. Structural study on Cubic-Tetragonal Transition of  $\text{CH}_3\text{NH}_3\text{PbI}_3$ . *J. Phy. Soc. Jap.*, **2002**, *71*, 1694-1697.
- [5] Wei, G., Chuan-Jia T., Yanning, Z., Li-Min L. Theoretical Progress on the Relationship between the Structures and Properties of Perovskite Solar Cells 2000022
- [6] Gollino, L., Pauporté, Th. Lead-Less Halide Perovskite Solar Cells. *Sol. RRL* **2021**, *5*, 2000616.

- [7] Gregor, K., Shijing, S., Anthony, K., Cheetham, Solid-state principles applied to organic-inorganic perovskites: new tricks for an old dog, *Chem. Sci.* **2014**, *5*, 4712-4715.
- [8] Liu, X., Hong, R., Tian, C. Tolerance factor and the stability discussion of ABO<sub>3</sub>-type ilmenite. *J. Mat. Sci.* **2008**, *20*, 323.
- [9] Tze, C., Nripan, M. Advancements in perovskite solar cells: photophysics behind the photovoltaics. *Energ. Environ. Sci.* **2014**, *7*, 2518-2534.
- [10] Li, C., Lu, X., Ding, W., Feng, L., Gao, Y., Guo, Z. Formability of ABX<sub>3</sub> (X = F, Cl, Br, I) halide perovskites. *Acta Crystallogr. B* **2008**, *64*, 702-707.
- [11] Li, G., Zhu, R., Yang, Y. Polymer solar cells. *Nat. Photonics* **2012**, *6*, 153-161.
- [12] Fei, Z., Haipeng, L., Jinhui, T., Joseph J. Berry, Matthew, C. Beard, Kai, Z. Advances in Two-Dimensional Organic-Inorganic Hybrid Perovskites. *Energ. Environ. Sci.* **2020**, *13*, 1154-1186
- [13] Yella, A., Lee, H. W., Tsao, H. N., et al. Porphyrin-Sensitized Solar Cells with Cobalt (II/III)-Based Redox Electrolyte Exceed 12 Percent Efficiency. *Science*, **2011**, *334*, 629-634.
- [14] Chiba, Y., Islam, A., Watanabe, Y., et al. Dye-sensitized solar cells with conversion efficiency of 11.1%. *Japanese Journal of Applied Physics Part 2-Letters & Express Letters*, **2006**, *45*, 638-640.
- [15] Grätzel, M. Dye-sensitized solar cells. *J Photoch. Photobio. C* **2003**, *4*, 145-153.
- [16] Kim, B. J., Kim D. H., Lee, Y. Y. et al. Highly efficient and bending durable perovskite solar cells: Toward a wearable power source. *Energ. Environ. Sci.* **2015**, *8*, 916-921
- [17] Lee, M. M., Teuscher, E. J., Miyasaka, T. et al. Efficient hybrid solar cells based on meso-structured organometal halide perovskites. *Science*, **2012**, *338*, 643-647.
- [18] Noh, J. H., Im, S. H., Heo, J. H. et al. Chemical management for colorful, efficient and stable inorganic-organic hybrid nanostructured solar cells. *Nano Lett.* **2013**, *13*, 1764-1769.
- [19] Chen, Q., Wu J, Ou, X. et al. Al-inorganic perovskite nanocrystal scintillators. *Nature*, **2018**, *561*, 88.
- [20] Feng, J., Gong, C., Gao, H. et al. Single-crystalline layered metal-halide perovskite nanowires for ultrasensitive photodetectors. *Nat. Electronics* **2018**, *1*, 404-410.
- [21] Liu, X., Yu, D., Song, X. et al. Metal halide perovskites: Synthesis, ion migration, and application in field-effect transistors. *Small*, **2018**, *14*, 1801460.
- [22] Zhang, Q., Yin, Y. Al Inorganic metal halide perovskite nanocrystals: Opportunities and challenges. *JACS*, **2018**, *4*, 668-679.
- [23] Huang, H., Susha, A. S., Kershaw, S. V. et al. Control of emission color of high quantum yield CH<sub>3</sub>NH<sub>3</sub>PbBr<sub>3</sub> perovskite quantum dots by precipitation temperature. *Adv. Sci.* **2015**, *2*, 1500194.
- [24] Noh, J. H., Im, S. H., Heo, J. H. et al. Chemical management for colorful, efficient and stable inorganic-organic hybrid nanostructured solar cell. *Nano Lett.* **2013**, *13*, 1764-1769.
- [25] Zhang, F., Zhong, H., Chen, C. et al. Brightly luminescent and color-tunable colloidal CH<sub>3</sub>NH<sub>3</sub>PbX<sub>3</sub> (X=Br, I, Cl) quantum-dots: Potential alternatives for display technology. *ACS Nano* **2015**, *9*, 4533-4542.
- [26] Imran, M. Caligiuri, V., Wang, M. et al. Benzoyl halides as alternative precursors for the colloidal synthesis of lead-based halide perovskite nanocrystals. *J.A.C.S.* **2018**, *140*, 2656-2664.
- [27] Jaramilloquintero, O. A., Sanchez, R. S., Rincon, M. et al. Bright visible-infrared light emitting diodes based on hybrid halide perovskite with Spiro-OMeTAD as a hole-injecting layer. *J. Phy. Chem. Lett.* **2015**, *6*, 1883-1890.
- [28] Kim, Y. H., Cho, H., Heo, J. H. et al. Multicolored organic/inorganic hybrid perovskite light-emitting diodes. *Adv. Mat.* **2015**, *27*, 1248- 1254.

- [29] Kumawatnk, D. E. Y. A., Kumara et al. Band gap tuning of  $\text{CH}_3\text{NH}_3\text{Pb}(\text{Br}_{1-x}\text{Cl}_x)_3$  hybrid perovskite for blue electroluminescence. *ACS Appl. Mat. Inter.* **2015**, 7, 13119- 13124.
- [30] Tan, Z., Kan, Z. K., Moghanddam, R. S. Lai, M. L. et al. Bright light-emiting diodes based on organometal halide perovskite. *Nat. Nanotechnology* **2014**, 9, 687-692.
- [31] Kumawat, N. K., Dey, A., Narasimhan, K. L. et al. Near infrared to visible electroluminescent diodes based on organo-metallic halide perovskites: Structural and optical investigation. *ACS Photo.* **2015**, 2, 349-354.
- [32] Yantaran, N., Bhaumik, S., Yan, F. et al. Inorganic halide perovskites for efficient light-emitting diodes. *J. Phy. Chem. Lett.* **2015**, 6, 4360-4364.
- [33] Song, J., Li, J., Li, X., et al. Quantum dot ligh-emitting diodes based on inorganic perovskite cesium lead halides ( $\text{CsPbX}_3$ ). *Adv. Mat.* **2015**, 27, 7162-7167.
- [34] Pan, Q., Hu, H., Zou, Y. et al. Microwave-assisted synthesis of high-quality “al l-inorganic” $\text{CsPbX}_3$  (X = Cl, Br, I)perovskite nanocrystals and their applicaion in light emitting diodes. *J. Mat. Chem. C* **2017**, 5, 10947-10954.
- [35] Chen, M., Zou, Y., Wu, L. et al. Solvothermal synthesis of high quality al inorganic cesium lead halide perovskite nanocrystals: From nano-cube to ultrathin nanowire. *Adv. Fun. Mat.* **2017**, 27, 1701121.
- [36] Chen, X., Zhang, F., Ge, Y. et al. Centimeter-sized  $\text{Cs}_4\text{PbBr}_6$  crystals with embedded  $\text{CsPbBr}_3$  nanocrystals showing superior photoluminescence: Non-stoichiometry induced transformation and light-emitting applications. *Adv. Fun. Mat.* **2018**, 28, 1706567.
- [37] Rain, G, Becker, M. A., Bodnarchuk, M. I. et al. Superfluorescence from lead halide perovskite quantum dot superlattices. *Nature* **2018**, 563, 671-675.
- [38] Protesescu, L., Yakunin, S., Bodnarchuk, M.I. et al. Nanocrystals of cesium lead halide perovskites ( $\text{CsPbX}_3$ , X=Cl, Br, and I):Novel optoe- lectronic materials showing bright emission with wide color gamut. *Nano Lett.* **2015**, 15, 3692- 3696.
- [39] Ramasamy, P., Lim, D. H., Kim, B. et al. Al-inorganic cesium lead halide perovskite nanocrystals for photodetector applications. *Chem. Comm.* **2016**, 52, 2067-2070.
- [40] Kwak, D. H., Lim, D. H. et al. High performance hybrid graphene  $\text{CsPbBr}_{3-x}\text{I}_x$  perovskite nanocrystal photodetector. *RSC Adv.* **2016**, 6, 65252-65256
- [41] Feng, J., Gong, C., Gao, H. et al. Single-crystalline layered metal-halide perovskite nanowires for ultrasensitive photodetectors. *Nat. Electronics*, **2011**, 404-410.
- [42] Becquerel, A. E. Recherches sur les effets de la radiation chimique de la lumiere solaire, au moyen descourants electriques. *C. R. Acad. Sci. Paris* **1839**, 561-567.
- [43] Berge, C., Zhu, M., Brendle, W. et al. 150-mm layer transfer for monocrystalline silicon solar cells. *Sol. Energ. Mat. Sol. C.* **2006**, 90, 3102-3107.
- [44] Campbell, P., Green, M. A. High performance light trapping textures for monocrystalline silicon solar cells. *Sol. Energ. Mat. Sol. C.* **2001**, 65, 369-375.
- [45] Fossum, J. G., Lindholm, F. A. Theory of grain-boundary and intragrain recombination currents in polysilicon p-n-junction solar-cells. *Ieee T. Electron. Dev.* **1980**, 27, 692-700.
- [46] Fujiwara, K., Pan, W., Usami, N. et al. Growth of structure-controlled polycrystalline silicon ingots for solar cells by casting [J]. *Acta Materialia*, 2006,54:3191-3197.
- [47] Seager, C. H., Ginley, D. S., Zook, J. D. Improvement of polycrystalline silicon solar-cells with grain-boundary hydrogenation techniques [J]. *Applied Physics Letters*, 1980,36:831-833.

- [48] De Wild, J., Rath, J. K., Meijerink, A. et al. Enhanced near-infrared response of a-Si:H solar cells with beta-NaYF<sub>4</sub>:Yb<sup>3+</sup> (18%), Er<sup>3+</sup> (2%) upconversion phosphors [J]. *Sol. Energ. Mat. Sol. C.* **2010**, *94*, 2395-2398.
- [49] Ferry, V. E., Verschuuren, M. A., Li, H. B. T. et al. Improved red-response in thin film a-Si:H solar cells with soft-imprinted plasmonic back reflectors. *Appl. Phys. Lett.* **2009**, *95*, 183503.
- [50] Ferry, V. E., Verschuuren, M. A., Van Lare, M. C. et al. Optimized Spatial Correlations for Broadband Light Trapping Nanopatterns in High Efficiency Ultrathin Film a-Si:H Solar Cells. *Nano Lett.* **2011**, *11*, 4239-4245.
- [51] Aramoto, T., Kumazawa, S., Higuchi, H. et al. 16.0% efficient thin-film CdS/CdTe solar cells. *Japanese Journal of Applied Physics* **1997**, *36*, 6304-6305.
- [52] Aranovich, J. A., Golmayo, D., Fahrenbruch, A. L. et al. Photo-voltaic properties of ZnO-CdTe heterojunctions prepared by spray pyrolysis. *J. Appl. Phys.* **1980**, *51*, 4260-4268.
- [53] Kaelin, M., Rudmann, D., Kurdesau, F. et al. Low-cost CIGS solar cells by paste coating and selenization. *Thin Solid Films* **2005**, *480*, 486-490.
- [54] Kaelin, M., Rudmann, D., Tiwari, A. N. Low cost processing of CIGS thin film solar cells. *Sol. Ener.* **2004**, *77*, 749-756.
- [55] Bowden, S., Das, U., Herasimenka, S., Birkmire, R., Stability of amorphous/crystalline silicon heterojunction. *IEEE Xplore* **2008**.
- [56] Chen, H.-Y., Hou, J., Zhang, S. et al. Polymer solar cells with enhanced open-circuit voltage and efficiency. *Nat. Photo.* **2009**, *3*, 649-653.
- [57] Guenes, S., Neugebauer, H., Sariciftci, N. S. Conjugated polymer-based organic solar cells. *Chem. Rev.* **2007**, *107*, 1324-1338.
- [58] Yella, A., Lee, H. W., Tsao, H. N. et al. Porphyrin-Sensitized Solar Cells with Cobalt (II/III)-Based Redox Electrolyte Exceed 12 Percent Efficiency. *Science* **2011**, *334*, 629-634.
- [59] Chiba, Y., Islam, A., Watanabe, Y. et al. Dye-sensitized solar cells with conversion efficiency of 11.1%. *Japanese Journal of Applied Physics* **2006**, *45*, L638-L640.
- [60] Kamat, P. V. Quantum Dot Solar Cells. Semiconductor Nanocrystals as Light Harvesters. *J. Phys. Chem. C*, **2008**, *112*, 18737-18753.
- [61] Kongkanand, A., Tvrđy, K., Takechi, K., et al. Quantum dot solar cells. Tuning photoresponse through size and shape control of CdSe-TiO<sub>2</sub> architecture. *J. A. C. S.* **2008**, *130*, 4007-4015.
- [62] Miyasaka, T., Kojima, A., Teshima, K. et al. Organometal Halide Perovskites as Visible-Light Sensitizers for Photovoltaic Cells. *J. A. C. S.* **2009**, *131*, 6050-6051.
- [63] Kim, H.-S., Lee, C.-R., Im, J.-H. et al. Lead Iodide Perovskite Sensitized All-Solid-State Submicron Thin Film Mesoscopic Solar Cell with Efficiency Exceeding 9%. *Sci. Rep-UK.* **2012**, *2*, 591.
- [64] Oregan, B., Grätzel, M. A Low-Cost, High-Efficiency Solar-Cell Based on Dye-Sensitized Colloidal TiO<sub>2</sub> Films. *Nature* **1991**, *353*, 737-740.
- [65] Kamat, P. V. Quantum Dot Solar Cells. The Next Big Thing in Photovoltaics. *J. Phys. Chem. Lett.* **2013**, *4*, 908-918.
- [66] Topsøe, H. Krystallographisch-chemische untersuchungen homologer verbindungen. *Zeitschrift für Kristallographie* **1884**, *8*, 246-296.
- [67] Mitzi, D. B., Wang, S., Feild, C. A. et al. Conducting layered organic-inorganic halides containing (110)-oriented perovskite sheets. *Science*, **1995**, *267*, 1473-1476.

- [68] Mitzi, D. B., Chondroudis, K., Kagan, C. R. Organic-inorganic electronics. *IBM J. Res. Dev.* **2001**, *45*, 29-45.
- [69] Green, M. A., Ho-Baillie, A., Snaith, H. J. The emergence of perovskite solar cells. *Nat. Photonics* **2014**, *8*, 506-514.
- [70] Jeong, M., Choi, I., Go, E., Cho, Y. et al. Stable perovskite solar cells with efficiency exceeding 24.8% and 0.3-V voltage loss. *Science* **2020**, *369*, 1615-1620
- [71] Burschka, J., Dualeh, A., Kessler, F. et al. Tris(2-(1H-pyrazol-1-yl) pyridine) cobalt(III) as p-Type Dopant for Organic Semiconductors and Its Application in Highly Efficient Solid-State Dye-Sensitized Solar Cells. *J. A. Chem. Soc.* **2011**, *133*, 18042-18045.
- [72] Kim, H.-S., Lee, C.-R., Im, J.-H. et al. Lead Iodide Perovskite Sensitized All-Solid-State Submicron Thin Film Mesoscopic Solar Cell with Efficiency Exceeding 9%. *Sci. Rep-UK.* **2012**, *2*, 591.
- [73] Lingyan, L., Linqin, J., Yu, Q., Yunlong. Y. Modeling and analysis of HTM-free perovskite solar cells based on ZnO electron transport layer, *Superlattice Microst.* **2017**, *104*, 167-177.

## Chapter II. Exploring perovskite solar cells: From the cation composition to the cell structure

### II.1 Mono- to Triple-Cation Hybrid Perovskites for High Efficiency Solar Cells

During the last years, innovative film processings have been developed for increasing the perovskite solar cells (PSCs) performances and stability. The two most fruitful have been (i) to complexify the perovskite composition by mixing monovalent cations and (ii) to add additives in the perovskite precursor solution (PPS) which are eliminated upon the film annealing and post-deposition processing step. In the present work, perovskite films varying in their monovalent cation content, from one to three (namely  $\text{MAPbI}_3$ ,  $\text{Cs}_{0.08}\text{FA}_{0.80}\text{MA}_{0.12}\text{Pb}(\text{I}_{0.88}\text{Br}_{0.12})_3$  and  $\text{FA}_{1-x}\text{MA}_x\text{PbI}_3$  compounds) and optimized to reach high efficiency up to 22.2% have been thoroughly compared for their properties, performances and stability. These cells have also been investigated by impedance spectroscopy and the results are given in the **Annex A.II.1**.

#### II.1.1 Introduction

The structural unit of OIHP compounds contains an anionic corner-sharing octahedral network which is stabilized by cations. The stability of the 3D perovskite phase is limited by geometry and oxidation state restrictions, quantified by a tolerance factor ( $t_f$ ). The well-known Goldsmith tolerance factor has been refined recently by Bartel et al. [1]:

$$t_f = \frac{r_x}{r_B} - n_A \left( n_A - \frac{r_A/r_B}{\ln(r_A/r_B)} \right) \quad (\text{II.1})$$

where  $n_A$  is the oxidation state of A (+1),  $r_i$  is the ionic radius of ion i (2.70 Å for methyl ammonium (MA), 2.79 Å for formamidinium (FA), 1.81 Å for Cs and 1.19 Å for  $\text{Pb}^{2+}$ ),  $r_A > r_B$  by definition.  $t_f < 4.18$  indicates that the perovskite structure is allowed. MA and FA are the two main organic monovalent cations that can be employed as organic A. However, due to the large size of FA, increasing the complexity of the perovskite was proved necessary to increase the PSC stability and performances. [2-4] Above the pioneering popular monovalent mono-cation  $\text{MAPbI}_3$  compound, a huge research effort has been directed towards the development of double-cation  $\text{FA}_{1-x}\text{MA}_x\text{PbX}_3$  and triple-cation  $\text{M}^a_y(\text{FA}_{1-x}\text{MA}_x)\text{PbX}_3$ , (with  $\text{M}^a$  an alkali metal) perovskites to improve the device

performances and stability. In the latter case, Cs is the most popular elemental monovalent cation incorporated. However, the full entropic stabilization of this triple cation perovskite also requires the addition of Br in complement to I for X. [2]

Alternative strategies of stabilization by using additives have been developed lately [5] and, to get stable double cation perovskite, we have developed the use of MACl as an additive in the  $FA_{1-x}MA_xPbI_3$  precursor solution. This compound has allowed the direct deposition of the perovskite phase upon the spin-coating and then the growth of well-crystallized  $FA_{1-x}MA_xPbI_3$  layers upon the annealing post-deposition step.

The aim of this subsection is to fully investigate the effect of the number of monovalent cations on the electrical response of PSCs with high efficiency in their category. The performance of the studied PSCs attained up to 22.1 % in the case of the  $FA_{1-x}MA_xPbI_3$  one. More precisely, the compared perovskites are:  $MAPbI_3$ ,  $FA_{0.94}MA_{0.06}PbI_3$  and  $Cs_{0.08}FA_{0.80}MA_{0.12}Pb(I_{0.88}Br_{0.12})_3$ . I have made a thorough optimization work of these cells upon my PhD in collaboration with Tao Zhu, another PhD student of Pauporté's group. The basic electrical characterization of a PSC just consists in measuring their  $J-V$  curves in the reverse and forward scan directions and in quantifying the hysteresis amplitude. In the present work, these measurements have been completed by full characterizations of the perovskite films properties and by an investigation of the effect of light intensity on the steady state  $V_{oc}$  which provides information and quantifications about the recombination mechanism. Their study by impedance spectroscopy measurements is also detailed in the **Annex II-Chapter II**. which gives an in-depth and complete view of the physical phenomena occurring in PSCs in operation. With help of complementary measurements, spectral features have been assigned to physical phenomena. The various relaxations have been decomposed and quantified using electrical elements. Their variation has been analyzed with the applied voltage and the chemical nature of the perovskite. The present comparative study has allowed us to clarify the assignment of some electrical elements and to confirm others. Moreover, we have attached a special attention to the stability of the systems under irradiation and electrical stresses and upon their long term storage in a glovebox, since these measurements provide a good quantification of the PSC stability.

## II.1.2 Experimental

### II.1.2.1 Preparation of Substrate

Fluorine-doped SnO<sub>2</sub> (FTO) substrates (TEC 7 from Pilkington) were etched pattern by zinc powder and 10% HCl solution prior to be cleaned with soap and water. The substrates were subsequently immersed for 20 min in a concentrated 2.2M NaOH in ethanol/water (10:1 v/v %) and then rinsed with deionized water in an ultrasonic bath for 15 min.[6,7] The substrates were subsequently heated at 500°C for 15 min. The compact TiO<sub>2</sub> hole blocking layer, noted *c*-TiO<sub>2</sub>, was prepared by aerosol spray pyrolysis. The TiO<sub>2</sub> nanoparticle solution employed for the preparation of the mesoporous layer, noted *mp*-TiO<sub>2</sub>, was prepared in advance and stirred for at least 12h. The TiO<sub>2</sub> NR30-D paste (from Greatcell) was diluted in ethanol with a 1:7 w/w ratio. 45 μL of the solution was dropped on the *c*-TiO<sub>2</sub> layer and spin-coated at 2000 rpm for 15 s. The layer was then dried on a hotplate at 70 °C for 5-10 min and finally heated at 500 °C under an air flux for 30 min, cooled down to 200 °C and removed from the hotplate.

### II.1.2.2 Preparation of Perovskite films

MAPI layers preparation: The MAPbI<sub>3</sub> precursor solution had a 1.45M concentration. 668.5 mg PbI<sub>2</sub> and 230.5 mg MAI were mixed in 1mL DMSO. The solution was stirred and kept warm at 100°C for 2h before use. The Spin-coating program was 1000 rpm for 10s and 6000 rpm for 30 s. 100 μL of chlorobenzene was dripped 30s after the starting of the spinning routine. The layers were finally annealed on a hotplate at 105 °C for 60 min. The best performances were achieved after the device preparation. These layers are denoted MAPI throughout the chapter.

CsFAMA layers preparation: A 1.35M precursor solution corresponding to a Cs<sub>0.08</sub>FA<sub>0.80</sub>MA<sub>0.12</sub>Pb(I<sub>0.88</sub>Br<sub>0.12</sub>)<sub>3</sub> perovskite layer composition was prepared. First, 179 mg of formamidinium iodide (FAI), 17.4 mg of methylammonium bromide (MABr), 27.0 mg of CsI, 548 mg of PbI<sub>2</sub> and 57.1 mg of PbBr<sub>2</sub> were mixed in 220 μL DMSO and 780 μL DMF. The solution was stirred for a minimum of 3-4 h at room temperature in a N<sub>2</sub> filled glovebox before use.[7-9] 45 μL of this solution was placed on top of the substrates. A two-step spin-coating program was employed: first spinning at 1000 rpm for 10 s and then at 6000 rpm for 30 s. 100 μL of chlorobenzene was dripped 20

s after the starting of the spinning routine. The films were then annealed at 105 °C for 1 h in a dry atmosphere. The best performances and lower hysteresis index (*HI*) were achieved after 7-8 days of storage in the N<sub>2</sub> filled glovebox. These layers are denoted CsFAMA throughout the chapter.

*FAMA layers preparation:* A mixed cation precursor solution with a 1.2M concentration was prepared by mixing 206 mg of formamidinium iodide (FAI, greatcell), 553 mg of PbI<sub>2</sub> (TCI), and 38.9 mg of methylammonium chloride (MACl, Alfa aesar) in 800 μL DMF and 200 μL DMSO. The solutions were stirred for a minimum of 2h at room temperature in a nitrogen filled glovebox. 45 μL of this solution was placed on top of the substrates. A two-step spin-coating program was ran: first spinning at 1000 rpm for 10 s and then at 6000 rpm for 30 s. 100 μL of chlorobenzene was dripped 20 s after the starting of the spinning routine. The films were then annealed at 153 °C for 13 min. The PEAI post-deposition treatment consisted in dropping 60 μL of a 10 mM 2-Phenylethylamine Hydroiodide (PEAI) solution (2.49 mg in 1 mL of isopropanol) onto the perovskite film after cooling. A one-step spin-coating program was employed: 2000 rpm/s acceleration, 3000rpm for 20s. The best performances and lowest *HI* were achieved after 3-4 days of storage in the N<sub>2</sub> filled glovebox. These FA<sub>1-x</sub>MA<sub>x</sub>PbI<sub>3</sub> layers are denoted FAMA throughout the chapter.

The hole transporting material (HTM) solution was prepared by dissolving 78 mg of Spiro-OMeTAD (Borun New Material Technology) in 1 mL of chlorobenzene. Then, 17.9 μL of bis(trifluoromethylsulfonyl)imide lithium salt solution (Li-TFSI) (Sigma Aldrich) solution (517 mg in 1 mL ACN), 30.4 μL of TBP (tert-butylpyridine) (Sigma Aldrich) and 14 μL of tris(2-1H-pyrazol-1-yl)-4-tert-butylpyridine)-cobalt(III) tris (bis(trifluoromethylsulfonyl)imide) (Dyesol, FK209) (376 mg in 1 mL acetonitrile) were added to this solution. 40 μL of the HTM solution was spin-coated at 4000 rpm for 30 s. Finally, the device was completed by thermally evaporating a 70-80 nm thick gold back contact on the Spiro-OMeTAD layer [7].

### ***II.1.2.3 Characterization methods***

The structure of the organometal lead perovskite films was characterized by a PANalytical X-Pert high-resolution X-ray diffractometer (XRD) operated at 40 kV and 45 mA and using the CuK $\alpha$  radiation with  $\lambda = 1.5406 \text{ \AA}$ . The film specular absorbance was measured by a Cary 5000 UV-Vis-NIR

spectrophotometer. A glass/FTO/*c*-TiO<sub>2</sub>/*mp*-TiO<sub>2</sub> sample was employed for the baseline. The photoluminescence spectra were measured by a Cary Eclipse fluorescence spectrophotometer. The morphology of perovskite thin films was measured using a field-emission SEM equipment (Zeiss Supra 40) in the in-lens mode.

The EDX spectra were measured with a Quantax system from Bruker operated at 15 kV. <sup>1</sup>H-NMR spectra were recorded on a Bruker Avance 500 MHz Neo spectrometer. Chemical shifts were measured in ppm using the residual DMSO solvent signal as an internal reference. Perovskite layers, deposited on a sprayed *c*-TiO<sub>2</sub> layer, were dissolved in DMSO-d<sub>6</sub> solvent (99.96%D, H<sub>2</sub>O<0.01%, Eurisotop) and the NMR spectra of the solutions were measured. These solutions were highly stable.

The *J-V* curves were recorded by a Keithley 2410 digital sourcemeter, using a 0.1 V.s<sup>-1</sup> voltage scan rate.[10] The solar cells were illuminated with a solar simulator (Abet Technology Sun 2000) filtered to mimic AM 1.5G conditions (100 mW/cm<sup>2</sup>).[10] The illuminated surface was delimited by a black mask with an aperture diameter of 3 mm. The power density was calibrated at 100 mW.cm<sup>-2</sup> by the use of a reference silicon solar cell.[11] The tracking experiments were performed under ambient conditions. The current was followed at the voltage of the maximum power.

The external quantum efficiency (*EQE*) spectra were measured using an Oriel QUANTX-300 system. The light beam was chopped at 77Hz. The monochromatic illumination was calibrated by a NIST-calibrated Si photodiode.

The sample morphologies were examined with a high resolution Ultra 55 Zeiss FEG field-emission scanning electron microscope (FE-SEM) in the in-lens mode. The time-resolved photoluminescence (TRPL) measurements were performed at INSP, Sorbonne University (collaboration with Dr L. Coolen) under microscope observation (numerical aperture 0.7). The perovskites layers were spin-coated onto a glass/FTO/*c*-TiO<sub>2</sub>/*mp*-TiO<sub>2</sub> substrate. The top of the OIHP layers were excited by a 470 nm diode laser (Picoquant) and the emission was filtered by a 488-nm longpass filter. It was analyzed for time-resolved photoluminescence decay, by a PerkinElmer SPCM avalanche photodiode combined with a Picoharp acquisition card (500 ps characteristic time of the total system response function) used with the laser in a pulsed mode at a 10 nW excitation power (pulse duration 70 ps).

## II.1.3 Characterizations of Perovskite Films

### II.1.3.1 SEM

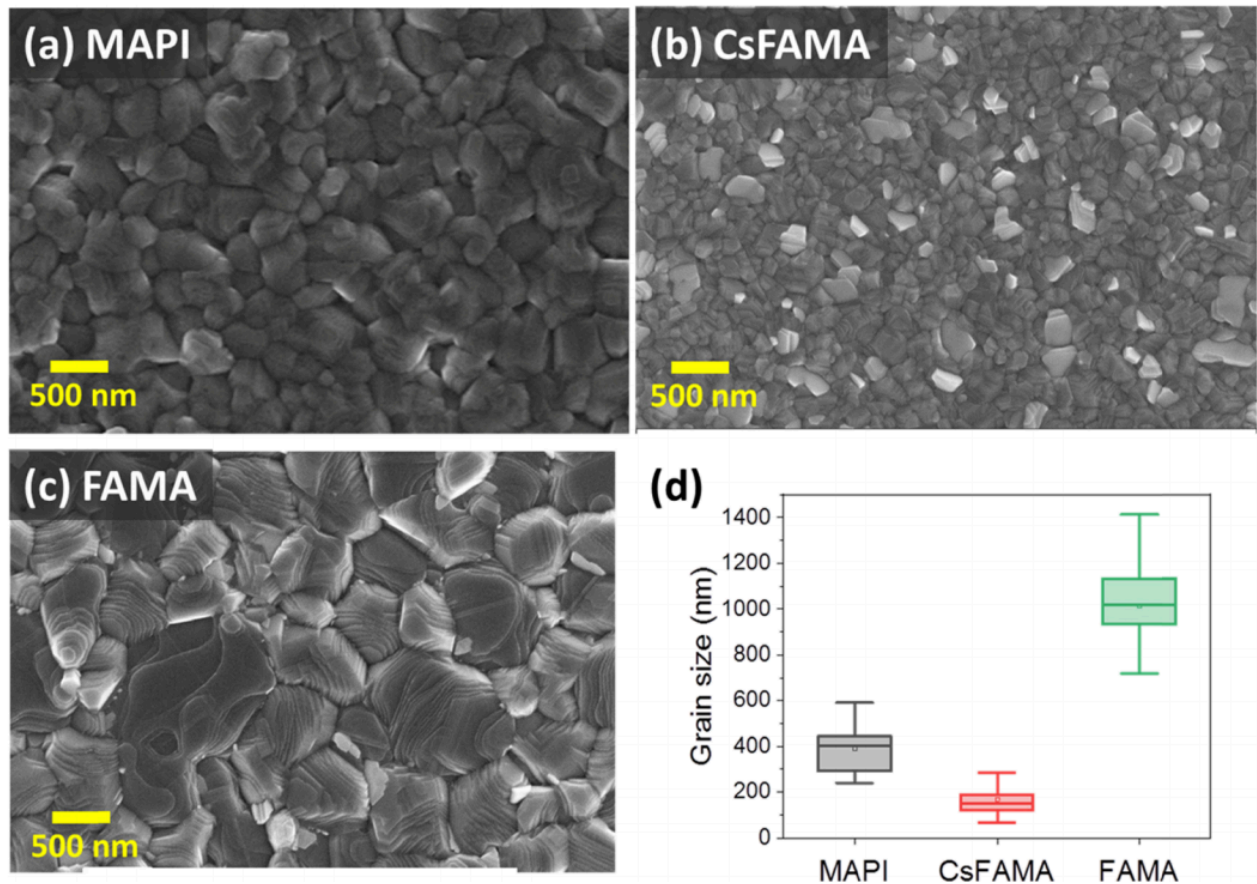


**Figure II.1** SEM top-views of the perovskite layers investigated. (a) MAPI, (b) CsFAMA and (c) FAMA. (d) Analysis of the grain size distribution in the perovskite layers.

The morphology of the three different perovskite films as revealed by SEM is disclosed in **Figure II.1**. Top views show their poly-crystallinity and that they were made of merged crystal grains. The crystal grain size and distribution analyses were performed using the Image J software (**Figure II.1d**). In the MAPI layer, they had an average size of 410 nm (**Figure II.1a**). The layers were well-covering, but pinholes were present. The CsFAMA layers were made of smaller crystal grains with an average size of 160 nm (**Figure II.1b**). They were compact, uniform with no pinholes. The bright grains observed on the surface were assigned to  $\text{PbI}_2$  by an EDX analysis (**Table II.2**). The FAMA layers were nicely compact, uniform and made of remarkably large crystal grains. Their average size was measured at 1020 nm (**Figure II.1c**). The formation of large grains is due to the use of a chloride additive (MAcI)

in the precursor solution. Chloride is known to favor the growth of well-crystallized layers.[11-15] In summary, using mixed cation precursor produces more compact layers and the presence of a chloride additive mediates the growth of the perovskite and produces large grains.

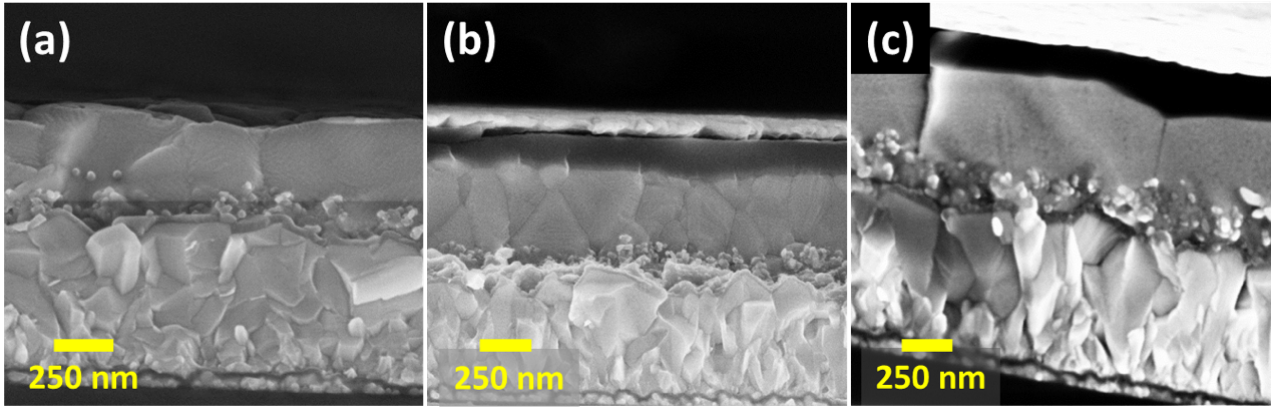


**Figure II.2 SEM cross-sectional views of the perovskite layers. (a) MAPI, (b) CsFAMA and (c) FAMA.**

Further information on the layers morphology was gained from SEM cross-sectional images (**Figure II.2**). They confirmed that the CsFAMA layer had the smaller grains (**Figure II.2b**). The images of the FAMA layer in **Figure II.2c** shows remarkable monolithic large crystal grains. The interesting point is that they extend through the entire perovskite layer thickness and that each large crystal is contacted on one side by  $\text{TiO}_2$  and, on the other side, by Spiro-OMeTAD. This ideal morphology contrasts with the CsFAMA film one where many grain boundaries are present in the layer bulk. Therefore, under light irradiation, the charges photogenerated in CsFAMA layers can encounter grain boundaries, can be trapped and recombine there before to be collected. The layers thicknesses were evaluated from the SEM views and found at 360-380 nm, 440-460 nm and 410-430 nm for MAPI, CsFAMA and FAMA, respectively.

### II.1.3.2 XRD

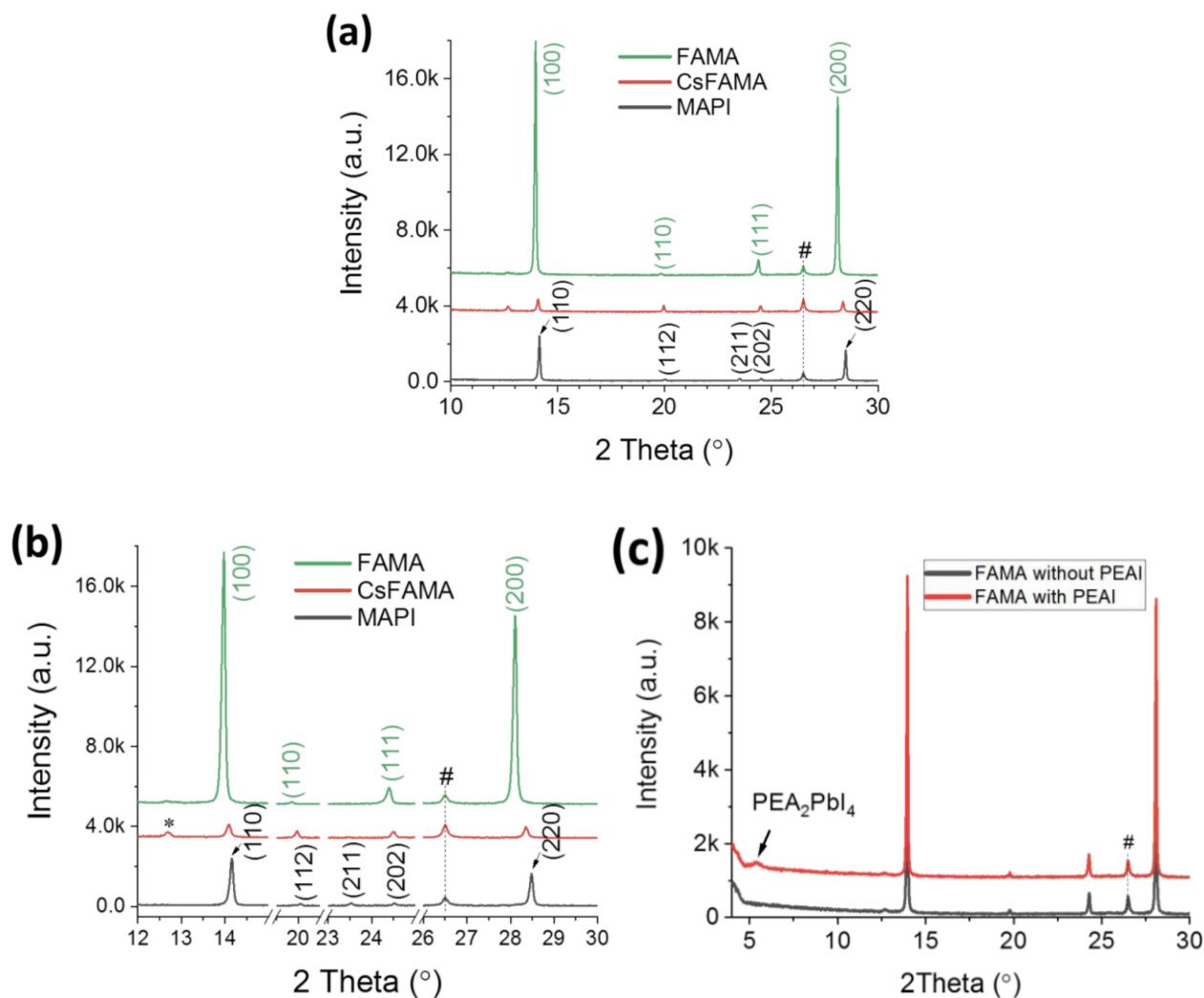


**Figure II.3** (a) XRD patterns of the perovskite layers. (b) Zoom view of (a). # denotes the FTO substrate peak, \* denotes the PbI<sub>2</sub> peak. (c) Effect of PEAI treatment on the FAMA XRD pattern.

**Figure II.3** shows the XRD patterns of the layers. The peak intensity reflects their crystallinity. CsFAMA presents the less intense peaks whereas FAMA has the most intense ones. MAPI is intermediate. CsFAMA and FAMA patterns have been indexed with the 3D perovskite cubic  $\alpha$ -phase. We note that for FAMA, the (h00) peaks are the most intense ones and it shows a strong texturisation of the layer, with these planes parallel to the surface. The MAPI diffraction diagram was indexed with the tetragonal structure. It is characterized by an extra-peak at 23.52°.[60] MAPI is phase pure with no PbI<sub>2</sub> diffraction peak present at 12.7°. FAMA is also phase pure with no  $\delta$ -phase present and almost no PbI<sub>2</sub>. On the other hand, PbI<sub>2</sub> is present in the CsFAMA layer. **Figure II.3c** shows that the PEAI

treatment produces an extra diffraction peak centered at  $5.35^\circ$  which is assigned to a  $(\text{PEA})_2\text{PbI}_4$  layer formed at the FAMA surface.

### II.1.3.3 Absorbance

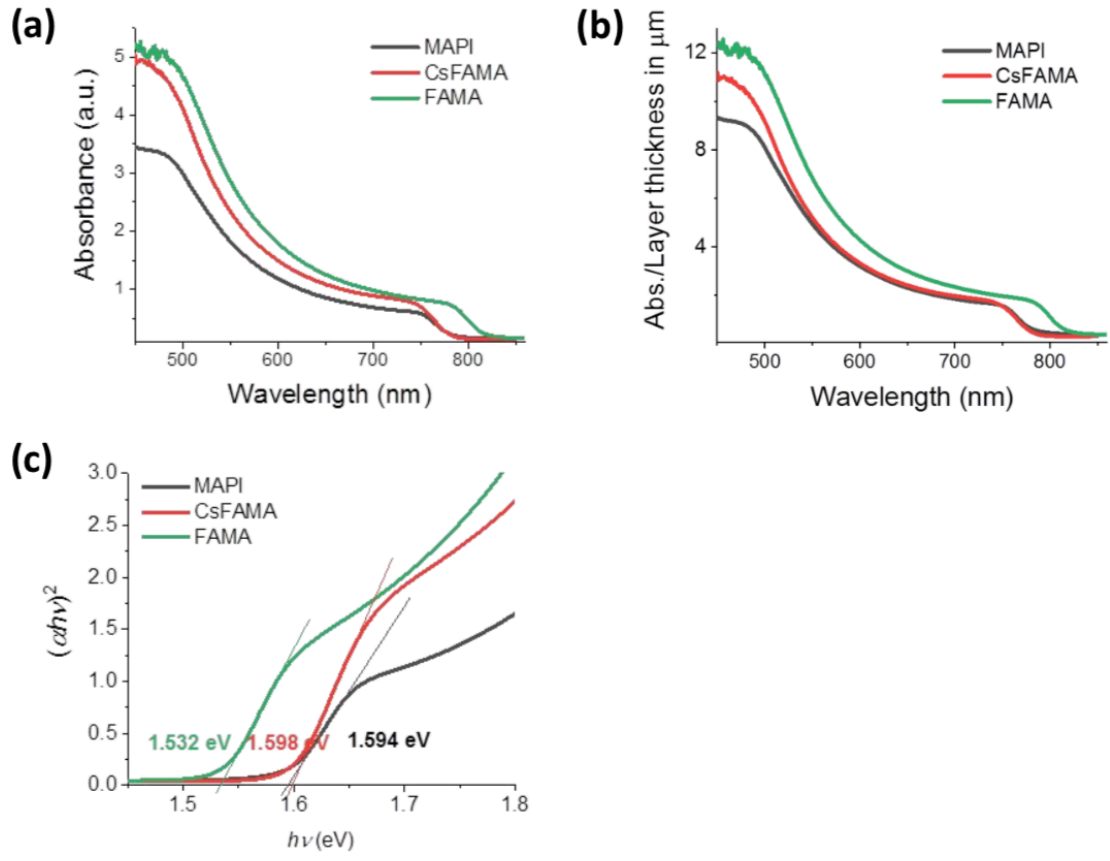


**Figure II.4** Optical characterizations of the perovskite layers. (a) Absorbance spectra; (b) spectra of (a), corrected of their thickness, (c) Tauc plots and bandgaps determination.

The ability of the layers to absorb light is a very important property for the photovoltaic application. The measured absorbance spectra are compared in **Figure II.4a** for the rough data and in **Figure II.4b** for the data corrected of the film thicknesses. The FAMA layers presented the best absorbance and the most extended absorption wavelength range due to a smaller optical bandgap ( $E_g$ ). In **Figure II.4b** FAMA was the material with the best absorbance. MAPI and CsFAMA presented a similar absorbance above 550 nm. Below this wavelength, the absorbance of CsFAMA was superior to that of MAPI. The near-band edge absorption was analyzed using the Tauc plots in **Figure 4c**. Considering a direct bandgap, the linear fit intersection with the energy axis gave optical bandgaps of 1.594 eV for MAPI,

1.598 eV for CsFAMA and 1.532 eV for FAMA. The latter is closer to the optimum bandgap value for a solar cell application as defined by the Shockley-Queisser maximum PCE curve.[65]

### II.1.3.4 Steady-state PL and TRPL

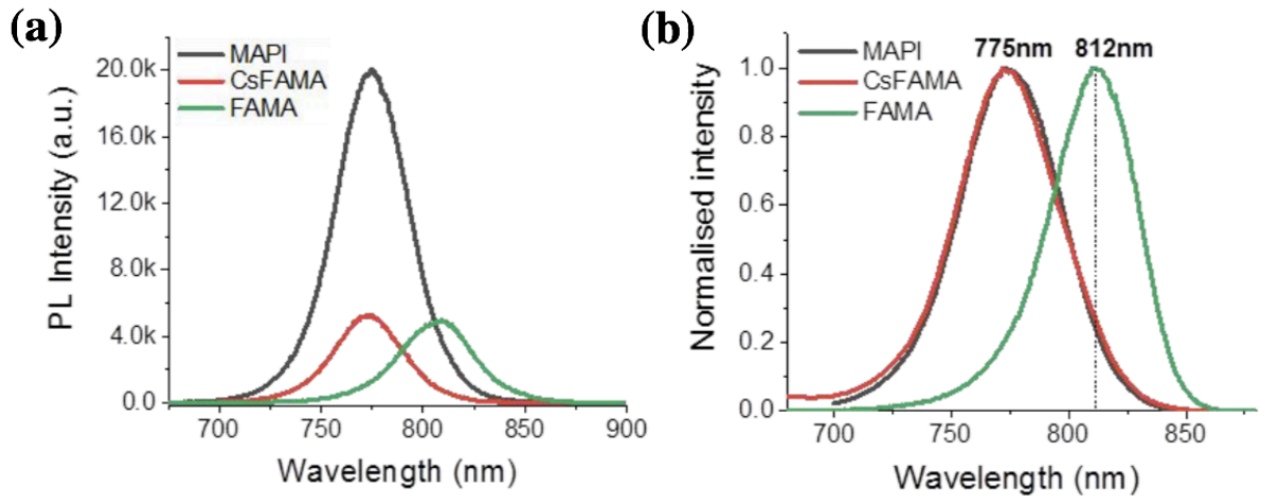


**Figure II.5** Optical characterizations of the perovskite layers. (a) Steady-state PL spectra. (b) Same as (a) after normalization.

The monitored steady PL spectra of the three perovskite layers are shown in **Figure II.5a**. On the normalized emission (**Figure II.5b**), the maximum emission wavelength was 775 nm for MAPI and CsFAMA and 812 nm for FAMA.

We also measured the time-resolved PL (TRPL) response of the films (**Figure II.6**). The curves were analyzed using a three exponential decay function. The decay curves have been first normalized and fitted by the tri-exponential function:

$$PL(t) = y_0 + Ae^{-t/\tau_{fast}} + Be^{-t/\tau_{int}} + Ce^{-t/\tau_{slow}} \quad (II.1)$$

The relative contribution ( $rc$ ) of each of these three terms to the static PL has been evaluated by integrating the relative exponential traces.

The integral is equal to the product of the amplitude and the decay time. Therefore, fast, intermediate and slow component relative contributions are defined as:

$$rc_{fast}(\%) = A\tau_{fast}/(A\tau_{fast} + B\tau_{int} + C\tau_{slow}) \quad (II.2a)$$

$$r_{C_{int}}(\%) = B\tau_{int}/(A\tau_{fast} + B\tau_{int} + C\tau_{slow}) \quad (II.2b)$$

$$r_{C_{slow}}(\%) = C\tau_{slow}/(A\tau_{fast} + B\tau_{int} + C\tau_{slow}) \quad (II.2c)$$

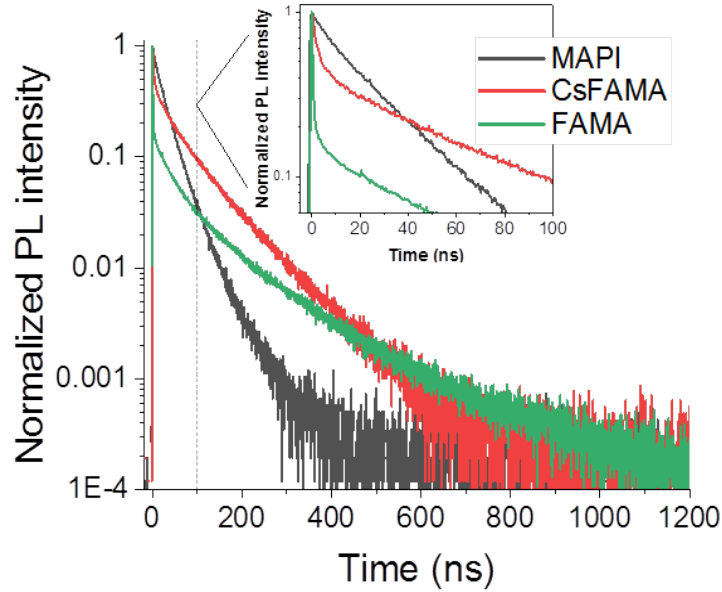


**Figure II.6 TRPL curves. The inset is a zoom view at short times.**

The results are gathered in **Table II.1**, CsFAMA and FAMA had a similar behavior. They presented first a fast decrease with characteristic times at 2.0 ns and 0.5 ns, respectively. The amplitude of the decay was markedly higher for FAMA compared to CsFAMA. The fast component is assigned to the non-radiative recombinations of the charges that are injected into TiO<sub>2</sub>. Our results show that the charge injection is faster and more efficient in FAMA perovskite compared to CsFAMA. For MAPI perovskite, the first decay component was much longer at 27 ns. It is the main relative contribution to the decay (75%). It suggests that, in the case of MAPI, the electron injection towards TiO<sub>2</sub> is slower and more difficult. The TRPL slow component ( $\tau_{slow}$ ) provides interesting information on the systems. This component is assigned to the bimolecular (radiative) or SRH (non-radiative) recombinations of the photogenerated charges in the bulk perovskite[57]. It scales with the crystal quality and it decreases with the density of recombination sites in the bulk and at the grain boundaries.  $\tau_{slow}$  is measured at 59 ns, 93 ns and 117 ns for MAPI, CsFAMA and FAMA (with PEAI treated), respectively. It shows that the bulk and grain boundary defect density is higher in MAPI compared to CsFAMA. FAMA presents

the fewer defects, the less grain boundaries and the best crystallographic quality. We can also note that the slow component represents the major relative component of the emission for CsFAMA and FAMA (77% and 74%).

**Table II.1 TRPL curve parameters determined by a triple-exponential decay function fitting.**

	A <sub>1</sub>	τ <sub>fast</sub> /ns	rc <sub>fast</sub> <sup>a</sup>	A <sub>2</sub>	τ <sub>int</sub> /ns	rc <sub>int</sub> <sup>a</sup>	A <sub>3</sub>	τ <sub>slow</sub> /ns	rc <sub>slow</sub> <sup>a</sup>
MAPI	0.736	26.9	0.75	0.161	5.13	0.03	0.100	58.8	0.22
CsFAMA	0.544	2.03	0.04	0.212	27.3	0.19	0.260	93.2	0.77
FAMA	0.826	0.47	0.04	0.102	24.10	0.22	0.070	117	0.74
FAMA*	0.323	2.81	0.03	0.457	28.0	0.38	0.196	102	0.59

<sup>a</sup>rc<sub>xx</sub>: fast, intermediate and slow relative contributions.

### II.1.3.5 Composition of the perovskites

**Table II.2 EDX analysis of the perovskite layers.**

Sample	Pb (M-series)	Cs (Cs/Pb) (L-series)	I (L-series)	Br (L-series)	Cl (Cl/I+Cl) (K-series)	I/Pb At. %	(I+Br) /Pb At. %
MAPI	5.36		16.61			3.10	
CsFAMA	10.51	0.82 (8%)	28.53	3.41			3.04
FAMA	8.45		26.15		0.1 (0.4%)	3.10	

EDX analyses were implemented to determine the composition of the layers (**Table II.2**). The I/Pb atomic ratio for MAPI and FAMA and (I+Br)/Pb ratio for CsFAMA have a theoretical value of 3. We found 3.1 for the formers and 3.04 for the latter. Within the uncertainty of the technique, all the layers were close to the stoichiometry. The slightly lower value for CsFAMA can be assigned to the presence of PbI<sub>2</sub>. In CsFAMA, the halogen ions were measured at 89 at.% for I and 11 at.% for Br. These values are close to the theoretical ones (88 mol.% and 12 mol.%, respectively, in the precursor solution). Cs also is measured at 8% of the monovalent ion composition which corresponds to the molar fraction in the precursor solution. Globally, the CsFAMA layer composition reproduces the precursor solution composition. This is due to the rather low annealing temperature (105°C) employed which prevented the sublimation of compound(s) during this step. The exact composition of the FAMA layer was determined in a dedicated study in Ref.[53] combining <sup>1</sup>H-NMR, <sup>13</sup>C-NMR and EDX from which we established the following formulae: FA<sub>0.94</sub>MA<sub>0.06</sub>PbI<sub>3</sub>. For this compound, we also noted that Cl did

not give a clear signal in the EDX spectra. The amount quantified was 0.4% of the halide content which is below the accuracy of the technique. Since MAI was added in a large molar fraction in the precursor solution (48 mol.% of  $\text{PbI}_2$ ), we can conclude that I was eliminated by sublimation upon the annealing step at  $153^\circ\text{C}$ .

## II.1.4 Characterizations of PSCs

### II.1.4.1 $J-V$ curves

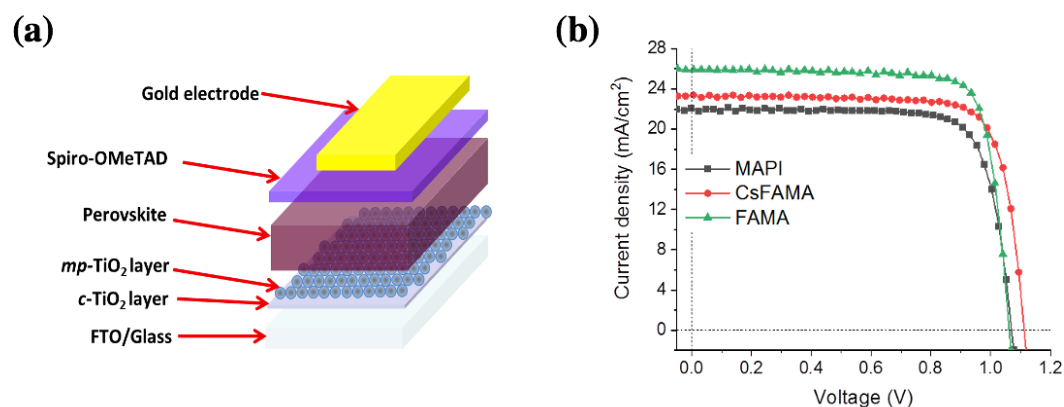


**Figure II.7 (a)** Exploded schematic view of the perovskite solar cells. **(b)** Reverse  $J-V$  curves of MAPI, CsFAMA and FAMA cells.

The FTO/ $c\text{-TiO}_2$ / $mp\text{-TiO}_2$ /PVK layers stacks were completed by spin-coating a film of Spiro-OMeTAD on its top and by evaporating a 70-80 nm thick gold back contact (**Figure II.7a**). The  $J-V$  curves are shown in **Figure II.7b** and **Figure A.II.6 (Annex II)** and the  $J-V$  curve parameters of the best cells are gathered in **Table II.3**. The maximum power conversion efficiency ( $PCE$ ) of MAPI cell achieved 18.93%, stabilized at 18.65%. It was 20.36%, stabilized at 20.03% for CsFAMA cells. In a paper published by my group, it was demonstrated that the intercalation of a 4-Chlorobenzoic acid self-assembled monolayer at the  $\text{TiO}_2$ /CsFAMA interface boosts the performance to 21.35%.[61] MAPI and CsFAMA compounds have the same  $E_g$ , however, CsFAMA cells present a higher  $J_{sc}$  and  $V_{oc}$ . The former is mainly due to a higher absorbance (**Figure II.4a**) and absence of pinholes. Pinholes in the MAPI layer can result in shunting pathways between the hole and electron transporting layers that lower the  $FF$  and  $V_{oc}$  parameters. The better  $V_{oc}$  of CsFAMA cells is assigned to lower recombinations occurring at the interfaces.

Table II.3 Typical photovoltaic  $J-V$  parameters of cells among the best.

Sample	Scan direction	$V_{oc}$ /V	$J_{sc}$ mA/cm <sup>2</sup>	FF /%	PCE /%	Stabilized PCE <sup>a</sup> /%	HI <sup>b</sup> /%
MAPI	Reverse	1.063	23.08	77.43	18.93	18.65	6.5
	Forward	1.059	22.51	73.99	17.70		
CsFAMA	Reverse	1.110	23.13	79.27	20.36	20.03	6.1
	Forward	1.101	23.13	75.00	19.10		
FAMA	Reverse	1.060	25.94	80.62	22.18	22.08	3.7
	Forward	1.052	25.93	78.26	21.35		

<sup>a</sup> Measured by tracking the Maximum Power Point.

<sup>b</sup> HI : Hysteresis index defined as  $[PCE(\%)_{rev} - PCE(\%)_{for}] * 100 / PCE(\%)_{rev}$

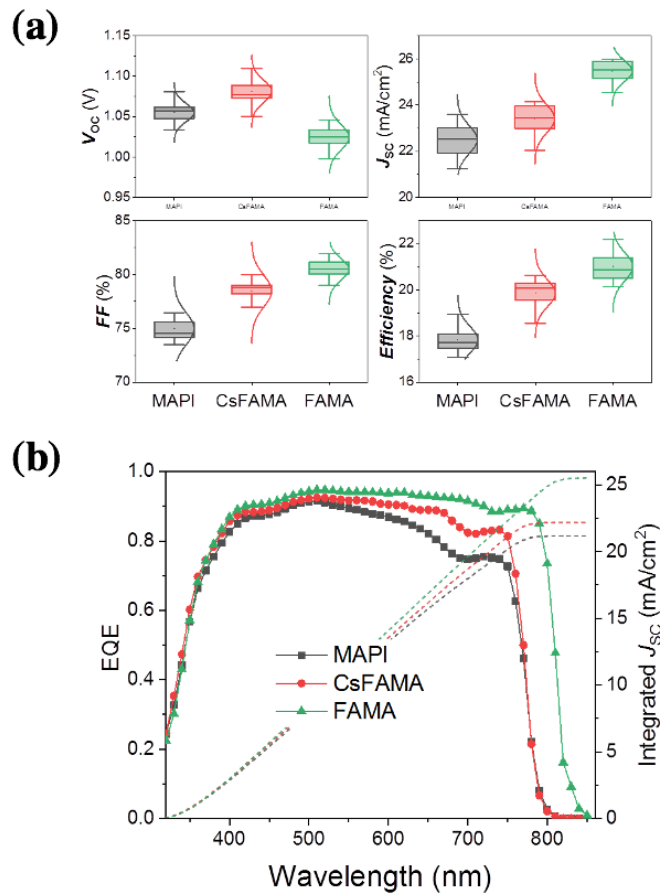
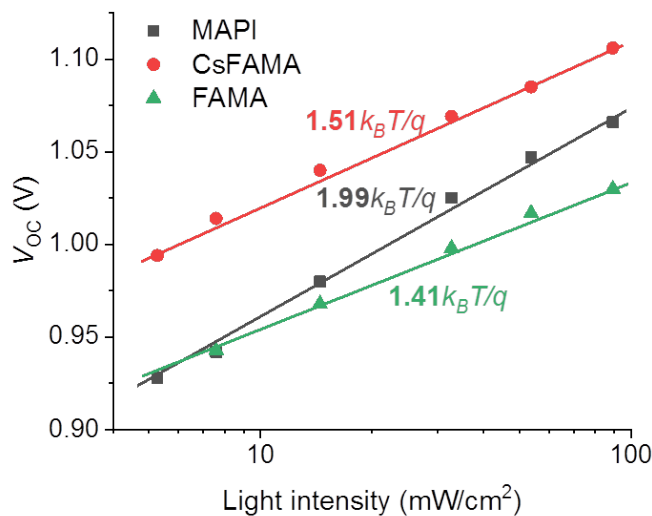


Figure II.8 (a) Statistical analysis of the PSCs performances and  $J-V$  curves parameters. (b)  $EQE$  spectra of the three perovskites with the integrated  $J_{sc}$  curves.

The FAMA cells exhibited the highest efficiency. The  $PCE$  could reach a remarkable 22.18 % value and the stabilized  $PCE$  achieved 22.08%.  $J_{sc}$  was boosted due to a wider wavelength range for the light harvesting (**Figure II.4**) and to the high structural quality and big grains (**Figure II.1**). These cells also presented the best  $FF$ . The lower bandgap is at the origin of the lower  $V_{oc}$  of the FAMA cells compared to the CsFAMA ones. All the trends obtained for the best cells were confirmed by the statistical analysis disclosed in **Figure II.8**.

We also noted that the hysteresis index ( $HI$ ) parameter is similar for the MAPI and the CsFAMA cells with values of ca. 6-7% for the best cells. Its average was 11-14% for MAPI and 6-8 % for CsFAMA cells. This parameter was significantly better in the case of the FAMA cells with reproducible and remarkably low values at only 3-4%.

#### II.1.4.2 External quantum efficiency (EQE) and $V_{oc}$ versus light intensity



**Figure II.9** Variation of  $V_{oc}$  as a function of the light power density. The curve slopes provide the ideality factor,  $n_{ID}$ , values (numbers in bold).

The ability of the PSCs to collect light and to generate charge with a high efficiency was studied by measuring their  $EQE$  spectra (**Figure II.8b**). MAPI cells presented the lowest performances, especially at high wavelengths, for which the irradiation penetration depth is the longest. The integration of the spectra gave a  $J_{sc}$  of 21.1 mA.cm<sup>-2</sup>. For the CsFAMA cell, the charge generation edge was similar but the  $EQE$  was higher compared to MAPI. The integration gave a  $J_{sc}$  of 22.2 mA.cm<sup>-2</sup>. Using the FAMA

perovskite produced two major effects: firstly, it shifted the charge generation edge toward higher wavelengths at about 820 nm, in good agreement with the absorbance spectra of **Figure II.4**; secondly, a high efficiency was achieved in the full visible and near-IR range. The integration of the spectrum provided a calculated  $J_{sc}$  of 25.5 mA.cm<sup>-2</sup> in good agreement with the  $J$ - $V$  measurements.

We measured the cells  $V_{oc}$  under various continuous light power densities ( $I$ ). A white light source (Schott lamp) was employed and the curves are disclosed in **Figure II.9** CsFAMA cells presented a superior  $V_{oc}$  over all the investigated light intensity range. The  $V_{OC}$  scaled logarithmically with  $I$  and followed the relationship:

$$qV_{OC} = E_g + n_{ID}kT \ln(I/I_0) \quad (II.3)$$

with  $q$  the elementary charge,  $k$  the Boltzmann constant,  $T$  the absolute temperature and  $n_{ID}$  the ideality factor. The latter parameter was determined from the curve fits. It is related to the main recombination phenomena occurring at the  $V_{oc}$ . [62] In classical semiconductor theory, a value of 1 for this parameter indicates a band-to-band recombination. Deviation of  $n_{ID}$  from 1 to 2 reflects the occurrence of trap-assisted Shockley-Read-Hall (SRH) recombination through perovskite intragap defects. [62] The higher is  $n_{ID}$ , the higher is the SRH recombination processes.  $n_{ID}$  was the lowest for FAMA at ~1.4 which had a superior quality compared to CsFAMA ( $n_{ID}$  ~1.5), and especially compared to MAPI ( $n_{ID}$  ~2.0) (**Figure II.9**). SRH recombination increases from FAMA, CsFAMA and MAPI. **Figure II.9** illustrates that for an optimized functioning over a large light power density, the  $n_{ID}$  parameter must be the lower.

#### **II.1.4.3 Electrical stability of the devices**

The future of the perovskite technology will depend on the ability of obtaining stable devices. Their robustness against electrical stresses and light irradiation are key parameters that must be carefully investigated. We performed a first test consisting in measuring the  $J$ - $V$  curves of the cells, before and after their electrical impedance spectroscopy (EIS) investigation (the EIS investigation is provided in the **Annex A.II.1**). EIS measurements, in which PSCs are submitted to a continuous light irradiation, to the application of many voltages and to a superimposed ac stimulus during more than one hour, are especially stressing for the PSCs. [63] **Table II.4** reports the  $J$ - $V$  curves results before and after the EIS

characterization for the different perovskites. The performances of the MAPI cells measured on the reverse scan slightly increased upon the measurements. The *PCE* of the forward scan was decreased due to the *FF* parameter mitigation. The CsFAMA cells were the most affected by the EIS measurements. Their efficiency was measured lower after the EIS characterization. FAMA devices were remarkably stable since they exhibited a slightly higher *PCE* after EIS characterizations due to the increase of the *V<sub>oc</sub>*. Their *HI* parameter remained low and almost unchanged.

**Table II.4 *J-V* curves parameters of PSCs with various perovskites before and after their investigation by EIS.**

Sample			<i>V<sub>oc</sub></i> /V	<i>J<sub>sc</sub></i> / mA.cm <sup>-2</sup>	<i>FF</i> / %	<i>PCE</i> / %	<i>HI</i> <sup>a</sup> / %
MAPI	Before	Reverse	1.045	22.19	78.42	18.18	12
		Forward	1.026	22.18	70.19	15.97	
	After	Reverse	1.057	23.19	75.87	18.60	16
		Forward	1.033	23.13	65.41	15.63	
CsFAMA	Before	Reverse	1.077	21.81	77.63	18.24	7
		Forward	1.052	21.81	73.63	16.88	
	After	Reverse	1.049	21.64	74.18	16.83	8
		Forward	1.027	21.66	69.23	15.40	
FAMA	Before	Reverse	1.035	25.65	79.62	21.13	2
		Forward	1.031	25.69	77.81	20.61	
	After	Reverse	1.044	25.71	79.36	21.29	3
		Forward	1.045	25.71	77.17	20.73	

<sup>a</sup>*HI* : Hysteresis index defined as  $[PCE(\%)_{rev}-PCE(\%)_{for}] * 100 / PCE(\%)_{rev}$

We also compared the stability of the unencapsulated solar cells under a one sun AM 1.5G light irradiation and at a relative humidity (RH) of 45%, tracking them at their maximum power points (MPP). The curves are disclosed in **Figure II.10a**. During 200 min, the MAPI cell presented the fastest decrease. The CsFAMA cell *PCE* decreased more slowly at the beginning but the two curves crossed at 200 min. After 300 min, the MAPI cell had lost 37% of its initial *PCE* and the CsFAMA cell 42%. The FAMA cell was remarkably stable and no *PCE* loss was observed. **Figures II.10b-d** are the *J-V* curves measured before and after the tracking experiments. MAPI cell presented a lower *V<sub>oc</sub>* and a

large hysteresis after the stability test. CsFAMA cell exhibited a decrease of the  $J_{sc}$  and an enlargement of the hysteresis. We noted a remarkable stability of the FAMA cell under the test since the  $J-V$  curves were unchanged after the long irradiation and tracking period.

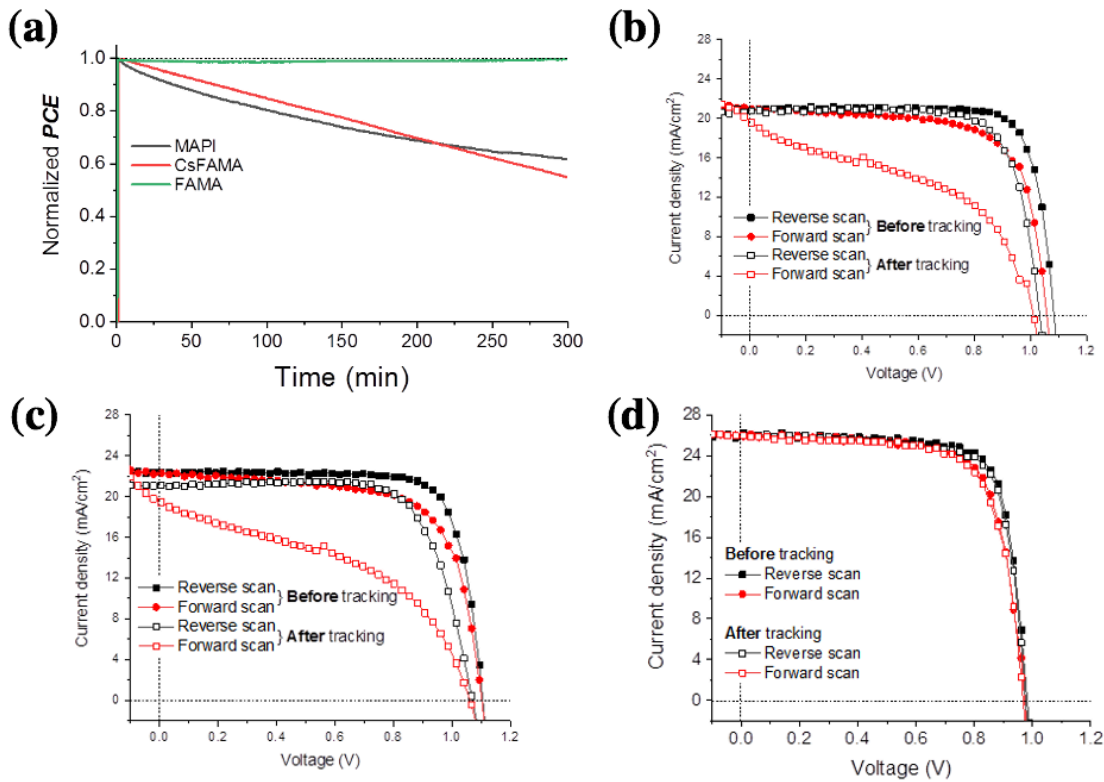


**Figure II.10 (a) Tracking of MAPI, CsFAMA and FAMA solar cells normalized power outputs under continuous one sun AM1.5G illumination (unencapsulated devices 45% RH). (b-d)  $J-V$  curves measured before and after the tracking experiment under 1sun AM1.5G illumination. (b) MAPI; (c) CsFAMA and (d) FAMA cells.**

This subsection focusses on the effect of the monovalent cation composition on the electrical properties of PSCs. A study of the PSCs stability under high moisture environment is given in **Figure II.11** and **Figure A.II.7 (Annex II)**. None of them, when unencapsulated, were highly robust when store in a chamber with a 90% RH at 20°C. MAPI was degraded quickly with a steep decrease below 50% of the initial value during the first hours. Even if the perovskite MAPI phase was detected after 150h of aging, the cell worked very badly. On the other hand, the MAPI cell was highly stable when stored in a glovebox filled with nitrogen. We experienced a 14 months long storage (**Table A.II.2, Annex II**). We found typically a stabilized initial PCE of 17.78% and 17.89% after the 14 months aging(**Figure**

**A.II.9, Annex II).** For the FAMA cell, the power output was stable for 20h and then decreased abruptly. The variation of the  $J-V$  curve parameters is shown in **Figure II.11**. After 120h, for all the cells, the efficiency was below 30% of the initial  $PCE$  and the best value was found for FAMA cell.

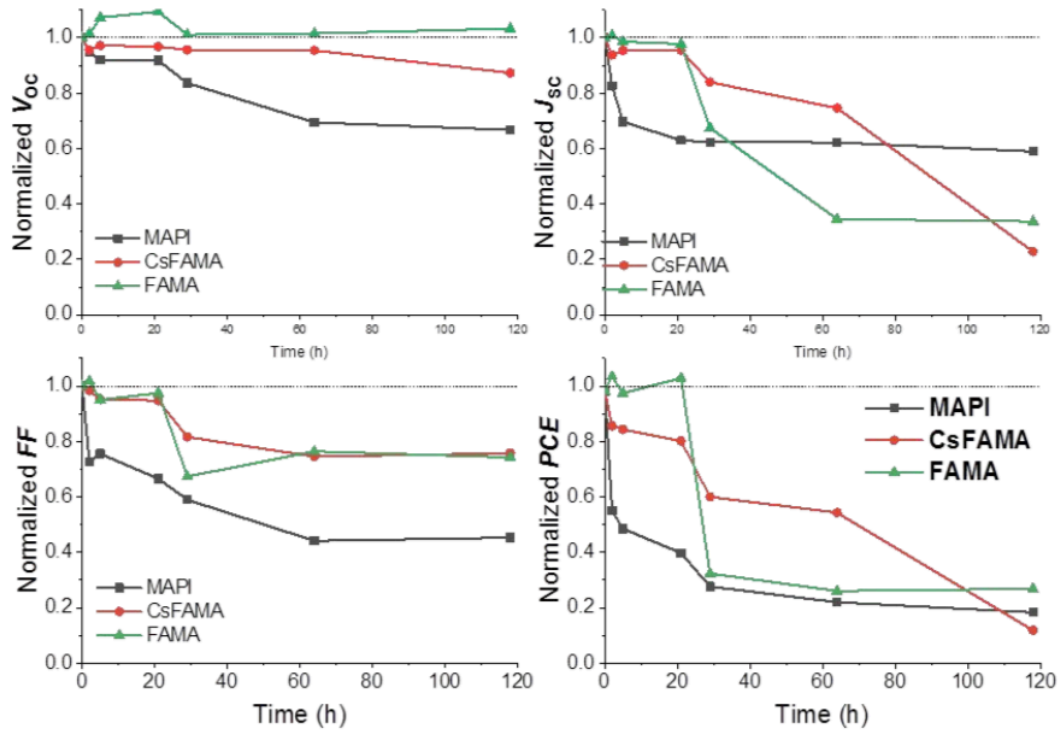


**Figure II.11** PCE and  $J-V$  curve parameters followed upon the unencapsulated PSC aging at 90 %RH.

It can be assigned to the presence of the hydrophilic MA cation in their structure. They should need additional efficient barrier layers against moisture to be fully stabilized. The final  $PCE$  was the best for FAMA. We have also found that MAPI was decomposed upon aging in  $PbI_2$  with the elimination of MAI (MAI can be degraded into volatile  $CH_3NH_3$ ,  $CH_3I$  and  $NH_3$  molecules)[64]. On the other hand, CsFAMA and FAMA were degraded in the photo-inactive one-dimensional (1D)  $\delta$ -phase that may be regenerated in their photoactive  $\alpha$ -phase, for instance by heating (**Figure A.II.8, Annex II**).

### II.1.5 Conclusions

In conclusion, we have fully investigated the electrical response of solar cells prepared with perovskites ranging from the mono-cation to the triple-cation composition. The best results have been found with the double MA/FA lead iodide compound which was prepared using MAI additive in the precursor solution. This strategy has been found the most accurate to achieve high efficiency and

stability. It is more efficient than to complicate the perovskite composition. FAMA presented the best morphology, crystallinity and optical properties for the application. The ideality factor decreased from MAPI, CsFAMA and FAMA. For the later SRH recombination with the less intensity was found.

## **II.2 Effects of 5-Ammonium Valeric Acid Iodide as Additive on two different structure of Perovskite solar cells**

To improve PSC stability, two approaches have been notably developed: the use of additives and/or post-treatments that can strengthen perovskite structures and the use of a non-typical architecture where three mesoporous layers, including a porous carbon back-contact without hole transporting layer, are employed. This section focusses on 5-ammonium valeric acid iodide (5-AVAI or AVA) as additive. By combining scanning electron microscopy (SEM), x-ray diffraction (XRD), time-resolved photoluminescence (TRPL), current-voltage measurements, ideality factor determination and in-depth electrical impedance spectroscopy (EIS) investigations on various layers stacks structures, we have discriminated the effects of mesoscopic embedding scaffold and AVA additive. It is found that both AVA additive and the triple mesoporous structure boost dramatically the PSC stability, while keeping a rather high power conversion efficiency (*PCE* of 16.9% instead of 18.1% for the control). It must be combined with the three mesoscopic structure to get a low defect quality perovskite compound. The high stability of TiO<sub>2</sub>/ZrO<sub>2</sub>/Carbon/Perovskite cells is found mainly due to the protection by the all-inorganic scaffold combined with the hydrophobic properties of carbon. These cells achieved a *PCE* of 14.4% in the present work.

### **II.2.1 Introduction**

In its classical architecture, perovskite solar cells are composed of an organo-lead halide perovskite layer which acts as the solar light absorber and by two selective contacts: a hole transporting layer (HTL) which is placed on the top of the PVK to collect and transport hole charge carriers and block electrons; while, on the other side is placed an electron transporting layer (ETL) which collects and transports electrons and blocks the photogenerated holes. 2,2',7,7'-tetrakis(N,N'-di-p-methoxyphenylamine)-9,9'-spirobifluorene (SpiroOMeTAD) is the most popular hole transporting material (HTM) and TiO<sub>2</sub> is a popular electron transporting material (ETM). However, a different cell

architecture has proved more suitable to get highly stable devices.[35-42] It is composed of three stacked mesoporous layers: TiO<sub>2</sub>/ZrO<sub>2</sub>/carbon. This porous stack is subsequently filled by the perovskite material using a drop-casting technique. In this architecture, no HTM is employed. ZrO<sub>2</sub> acts as an insulating layer which prevents the direct contact of the carbon back-contact with TiO<sub>2</sub> front selective contact. Besides the high stability, this type of cell architecture is compatible with screen-printing techniques and could enable a low-cost production at large scale of PSC panels.[35,40,41] Mei et al. were the first to develop these triple-mesoscopic solar cells.[35] In their pioneering work, they observed that 5-ammonium valeric acid iodide (HOOC(CH<sub>2</sub>)<sub>4</sub>NH<sub>3</sub>I, noted 5-AVAI or AVA) was an important additive for getting a good pore filling and a more complete contact of PVK with the *mp*-TiO<sub>2</sub> scaffold. They stressed that the carbon top electrode presents hydrophobic properties and acts as a barrier against moisture. Later, Grancini et al. [36] showed that AVA allows the dimensional engineering of the perovskite and the formation of a gradually-organized multidimensional interface. These authors achieved a 12.9% *PCE* with laboratory cells. They also prepared mini-modules which demonstrated a 11.2% efficiency stable for more than 10,000 h measured under AM 1.5G standard condition, at 55°C and short-circuit. Employing slot-die coating of AVA-MAPI, Xu et al. achieved a *PCE* of 12.9% on triple-mesoscopic mini-modules of 60 cm<sup>2</sup>. [41] Recently, these PSCs successfully passed the main items of IEC qualification tests, including the damp heat test, thermal cycling test, and ultraviolet preconditioning test, and exhibited over a 9,000 h operational stability.[42]

AVA is the classical additive employed in triple mesoscopic solar cells [35-39,42] even if 4-(aminomethyl) benzoic acid hydroiodide has also been shown very efficient.[37] AVA would play an active role in the high stability of PSCs due to surface defect passivation.[43]. Recently, Péan et al. [43] showed that Methylammonium (MA<sup>+</sup>) lead triiodide (MAPI) modified by AVA reduces the generation of superoxide when infiltrated in the triple-mesoporous layer stack. Its optimum content in the perovskite precursor solution is reported at 3-4% in the literature.[36,37] AVA additive has also been employed in lead-free PSCs.[45] It was shown to affect the growth of perovskite crystals based on formamidinium and tin. It plays on the crystal growth through hydrogen bond with I<sup>-</sup> and precursor SnI<sub>6</sub><sup>4-</sup> octahedral. It forms a protective layer and acts as a cross-linker at the grain boundaries. Consequently, this additive dramatically improves the performance of tin-based PSCs.[45] AVA has

also been employed recently to post-treat MAPbI<sub>3</sub> films that allowed a significant improvement of the solar cell performances and the stabilization of the PVK.[46]

The aim of the present section is to investigate the effect of AVA additive on PSCs with two different architectures: the structure employing a single TiO<sub>2</sub> mesoporous layer (noted *1mp*) and the one employing the (TiO<sub>2</sub>/ZrO<sub>2</sub>/C) triple mesoporous layers structure (noted *3mp*). The effects of AVA additive and of the host layers on the PVK properties and stability against moisture are first established. Then, the performances of the cells are characterized. We subsequently study the effect of light intensity on the cell electrical response at open circuit voltage ( $V_{oc}$ ) prior to investigate the effects of the applied voltage ( $V_{appl}$ ). The influence of AVA additive and cell architecture on the electrical impedance response of the devices has been also thoroughly reported and analyzed. These results are detailed in the **Annex A.II.2**.

## II.2.2 Experimental

*1mp* substrate preparation: The fluorine-doped SnO<sub>2</sub> (FTO) substrates (TEC 7 from Pilkington), a *c*-TiO<sub>2</sub> layer and a *mp*-TiO<sub>2</sub> layer were prepared as described in **Section II.1.2.1**.

*1mp* cells preparation:

Method of preparation of MAPbI<sub>3</sub> precursor solution was detailed in **Section II.1.2.2**. The (AVA)<sub>2</sub>MA<sub>56</sub>Pb<sub>57</sub>I<sub>172</sub> precursor solution had a 1.45M concentration. 668.5 mg PbI<sub>2</sub>, 12.4 mg 5-ammonium valeric acid iodide (TCI) (HOOC-(CH<sub>2</sub>)<sub>4</sub>-NH<sub>3</sub>I) (3.5% molar ratio of PbI<sub>2</sub>) and 222.4 mg MAI were mixed in 1mL DMSO. The solution was stirred and kept warm at 100°C for 2h before use. These solutions were spin-coated on the *1mp* substrate using a two-step program at 1000 rpm and 6000 rpm for 10 s and 30 s, respectively. 100 μL of chlorobenzene was dropped 30 s after starting the spinning routine. The films were subsequently annealed at 100 °C for 1 h. The hole transporting material (HTM) was prepared as detailed in **Section II.1.2.2**. The gold back-contact was deposited by thermal evaporation through a mask. The pure 2D perovskite (AVA)<sub>2</sub>PbI<sub>4</sub> layer was prepared by dissolving 553.2 mg PbI<sub>2</sub> and 294.2 mg 5-ammonium valeric acid iodide in 1 mL anhydrous DMSO and stirring at room temperature. The concentration of PbI<sub>2</sub> was 1.20M.

3mp cells preparation: For the triple mesoscopic devices,  $\text{PbI}_2$  and  $\gamma$ -Butyrolactone (GBL) were purchased from Sigma-Aldrich. Methylammonium iodide (MAI) and 5-ammonium valeric acid iodide were synthesized as previously reported [35]. The perovskite precursor solution was prepared by dissolving 461 mg  $\text{PbI}_2$ , 153 mg MAI and 8.6 mg 5-AVAI in 1.17 mL GBL. It was stirred at 60 °C overnight before use. We employed triple-mesoporous scaffold substrates provided by the Wuhan National Laboratory for Optoelectronics, Huazhong University of Science & Technology (HUST), Wuhan, China. For their preparation, the  $\text{TiO}_2$  paste was purchased from Greatcell Solar (30 NR-D). The  $\text{ZrO}_2$  paste and carbon paste were prepared as described in Ref.[52] Unless stated otherwise, all the materials were used as received without further purification. The FTO conducting glass substrates were first etched with a 1064 nm laser and then cleaned by ultrasonication with detergent solution, deionized water, and ethanol for 15 min, respectively. A *c*- $\text{TiO}_2$  layer was deposited on the Glass/FTO substrates by spray pyrolysis deposition at 450°C using diisopropoxytitaniumbis(acetyl acetate) solution. Then the *mp*- $\text{TiO}_2$  layer, the  $\text{ZrO}_2$  spacer layer and the carbon layer were layer-by-layer screen-printed onto the substrates. The  $\text{TiO}_2$  layer and  $\text{ZrO}_2$  layer were sintered at 500°C for 30 min, and the carbon layer was sintered at 400 °C for 30 min.

4~4.5  $\mu\text{L}$  of perovskite precursor solution was drop-casted on the top of the substrate carbon layer. After the precursor penetration into the mesoporous scaffold, the samples were annealed at 50 °C for 4h.

The layers and solar cells were characterized as already described in **Section II.1.2.2** and the **Annex A.II.2**.

### **II.2.3 Characterizations of Perovskite Films**

Before to develop the characterizations of the PVK layers, one must first precise the two architectures of PSC that have been considered in the present work. As shown in **Figure II.12**, perovskite layers were prepared either by deposition on a *mp*- $\text{TiO}_2$  layer (**Figure II.12a**, hereafter named *1mp*) or by infiltrating the perovskite precursor solution in a triple mesoporous layers stack combining  $\text{TiO}_2$ ,  $\text{ZrO}_2$  and carbon. MAPI perovskite was formed into the pores after an annealing step at 50°C in an oven (**Figure II.12b**, hereafter named *3mp*). The former corresponds to the standard cell structure where a

HTL, made of LiTFSI-doped Spiro-OMeTAD, is deposited on top of the PVK prior to evaporate the gold metal back-contact through a mask to obtain the device. For the latter, the perovskite layer preparation was the final step. The *3mp* cells are HTL-free. For the sake of comparison, we have also prepared *1mp* cells without the HTM layer (NoHTM), the gold back contact being directly evaporated onto the perovskite layer.

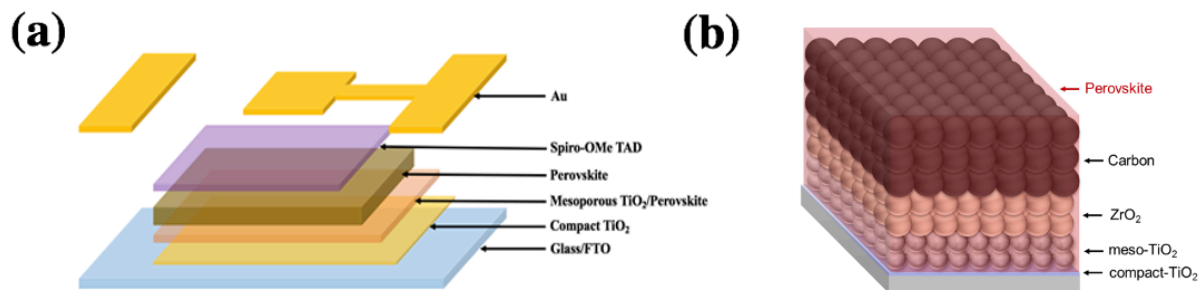


Figure II.12 Schematic figures of (a) single-mesoporous (*1mp*) and (b) carbon-based triple-mesoporous (*3mp*) device structures.

### II.2.3.1 SEM

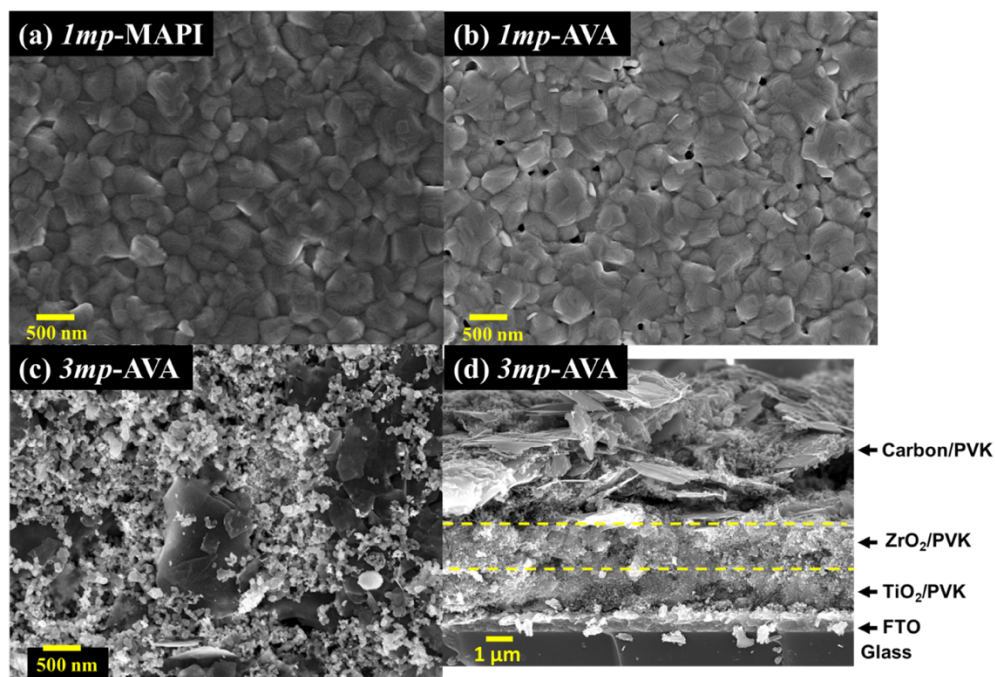
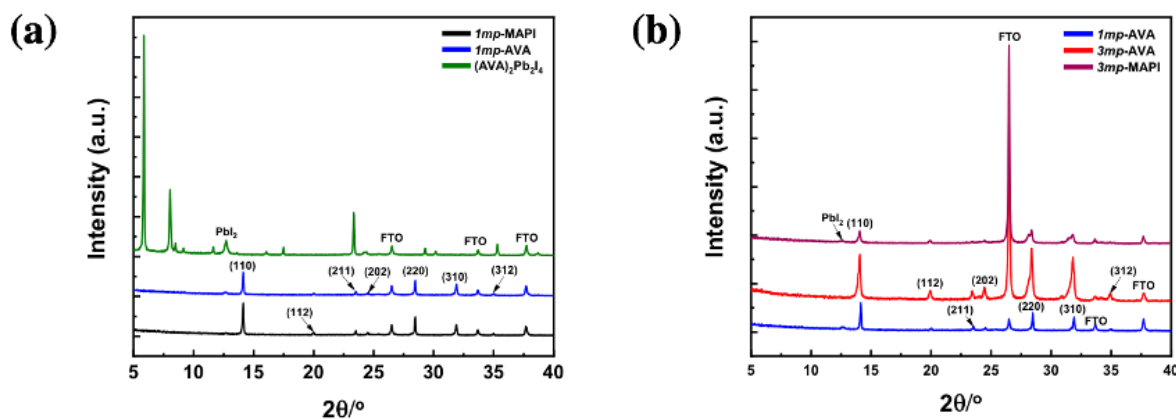


Figure II.13 (a-c) SEM top views of the (a) *1mp*-MAPI layer, (b) *1mp*-AVA layer and (c) *3mp*-AVA layer. The scale bar is 500 nm. (d) Cross sectional view of the *3mp*-AVA solar cell. The yellow dashed lines visualize the limits between the various mesoporous layers.

The surface morphology of the films was characterized by scanning electron microscopy (SEM). Top views in **Figure II.13** show that the *1mp* layer was filled and capped by the PVK material. The capping PVK layer presented less pinholes for MAPI compared to AVA-MAPI. The average grain size was measured at 320 nm for MAPI and 330 nm for AVA-MAPI. The top aspect was different in the case of the *3mp* substrate (**Figure II.13c**). We observed mesoscopic carbon and graphite flakes. AVA-MAPI filled the mesoporous layers stack and the top layer was not capped by the PVK material. **Figure II.13d** is a cross-sectional view of the *3mp*-cell where one can recognize the triple mesoporous stack which contains the PVK as schematized in **Figure II.13b**.

### II.2.3.2 XRD



**Figure II.14 (a)** XRD patterns of MAPI, AVA-MAPI and  $(\text{AVA})_2\text{PbI}_4$  perovskite layers deposited on *1mp* substrate. **(b)** XRD patterns of AVA-MAPI layers deposited on *1mp* and *3mp* substrates.

The effect of AVA additive on the structural properties of the MAPI layer was investigated by x-ray diffraction (XRD) measurements. **Figure II.14a** compares MAPI films prepared on *1mp* substrate with and without 3.5% of AVA additive. The amount of 3.5% was chosen as being among the best in the literature for performances of *3mp* cells.[45] **Figure II.14a** shows that both patterns are dominated by peaks at  $14.15^\circ$  and  $28.21^\circ$ . They correspond to the (110) and (220) planes of tetragonal MAPI and indicate a clear texturisation of the prepared layers. The peaks are slightly less intense with the AVA additive. In both cases, a small  $\text{PbI}_2$  diffraction peak at  $12.7^\circ$  is found. In **Figure II.14a**, the reference XRD pattern of the 2D  $(\text{AVA})_2\text{PbI}_4$  phase is also presented. Its comparison with the AVA-MAPI pattern shows that no peak of the 2D phase is present, so this phase is not present in a significant amount in the final layer.

### II.2.3.3 Time-resolved photoluminescence

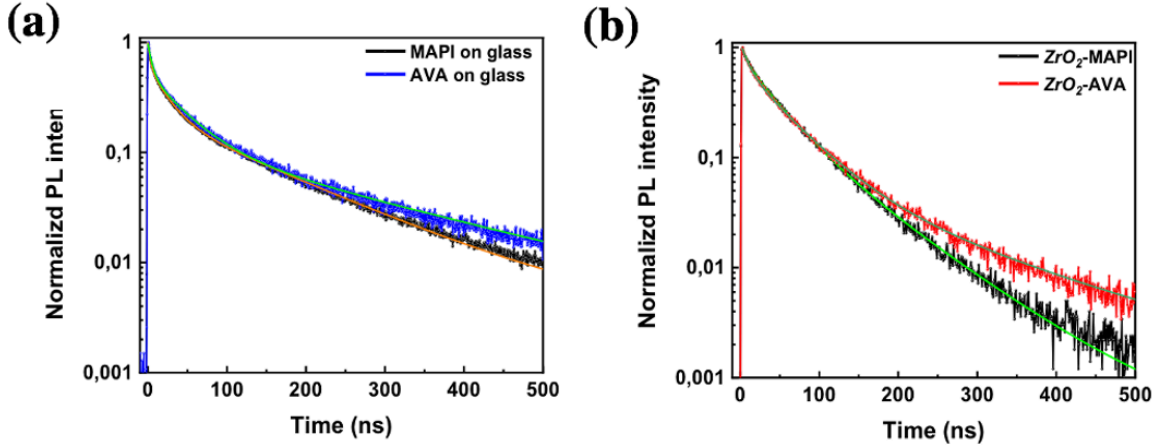


Figure II.15 (a) TRPL of *Imp*-MAPI and *Imp*-AVA layers deposited on glass substrate. (b) TRPL of *3mp*-MAPI and *3mp*-AVA layers deposited on ZrO<sub>2</sub>.

Table II.5 Fitting parameters by a triple exponential function of the TRPL curves of Figure II.15.

Fitting function: $y = A_1 \exp(-x/\tau_1) + A_2 \exp(-x/\tau_2) + A_3 \exp(-x/\tau_3) + y_0$											
	$y_0$	$A_1$	$\tau_{fast}$ (ns)	$RC_{fast}^a$	$A_2$	$\tau_{int}$ (ns)	$RC_{int}^a$	$A_3$	$\tau_{slow}$ (ns)	$RC_{slow}^a$	
MAPI on glass	7.6E-4	0.39	3.21	0.03	0.40	25.17	0.25	0.19	153.51	0.72	
AVA on glass	1.6E-3	0.452	5.31	0.05	0.39	42.14	0.36	0.12	227.45	0.59	
MAPI on ZrO <sub>2</sub> /Glass	3.8E-4	0.31	6.93	0.05	0.58	39.31	0.49	0.24	88.01	0.46	
AVA on ZrO <sub>2</sub> /Glass	5.6E-4	0.41	9.85	0.09	0.61	51.47	0.65	0.07	181.4	0.26	

<sup>a</sup> Relative contribution

The time-resolved photoluminescence (TRPL) curves of MAPI and AVA layers deposited on glass and on ZrO<sub>2</sub> mesoporous layer are shown in **Figure II.15** and **Figure A.II.10 (Annex II)**. We did not observe an exponential decay and we had to employ a triple exponential function to get a correct fit. The presence of at least three time constants shows the occurrence of several deexcitation pathways. The longest one ( $\tau_{slow}$ ) can be assigned to the radiative bulk component.[59] The fitting parameters are gathered in **Table II.5**. In **Figure II.15a**, for layers deposited on glass (an insulating substrate for which charge carrier transfer cannot occur),  $\tau_{slow}$  was measured at 154 ns for MAPI and 227 ns for the AVA layers. This component reflects the structural quality of the material which is then improved in the presence of AVA. This trend was confirmed for PVK layers deposited in the ZrO<sub>2</sub> scaffold (**Figure II.15b**) with  $\tau_{slow}$  increasing from 88 ns to 181 ns in the presence of AVA additive. The TRPL measurements show that the structural quality of PVK prepared on *Imp* substrate is better than the one prepared in the ZrO<sub>2</sub> scaffold.

### II.2.3.4 Stability

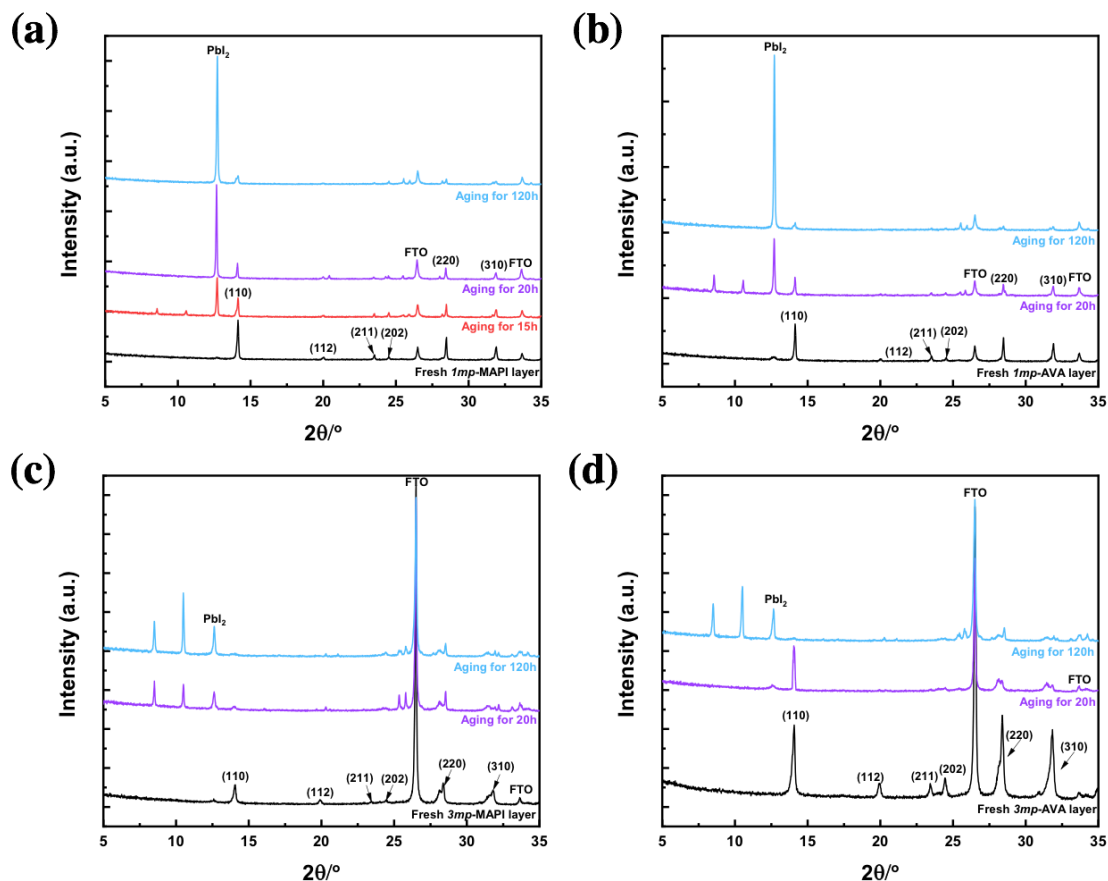


**Figure II.16** XRD pattern evolution of (a) *Imp*-MAPI, (b) *Imp*-AVA, (c) *3mp*-MAPI and (d) *3mp*-AVA layers upon aging in a 90% RH atmosphere for 120h (exposure time).

We have followed the stability of the four layers exposed to high humidity (relative humidity (RH) $\geq$ 90%) at room temperature since this parameter is critical for the future of the PSC technology. To discriminate the effect of AVA and scaffold on the PVK stability, we compared the aging of *Imp*-MAPI, *Imp*-AVA, *3mp*-MAPI and *3mp*-AVA. The phase degradation kinetic was followed by XRD in **Figure II.16**. We can see that, in all cases, the decrease of the PVK diffraction peaks was accompanied by the appearance of three other peaks. The ones at 8.58° and 10.6° are assigned to the monohydrate, MAPbI<sub>3</sub>·H<sub>2</sub>O phase [56] and the peak at 12.7° corresponds to PbI<sub>2</sub>. It clearly shows that under high moisture, MAPI forms a monohydrate species which further decompose into PbI<sub>2</sub> while MA is lost. We never observed the di-hydrate phase.[56] *Imp*-MAPI decomposed rapidly since after 15h, the pattern was dominated by the hydrate and PbI<sub>2</sub> phases (**Figure II.16a**). The layer degradation was slower for the *Imp*-AVA sample (**Figure II.16b**) since, after 20h, this sample still presented the

perovskite and hydrate phases when the *1mp*-MAPI XRD pattern was dominated by the  $\text{PbI}_2$  phase. After 120h, both layers were almost fully converted into  $\text{PbI}_2$ . For the *3mp* samples (Figures II.16c and II.16d), we also observed a reduction of the degradation kinetic with the presence of AVA. Moreover, we found that the *3mp* scaffold is also beneficial for the stability. The hydrate species was still present after 120h of moisture exposure while this phase completely disappeared for the *1mp* samples. These observations were confirmed by the layers aspect change with aging as displayed in Figure II.17. We can conclude that the high stability of *3mp* cells ( $\text{TiO}_2/\text{ZrO}_2/\text{Carbon}/\text{Perovskite}$ ) is mainly due both to the protection by the all-inorganic scaffold and to AVA. AVA can tune the crystallization of the perovskite in the scaffold leading to crystals with less bulk defects.

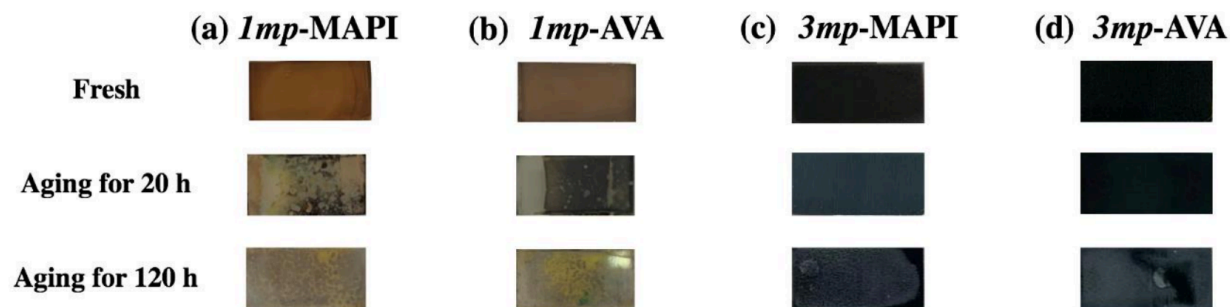


Figure II.17 Pictures of PVK layers: fresh and after 20 h and 120 h aging at  $\geq 90\%$  RH/RT. The black/grey aspect of the *3mp* samples is due to the carbon back electrode. (a) *1mp*-MAPI, (b) *1mp*-AVA, (c) *3mp*MAPI and (d) *3mp*-AVA.

## II.2.4 Characterizations of PSCs

### II.2.4.1 *J-V* curves and cell performances

**Table II.6** PCE, *J-V* curve parameters and HI of the best cells.

Cell structure	PVK	Scan direction	$V_{oc}$ [V]	$J_{sc}$ [mA cm <sup>-2</sup> ]	$FF^a$	$PCE$ [%]	$HI^b$
<i>Imp</i>	MAPI	Reverse	1.058	22.78	75.03	18.09	0.12
		Forward	1.044	22.70	66.91	15.86	
<i>Imp</i>	AVA	Reverse	1.040	22.05	73.54	16.86	0.31
		Forward	1.017	21.94	51.87	11.58	
<i>Imp</i>	AVA-NoHTM	Reverse	0.805	12.75	67.62	6.94	0.73
		Forward	0.790	6.71	35.56	1.89	
<i>3mp</i>	AVA	Reverse	0.932	22.88	67.62	14.41	0.00
		Forward	0.929	22.86	68.23	14.49	

<sup>a</sup> Fill factor. <sup>b</sup> Hysteresis index defined as:  $[PCE(\%)_{rev}-PCE(\%)_{for}]/PCE(\%)_{rev}$

*Imp*-MAPI, *Imp*-AVA, *Imp*-AVA-NoHTM and *3mp*-AVA solar cells were characterized by measuring their *J-V* curves. **Table II.6** gathers the results obtained for the best devices, **Figure II.18a** shows their reverse *J-V* curves and **Figure A.II.11 (Annex II)** the reverse and forward *J-V* curves. *Imp*-MAPI cells exhibited the best performances. Their maximum *PCE*, measured on the reverse scan, was 18.09%. Their steady-state *PCE*, obtained by tracking at the potential of the maximum power output,  $V_{max}$ , was found at 17.38% (**Figure II.18b**). We noticed that adding AVA was detrimental for the performances and the hysteresis of standard cells. The efficiency on the reverse scan decreased to about 16.86%. A large hysteresis was obtained in the presence of AVA. The *PCE* reduction was a consequence of lower  $V_{oc}$ ,  $J_{sc}$  and  $FF$ . We have also noted that the tracking curve showed a slow *Imp*-AVA cell response, but the stabilized *PCE* reached 15.91% (**Figure II.18b**). In spite of the large hysteresis, this cell stabilized *PCE* was close to the *PCE* value determined on the reverse scan. Our *Imp*-AVA cells were more efficient than those reported in the literature up to now.[36] **Figure II.18c** shows the statistical analysis of the cells *J-V* curve parameters which confirms the trend found for the best *Imp*-MAPI and *Imp*-AVA devices. The degraded performances of the *Imp*-AVA cells is due to the more defective morphology with pinholes.

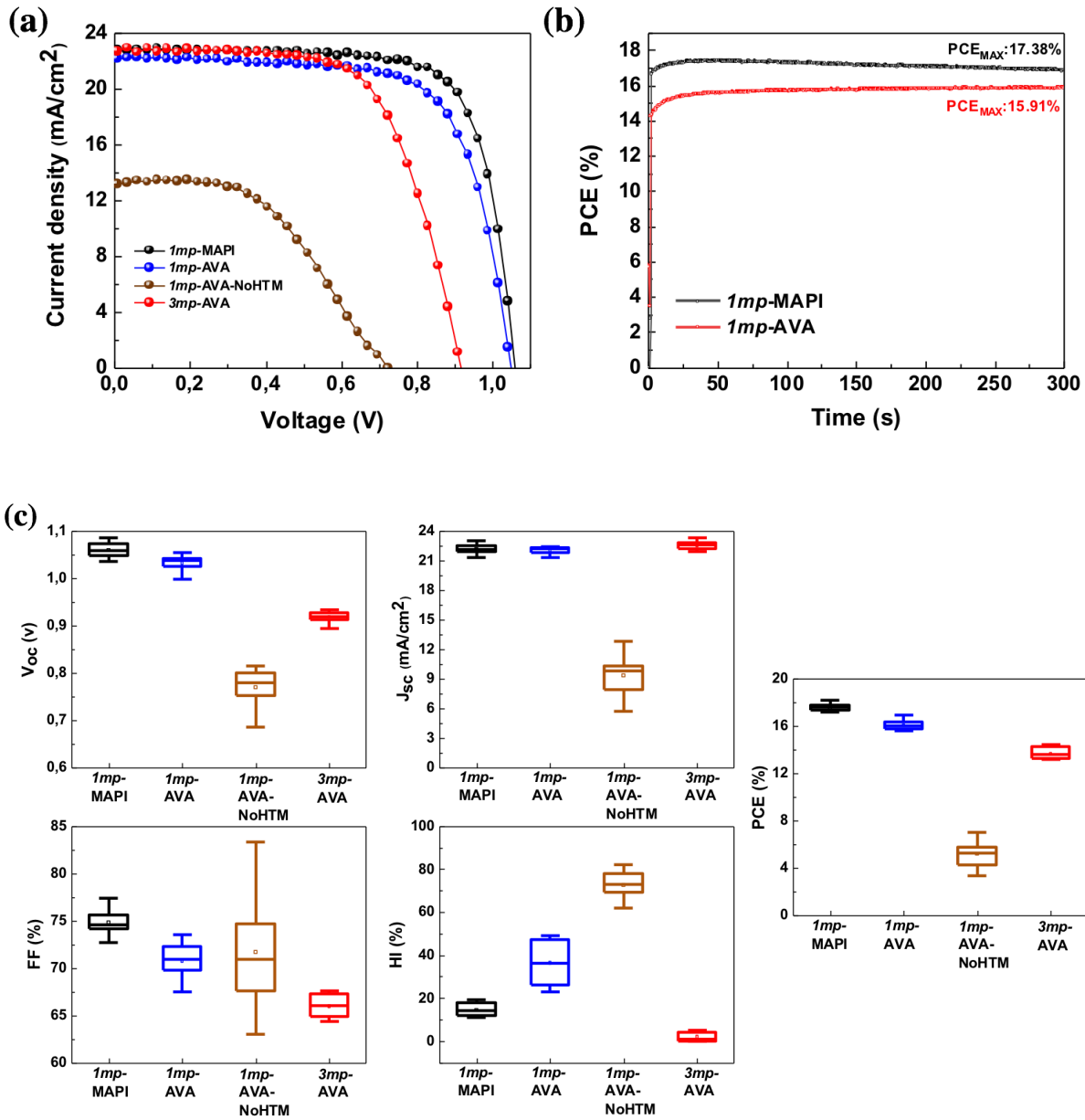
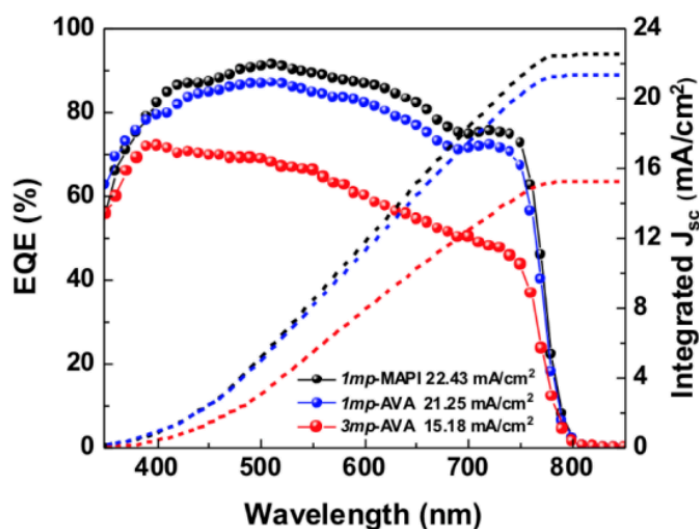


Figure II.18 (a) Reverse scan  $J-V$  curves of *1mp*-MAPI, *1mp*-AVA, *1mp*-AVA-NoHTM and *3mp*-AVA solar cells. (b) Tracking curves of *1mp*-MAPI and *1mp*-AVA best cells. (c) Statistical analysis of the solar cells  $J-V$  curve parameters and PCEs.

We have also compared *1mp*-AVA cells with and without HTL (Table II.6, Figures II.18a and II.18c). The efficiency dropped down in the absence of HTL because many recombinations occur at the gold back-electrode when in direct contact with the perovskite layer. The efficiency was measured less than 7%, the  $J-V$  curve was S-shaped and the hysteresis was very large. These cells presented the largest dispersion in their  $J-V$  curves parameters (Figure II.18c). Changing the cell structure and using the

three mesoscopic one changed dramatically the performances of the devices without HTM. In the case of *3mp* cells, with a carbon back-contact, the efficiency was much higher. The best cell achieved a *PCE* of 14.4% without significant hysteresis. For the *1mp*-AVA-NoHTM, the contact between perovskite and gold is poor. On the contrary, the mesoporous carbon layer can provide huge contact area for perovskite absorber, and thus assist the charge transfer. The absence of hysteresis can be assigned to the confined environment that would block the iodide ionic mobility.[54, 58] Compared to the *1mp*-MAPI cell, the lower efficiency is mainly due to lower  $V_{oc}$  and  $FF$  (**Figure II.18c**). The external quantum efficiency (*EQE*) curves of the cells are disclosed in **Figure II.19**. A good correlation is found between the  $J_{sc}$  calculated from the *EQE* spectra for the *1mp* cells. On the other hand, this parameter is significantly underestimated for the *3mp*-AVA cell due to its slow photoelectrical response.



**Figure II.19** External quantum efficiency (*EQE*) spectra and  $J_{sc}$  integration curves of the various cells.

#### II.2.4.2 Effect of light intensity at $V_{oc}$

The effects of AVA additive and cell architecture on the solar cells response to the light illumination at the open circuit voltage ( $V_{oc}$ ) have been investigated. **Figure II.20** and **Figure A.II.14 (Annex II)** shows the variation of this parameter with white light illumination power density (Intensity). For the investigated cells, the  $V_{oc}$  was superior with HTM compared to without HTM. Except for *1mp*-AVA-NoHTM cell, the  $V_{oc}$  scaled logarithmically with the light power density ( $I$ ) and followed

**Equation II.3.** As already mentioned,  $n_{ID}$  parameter is related to the main recombination phenomena occurring at the  $V_{oc}$ . [35] The values of  $n_{ID}$  are gathered in **Table II.7**. For *1mp*-cells with HTM and the *3mp*-cell, values between 1.8 and 2 are found which suggest that, at the open circuit, a Shockley-Read-Hall (SRH) recombination mechanism through perovskite intragap defects is the dominating recombination process at  $V_{oc}$ . [35] For the *1mp*-AVA-NoHTM cell the points were not aligned and **Eq.(II.2)** was not valid at low light intensity. It shows a fast decrease of the  $V_{oc}$  at low light intensity and that strong recombination occurs. In **Table II.7**, we compare  $n_{ID}$ , which was determined from the  $V_{oc}$ , and the  $n'_{ID}$  extracted from the EIS  $R_2$  curves (see **Annex A.II.2.1**). The two parameters are in good agreement and, more importantly, they vary in a similar manner with the cell type. We can conclude that  $R_2$  is a recombination resistance that measures the recombination in the bulk perovskite.

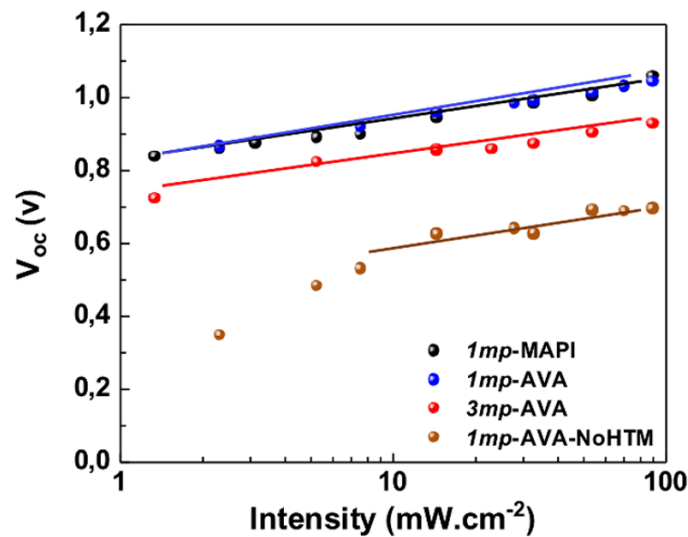


**Figure II.20**  $V_{oc}$  versus light intensity (power density) curves.

**Table II.7** Ideality factors obtained from open-circuit potential ( $n_{ID}$ ) and EIS ( $R_2$ ) ( $n'_{ID}$ ) measurements for the four different PSCs.

	$n_{ID}$	$n'_{ID}$
<i>1mp</i> -MAPI	1.99	1.56
<i>1mp</i> -AVA	1.89	1.92
<i>1mp</i> AVA-NoHTM <sup>a</sup>	3.50	3.44
<i>3mp</i> -AVA	1.82	1.64

<sup>a</sup> fit over the whole Intensity and  $V_{oc}$  range

## II.2.5 Conclusion

In summary, we have investigated the effect of AVA additive and of the cell structure on PSCs. In the presence of AVA, no 2D-perovskite phase was detected. AVA is deleterious for the PVK film morphology when *Imp* substrate is used while it is beneficial in reducing PVK bulk defects. Using a *3mp* scaffold leads to a significant improvement of the PVK structural quality as shown by TRPL and solves the potential problems of pinhole and related electrical shunt pathways. *Imp*-AVA cells achieved a PCE of 16.9%, stabilized at 15.9%. This efficiency is significantly lower with higher hysteresis compared to *Imp*-MAPI cells. The ideality factor study has shown recombinations via the SRH process at the open-circuit voltage. The  $R_2$  element extracted from the high frequency impedance spectra (See **Annex A.II.2**) also varies with the  $V_{oc}$  like a recombination resistance from which we have extracted an ideality factor comparable to the ones determined from the  $V_{oc}$  (**Table II.7**).

We have also unveiled that MAPI is degraded by moisture with the formation of a monohydrate MAPI intermediate phase prior to  $PbI_2$  formation and MA release. The mechanism is irrespective of the PVK environment. AVA has been shown beneficial for the stability of the MAPI layer. Moreover, a slower degradation has also been found when MAPI-AVA PVK is embedded in the triple mesoscopic scaffold. The high stability of  $TiO_2/ZrO_2/Carbon/PVK$  cells is due to the protection by the all-inorganic scaffold.

In this chapter, we mainly exploring perovskite solar cells from the cation composition to the cell structure and gain a deep comprehensive understanding. On the basis of this chapter, in the next chapter, we will further study the mono-cation formula of MAPI, and introduce gold nanoparticles to improve its absorption, so as to further enhance the performance of perovskite solar cell.

## References

- [1] Bartel, C. J., Sutton, C. B., Goldsmith, R., Ouyang, R., Musgrave, C. B., Ghiringhelli, L.M.; Scheffler., M. New tolerance factor to predict the stability of perovskite oxides and halides. *Sci. Adv.* **2019**, *5*, eaav0693.
- [2] Matsui, M., Seo, T., Domanski, J.-Y., Correa-Baena, K., Nazeeruddin, J.-P., Zakeeruddin, M. K., Tress, S. M., Abate, W., Hagfeldt, Grätzel, M. Cesium-containing triple cation perovskite solar cells: improved stability, reproducibility and high efficiency. *Energy Environ. Sci.* **2016**, *9*, 1989-1997.
- [3] Saliba, M., Matsui, T., Domanski, K., Seo, J.-Y., Ummadisingu, A., Zakeeruddin, S. M., Correa-Baena, J.-P., Tress, W.R., Abate, A., Hagfeldt, A., Grätzel, M. Incorporation of rubidium cations into perovskite solar cells improves photovoltaic performance. *Science* **2016**, *354*, 206-209.

- [4] Turren-Cruz, S.-H., Hagfeldt, A., Saliba, M. Methylammonium-free, high-performance, and stable perovskite solar cells on a planar architecture. *Science* **2018**, *362*, 449–453.
- [5] Kim, M., Kim, G.H., Lee, T.K., Choi, I.W., Choi, H.W., Jo, Y., Yoon, Y.J., Kim, J.W., Lee, J., Huh, D., Lee, H., Kwak, S.K., Kim, J. Y., Kim, D. S. Methylammonium Chloride Induces Intermediate Phase Stabilization for Efficient Perovskite Solar Cells. *Joule* **2019**, *3*, 1–14.
- [6] Ulfa, M., Wang, P., Shao, Z., Viana, B., Pauporté, T. Oxide Hole Blocking Selective Contacts in Perovskite Solar Cells. *Proc. SPIE* **2018**, *10533*, 105332R1-105332R10.
- [7] Zhu, T., Su, J., Labat, F., Ciofini, I., Pauporté, Th. Interfacial Engineering through Chloride-Functionalized Self-Assembled Monolayer for High Efficiency Perovskite Solar Cells. *ACS Appl. Mater Interfaces* **2020**, *12*, 744-752.
- [8] Nazeeruddin, M. K., Braukyla, T., Xia, R., Daskeviciene, M., Malinauskas, T., Gruodis, A., Jankauskas, V., Roldán-Carmona, C., Momblona, C., Getautis, V., Fei, Z. Inexpensive Hole Transporting Materials Derived from Tröger's Base Afford Efficient and Stable Perovskite Solar Cells. *Angew. Chem. Int. Ed.* **2019**, *58*, 11266–11272.
- [9] Xia, R., Fei, Z., Drigo, N., Bobbink, F. D., Huang, Z., Jasiūnas, R., Franckevičius, M., Gulbinas, V., Mensi, M., Fang, X., Roldán-Carmona, C. Retarding Thermal Degradation in Hybrid Perovskites by Ionic Liquid Additives. *Adv. Funct. Mater.* **2019**, *29*, 1902021.
- [10] Le Bahers, T., Labat, F., Pauporté, T., Ciofini, I. Effect of Solvent and additives on the open circuit voltage of ZnO based Dye-sensitized solar cells: A combined theoretical and experimental study. *Phys. Chem. Chem. Phys.* **2010**, *12*, 14710–14719.
- [11] Kusumawati, Y., Martoprawiro, M. A., Pauporté, Th. Effects of Graphene in Graphene/TiO<sub>2</sub> Composite Films Applied to Solar Cell Photoelectrode. *J. Phys. Chem. C* **2014**, *118*, 9974–9981.
- [12] Zong, B., Fu, W., Guo, Z.A., Wang, S., Huang, L., Zhang, B., Bala, H., Cao, J., Wang, X., Sun, G., Zhang, Z. Highly stable hole-conductor-free perovskite solar cells based upon ammonium chloride and a carbon electrode. *J. Colloid Interface Sci.* **2019**, *540*, 315–321.
- [13] Rong, Y., Hou, X., Hu, Y., Mei, A., Liu, L., Wang, P., Han, H. Synergy of ammonium chloride and moisture on perovskite crystallization for efficient printable mesoscopic solar cells. *Nat. Commun.* **2017**, *8*, 14555.
- [14] Dai, X.Z., Deng, Y.H., Charles, H., Brackley, V., Chen, S.S., Rudd, P.N., Xiao, X., Lin, Y., Chen, B., Huang, J.S. Scalable Fabrication of Efficient Perovskite Solar Modules on Flexible Glass Substrates. *Adv. Energy Mater.* **2020**, *10*, 1903108.
- [15] Aldibaja, F.K., Badia, L., Mas-Marza, E., Sanchez, R.S., Barea, E.M., Mora-Sero, I. Effect of different lead precursors on perovskite solar cell performance and stability. *J. Mater. Chem. A* **2015**, *3*, 9194-9200.
- [16] Xie, F., Chen, C.-C., Wu, Y., Li, X., Cai, M., Liu, X., Yang, X., Han, L. Vertical Recrystallization for Highly Efficient and Stable Formamidinium-Based Inverted-Structure Perovskite Solar Cells, *Energy Environ. Sci.* **2017**, *10*, 1942-1949.
- [17] Tress, W., Yvari, M., Domanski, K., Yadav, P., Niesen, B., Correa Baena, J.P., Hagfeldt, A., Graetzel, M. Interpretation and evolution of open-circuit voltage, recombination, ideality factor, subgap defect states during reversible light-soaking and irreversible degradation of perovskite solar cells. *Energy Environ. Sci.* **2018**, *11*, 151–165.
- [18] Jacobs, D. A., Shen, H., Pfeffer, F., Peng, J., White, T. P., Beck, F.J., Catchpole, K.R. The two faces of capacitance: New interpretations for electrical impedance measurements of perovskite solar cells and their relation to hysteresis. *J. Appl. Phys.* **2018**, *124*, 225702.

- [19] Ulfa, M., Zhu, T., Goubard, F., Pauporté, T. Molecular versus polymeric hole transporting materials for perovskite solar cell application. *J. Mater. Chem. A* **2018**, *6*, 13350–13358.
- [20] Ulfa, M., Wang, P.J., Zhang, J., Liu, W., Marcillac, D., Coolen, L., Peralta, S., Pauporté, T. Charge Injection and Electrical Response in Low-Temperature SnO<sub>2</sub>-Based Efficient Perovskite Solar Cells. *ACS Appl. Mater. Interfaces* **2018**, *10*, 35118–35128.
- [21] Ulfa, M., Pauporté, T., Bui, T.T., Goubard, F. Impact of Organic Hole Transporting Material and Doping on the Electrical Response of Perovskite Solar Cells. *J. Phys. Chem. C* **2018**, *122*, 11651–11658.
- [22] Almora, O., Aranda, C., Mas-Marzá, E., Garcia-Belmonte, G. On Mott-Schottky analysis interpretation of capacitance measurements in organometal perovskite solar cells. *Appl. Phys. Lett.* **2016**, *109*, 173903.
- [23] Pascoe, A.R, Duffy, N.W., Scully, A.D., Huang, F., Cheng, Y.B. Insights into Planar CH<sub>3</sub>NH<sub>3</sub>PbI<sub>3</sub> Perovskite Solar Cells using Impedance Spectroscopy. *J. Phys. Chem. C* **2015**, *119*, 4444–4453
- [24] Juarez-Perez, E.J., Wußler, M., Fabregat-Santiago, F., Lakus-Wollny, K., Mankel, E., Mayer, T., Jaegermann, W., Mora-Sero, I. Role of the Selective Contacts in the Performance of Lead Halide Perovskite Solar Cells. *J. Phys. Chem. Lett.* **2014**, *5*, 680–685.
- [25] Juarez-Perez, E.J., Sanchez, R.S., Badia, L., Garcia-Belmonte, G., Kang, Y.S., Mora-Sero, I., Bisquert, J. Photoinduced Giant Dielectric Constant in Lead Halide Perovskite Solar Cells. *J. Phys. Chem. Lett.* **2014**, *5*, 2390–2394.
- [26] Dualeh, A., Moehl, T., Tétreault, N., Teuscher, J., Gao, P., Nazeeruddin, M.K., Grätzel, M. Impedance Spectroscopic Analysis of Lead Iodide Perovskite-Sensitized Solid-State Solar Cells. *Sci. Rep.* **2014**, *8*, 362–373.
- [27] Gonzalez-Pedro, V., Juarez-Perez, E.J., Arsyad, W.S., Barea, E.M., Fabregat-Santiago, F., Mora-Sero, I., Bisquert, J. General Working Principles of CH<sub>3</sub>NH<sub>3</sub>PbX<sub>3</sub> Perovskite Solar Cells. *Nano Lett.* **2014**, *14*, 888–893.
- [28] Almora, O., Zarazua, I., Mas-Marza, E., Mora-Sero, I., Bisquert, J., Garcia-Belmonte, G. Capacitive Dark Currents, Hysteresis, and Electrode Polarization in Lead Halide Perovskite Solar Cells. *J. Phys. Chem. Lett.* **2015**, *6*, 1645–1652.
- [29] Guerrero, A., Juarez-Perez, E.J., Bisquert, J., Mora-Sero, I., Garcia-Belmonte, G. Electrical Field Profile and Doping in Planar Lead Halide Perovskite Solar Cells. *Appl. Phys. Lett.* **2014**, *105*, 133902.
- [30] Kim, H.-S., Mora-Sero, I., Gonzalez-Pedro, V., Fabregat-Santiago, F., Juarez-Perez, E. J., Park, N.-G., Bisquert, J. Mechanism of Carrier Accumulation in Perovskite Thin-Absorber Solar Cells. *Nat. Commun.* **2013**, *4*, 2242.
- [31] Zarazua, I., Han, G.F., Boix, P.P., Mhaisalkar, S., Fabregat-Santiago, F., Mora-Sero, I., Bisquert, J., Garcia-Belmonte, G. Surface Recombination and Collection Efficiency in Perovskite Solar Cells from Impedance Analysis. *J. Phys. Chem. Lett.*, **2016**, *7*, 5105-5113.
- [32] Yang, T.-Y., Gregori, G., Pellet, N., Grätzel, M., Maier, J. The Significance of Ion Conduction in a Hybrid Organic-Inorganic Lead Iodide-Based Perovskite Photosensitizer. *Angew. Chem., Int. Ed.* **2015**, *54*, 7905–7910.
- [33] Anaya M., Zhang, W., Clasen Hames, B., Li, Y., Fabregat-Santiago, F., Calvo, M.E., Snaith, H.J., Miguez, H., Mora-Sero I. Electron Injection and Scaffold Effects in Perovskite Solar Cells. *J. Mater. Chem. C* **2017**, *5*, 634-644.
- [34] Brug, G.J., Van Der Eeden, A.L.G., Sluyters-Rehbach, M., Sluyters, J.H. The Analysis of Electrode Impedance Complicated by the Presence of a Constant Phase Element. *J. Electroanal. Chem.* **1984**, *176*, 275-295.

- [35] Mei, A., Li, X., Liu, L., Ku, Z., Liu, T., Rong, Y., Xu, M., Hu, M., Chen, J., Yang, Y., Grätzel, M., Han, H. A hole-conductor-free, fully printable mesoscopic perovskite solar cell with high stability. *Science* **2014**, *345*, 295-298.
- [36] Grancini, G., Roldan-Carmona, C., Zimmermann, I., Mosconi, E., Lee, X., Martineau, D., Nabey, S., Oswald, F., De Angelis, F., Graetzel, M., Nazeeruddin M. K. One-Year stable perovskite solar cells by 2D/3D interface engineering. *Nature Commun.* **2017**, *8*, 15684.
- [37] Hu, Y., Zhang, Z., Mei, A., Jiang, Y., Hou, X., Wang, Q., Du, K., Rong, Y., Zhou, Y., Xu, G., Han, H. Improved performance of printable perovskite solar cells with bifunctional conjugated organic molecule. *Adv. Mater.* **2018**, *30*, 1705786.
- [38] Santhosh, N., Sitaaraman, S.R., Pounraj, P., Govindaraj, R., Senthil Pandian, M., Ramasamy, P. Fabrication of hole-transport-free perovskite solar cells using 5-ammonium valeric acid iodide as additive and carbon as counter electrode. *Mater. Lett.* **2019**, *236*, 706–709.
- [39] Papadatosa, D., Sygkridoua, D., Stathatos, E. Carbon-based, novel triple cation mesoscopic perovskite solar cell fabricated entirely under ambient air conditions. *Mater. Lett.* **2020**, *268*, 127621.
- [40] Rong, Y., Hu, Y., Mei, A., Tan, H., Saidaminov, M., Sang Il Seok, McGehee, M. D., Sargent, E. H., Han, H. Challenges for commercializing perovskite solar cells. *Science* **2018**, *361*, 8235.
- [41] Xu, M., Ji, W., Sheng, Y., Wu, Y., Cheng, H., Meng, J., Yan, Z., Xu, J., Mei, A., Hu, Y., Rong, Y., Han, H. Efficient triple-mesoscopic perovskite solar mini-modules fabricated with slot-die coating. *Nano Energy* **2020**, *74*, 104842.
- [42] Mei, A., Sheng, Y., Ming Y., Hu, Y., Rong Y., Zhang W., Luo S., Na G., Tian, C., Hou, X., Xiong, Y., Zhang, Z., Liu, S., Uchida, S., Kim, T.W., Yuan, Y., Zhang, L., Zhou, Y., Han H. Stabilizing perovskite solar cells to IEC61215:2016 standards with over 9,000-h operational tracking. **2020**, *4*, 1-15
- [43] Lin, C-T., De Rossi, F., Kim, J., Baker, J., Ngiam, J., Xu, B., Pont, S., Aristidou, N., Haque, S. A., Watson, T., McLachlan, M. A., Durrant, J.R. Evidence for surface defect passivation as the origin of the remarkable photostability of unencapsulated perovskite solar cells employing aminovaleric acid as a processing additive. *J. Mater. Chem. A* **2019**, *7*, 3006-3011.
- [44] Péan, E.V., De Castro, C.S., Dimitrov, S., De Rossi, F., Meroni, S., Baker, J., Watson, T., Davies, M. L. Investigating the superoxide formation and stability in mesoporous carbon perovskite solar cells with an aminovaleric acid additive. *Adv. Funct. Mater.* **2020**, *30*, 1909839.
- [45] Kayesh, M.E., Matsuishi, K., Kaneko, R., Kazaoui, S., Lee, J-J., Noda, T., Islam, A. Coadditive engineering with 5-ammonium valeric acid iodide for efficient and stable Sn perovskite solar cells. *ACS Energy Lett.* **2019**, *4*, 278–284.
- [46] Wei, N., Chen, Y., Miao, Y., Zhang, T., Wang, X., Wei, H., Zhao, Y. 5-Ammonium Valeric Acid Iodide to Stabilize MAPbI<sub>3</sub> via a Mixed-Cation Perovskite with Reduced Dimension. *J. Phys. Chem. Lett.* **2020**, *11*, 8170-8176.
- [47] Tress, W., Yavari, M., Domanski, K., Yadav, P., Niesen, B., Baena, J.P.C., Hagfeldt, A., Graetzel, M. Interpretation and evolution of open-circuit voltage, recombination, ideality factor and subgap defect states during reversible light-soaking and irreversible degradation of perovskite solar cells. *Energy Environ. Sci.* **2018**, *11*, 151–165.
- [48] Ulfa, M., Wang, P., Zhang, J., Liu, J., Daney de Marcillac, W., Coolen, L., Peralta, S., Pauporté, T. Charge injection and electrical response in low temperature SnO<sub>2</sub>-based efficient perovskite solar cells. *ACS Appl. Mater. Interfaces* **2018**, *10*, 35118–35128.

- [49] Ulfa, M., Zhu, T., Goubard, F., Pauporté, Th. Molecular versus polymeric hole transporting materials for perovskite solar cell application. *J. Mater. Chem. A* **2018**, *6*, 13350–13358.
- [50] Zhu, T., Su, J., Labat, F., Ciofini, I., Pauporté T. Interfacial engineering through chloride-functionalized self-assembled monolayer for high efficiency perovskite solar cells. *ACS Appl. Mater Interfaces*, 2020, *12*, 744–752.
- [51] Ulfa, M., Wang, P., Shao, Z., Viana, B., Pauporté, T. Oxide hole blocking selective contacts in perovskite solar cells. *Proc. SPIE* **2018**, *10533*, 105332R1–105332R10.
- [52] Ku, Z., Rong, Y., Xu, M. Liu, T. Han, H. Full printable processed mesoscopic  $\text{CH}_3\text{NH}_3\text{PbI}_3/\text{TiO}_2$  heterojunction solar cells with carbon counter electrode. *Sci. Rep.* **2013**, *3*, 3132.
- [53] Zhu, T., Zheng, D., Rager, M.-N., Pauporté, Th. Actual organic cations composition determination in perovskite thin films. Application to formamidinium lead iodide stabilization for high efficiency solar cells. *Sol. RRL* **2020**, 2000348.
- [54] Lee, H., Gaiaschi, S., Chapon, P., Marronnier, A., Lee, H., Vanel, J.C., Tondelier, D., Bourée, J.-E., Bonnassieux, Y., Geffroy, B. Direct Experimental Evidence of Halide Ionic Migration under Bias in  $\text{CH}_3\text{NH}_3\text{PbI}_{3-x}\text{Cl}_x$ -Based Perovskite Solar Cells Using GD-OES Analysis. *ACS Energy Lett.* **2017**, *2*, 943–949.
- [55] Zheng, D., Zhu, T., Pauporté, Th. Using Monovalent- to Trivalent-Cation Hybrid Perovskites for Producing High-Efficiency Solar Cells: Electrical Response, Impedance, and Stability. *ACS Appl. Energy Mater.* **2020**, *3*, 10349–10361.
- [56] Leguy, A., Hu, Y., Campoy-Quiles, M., Alonso, M.I., Weber, O.J., Azarhoosh, P., van Schilfgaarde, M., Weller, M.T., Bein, T., Nelson, J., Docampo, P., Barnes, P.R.F. Reversible Hydration of  $\text{CH}_3\text{NH}_3\text{PbI}_3$  in Films, Single Crystals, and Solar Cells. *Chem. Mater.* **2015**, *27*, 3397–3407.
- [57] Zuo, L., Chen, Q., De Marco, N., Hsieh, Y. T., Chen, H, Sun, P., Chang, S. Y., Zhao, H., Dong, S., Yang, Y. Tailoring the Interfacial Chemical Interaction for High-Efficiency Perovskite Solar Cells. *NanoLett.* **2017**, *17*, 269-275.
- [58] Daming, Z., Zhu, T., Pauporte, Th. A Coadditive Strategy for Blocking Ionic Mobility in Methylammonium-Free Perovskite Solar Cells and High-Stability Achievement. *Solar RRL* **2021**, 2100010.
- [59] Zhu, T., Zheng, D., Liu, J., Coolen, L., Pauporté, Th. Electrical response of high efficiency and stable solar cells based on MAOI mediated grown  $\text{FA}_{0.94}\text{MA}_{0.06}\text{PbI}_3$  perovskite. *ACS Appl. Mater. Interfaces* **2020**, *12*, 37197–37207.
- [60] Kim, H.S., Lee, C.R., Im, J.H., Lee, K.H., Moehl, T., Marchioro, A., Moon, S.J., Robin, H.B., Yum, J.H., Moser, J.E., Gratzel, M. Lead Iodide Perovskite Sensitized All-Solid-State Submicron Thin Film Mesoscopic Solar Cell with Efficiency Exceeding 9%. *Sci. Rep.* **2012**, *2*, 591.
- [61] Zhang, J., Barboux, P., Pauporté, Th. Electrochemical Design of Nanostructured ZnO Charge Carrier Layers for Efficient Solid-State Perovskite-Sensitized Solar Cells. *Adv. Energy Mater.* **2014**, *4*, 1400932.
- [62] Leblanc, A., Mercier, N., Allain, M., Dittmer, J., Fernandez, V., Pauporté, T. Lead- and Iodide-Deficient  $(\text{CH}_3\text{NH}_3)\text{PbI}_3$  (d-MAPI): The Bridge between 2D and 3D Hybrid Perovskites. *Angew. Chem., Int. Ed.* **2017**, *56*, 16067–16072.
- [63] Pitarch-Tena, D., Ngo, T.T., Vallés-Pelarda, M., Pauporté, Th., Mora-Seró, I. Impedance Spectroscopy Measurements in Perovskite Solar Cells. Device Stability During the Measurement and Noise Reduction. *ACS Energy Lett.* **2018**, *3*, 1044–1048.
- [64] Miao, J. L., Zhang, F. J. Recent progress on highly sensitive perovskite photodetectors. *J. Mater. Chem. C* **2019**, *7*, 1741-1791.

[65] Martin, S., Christian, M. W., Yohai, A., Andreas, P., Lorena, P., Pietro, C., Dieter, N. Approaching the Fill Factor Shockley Queisser Limit in Stable, Dopant-Free Triple Cation Perovskite Solar Cells. *Energy Environ. Sci.* **2017**, *10*, 1530-1539.

## **Chapter III. Effects of gold nanoparticles on the growth and performances of MAPbI<sub>3</sub> perovskite solar cells.**

### **III.1 Introduction**

The use of plasmonic materials is frequently proposed as a means to enhance the performance of photovoltaic devices. [1–6] In particular, the uses of plasmonic materials and arrangements of them have been explored for almost all types of solar cells,[7] either for solid-state[8, 9] or solution containing ones.[10–22] In photovoltaic devices, effective light management can be accomplished by 1) reduction of reflection losses at the cell surface and 2) by trapping light in the absorbing layer.[23, 32] The localized surface plasmon resonance (LSPR) and light scattering effective of plasmonic materials can enhance the light absorption and dramatically improve the photovoltaic performances of solar cells. For the typical film thicknesses for which high structural quality is attained, photon capture is not as high in the range of  $600 \text{ nm} < \lambda < 780 \text{ nm}$  as it is for shorter wavelengths because the perovskite extinction coefficient rapidly decays in the red/near-infra-red range. Because the number of solar photons peaks at longer visible wavelengths, this weaker, red absorption affects significantly the efficiency of the incident photon-to-electron conversion process. As an effective route toward near-field light enhancement, metal nanostructures with subwavelength dimensions can couple incident photons with conduction electrons, giving rise to LSPRs. Although there are many works on the application of plasmonic materials in perovskite solar cells, two problems remain that people ignore in the research of plasmonic materials: 1) many people only do qualitative simulation research to prove that the added nanoparticles have the effect of enhancing absorption, while only few people simulate and make specific analysis from both qualitative and quantitative perspectives at the same time;[25, 26] 2) Most researchers pay too much attention to the light absorption enhancement produced by plasmonic materials, while few people pay attention to the influence of plasmonic materials on the perovskite film itself, such as the crystal orientation or the quality of the film. Whether gold nanoparticles can effectively improve the crystallinity of perovskite is still under debate. By using relative higher concentration of NPs, some researcher did not found any enhancement on crystallization [27-29], especially from XRD results, but someone others found that NPs has effects

on grain size,  $\text{PbI}_2$  formation [30] and crystallinity of the perovskite film [31]. One must know and take care that the improvement of crystal quality of perovskite film can also greatly improve the overall absorption of the film.

Based on the above analysis, in this chapter, we will comprehensively analyze the effect of Au\_NPs inclusion in the PVK ( $\text{MAPbI}_3$ ) film through the combination of absorption simulation and experiments. Our results show that the effect of Au\_NPs on the improvement of the quality of the perovskite layer is far greater than that of the increase in light harvesting. In order to further boost the performance of perovskite solar cells, we introduced a post-treatment technique, leading to the formation of a 2D capping layer on the top-surface of  $\text{MAPbI}_3$  perovskite layer. The 2D capping layer forms a barrier that protect the underneath 3D perovskite films and constitutes an intermediate energy band mitigating exciton recombination. Among a variety of ammonium compounds, we found that n-propylamine hydroiodide (or n-propylammonium iodide, noted PAI) has a beneficial effect on Au\_NPs/ $\text{MAPbI}_3$  composite samples. Moreover, we will go through various testing methods to prove that post-processing with PAI is indispensable to boost the performance of perovskite solar cells.

## III.2 Experimental

The preparations of substrates, compact  $\text{TiO}_2$  layer and mesoporous  $\text{TiO}_2$  layer were conducted as detailed in **Chapter II, Section II.1.2.1**.

### III.2.1 Preparation of Pristine and Composite Perovskite Films

Gold Nanoparticles (Au\_NPs) preparation: The Au NPs were obtained by a Turkevitch synthesis, based on Au(III) reduction by citrate at  $100^\circ\text{C}$ . The concentration in Au was 0.25 mM. By centrifugation of the solution, it was possible to concentrate the NPs. Then, DMSO was added in the concentrated solution ( $\sim 0.2$  ml) and the solution was heated to remove the water. We obtained 0.5 mL in DMSO from 60 mL in water (concentration factor 120 compared to the mother solution). The solution was dark red, meaning that there was no aggregation. To increase the concentration, we prepared 189 mL of 17.1 nm ( $s=0.07$ ) sized NPs solution in water and concentrated it the same way. We obtained 0.45 mL in DMSO (concentration factor 420). The concentration in Au NPs was

[NPs] $\sim 7.10^{-7}$  M. During the evaporation of water and replacement by DMSO, the solution turned purple, indicating aggregation of the NPs. This was probably due to the decrease of the citrate/Au ratio during the concentration process, leading to the decrease of pH and the removal of citrate at the surface of the NPs. Nevertheless, adding citrate did not stabilize the NPs.

Finally, we used a sample of intermediate concentration with a factor of concentration of 252 (0.75 mL of DMSO from 189 mL of 14.3 nm sized Au NPs solution in water). This solution was dark red, and the same Au NPs concentration was obtained ([NPs] $\sim 7.10^{-7}$  M), with Au concentration of [Au] $\sim 0.06$  M.

MAPI layers with/without Au\_NPs preparation: The MAPbI<sub>3</sub> precursor solution concentration was 1.35M. 622.3 mg PbI<sub>2</sub>, 214.6 mg MAI and 0  $\mu$ L, 15  $\mu$ L, 30  $\mu$ L, 45  $\mu$ L of Gold nanoparticles solution were mixed in 1000  $\mu$ L, 985  $\mu$ L, 970  $\mu$ L, 955  $\mu$ L DMSO, respectively. The solution was stirred and kept warm at 60°C for 2h before use. The Spin-coating program was 1000 rpm for 10s and 4000 rpm for 30 s. 100  $\mu$ L of chlorobenzene was dripped 30s after the starting of the spinning routine. The layers were finally annealed on a hotplate at 105 °C for 60 min. The best performances were achieved after the device preparation. These layers are denoted Ref, Au\_NPs-15, Au\_NPs-30 and Au\_NPs-45 throughout the chapter.

PAI Post-treatment: The PAI post-treatment consisted of dropping 60  $\mu$ L of a 4 mg/mL propylamine hydroiodide (PAI) solution onto the perovskite film after cooling. A one-step spin-coating program was employed (2000 rpm/s acceleration, 3000 rpm for 20s). After that, the sample did not need to be reheated. The optimized treated films are noted Au\_NPs-30/PAI, hereafter.

The preparation of the hole transporting material solution was conducted as detailed in **Chapter II, Section II.1.2.2.**

### **III.2.2 Characterizations Method**

The layers characterizations by XRD, SEM, UV-vis absorbance, EDX, steady-state PL and TRPL are described in **Chapter II, Section II.1.2.3.**

The differential scanning calorimetry (DSC) curves were measured on precipitated sample adducts by a DSC 3 apparatus from STAR System, operated under N<sub>2</sub> atmosphere with a heating rate of 10 °C/min. Glow-Discharge Optical Emission Spectrometry (GD-OES) analyses were performed using a HORIBA Jobin Yvon GD Profiler 2 equipment. This instrument was equipped with a RF-generator (at 13.56 MHz), a standard HORIBA Jobin Yvon glow discharge source with a cylindrical anode of 4 mm internal diameter and two optical spectrometers (a polychromator and a monochromator) for fast-optical detection. The Ar plasma was generated at an Ar pressure of 420 Pa and an applied power of 17 W. The precursor layer or the perovskite layer or the solar cell was mounted on an O-ring at one side of the plasma chamber and used as a cathode.

The measurements of  $J-V$  curves, maximum power point tracking and  $EQE$  spectra of the devices were described in **Chapter II, Section II.1.2.3**.

### III.3 Characterizations of perovskite Films

#### III.3.1 TEM, SEM and AFM

(a)



(b)

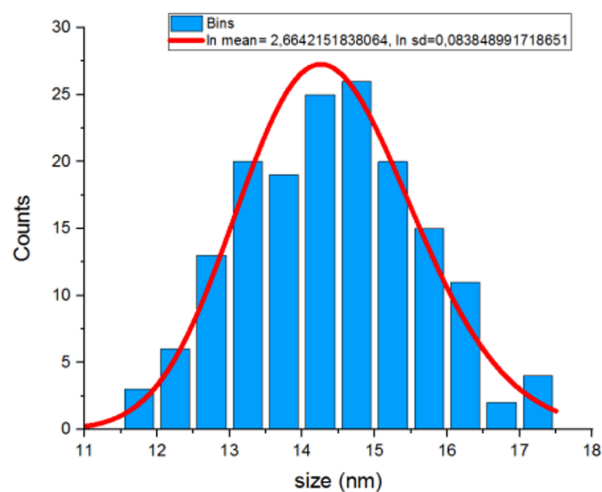


**Figure III.1 (a) TEM top-view images of Gold Nanoparticles and (b) Statistical grain size analysis.**

Our original intention was to synthesize small-size gold nanoparticles, making them more widely distributed in the perovskite layer. We firmly believed that the large size gold particles will tear the perovskite film due to centrifugal force in the process of spin coating perovskite precursor solution, while the small size gold nanoparticles will reduce this effect.

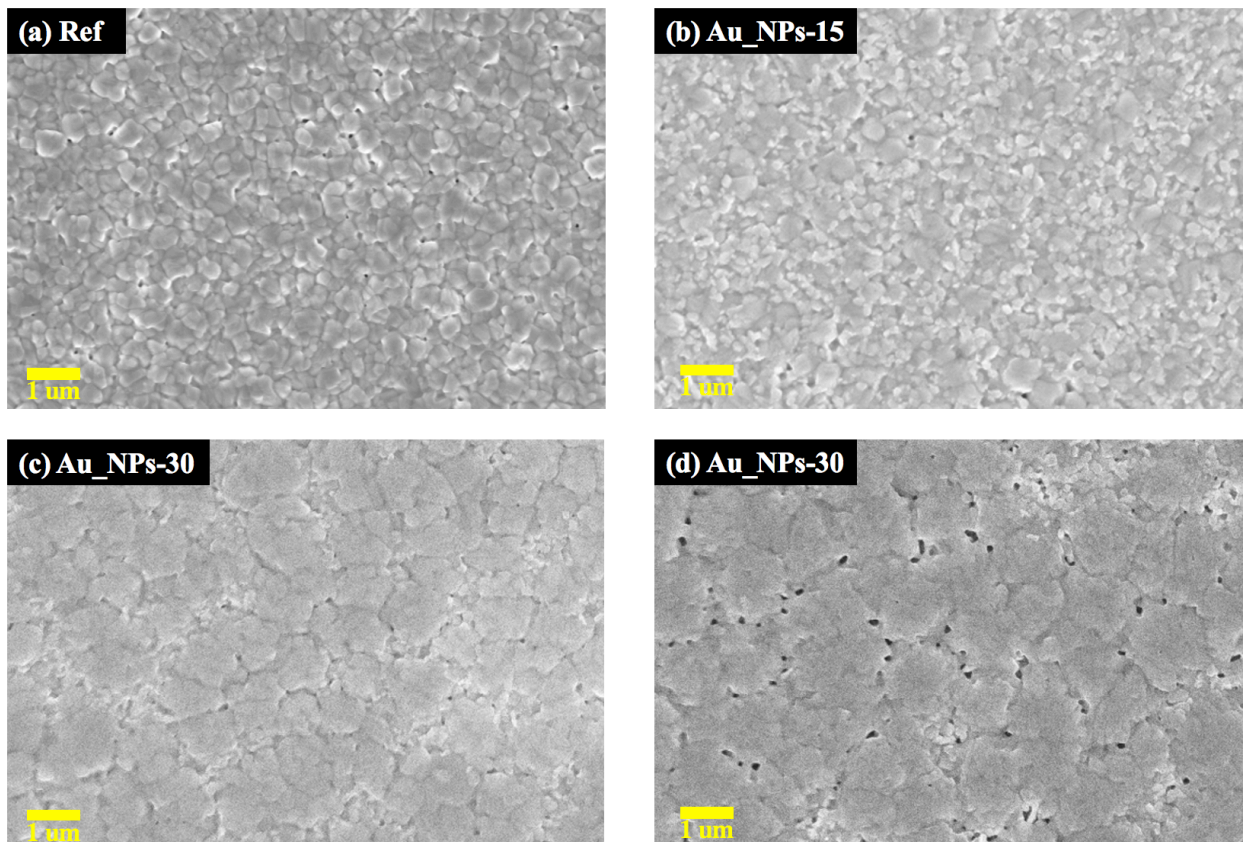


**Figure III.2 (a-d) SEM top-view images of perovskite layers prepared with different volume of Au\_NPs: (a) Ref, (b) Au\_NPs-15, (c) Au\_NPs-30, (d) Au\_NPs-45. (the scale bar is 1  $\mu$ m).**

Due to the small size of the gold nanoparticles we synthesized, it was difficult to observe the morphology of the gold nanoparticles by means of SEM inspection, therefore, we used top-surface TEM to detect the morphology of the gold nanoparticles. Their spherical shape is clearly revealed in **Figure III.1a**. Their size distribution is given in **Figure III.1b**. They had a size smaller than 20 nm and most of the gold nanoparticles were 13~16 nm in size (average 14.3 nm).

**Figure III.2** shows the effect of different volume of Au\_NPs solution on the film morphology. The pristine sample presented small-size perovskite grains with pinholes between them. These pinholes

were not real ones, but were due to the irregular stacking of crystals caused by excessive growth of  $\text{PbI}_2$  during the film formation process. The perovskite was non-compact and its surface was very rough. After the introduction of 15  $\mu\text{L}$  Au\_NPs in the perovskite precursor solution, a lot of small grains were distributed among the large island-like grains. It seems that the Au\_NPs inhibited the fast crystallization of perovskite film. When 30  $\mu\text{L}$  Au\_NPs was added (**Figure III.2c**), these small grains in **Figure III.2b** were reduced significantly and replaced by large compact island like crystals of  $\sim 2$   $\mu\text{m}$  in size. Increasing the volume up to 45  $\mu\text{L}$  led to the further increase of the grain size but a lot of pinholes appeared between them (**Figure III.2d**).

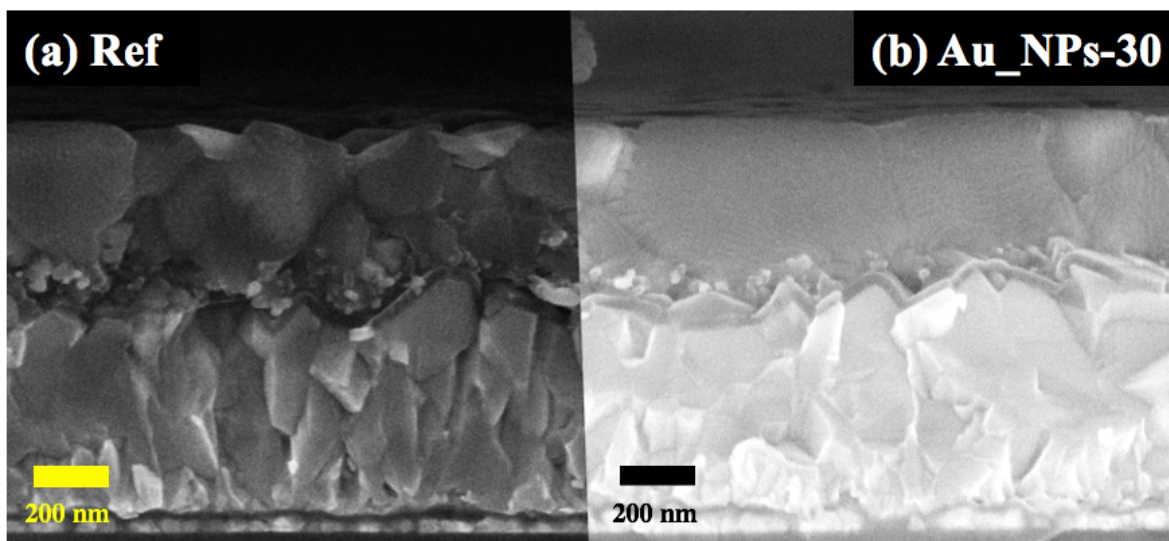
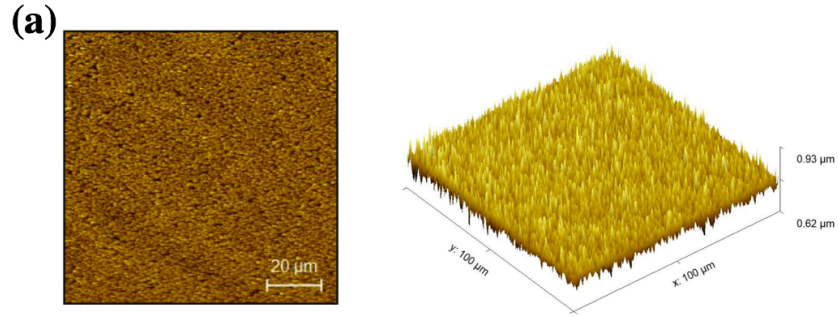
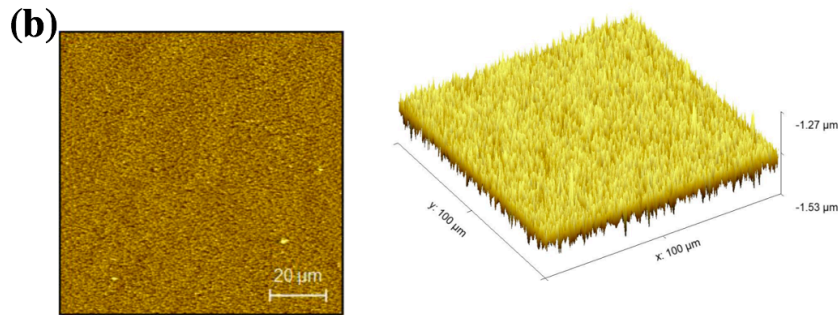


**Figure III.3** SEM cross-sectional views of perovskite layers deposited on glass/FTO/c-TiO<sub>2</sub>/mp-TiO<sub>2</sub>.

To double check that Au\_NPs can influence of the process of film formation, we imaged their cross-section by SEM. In **Figure III.3**, we can see on the cross-sectional view without Au\_NPs that the layer is made of stacked multiple perovskite crystals. Compared to the Ref sample, the quality of perovskite film was obviously improved for the Au\_NPs-30 sample. The perovskite grains were large and homogeneous in size. We observed a monolithic morphology which is the targeted one for the efficient charge transfer across the  $\text{MAPbI}_3$  layer thickness.



RMS Roughness: 30.59 nm



RMS Roughness: 24.33 nm

**Figure III.4** AFM images of MAPbI<sub>3</sub> perovskite layer surfaces. Effect of Au\_NPs: (a) Ref and (b) Au\_NPs-30 layers.

In order to verify our above analysis, we did AFM measurement to check the roughness of the perovskite layers. In **Figure III.4**, we can see that the rms roughness of sample without Au\_NPs is 30.59 nm and that this parameter is decreased to 24.33 nm for the sample with embedded Au\_NPs. These values are consistent with what we saw in the top-surface SEM.

From the above results, we can conclude that the Au\_NPs have a great influence on the crystallization process of perovskite layer. The addition of an appropriate volume of Au\_NPs can increase the grain size and reduce the crystal defects of perovskite surface. The improved surface morphology of perovskite film is beneficial for the photo-induced charge carrier transportation and separation.

### III.3.2 XRD

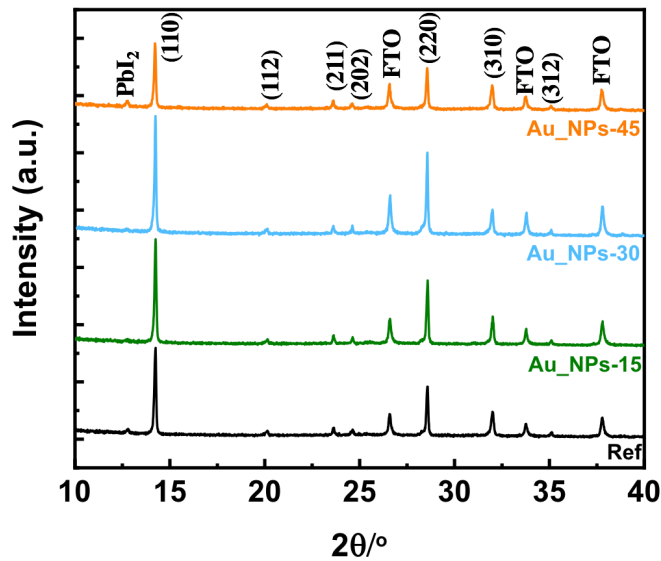


Figure III.5 XRD patterns for different volume of Au\_NPs added to the perovskite precursor solution.

The XRD results are displayed in **Figure III.5**. With the increased volume of Au\_NPs, the (110) peak of MAPbI<sub>3</sub> gradually increased, while the intensity of PbI<sub>2</sub> at 12.6 degree gradually decreased. The peak intensity increase sign a higher quality of the perovskite film and it proves that 30  $\mu$ L of Au\_NPs can better control the ratio of PbI<sub>2</sub> growth and maximize the crystalline quality. We also found that too much Au\_NPs is detrimental for the layer quality. It is manifested by the appearance of PbI<sub>2</sub> peak in the Au\_NPs-45 sample pattern and the decrease of the intensity of the (110) peak. These results are consistent with the morphology obtained by SEM (**Figure III.2d**).

### III.3.3 DSC

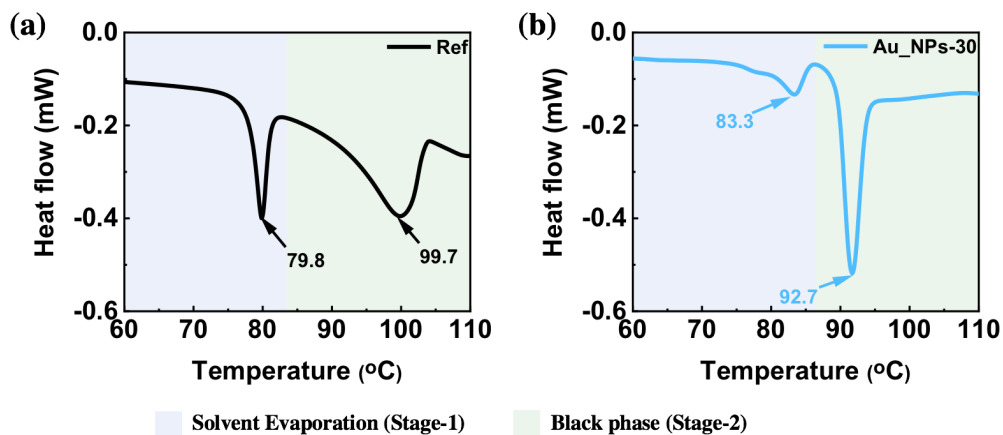


Figure III.6 DSC curves of (a) Ref and (b) Au\_NPs-30 sample adducts.

Differential Scanning Calorimetry (DSC) was then employed to further understand the effect of Au\_NPs on the formation of the crystallized perovskite. The curves were measured on the two samples prepared as powders adducts (**Figures III.6**). A first Ref endothermic peak was observed at  $\sim 75^{\circ}\text{C}$ - $85^{\circ}\text{C}$ , assigned to the evaporation of DMSO (DMF was eliminated upon washing the adducts by diethyl ether)[26] since DMSO mixed with  $\text{PbI}_2$  has been shown to start to evaporate at a temperature as low as  $75^{\circ}\text{C}$ . [32] First, a higher peak temperature was found for Au\_NPs-30 sample ( $83.3^{\circ}\text{C}$ ) compared to Ref sample ( $79.8^{\circ}\text{C}$ ). It suggests that the presence of Au\_NPs prolongs the period of solvent evaporation. The evaporation temperature increased by  $3.5^{\circ}\text{C}$  with Au\_NPs introduced into PPS. This means that the presence of gold nanoparticles renders difficult the evaporation of the surrounding DMSO solvent. To prove this, we did DSC test on Au\_NPs solution. In **Figure A.III.1 (Annex III)**, the endothermic peak of Au\_NPs was measured as high as  $172.8^{\circ}\text{C}$ , which is much higher than  $79.8^{\circ}\text{C}$ . Next, the second endothermic peak of the Ref sample was  $99.7^{\circ}\text{C}$ , which has gone through a long phase change process from  $\sim 81^{\circ}\text{C}$  to  $\sim 104^{\circ}\text{C}$ . This endothermic peak is assigned to the perovskite crystallization. Interestingly, the sample with Au\_NPs presented a sharp endothermic peak at  $92.7^{\circ}\text{C}$ ,  $7^{\circ}\text{C}$  lower than the Ref one, and had a short period of phase transition. The shortening of the phase transition process indicated a faster crystallization rate. Because of this gap, the quality of thin films changed greatly. Here, we can conclude that in the  $\text{MAPbI}_3$  system, the conventional crystallization rate will lead to excessive growth of lead iodide, resulting in the stacking of grains. On the contrary, the phenomenon can be avoided by accelerating the crystallization rate properly by introducing Au\_NPs.

### **III.3.4 GD-OES**

In order to get a deep understanding of the effect of Au\_NPs on the film formation process, we pioneered the employment of an original technique, the GD-OES. We first followed the movement of main inorganic elements composing perovskite layer upon annealing process. Through the distribution of these elements and their motion trajectory, we have been able to better understand the process of crystallization and the quality of the final perovskite layer. At the same time, we have also been able to determine the gold nanoparticles distribution in the layer. Secondly, by tracing the sulfur element in

DMSO, we have determined the growth direction of the film, and have been able to understand the effect of Au\_NPs on the crystallization of MAPbI<sub>3</sub>.

**a- Main inorganic elements distribution upon annealing**

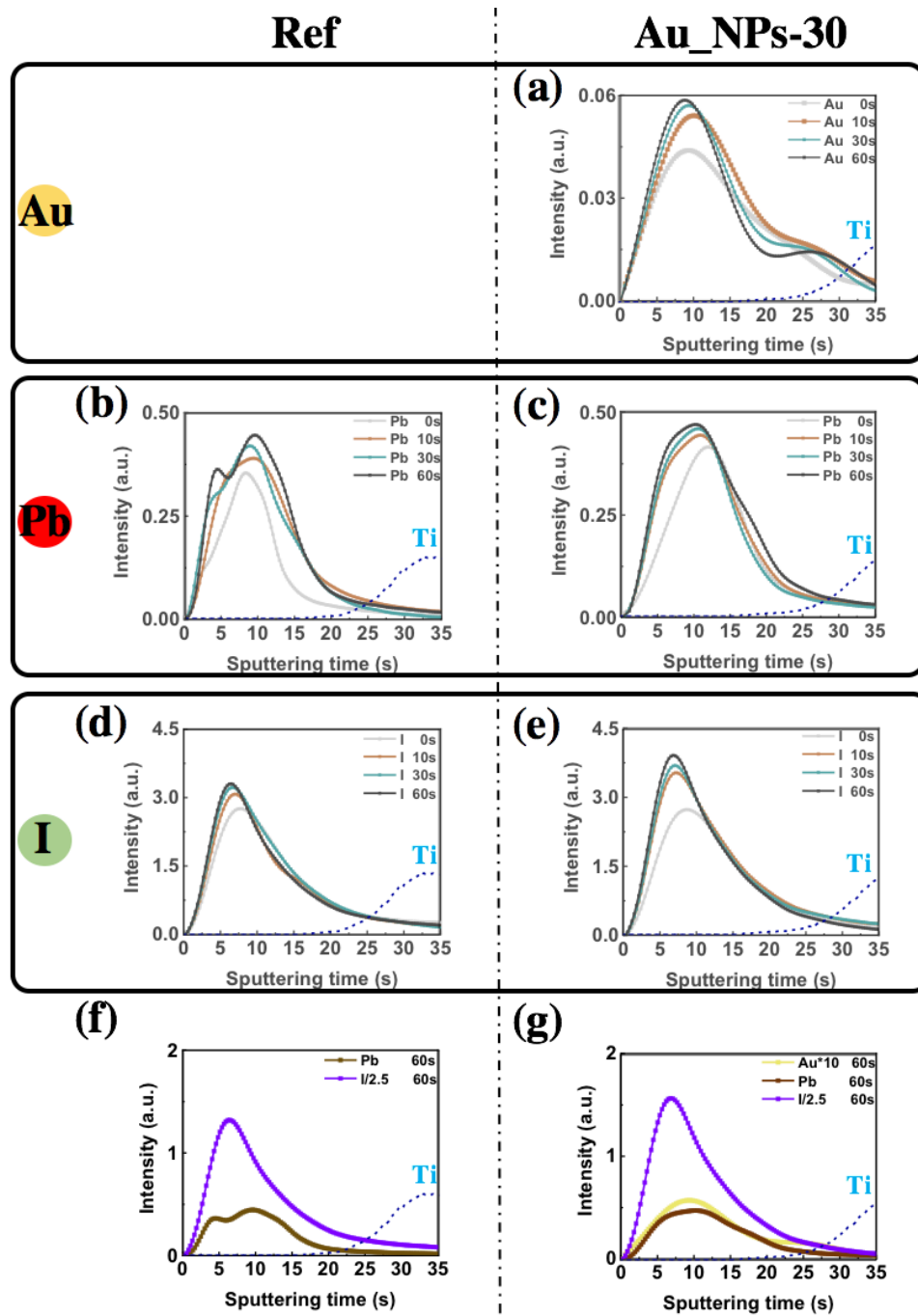
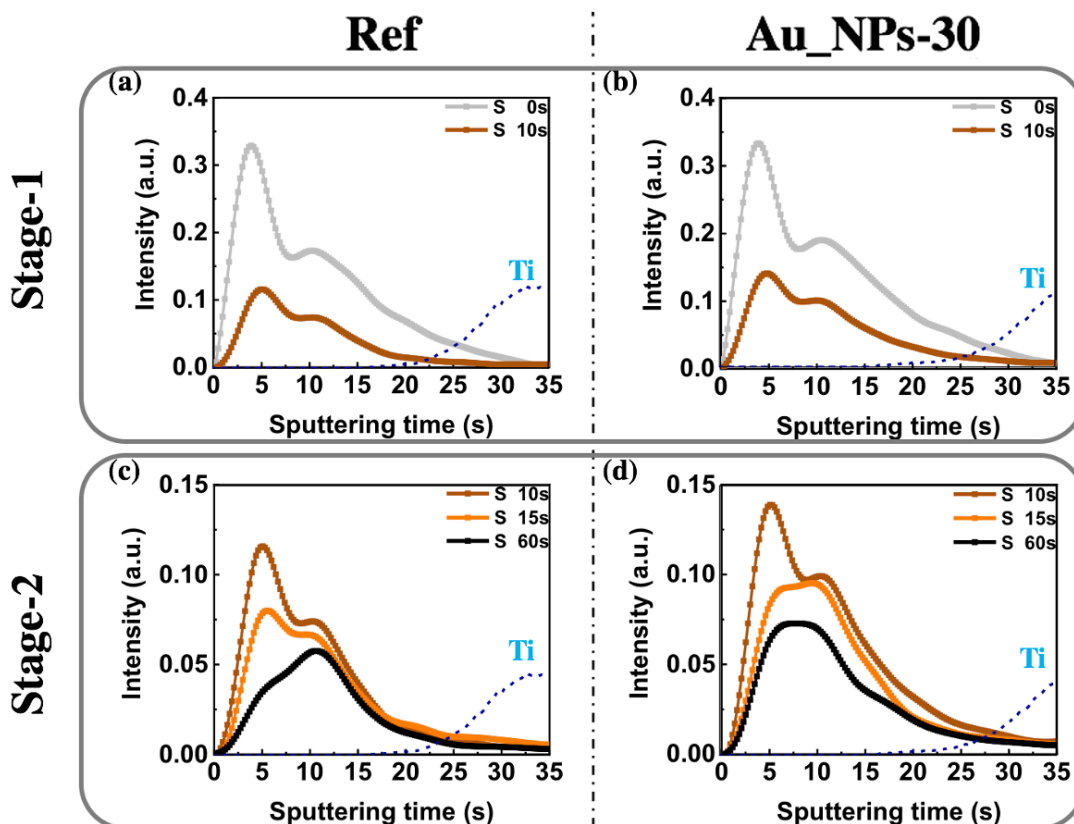


Figure III.7 The GD-OES distribution curve of the main elements composing the perovskite film upon annealing by using (a) Distribution of gold. (b, c) Distribution of lead. (d, e) Distribution of iodine. (f, g) All metal ion fractions after 60s of annealing, (f) Ref and (g) Au\_NPs-30. The annealing time is given in seconds.

In **Figure III.7**, we present the movement of main elemental ions for the Ref and the Au\_NPs-30 sample upon annealing. We first followed Au and found that the distribution of gold nanoparticles becomes wider with the annealing time and that the main peak gradually moves toward the upper layer of the perovskite. After annealing for 30s, the second peak of Au\_NPs appeared, which shows that the gold nanoparticles are not well diffuse into the interface layer of perovskite and titanium oxide, but enriched the titanium dioxide layer (**Figure III.7a**). In **Figure III.7b** and **7c**, the distribution of Pb became boarder with annealing time in both samples. However, the big difference is that there are two peaks in the Pb distribution of sample without gold nanoparticles (**Figure III.7b**) while Pb is uniformly distributed in the Au\_NPs30 sample (**Figure III.7c**). The reason for this is that the slow crystallization leads to a stack of multiple crystals in the longitudinal direction of the perovskite layer (**Figure III.3a**), which leads to discontinuous detection signal peaks (that is, two peaks). In other words, it is precisely because of the addition of gold nanoparticles that speeds up the film formation process, making the perovskite film homogeneous (**Figure III.3b**), that we can see the continuous Pb curve. It is also the reason why, we can see that the distribution of I in **Figure III.7d** is wider than that in **Figure III.7e**. By comparing **Figure III.7f** and **7g**, we can conclude that the high quality of Au\_NPs-30 perovskite layer produces a stronger intensity and a boarder distribution for each element. In order to better show these elements distribution in same Figure after annealing 60s, the intensity of Au is multiply by 10 and the intensity of I divided by 2.5.

#### **b- Solvent elimination upon annealing**

The residual solvent elimination is an important aspect of the synthesis which occurs upon the film crystallization and growth. Indeed, the solvent employed is only DMSO and S element contained in DMSO can be tracked by GD-OES. The S element profiles for the various films and various annealing times are presented in **Figures III.8a-d**. By increasing the sputtering time, deeper part of the PVK layer is analyzed until reaching the *meso*-TiO<sub>2</sub> layer (dashed blue line in **Figures III.8a-d**). Before annealing, the DMSO profile is asymmetrical in every case and we observe that the outer part of the film is richer in solvent than the inner part.



**Figure III.8** Evolution of GD-OES S (sulphur) profile in the perovskite precursor layer upon annealing. (Dashed line in (a-d): Ti profile corresponding to the *meso*-TiO<sub>2</sub>).

For the annealing, our results distinguish two stages. The first one occurs during the first 10 s of annealing on a hotplate. The initial film changes from light yellow translucent to black (**Figure III.9**). During this stage (stage-1), the most superficial residual solvent evaporates and is almost fully eliminated at the uttermost surface while these two kinds of perovskite present in the wet layer is fully transformed into the black phase (**Figure A.III.2, Annex III**). The next stage (stage-2) corresponds to 10s to 60s annealing times, when the film becomes black. We observed a clear effect of Au\_NPs on the solvent distribution upon annealing. In the case of Ref sample, DMSO was eliminated fast near the surface (**Figures III.8c**). However, less solvent remained in the deeper part of the layer. Moreover, the evaporation rate of first peak which represents the layer near the surface was faster than the second peak that represents the layer near the TiO<sub>2</sub> layer. Therefore, the overall grains grow downward, that is from the top to the bottom. It favors the multiple and oblique grain boundaries and rather small perovskite grains.

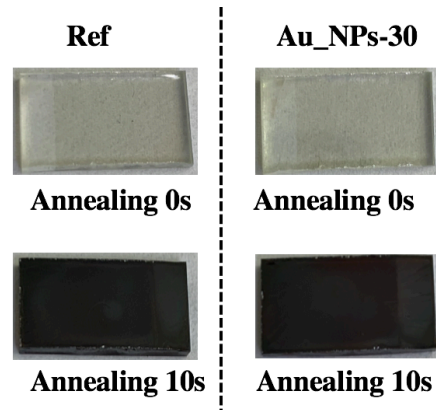


Figure III.9 Change of perovskite film color upon the first 10 seconds of annealing.

In the presence of Au\_NPs, the profiles are different. For Au\_NPs-30, the S profile is more extended throughout the layer thickness. Upon annealing, the solvent profile decreases uniformly throughout the layer thickness (Figure III.8d). In this case a bulk grain lateral growth occurs, and it results in more homogeneous films with big monolithic grains as shown in the cross-section SEM view (Figure III.3b). For all the investigated samples, Figure A.III.3 (Annex III) shows that the solvent was fully eliminated after 4 min of annealing. A striking result of this study is that the Au\_NPs regulates the solvent elimination and then the growth of the film in its full depth. It boosts the quality of the film.

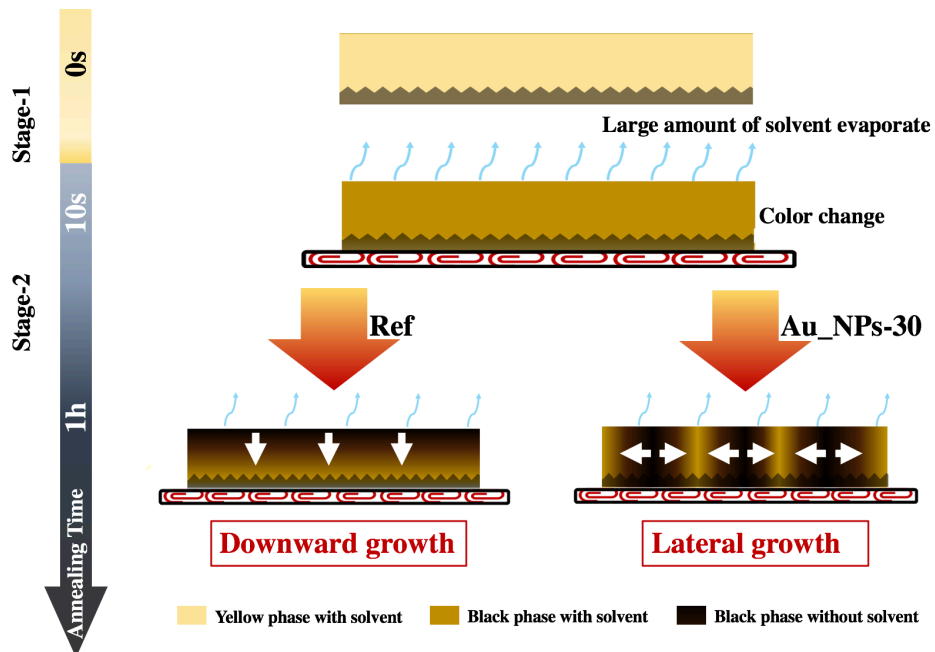


Figure III.10 Schematic of the film formation processes upon annealing observed for Ref and Au\_NPs-30 samples: Grain growth direction and mechanism.

In summary, this study illustrates that the grain growth is linked to the solvent elimination from the film and we can distinguish different cases as schematized in **Figure III.10**. For the Ref sample, the solvent is better eliminated at the top and the film grows downward, and then it is formed of multiple-boundaries grains. For the Au\_NPs-30 sample, the solvent is homogeneously eliminated in the depth of the film which leads to the lateral growth of the grains and results in monolithic large grains with low defect density. It is the targeted morphology for high efficiency.

### III.3.5 EDX

**Table III.1 EDX analysis of the perovskite layers.(Atomic values)**

Ref	Measurement	Pb (M-series)	I (L-series)	I/Pb At. ratio
	1	39.69	14.19	2.79
	2	36.18	12.50	2.89
	3	39.67	14.68	2.70
	4	38.18	13.79	2.77
	5	37.77	13.30	2.83
	Average	38.29	13.69	2.79

Au_NPs-30	Measurement	Pb (M-series)	I (L-series)	I/Pb At. ratio
	1	39.28	13.35	2.97
	2	40.04	13.02	3.07
	3	39.06	12.92	3.02
	4	38.98	13.02	2.99
	5	38.99	13.18	2.98
	Average	39.27	13.09	3.01

EDX analyses were implemented to determine the composition of perovskite layers (**Table III.1**). Since the ingredients that make up MAPI are relatively simple, we focused on the I/Pb atomic ratio for Ref and Au\_NPs samples. In theory, the closer this value is to 3, the higher is the crystal quality. In order to make the test data more real and accurate, we selected five different positions on the perovskite

surface (measurement size is  $100\mu\text{m} * 100\mu\text{m}$ ), and then take the average value. We found 2.79 for the sample without Au\_NPs and 3.01 for the sample with Au\_NPs. The Au\_NPs-30 sample has a value very close to the stoichiometry and has then a high quality of perovskite layer. The lower value for Ref sample can be assigned to the presence of  $\text{PbI}_2$  and this result is consistent with XRD result, the peak of  $\text{PbI}_2$  appeared in the XRD patterns of Ref.

### III.3.6 Absorbance

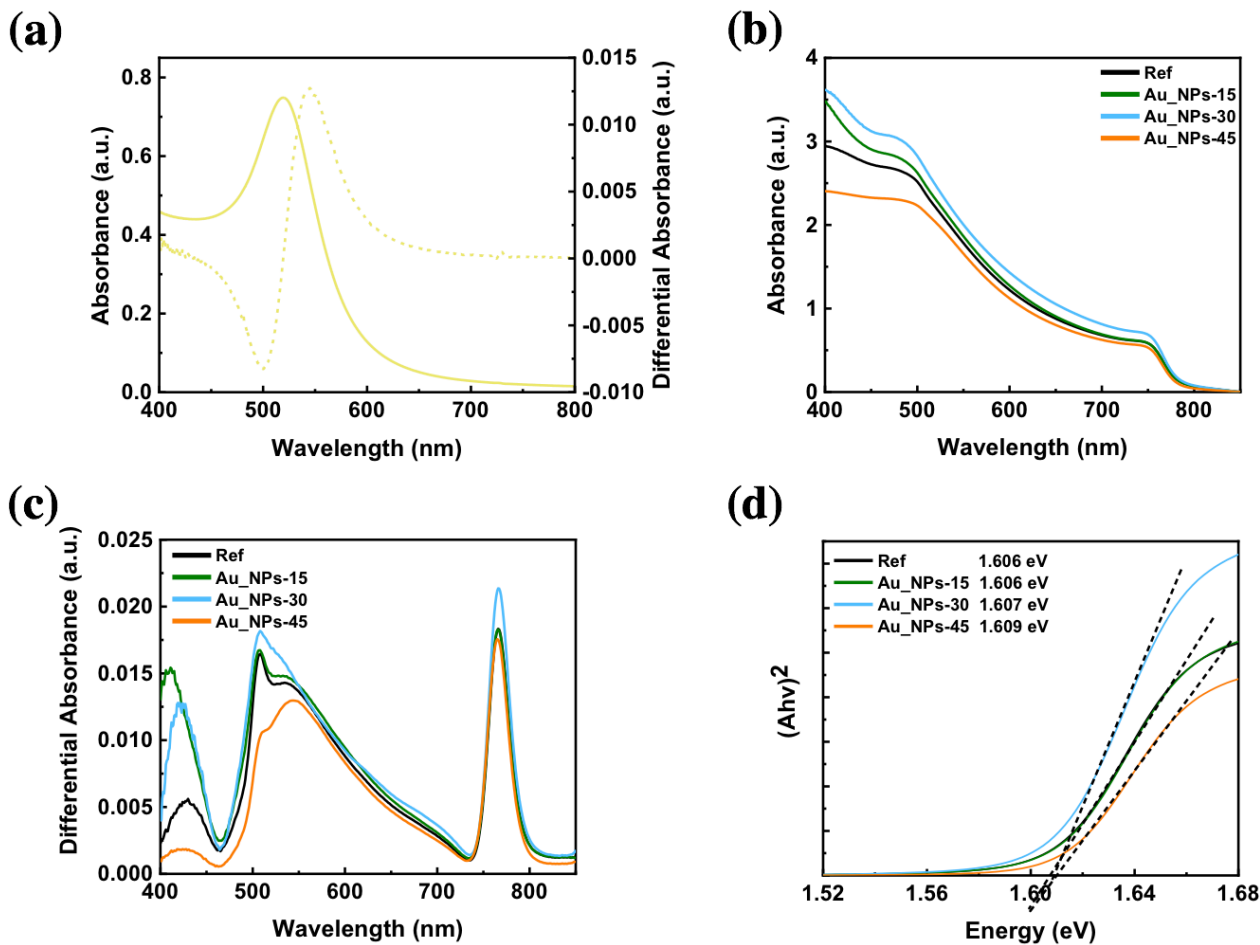


**Figure III.11** (a) The absorbance spectrum of Au\_NPs (solid line) and corresponding Differential Absorbance spectrum (dash line). (b) Effects of different volume of Au\_NPs on the layer absorbance and (c) corresponding differential absorbance. (d) Tauc plots of the absorbance curves and optical direct bandgap determination.

For the solution-processed solar cells, adding the plasmonic materials in the solution is an easy and efficient approach that should enhance the light absorption mainly by localized plasmon resonance (LSPR) while, due to the small size of the NPs, the reflection effects can be considered as negligible.

LSPR is a collective oscillation of conduction band electrons in metal nanoparticles excited by the electromagnetic incident light. There have been several papers published claiming the boosting of PSC performances in gold particles/perovskite composite devices due to this effect. [33]

In **Figure III.11a**, we first analyzed the absorption of 14.3 nm gold nanoparticles in DMSO solution and found a main absorption peak at 522 nm. However, this result is tested in DMSO solution, and the absorption of Au\_NPs in different media will cause a certain offset. Therefore, the enhancement near 522nm in the absorption spectrum of the perovskite with Au\_NPs is not necessarily due to Au\_NPs. Based on the above conjecture, **Figure III.11b** shows the absorption spectra of perovskite films with various additions of the Au\_NPs. These spectra share features similar to typical perovskite films: an absorption edge at around 785 nm. After adding 15  $\mu$ L of Au\_NPs at first, we only found a small absorption enhancement in the 500-600 nm range. However, we observed an obvious enhancement of light absorption in the spectral range of 400–770 nm, especially in the range of 600-770 nm. When the addition of gold nanoparticles increased to 45  $\mu$  L, the absorption of perovskite films decreased sharply due to the poor crystallinity as shown in **Figure III.5**. In order to see more clearly the difference of absorption, we drawn the differential spectra. In **Figure III.3c**, after differential, we couldn't observe a feature assignable to the absorbance of the NPs. We analyzed the near-band edge absorption using the Tauc plots in **Figure III.11d**. Considering a direct bandgap, the linear fit intersection with the energy axis gave optical bandgaps of 1.606 eV for Ref and Au\_NPs-15, 1.607 eV for Au\_NPs-30 and 1.609 eV for Au\_NPs-45. The basically unchanged bandgap value indicates that the introduction of gold nanoparticles does not cause a marked change in the MAPI perovskite lattice.

Three possible mechanisms may explain the enhancement of absorption in the presence of Au\_NPs:

- 1) The crystal quality of the perovskite layer is greatly improved, and the absorption is enhanced;
- 2) Due to the successful implantation of Au\_NPs into the perovskite layer, light is trapped in the absorbing layer. In other word, the Au\_NPs with subwavelength dimensions can couple incident photons with conduction electrons, giving rise to localized surface plasmon resonance phenomenon (LSPR);
- 3) The combination of the above two reasons.

Through the previous XRD, DSC, GD-OES and other test results analysis, we already proof that embed Au\_NPs in perovskite layer greatly enhance the film structural quality and reduces grain boundaries. Therefore, the above conjecture mechanism 1 occurs. To test mechanisms 2 and 3 we have performed simulations which are detailed below. (see Section III.4, Chapter III).

### III.3.7 Steady-state PL and TRPL

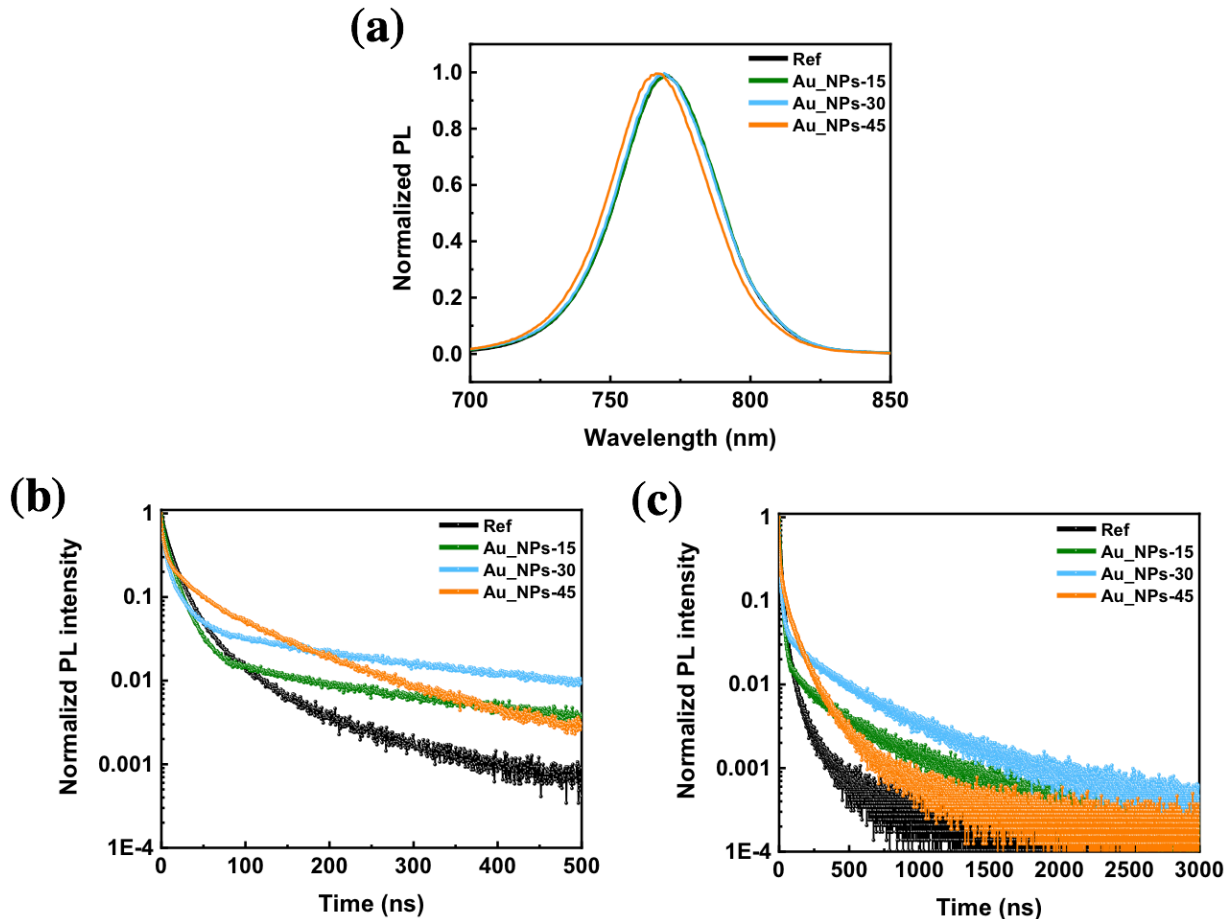


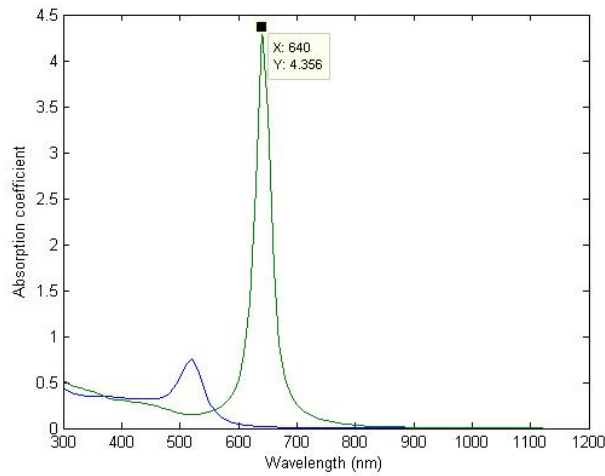
Figure III.12 (a) Steady-state PL and (b,c) TRPL curves of Ref, Au\_NPs-15, Au\_NPs-30 and Au\_NPs-45 samples. (sample are deposited on Glass )

Figure III.12a shows the PL spectra measured with a laser excitation at 500 nm wavelength from perovskite side and at room temperature. There is a small blue shift in the emission peak of Au\_NPs sample compared to the Ref sample and this result is also in good agreement with the measured optical band gaps (Figure III.11d). Generally, the spontaneous radiative recombination between trap states leads to a red-shifted emission peak compared with that from the band edge transition and passivation

of these trap states can blue-shift the PL peak. However, in our results, there is a small blue shift with the addition of gold nanoparticles, the blue shift is not particularly obvious on the whole, which may be because the gold nanoparticles we added only occupy a small part of the volume of the whole perovskite. According to our calculations, the volume ratio of the added gold nanoparticles to the entire perovskite is only 0.009%, which confirms our above word (**Formula A.III.1 in Annex III**). Further, the PL decay profiles of MAPI films without and with the presence of Au\_NPs are displayed in **Figure III.12b** and **12c**. The PL decay data were adequately fitted using a triple-exponential function and the results are displayed in **Table A.III.1, Annex III**. The Ref film provided  $\tau_{fast}$  (4.39 ns) and  $\tau_{slow}$  (61.97 ns), while the Au\_NPs-30 sample gave 2.37 ns ( $\tau_{fast}$ ) and 323.26 ns ( $\tau_{slow}$ ). The fast component ( $\tau_{fast}$ ) can be due to non-radiative recombination near defects. Its relative contribution ( $RC_{fast}$ ) decreased from 0.12 to 0.02 (**Table A.III.1, Annex III**) and, then, Au\_NPs reduce the importance of this component. The higher decay values of  $\tau_{slow}$  indicated that the bulk perovskite of the deposited films possessed a better quality and less defects in the composite with larger numbers of carriers after 1,500 ns, attributed to the strong suppression of non-radiative recombination.

#### **III.4 Simulations of gold nanoparticles optical effect**

These simulations have been implemented by Dr. Laurent Coolen and Prof. Catherine Schwob at the Institut des Nanosciences de Paris (Sorbonne Université). First, we will use Mie's analytical theory to describe absorption and scattering by a sphere in a medium. We can use it here to estimate the LSPR wavelength and the absorption cross-section. Please note that we take not the MAPI index for the Mie calculation, but only the real component of the MAPI index: its imaginary component (related to absorption) is not included in the equation.



**Figure III.13** The absorption coefficient of Au\_NPs in water (blue) and in MAPbI<sub>3</sub> (green).

In **Figure III.13**, we can see that the LSPR of Au\_NPs in water is 520 nm with an absorbance cross-section of 115 nm<sup>2</sup>. In MAPbI<sub>3</sub> system, however, the LSPR of Au\_NPs is 640 nm with absorbance cross-section 670 nm<sup>2</sup>, in which the absorption cross-section area is equal to Absorption coefficient  $\times \pi R^2$ . The larger cross-section area of absorbance shows that Au\_NPs have a strong effect on MAPbI<sub>3</sub> system compared to the water one.

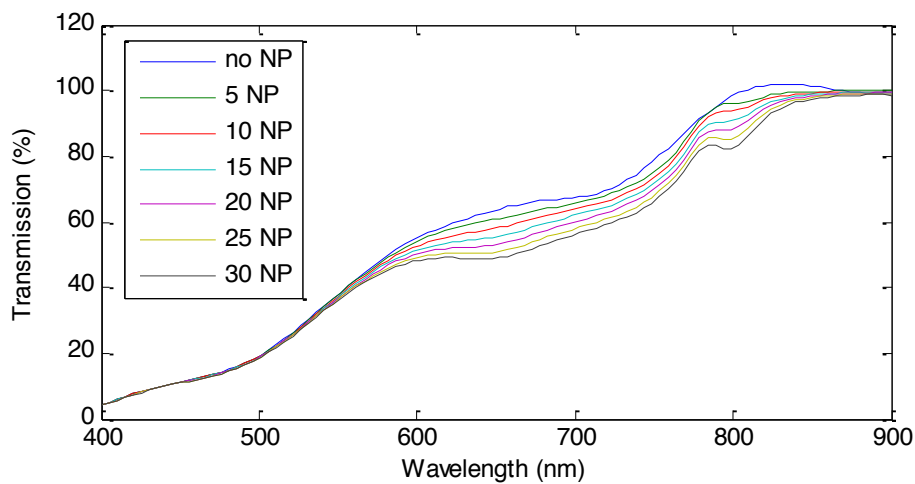


**Figure III.14** Transmission through a 200x200x100 nm<sup>3</sup> volume of MAPbI<sub>3</sub> for different numbers of Au\_NPs

We quantified the effect of the Au\_NPs by dividing the transmission spectrum by the reference spectrum without Au\_NPs. Despite some small oscillations which might be due to numerical errors, the effect of the Au\_NPs is clear by using Lumerical software, with an absorption dip at 650 nm (**Figure III.14**), not far from the Mie LSPR resonance. It is very positive that the LSPR effect is in the spectral range where MAPbI<sub>3</sub> absorption needs to be optimized. The relative decrease of transmission is around 20 % for 30 NP, which corresponds to a Au\_NPs volume fraction of 1 %. However, we have calculated in **Section III.3.6 and in the Annex** that the amount of gold nanoparticles we added in the experiment was much less at 0.009% of the total volume of MAPI and that using higher concentrations caused defective films. That means if we want to see obvious enhancement caused by Au\_NPs, just like **Figure III.14** showed to us, we need to add 100 times more NPs. The above simulation has been carried out for a 200x200x100 nm<sup>3</sup> cell volume, in order to make the simulation more reliable, we also simulated cell area with 500x500x100 nm<sup>3</sup> and the results are almost same for the sample with or without Au\_NPs (**Figure A.III.4, Annex III**).

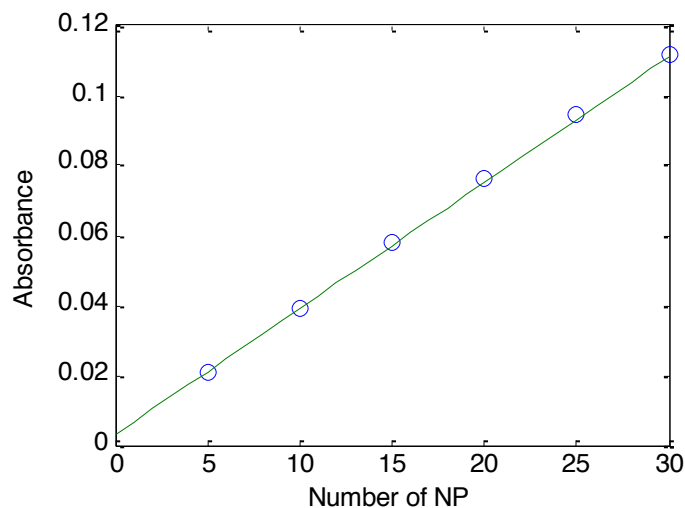


**Figure III.15 Additional Absorbance simulation of various number of Au\_NPs embedded on perovskite layer.**

To prove that the addition of a small amount of Au\_NPs will definitely affect the light absorption of the surrounding perovskite, different numbers of Au\_NPs embedded in perovskite were simulated at INSP (Sorbonne Université) and the result is plotted in **Figure III.15**. We calculated T, the average of normalized transmission from 650 nm to 670 nm, and then  $A = -\log_{10}T$  which is the additional

absorbance. Based on this definition, the obtained linear curves by using Beer-Lambert law (**Formula A.III.2, Annex III**). Through this curve, we have been able to roughly know the effect of added gold nanoparticles on the absorption, although this value is very small.

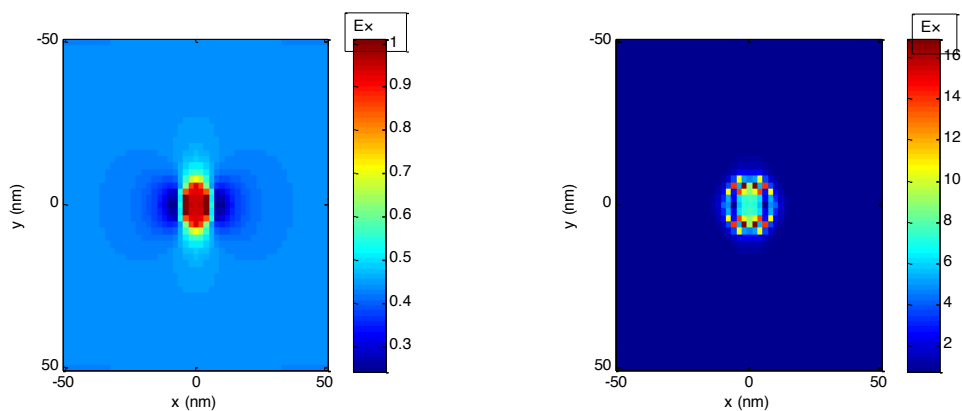


**Figure III.16 Electric field  $E^2$  distribution in a (x,y) plane passing through the middle of the Au\_NP. Off resonance (Left) Near LSPR (Right).**

In the above simulation results, we found a stronger absorbance for the MAPbI<sub>3</sub> containing Au\_NPs, but we still did not know the essential reason for the enhancement. Here we considered three hypotheses: 1) It is due to Au\_NPs absorption; 2) It is due to increased MAPbI<sub>3</sub> absorption; 3) Both Au\_NPs and MAPbI<sub>3</sub> have effect on absorption. To prove this, we further built a 100x100x100 nm<sup>3</sup> cell and use two wavelengths including 500 nm (off resonance) and 640 nm (near LSPR) to check their effect. From **Figure III.16**, we found that, in (x, y) plane, the electric field is enhanced in the Au\_NPs by a factor 6-15 at LSPR wavelength and only by a factor 2 at off-resonance wavelength. Moreover, there was also an Electric field  $E^2$  dependence on the z axis. In **Figure III.17**, the exponential decay (straight line) is due to the MAPbI<sub>3</sub> absorption. This decay is faster at 500 nm because the MAPbI<sub>3</sub> absorption is stronger. The Au\_NP is centered at z = 50 nm, the electric field is stronger inside and near the Au\_NP, especially at 640 nm (LSPR).

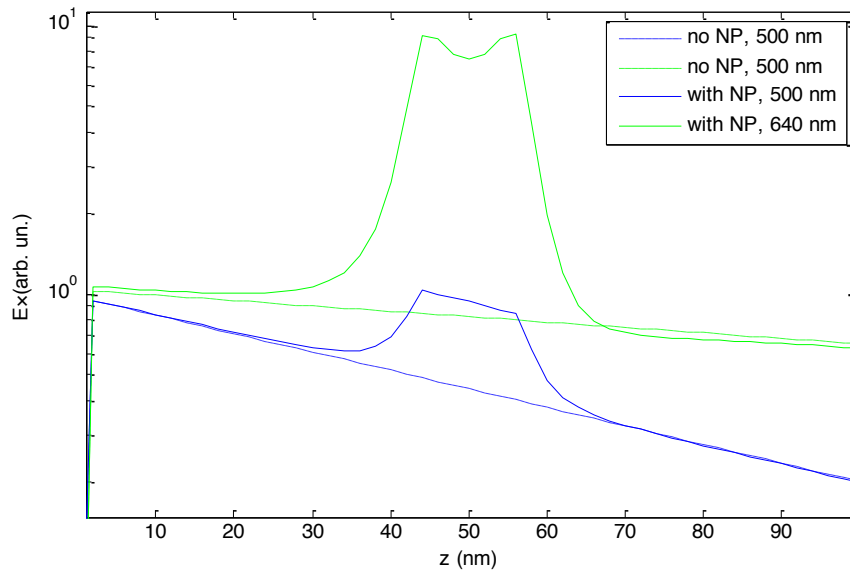


**Figure III.17** Electric field  $E^2$  on the (Oz) axis.

By integrating the electric field  $E^2$  over the volume of either the MAPI or the gold portions (**Formula A.III.3, Annex III**), we can extract the absorption in each portion of the simulated cell. We also can conclude to an increase in relative absorption and found that the Au\_NPs induces negligible absorption change at off-resonance (500 nm) wavelength (**Table III.2**). This result agrees with the transmission spectra (**Figure III.14**). Near the LSPR (640 nm), the Au\_NP induces +1.5 % losses while the MAPbI<sub>3</sub> induces +2.2 % losses. Therefore, additional absorption by MAPbI<sub>3</sub> is dominant, but the additional absorption by the Au\_NP creates significant losses, which means that 41 % of the absorption enhancement at LSPR corresponds to losses in the Au\_NP, while 59 % of the absorption enhancement corresponds to absorption in the active MAPI medium. The total relative 3.7 % absorption enhancement is consistent with the transmission spectra and it corresponds to  $A = 0.016$  in the previous calculations, which is associated 3.7 NP in the curve of  $A$  as a function of the number of Au\_NP in a  $200 \times 200 \times 100 \text{ nm}^3$  volume, which is comparable with the present simulation. It corresponds to a volume fraction of 0.16 %.

**Table III.2 Calculated additional absorption under different wavelengths in the Au\_NP and MAPI.**

Wavelength (nm)	Additional absorption in the Au_NP [%]	Additional absorption in the MAPbI <sub>3</sub> [%]	Total Additional absorption [%]
500 (Off resonance)	+0.2%	-0.1%	+0.1%
640 (LSP resonance)	+1.5%	+2.2%	+3.7%

In summary, additional absorption caused by Au\_NPs has been successfully simulated and the mechanism effect of Au\_NPs on the absorbance. Although there is a certain gap between the simulated addition amount and the addition amount in our experiment, an enhancement of the light absorption of the MAPb<sub>3</sub>I perovskite layer to a certain extent has been shown but for a concentration that is not reachable experimentally. After the above analysis, from the experimental point of view, the addition of Au\_NPs makes the absorption of the prepared perovskite layer enhanced mainly due to the control of the film formation and growth and by the resulting improvement of the quality of the perovskite film. We can also conclude to a negligible effect of LSPR effect in our experiments.

### III.5 Characterizations of PAI Treated perovskite Films

As we all know, compared to other formulations of perovskite, the stability of MAPbI<sub>3</sub> is not very good. Because of the presence of MA, the lattice structure of perovskite is difficult to maintain at high temperature and/or high humidity for a long time. This point has already been detailed in **Section II.1, Chapter II**. Recently, the spin-coating of small-molecule organics dissolved in isopropyl alcohol (IPA) on 3D perovskite films, which is called post-treatment technique, has become more and more popular and has been widely used. This post-treatment technique aims at forming a 2D capping layer on the top-surface of 3D perovskite layer and constitutes an intermediate energy band mitigating exciton recombination. It also acts as a barrier against degradation agents. In this section, we will fully describe the effect of PAI post-treatment on MAPbI<sub>3</sub> perovskite layer by using various characterization methods.

### III.5.1 SEM and AFM

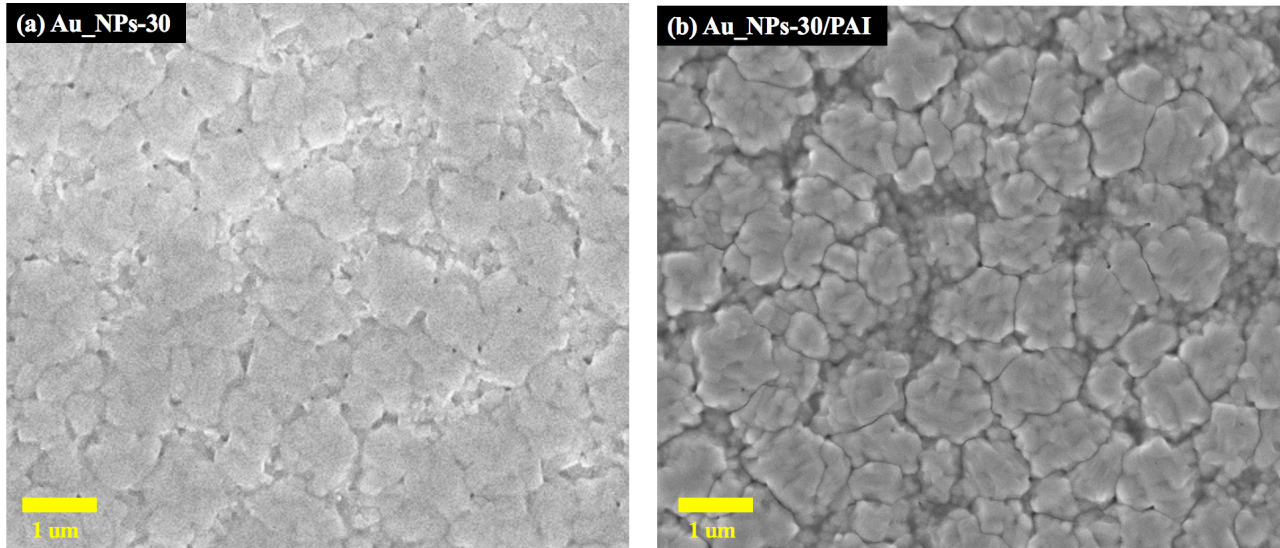


**Figure III.18** SEM top-view images of sample perovskite layers (a) before (Au\_NPs-30) and (b) after (Au\_NPs-30/PAI) PAI post-treatment. (The scale bar is 1  $\mu\text{m}$ ).

**Figure III.18** compares the top-surface SEM images before and after the surface processing. We can find that the pinholes on the processed sample have basically disappeared (**Figure III.18b**). The disappearance of these pinholes shows that the post-treatment process reduces the height difference between the grains, therefore, pinholes originally caused by the stacking of grains with each other disappeared and the layer became more compact. The decrease of the height difference between grains will inevitably lower the surface roughness of perovskite layer after the post-treatment. To prove this point, we did AFM measurements and found that the value of roughness was decreased from 24.33 nm RMS for Au\_NPs-30 sample to 20.50 nm RMS for Au\_NPs-30/PAI sample. The smooth surface after post-treatment favors the connection between the perovskite layer and the HTM layer, which is more conducive to the transfer of electric charges.

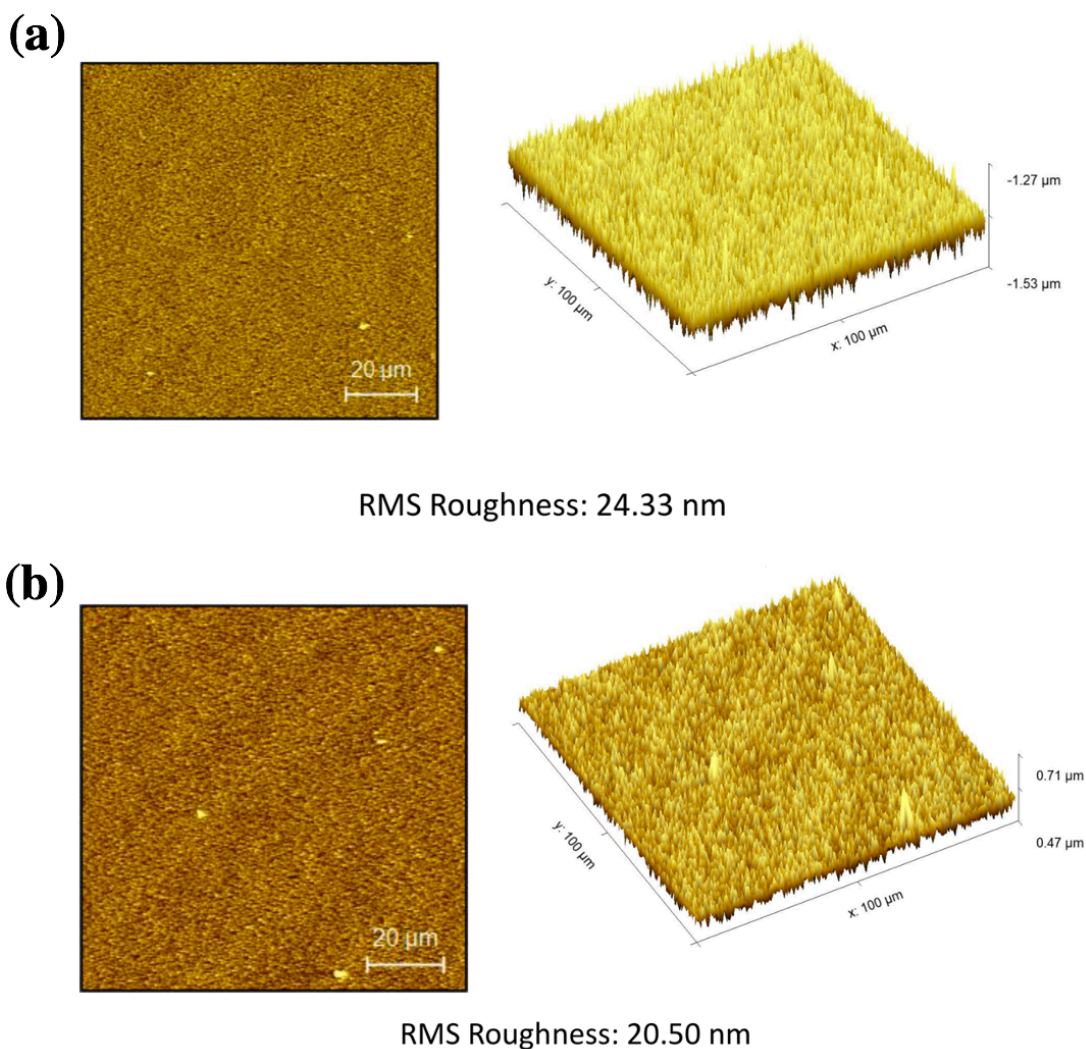


**Figure III.19** AFM images of MAPbI<sub>3</sub> perovskite layer surfaces. Effect of (a) before (Au\_NPs-30) and (b) after (Au\_NPs-30/PAI) PAI post-treatment.

### III.5.2 XRD

In **Figure III.20**, we performed XRD measurements to show the influence of the post-treatment on the crystallization. In order to make the results more compelling, we separately analyzed two samples with gold nanoparticles, Au\_NPs-30 and Au\_NPs-45, before and after processing. As for the low angle XRD result of Au\_NPs-30 (**Figure III.20a**), we could hardly see any obvious enhancement from the intensity of (110) peak. However, we could clearly see the enhancement of the (220) peak at larger angle (**Figure III.20b**), because peak enhancement is more apparent at large angle. The moderate peak enhancement can be explained by the recrystallization at the grain boundary after using PAI post-

treatment. The effect of post-treatment on the surface of the perovskite layer was more clearly reflected in the XRD results of the Au\_NPs-45 sample (**Figure III.20c and d**). Both (110) and (220) peaks were obviously enhanced, which shows that the surface crystal defects of the Au\_NPs-45 sample were much larger than that of the Au\_NPs-30 sample, so the same post-treatment had more obvious effects on the Au\_NPs-45 sample. After the above analysis, we can draw the conclusion that, the surface becomes smoother after the post-treatment not only because the height difference caused by the stacking of the grains is reduced, but the more essential reason is that the small-molecule organics used in the post-treatment recrystallize the grain boundaries.

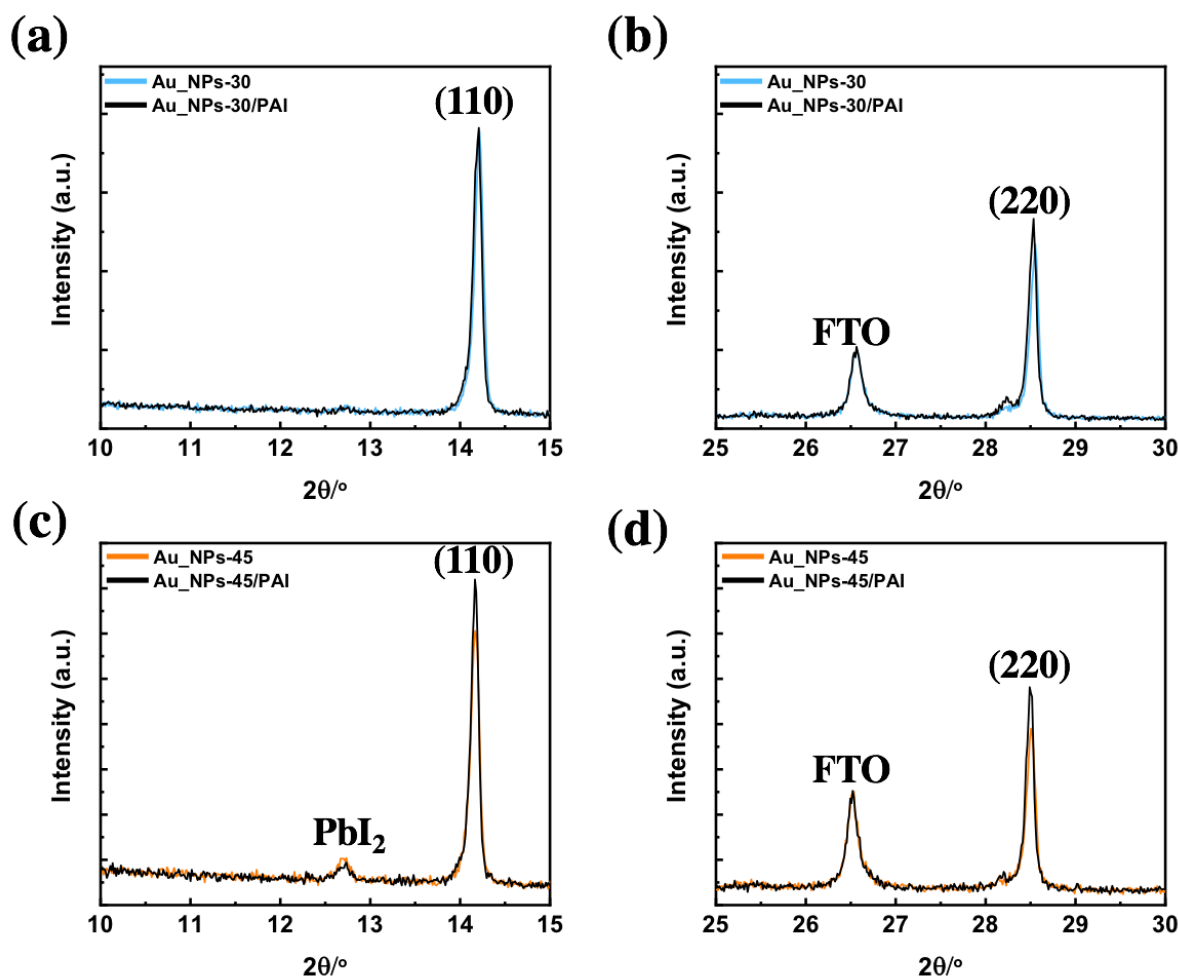


**Figure III.20** XRD patterns of same sample before and after PAI post-treatment. (a, b) Au\_NPs-30 and (c, d) Au\_NPs-45.

### III.5.3 Absorbance and Steady-state PL

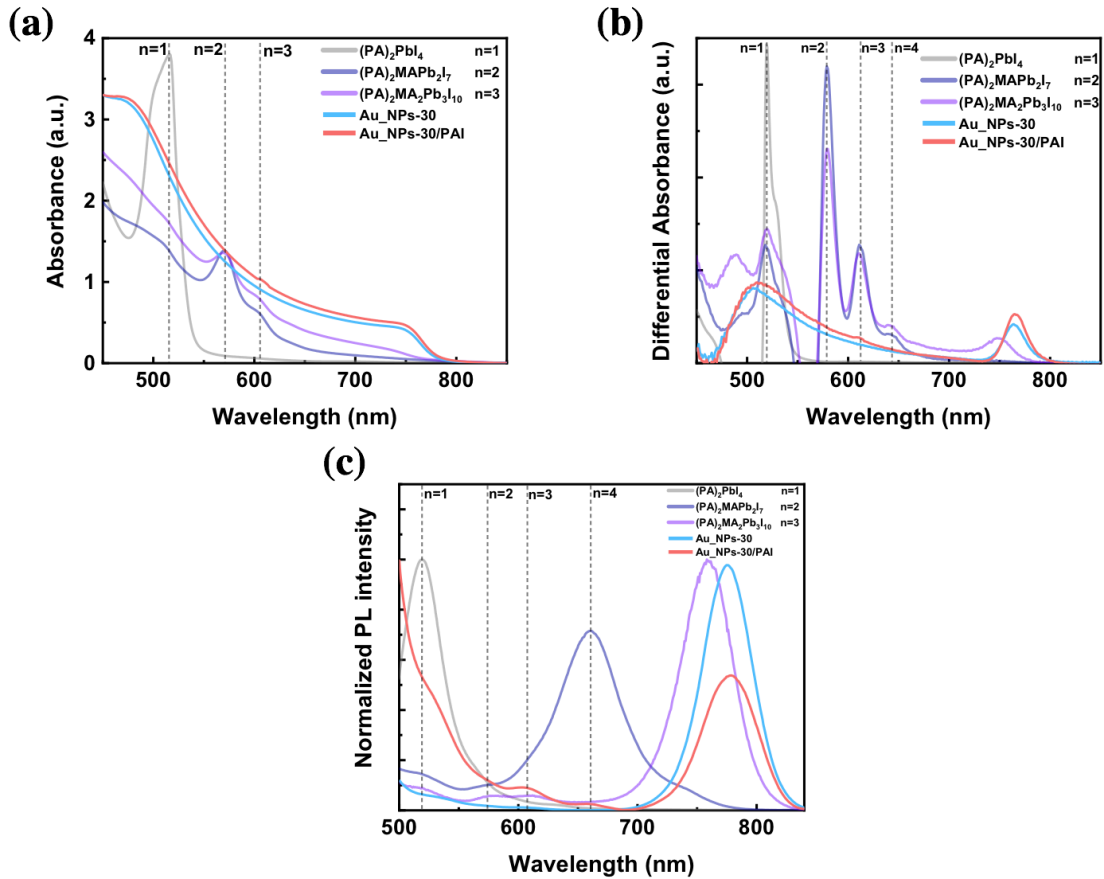


**Figure III.21** The same sample was measured before and after the PAI treatment. (a) absorbance spectra and (b) absorbance differential spectra of Au\_NPs-30 layers before and after the PAI treatment. (c) photoluminescence spectrum of Au\_NPs-30 sample before and after PAI post-treatment. Comparison with (PA)<sub>2</sub>PbI<sub>4</sub> (n=1), (PA)<sub>2</sub>MAPb<sub>2</sub>I<sub>7</sub> (n=2) and (PA)<sub>2</sub>MA<sub>2</sub>Pb<sub>3</sub>I<sub>10</sub> (n=3) reference 2D layers.

At the beginning of this section, we have already mentioned that the use of post-processing makes it form a 2D intermediate layer between 3D perovskite and HTM to avoid exciton recombination. However, no 2D XRD peaks could be detected (**Figure A.III.5, Annex III**). In order to confirm the formation of the 2D intermediate layer, we used UV-vis and steady-state PL measurements. In **Figure III.21a**, we found that there is only a small peak at around 610 nm, which indicates that the pure phase was formed after post-treatment. Compared to the formation of multiple phases, we are more inclined to the formation of a pure phase because it will be more stable. By comparing with the reference 2D perovskite absorption peak, we found that this peak belongs to n=3 2D perovskite. By differentiating **Figure III.21a**, we can see the position of this peak more clearly in **Figure III.21b**. Moreover, the

result of steady-state PL further confirmed the formation of the n=3 2D phase along with a small amount of n=4 2D phase (Figure III.21c).

### III.6 Characterizations of PSCs

In this section, we discuss the effect of Au\_NPs and PAI treatment on the overall performance of perovskite solar.

**Table III.3 Best cells  $J$ - $V$  curves parameters of solar cells.**

Name	Capping layer	Scan direction	$V_{oc}$ [V]	$J_{sc}$ [mA. cm <sup>-2</sup> ]	$FF$	PCE [%]	$HI^{(a)}$ [%]
Ref	NO	Reverse	1.037	21.83	76.32	17.25	17
		Forward	1.001	21.81	65.24	14.24	
Au_NPs-15	NO	Reverse	1.042	22.47	75.62	17.70	16
		Forward	1.032	22.23	64.73	14.84	
Au_NPs-30	NO	Reverse	1.059	23.37	76.81	19.01	16
		Forward	1.047	23.11	66.12	16.02	
Au_NPs-45	NO	Reverse	1.035	19.58	68.64	13.91	13
		Forward	1.011	19.69	60.62	12.07	
Au_NPs-30/PAI	YES	Reverse	1.103	23.26	79.68	20.44	13
		Forward	1.091	23.14	70.42	17.78	

<sup>a)</sup>  $HI = (PCE_{Rev} - PCE_{For}) * 100 / PCE_{Rev}$

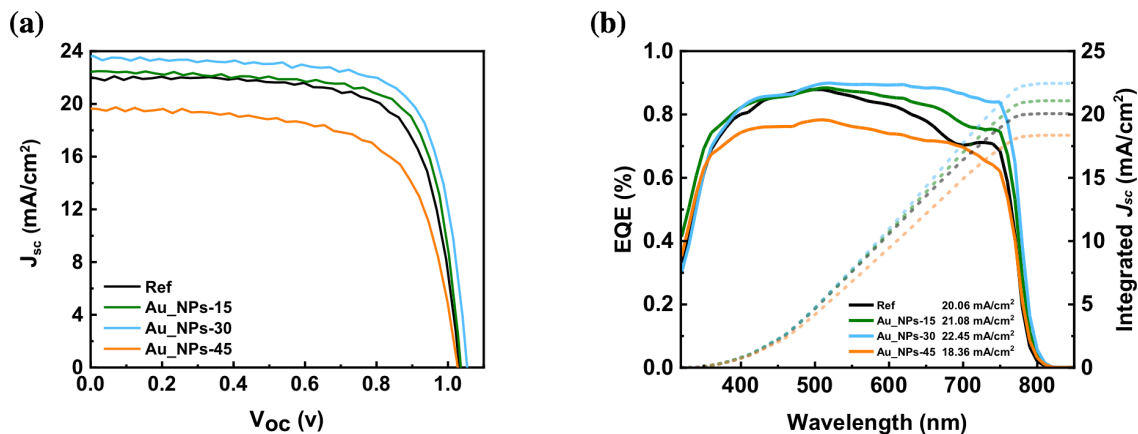


**Figure III.22 (a) Reverse  $J$ - $V$  curves, (b)  $EQE$  and  $J_{sc}$  integration curves of the best cells listed in Table III.3.**

**Table III.3** and **Figure III.22** summarize the best cell results for different volume of Au\_NPs. The Ref cells exhibited moderate performances with a *PCE* at 17.25 % on the reverse scan (**Figure III.22a**). After the introduction of Au\_NPs, all the parameters of the solar cell were enhanced, especially  $V_{oc}$  and  $J_{sc}$ , and the best one is Au\_NPs-30 which achieved 19.01% for the reverse scan. However, too much Au\_NPs caused a decrease in performance assigned to the reduced quality of the perovskite layer as described above (**Figure III.2d**). In **Figure III.22b** shows the typical *EQE* spectra of the Ref device and the ones with different additions of Au\_NPs. Compared with Ref sample, the *EQE* results of Au\_NPs-15 and Au\_NPs-30 have been significantly enhanced in the 520-780 nm range which is consistent with the absorbance spectra results (**Figure III.11b**). On the one hand, the red domain increases (with no increase at 400-500 nm) is typical of enhancement of optical absorption, either by enhanced absorption of the MAPI layer or by increased MAPI layer thickness. On the other hand, the decreased *EQE* over the whole spectrum for the 45  $\mu$ L cell is typical of a decreased electrical performance. Moreover, the integrated  $J_{sc}$  shown in **Figure III.22b** confirms the current increase from 20.06 mA/cm<sup>2</sup> for Ref sample to 22.45 mA/cm<sup>2</sup> for Au\_NPs-30 sample. The Au\_NPs-30 treatment is post-treated with PAI solutions of different concentrations (**Table A.III.2, Annex III**), the final 4mg/mL PAI solution provided the best enhancement with a highest *PCE* of 20.44%. Compared with Au\_NPs-30 sample, the most significant change of Au\_NPs-30/PAI is the higher  $V_{oc}$ , which increase from 1.035 V to 1.103 V (**Table III.3**). The voltage of perovskite solar cell is directly related to the quality of perovskite film and of the interfaces. The surface defects of the film after post-treatment are repaired due to recrystallization and the interfacial layer favors the fast charge transfer. It results in a large voltage improvement with the PAI post-treatment. The post-treatment did not influenced the  $J_{sc}$  parameter (**Figure A.III.6, Annex III**).

The statistical analysis of the effect of the Au\_NPs volume on the  $J$ - $V$  curve parameters is disclosed in **Figure III.23**. We can clearly see that the addition of Au\_NPs mainly improves the  $J_{sc}$  and  $V_{oc}$  parameters. There is also a small increase in  $FF$ , but it has no effect on  $HI$ . However, using PAI post-treatment favors all performance parameters of perovskite solar cell (**Figure III.24**), especially the  $V_{oc}$  and  $FF$  ones. In conclusion, the post-treatment can greatly enhance the performance of solar cell.

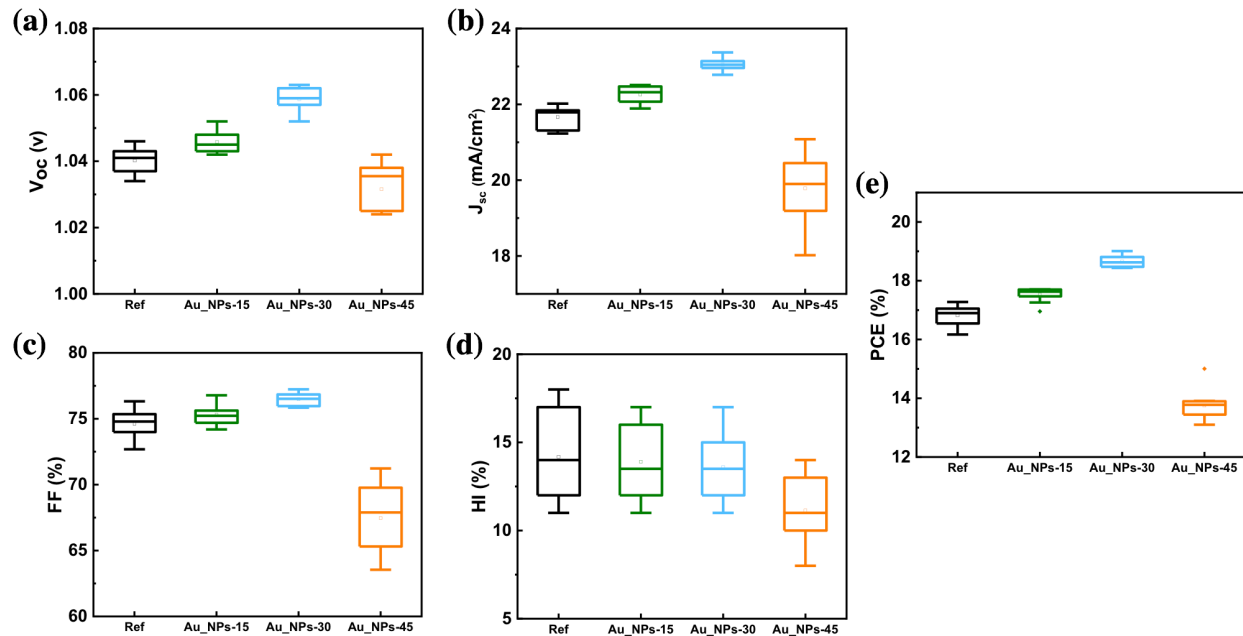


Figure III.23 Statistical analysis of all parameters of perovskite solar cells with different amount of Au\_NPs. (For each condition, we prepared 15 cells.)

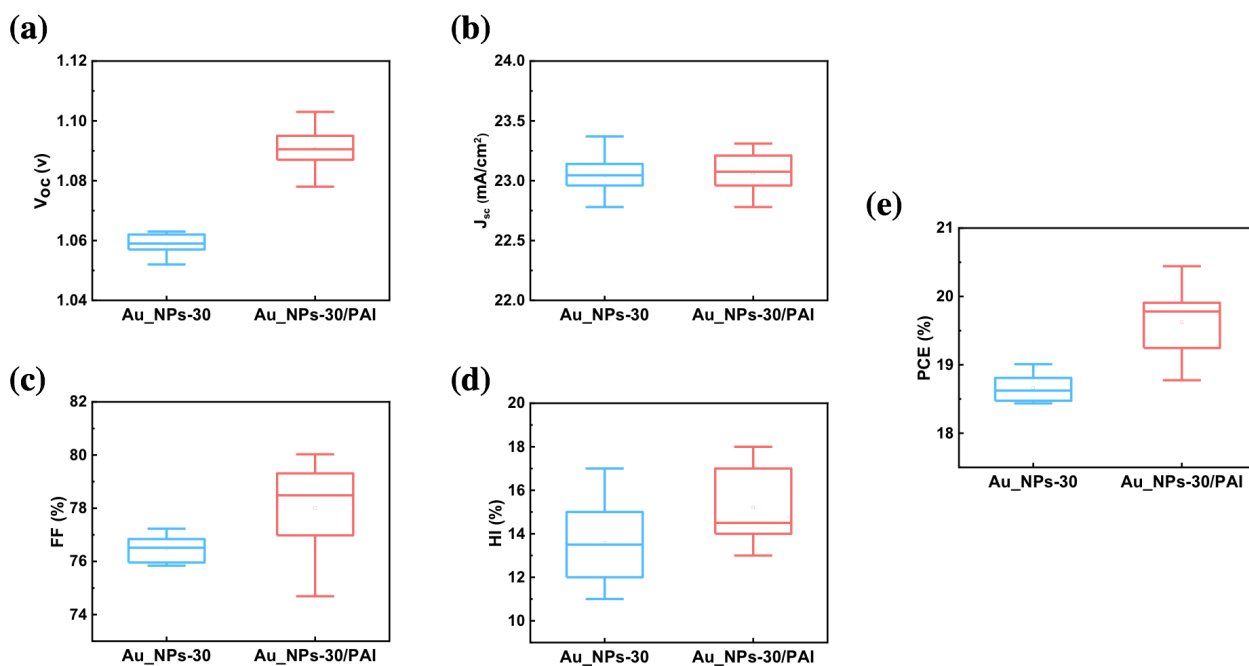
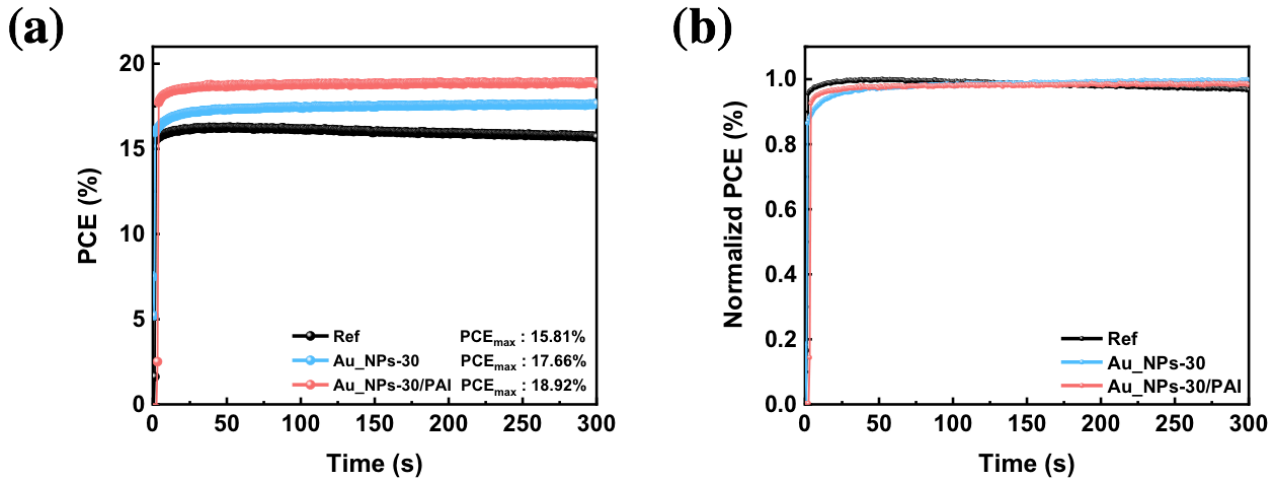


Figure III.24 Statistical analysis of the  $J$ - $V$  curve parameters with (Au\_NPs -30) and without (Au\_NPs -30/PAI) PAI post-treatment. (4mg.mL<sup>-1</sup> PAI concentration in IPA). (For each condition, we prepared 15 cells.)



**Figure III.25** (a) *PCE* tracking at the maximum power and steady-state *PCE*. (b) Same as (a) after normalization.

**Figure III.25a** presents the *PCE* tracking at the maximum power point and corresponding steady-state *PCE*. The first notice is that the Au\_NPs/PAI sample with post-treatment exhibited the best *PCE* (18.92%) compared to Au\_NPs-30 (17.66%). As for the Ref cell, it had a moderate *PCE* of 15.81%. We also clearly see that the overall trend of steady-state *PCE* of Ref decreases with times, which shows the poor stability of Ref cells. In order to better compare the influence of post-treatment on the time trend of efficiency, we normalized **Figure III.25a** and found that the efficiency of sample Au\_NPs-30/PAI increased a little bit more slowly than sample Au\_NPs-30. It suggests some initial interfacial reorganization before stabilization and improvement.

### III.7 Conclusions

In this chapter, we successfully prepared a MAPI perovskite solar cell with an outstanding efficiency of 19.01% through the addition of Au\_NPs, and further improved the efficiency of the cell to 20.44% through PAI post-treatment. Based on above good results, we conducted a detailed analysis and demonstrated the mechanism of Au\_NPs in MAPbI<sub>3</sub> perovskite through a combination of simulation and experiments. Simulation and analysis of the Au\_NPs in both qualitative and quantitative aspects have been performed. The quantitative analysis indicated that Au\_NPs must be added at 1% (volume fraction) to get an absorption enhancement of 20%. However, the actual value in our case was much

less at 0.009%, that would correspond theoretically to an increase of 0.18% in the absorption simulation. However, from the results of qualitative analysis, we know the total relative absorption enhancement is mainly due at 59 % to the absorption in the active MAPI medium while 41 % of the absorption enhancement at LSPR corresponds to losses in the Au\_NPs.

By a large number of experiments and different test methods (GD-OES, XRD, DSC, etc.), we have shown that Au\_NPs govern the growth direction of perovskite layer and the quality of film formation. Therefore, we have concluded that the addition of Au\_NPs makes the perovskite efficiency significantly improved, mostly because the quality of the film has been improved. Only a negligible effect of the enhancement can be assigned to the plasmonic enhancement of absorption.

Although the introduction of Au\_NPs and the application of PAI post-treatment technology we have improved the overall performance of perovskite solar cells with MAPbI<sub>3</sub> as the active layer, there is still a big gap from commercialization. In order to further increase the stability and efficiency, in **Chapter IV**, we develop the MA-free Cs<sub>x</sub>FA<sub>1-x</sub>PI perovskite system, and we show the enhancement of the performance in all their aspects by introducing targeted chloride additives.

## References

- [1] Atwater, H. A.; Polman, A. *Nat. Mater.* **2010**, *9*, 205–213.
- [2] Schuller, J. A.; Barnard, E. S.; Cai, W.; Jun, Y. C.; White, J. S.; Brongersma, M. L. *Nat. Mater.* **2010**, *9*, 193–204.
- [3] Kume, T.; Hayashi, S.; Ohkuma, H.; Yamamoto, K. *Jpn. J. Appl. Phys.* **1995**, *34*, 6448–6451.
- [4] Stenzel, O.; Stendal, A.; Voigtsberger, K.; von Borczyskowski, C. *Sol. Energy Mater. Sol. Cells* **1995**, *37*, 337–348.
- [5] Ferry, V. E.; Munday, J. N.; Atwater, H. A. *Adv. Mater.* **2010**, *22*, 4794–4808.
- [6] Pala, R. A.; White, J.; Barnard, E.; Liu, J.; Brongersma, M. L. Design of Plasmonic Thin-Film Solar Cells with Broadband Absorption Enhancements. *Adv. Mater.* **2009**, *21*, 3504–3509.
- [7] Aberasturi, D.J.; Serrano-Montes, A.B.; Liz-Marzán, L.M. *Adv. Opt. Mater.* **2015**, *3*, 602–617.
- [8] Catchpole, K. R.; Polman, A. *Phys. Lett.* **2008**, *93*, 191113.
- [9] Pryce, I. M.; Koleske, D. D.; Fischer, A. J.; Atwater, H. A. *Appl. Phys. Lett.* **2010**, *96*, 153501.
- [10] Wu, J.-L.; Chen, F.-C.; Hsiao, Y.-S.; Chien, F.-C.; Chen, P.; Kuo, C.-H.; Huang, M. H.; Hsu, C.-S. *ACS Nano* **2011**, *5*, 959–967.
- [11] Yang, X.; Chueh, C.-C.; Li, C.-Z.; Yip, H.-L.; Yin, P.; Chen, H.; Chen, W.-C.; Jen, A. K.-Y. *Adv. Energy Mater.* **2013**, *3*, 666–673.
- [12] Gan, Q.; Bartoli, F. J.; Kafafi, Z. H. *Adv. Mater.* **2013**, *25*, 2385–2396.

- [13] Standridge, S. D.; Schatz, G. C.; Hupp, J. T. *J. Am. Chem. Soc.* **2009**, *131*, 8407–8409.
- [14] Brown, M. D.; Suteewong, T.; Kumar, R. S. S.; D’Innocenzo, V.; Petrozza, A.; Lee, M. M.; Wiesner, U.; Snath, H. J. *Nano Lett.* **2011**, *11*, 438–445.
- [15] Choi, H.; Chen, W. T.; Kamat, P. V. Know Thy *ACS Nano* **2012**, *6*, 4418–4427.
- [16] Kawawaki, T.; Tatsuma, T. *Phys. Chem. Chem. Phys.* **2013**, *15*, 20247–20251.
- [17] Kawawaki, T.; Wang, H.; Kubo, T.; Saito, K.; Nakazaki, J.; Segawa, H.; Tatsuma, T. *ACS Nano* **2015**, *9*, 4165–4172.
- [18] Erwin, W. R.; Zarick, H. F.; Talbert, E. M.; Bardhan, R. *Energy Environ. Sci.* **2016**, *9*, 1577–1601.
- [19] Arinze, E. S.; Qiu, B.; Nyirjesy, G.; Thon, S. M. *ACS Photonics* **2016**, *3*, 158–173.
- [20] Hsiao, Y.-S.; Charan, S.; Wu, F.-Y.; Chien, F.-C.; Chu, C.-W.; Chen, P.; Chen, F.-C. *J. Phys. Chem. C* **2012**, *116*, 20731–20737.
- [21] Choi, H.; Lee, J.-P.; Ko, S.-J.; Jung, J.-W.; Park, H.; Yoo, S.; Park, O.; Jeong, J.-R.; Park, S.; Kim, J. Y. *Nano Lett.* **2013**, *13*, 2204–2208.
- [22] Chuang, M.-K.; Lin, S.-W.; Chen, F.-C.; Chu, C.-W.; Hsu, C.-S. *Nanoscale* **2014**, *6*, 1573–1579.
- [23] Sun, S. Y.; Salim, T.; Mathews, N.; Duchamp, M.; Boothroyd, C.; Xing, G. C.; Sum, T. C.; Lam, Y. M. *Energy Environ. Sci.* **2014**, *7*, 399.
- [24] Wang, H. P.; Lien, D. H.; Tsai, M. L.; Lin, C. A.; Chang, H. C.; Lai, K. Y.; He, J. H. *J. Mater. Chem. C* **2014**, *2*, 3144.
- [25] Chun, M.; Changxu, L.; Huang, J.; Ma, Y.; Liu, Z.; Li, L.; Thomas, D.; Yu, H.; Andrea, F.; Tom, W. *Sol. RRL* **2019**, 1900138.
- [26] Grancini, G.; Roldán-Carmona; Zimmermann, C. I.; Mosconi, E.; Lee, X.; Martineau, D.; Narbey, S.; Oswald, F.; De Angelis, F.; Graetzel, M.; Nazeeruddin, M. K. *Nature Commun.* **2017**, *8*, 15684;
- [27] Xiaoqian, M.; Ben, M.; Tianyan, Y.; Xin, X.; Liuquan, Z.; Wie, W.; Kun, C.; Lingling, D.; Shufen, C.; Wei, H. *ACS Appl. Energy Mater.* **2019**, *2*, 3605–3613.
- [28] Runsheng, W.; Bingchu, Y.; Chujun, Z.; Yulan, H.; Yanxia, C.; Peng, L.; Conghua, Z.; Yuying, H.; Junliang, Y. *J. Phys. Chem. C* **2016**, *120*, 6996–7004.
- [29] Wunjhen, C.; Yuchang, L.; Gautham, K.; Shunyu, X.; Fangchung, C. *Synthetic Metals* **2021**, *273*, 116675.
- [30] Pingli, Q.; Tong, W.; Zhengchun, W.; Lanxiao.; Liang, M.; Feihong.; Lun, X.; Xiangbai, C.; Haixia, L.; Xueli, Y.; Guojia, F. *Adv. Funct. Mater.* **2020**, *30*, 1908408.
- [31] Zhiyuan, H.; Chi, Z.; Rangwei, M.; Xuanhui, L.; Mengwei, C.; Haifei, L.; Yingping, Y. *Nanomaterials* **2020**, *10*, 2364
- [32] Yang, W.S.; Noh, J.H.; Jeon, N.J.; Kim, Y.C.; Ryu, J.; Seo, S.; Seok, S.I. *Science* **2015**, *348*, 1234.
- [33] Carretero-Palacios, S.; Jiménez-Solano, A.; Míguez, H. *ACS Energy Lett.* **2016**, *1*, 323–331.

# Chapter IV. Synergistic Effects of Ammonium Chloride and Potassium Chloride Additives on the Growth of Methylammonium-Free Perovskite Films for Efficient, Hysteresis-Free, Highly Stable Solar Cells

## IV.1 Introduction

A great strength of PSCs is that most functional layers, especially the perovskite one, are prepared at mild temperature ( $\leq 160^\circ\text{C}$ ) from perovskite precursor solutions (PPSs). The chemistry of these solutions is key for the final properties of the absorber film and PPSs must be formulated with care to optimize the final PV properties of the films. They contain two kinds of important components for the final PSC performance, (i) those which will form the film and will define the final composition of the layer and (ii) those that help the synthesis of the film and are eliminated upon the final annealing step. They are dissolved in polar aprotic organic solvents. By working on this chemistry and on the crystallization control, the device performance, as well as the material thin film stability, can be dramatically increased, not only by reaching the intrinsic entropic stabilization, but also by enhancing the crystallinity, suppressing defect formation, and stabilizing grain boundaries. From the point of view of the composition, methylammonium ( $\text{MA}^+$ )-free PVKs are desirable since  $\text{MA}^+$  can decompose with heating, outgases with time and is hygroscopic.[1] This led many research groups to develop new perovskites and notably to add cesium for the entropic stabilization of formamidinium lead iodide (FAPbI<sub>3</sub>).[1-12] In most cases, Rb and/or Br ions are also added to tune the tolerance factor and get stabilization.[1-8] On the other hand, stable  $\text{Cs}_x\text{FA}_{1-x}\text{PbI}_3$  perovskites remain poorly documented.[9-12] Other important targets include the growth of well-covering, pinhole-free, well-crystallized films composed of large grains. These characteristics are reached by finely controlling the nucleation and growth of the perovskite grains forming the film during the annealing treatment of the layer.[13,14] At this stage, the amount of grain boundaries as well as the structural and grain boundaries defects such as Frenkel defects[15] must be drastically limited.[16-18] Employing additives in the PPS appears to me as the most pertinent approach to address these various objectives. For further performance and stability improvements, the above-described engineering must be completed by a post-deposition

treatment of the PVK layer surface. Usually, the perovskite film surface is treated to produce an interfacial layer of low dimensional perovskite.[19-26]

The present chapter focuses on the simple  $\text{Cs}_{0.1}\text{FA}_{0.9}\text{PbI}_3$  perovskite. Utilizing only I as the halogen without Br is a requirement to minimize the bandgap and then approach the Shockley-Queisser limit for the maximum PCE. Moreover, simplifying the composition avoids aging by phase separation.[1] In this chapter, we report on the use of ammonium chloride ( $\text{NH}_4\text{Cl}$ ) and potassium chloride (KCl) mixed additives to control the crystallization and get the desirable lateral growth of the perovskite films. Their mixture allows the formation of an initial yellow translucent layer after a one-step spin-coating with dripping chlorobenzene antisolvent. This layer contains  $\text{Cs}_{0.1}\text{FA}_{0.9}\text{PbI}_3$  in a  $\delta$ -phase and also in the  $\alpha$ -phase in a significant amount combined with wetting solvent. By using DSC and GD-OES techniques, we highlight the formation mechanism of the film upon annealing. Two phases are distinguished: first the superficial residual solvent is eliminated then the elimination of the solvent in the depth of the film determines the final morphology of the layer. We show that when the chloride mixture is employed, the solvent is homogeneously eliminated across the layer, leading to a lateral growth of the grains. It results in large, monolithic and defect-poor grains with good coverage of the substrate. We have also employed the GD-OES technique to investigate the mobility of I in the PVK layers, to demonstrate that K blocks the ionic mobility and to correlate iodide displacement with the  $J$ - $V$  curve hysteresis. Finally, we prove these PSCs to be highly resistant to electrical, light, moisture, and temperature external stressors.

## IV.2 Experimental

The preparation of substrates,  $c$ - $\text{TiO}_2$  layer and  $mp$ - $\text{TiO}_2$  layer are conducted as detailed in **Chapter II, Section II.1.2.1**.

### IV.2.1 Preparation of Films and powder adducts

**[ $\text{Cs}_{0.1}\text{FA}_{0.9}\text{PbI}_3$  with Ammonium Chloride]** A mixed cation precursor solution with a 1.0M concentration was prepared by mixing 156 mg of Formamidinium Iodide (FAI, greatcell), 461 mg of Lead Iodide ( $\text{PbI}_2$ , TCI), 26 mg Cesium Iodide (CsI, TCI) and 5 mg, 10 mg, 15 mg, 20 mg and 25 mg

(10 mol%, 20mol%, 30 mol%, 40 mol% and 50 mol%, respectively) of Ammonium Chloride ( $\text{NH}_4\text{Cl}$ , Alfa aesar) in 900  $\mu\text{L}$  DMF and 100  $\mu\text{L}$  DMSO. The solutions were stirred for a minimum of 3-4h at 50 °C in a  $\text{N}_2$  glovebox. 45  $\mu\text{L}$  of this solution was placed on top of the substrates. A two-step spin-coating program was employed: first spinning at 1000 rpm for 10 s and then at 4000 rpm for 20 s. 100  $\mu\text{L}$  of chlorobenzene was dripped 15~20 s after the starting of the spinning routine. The films were then annealed at 155 °C for 15 min. These films and corresponding solar cells are noted AC-10, AC-20, AC-30, AC-40 and AC-50.

**[ $\text{Cs}_{0.1}\text{FA}_{0.9}\text{PbI}_3$  with Potassium Chloride]** A mixed cation precursor solution with a 1.0M concentration was prepared by mixing 156 mg of Formamidinium Iodide (FAI, greatcell), 461 mg of  $\text{PbI}_2$  (TCI), 26 mg Cesium Iodide (CsI, TCI) and 3.7 mg, 6.7 mg, 9.7 mg (5 mol%, 9mol%, 13 mol%, respectively) of Potassium Chloride (KCl, Alfa aesar) in 900  $\mu\text{L}$  DMF and 100  $\mu\text{L}$  DMSO. The solutions were stirred for a minimum of 3-4 h at 50 °C in a  $\text{N}_2$  glovebox. 45  $\mu\text{L}$  of this solution was placed on top of the substrates. A two-step spin-coating program was employed: first spinning at 1000 rpm for 10 s and then at 4000 rpm for 20 s. 100  $\mu\text{L}$  of chlorobenzene was dripped 15~20 s after the starting of the spinning routine. The films were then annealed at 155 °C for 20 min. These films and corresponding solar cells are noted KC-5, KC-9 and KC-13.

**[ $\text{Cs}_{0.1}\text{FA}_{0.9}\text{PbI}_3$  with Potassium Chloride and Ammonium Chloride]** A mixed cation precursor solution with a 1.0M concentration was prepared by mixing 156 mg of Formamidinium Iodide (FAI, greatcell), 461 mg of Lead Iodide ( $\text{PbI}_2$ , TCI), 26 mg Cesium Iodide (CsI, TCI), 10 mg and 15 mg (20 mol% and 30 mol%) of Ammonium Chloride ( $\text{NH}_4\text{Cl}$ , Alfa aesar) and 3.7 mg and 6.7 mg (5 mol% and 9 mol%) of Potassium Chloride (KCl, Alfa aesar) in 900  $\mu\text{L}$  DMF and 100  $\mu\text{L}$  DMSO. The solutions were stirred for a minimum of 7-8 h at 50 °C in a  $\text{N}_2$  glovebox. 45  $\mu\text{L}$  of this solution was placed on top of the substrates. A two-step spin-coating program was employed: first spinning at 1000 rpm for 10 s and then at 4000 rpm for 20 s. 100  $\mu\text{L}$  of chlorobenzene was dripped 15~20 s after the starting of the spinning routine. The films were then annealed at 155 °C for 20 min. These films and corresponding solar cells are noted KC-5/AC-20, KC-5/AC-30, KC-9/AC-20 and KC-9/AC-30.

The preparation of hole transporting material solution were conducted as detailed in **Chapter II, Section II.1.2.2**.

**Synthesis of adduct powders:** First, 0.5 mL of precursor solutions were prepared by using the recipe mentioned above. Second, 10 mL of diethyl ether was added to precipitate the corresponding adduct. The precipitates were collected and dried in N<sub>2</sub> filled Glovebox overnight.

#### **IV.2.2 Characterizations Method**

The layers characterizations by XRD, SEM, UV-vis absorbance, steady-state PL and TRPL are described in **Chapter II, Section II.1.2.3**. The EDX mapping images were measured with a Quantax system from Compact 30mm Bruker operated at 15 kV. The differential scanning calorimetry (DSC) curves was measured on precipitated sample adducts by a DSC 3 apparatus from STAR System, operated under N<sub>2</sub> atmosphere with a heating rate of 10 °C/min.

Glow-Discharge Optical Emission Spectrometry (GD-OES) analyses were performed using a HORIBA Jobin Yvon GD Profiler 2 equipment. This instrument was equipped with a RF-generator (at 13.56 MHz), a standard HORIBA Jobin Yvon glow discharge source with a cylindrical anode of 4 mm internal diameter and two optical spectrometers (a polychromator and a monochromator) for fast-optical detection. The Ar plasma was generated at an Ar pressure of 420 Pa and an applied power of 17 W. The precursor or perovskite layer or the solar cell was mounted on an O-ring at one side of the plasma chamber and used as a cathode.

The *J-V* curves, maximum power point tracking and *EQE* spectra of the devices were measured as described in **Chapter II, Section II.1.2.3**.

### **IV.3 Characterizations of perovskite Films**

#### **IV.3.1 SEM and AFM**

We have first focused our attention on ammonium chloride (NH<sub>4</sub>Cl) additive. We have supposed that this compound should present the advantage to mediate the layer growth, while being fully eliminated at the end of the synthesis, upon the annealing step performed at 155°C for 15 min. We prepared layers with NH<sub>4</sub>Cl additive in the precursor solution varying between 10 mol% to 50 mol% of the molar

content of  $\text{PbI}_2$  (noted AC-10 to AC-50 samples). They have been compared to pristine layers (noted w/o). **Figure A.IV.1 (Annex IV)** shows SEM top-view images of the films. The w/o one presented pinholes and many bright grains dispersed onto the surface corresponding to  $\text{PbI}_2$ . The perovskite grains were rather small with a mean size measured at  $\sim 400$  nm. Adding  $\text{NH}_4\text{Cl}$  at 10 mol% was beneficial since the pinholes were eliminated and the quantity of  $\text{PbI}_2$  was reduced (**Figure A.IV.1, Annex IV**). Increasing  $\text{NH}_4\text{Cl}$  up to 30 mol% led to a continuous enlargement of the perovskite grain size (**Figures A.IV.1c-e, Annex IV**). Then, the grain size decreased. Moreover, at 50 mol%, pinholes were present again (**Figure A.IV.1f, Annex IV**). **Figure A.IV.1g (Annex IV)** discloses the statistical grain size analysis done with the Image J software. The highest mean grain size was recorded for AC-30 at  $\sim 750$  nm mean value.

We have secondly prepared films with KCl varying in the precursor solution at 5 mol%, 9 mol% and 13 mol% of the molar  $\text{PbI}_2$  content (KC-5, KC-9 and KC-13 samples, respectively). Layers SEM top views are presented in **Figure A.IV.2 (Annex IV)**. KCl additive suppresses pinhole formation. It also favors the growth of large grains and eliminates  $\text{PbI}_2$  extra-phase.

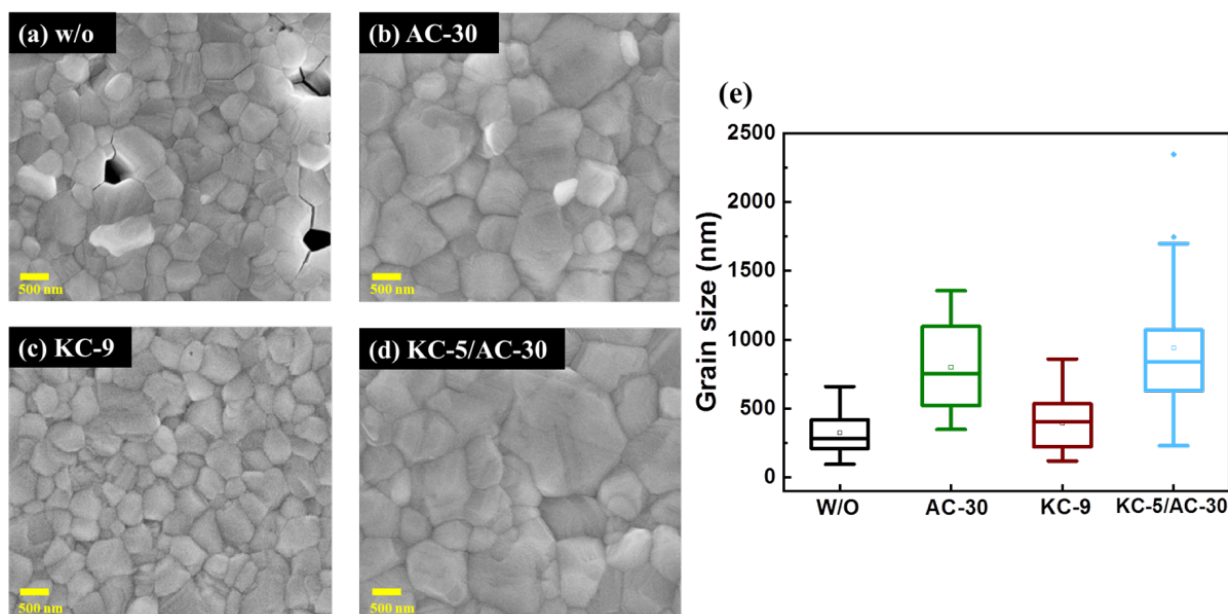


**Figure IV.1 (a-d) SEM top-view images of  $\text{Cs}_{0.1}\text{FA}_{0.9}\text{PbI}_3$  layers prepared with different optimized amounts of additive: (a) w/o, (b) AC-30, (c) KC-9, (d) KC-5/AC-30 (the scale bar is 500 nm). (e) Statistical grain size analysis.**

Our idea was then to mix the two chloride additives to achieve synergistic beneficial effects and to boost the performances and properties of the PSCs. Four different mixtures were notably investigated which kept the total amount of chloride ion between 25 mol% and 39 mol% of  $\text{PbI}_2$  molar amount in the precursor solution, namely: KC-5/AC-20, KC-5/AC-30, KC-9/AC-20 and KC-9/AC-30. To make a long story short, the best performances were achieved for KC-5/AC-30 (See **Figure A.IV.3** and **Table A.IV.1** in the **Annex IV**). In the following, we focus on the additives' effects understanding based on the comparisons between four kinds of layers and solar cells: w/o, AC-30, KC-9 and KC-5/AC-30. **Figures IV.1a-d** compares the morphology of the four samples. The mixed additive sample combines the beneficial effects of  $\text{NH}_4\text{Cl}$  and  $\text{KCl}$  additives. Indeed, the layers have no pinholes and they exhibit grains as large as in AC-30 films. This is confirmed by the statistical analysis shown in **Figure IV.1e**. Moreover, like KC-9 sample, there are almost no  $\text{PbI}_2$  bright grains on their surface. The films' surface was analyzed by atomic force microscopy (AFM) (**Figure A.IV.4, Annex IV**). The root-mean-square (RMS) roughness of the pristine sample was 51.1 nm. The additives smoothed the surfaces since the RMS roughness was 32.8 nm, 25.6 nm and 27.8 nm for AC-30, KC-9 and KC-5/AC-30 samples, respectively.

### **IV.3.2 XRD**

X-ray diffraction (XRD) was employed to check the phase and the purity of the produced compounds. The result of XRD patterns of samples with AC in **Figure A.IV.5 (Annex IV)**, show that all the films were texturised with the (001) plane parallel to the substrate. The perovskite diffraction peak intensity increased up to AC-30 and then diminished.  $\text{PbI}_2$  parasitic phase was present whatever the concentration of  $\text{NH}_4\text{Cl}$  employed. The relative intensity of the  $\text{PbI}_2$  diffraction peaks compared to the perovskite ones was only slightly reduced by the  $\text{NH}_4\text{Cl}$  additive. In summary,  $\text{KCl}$  additive favored the growth of large grains and eliminated  $\text{PbI}_2$  extra-phase, it was confirmed by XRD measurements (**Figure A.IV.6, Annex IV**). If this additive does not seem favorable to the crystallinity, the obtained compounds are perovskite phase pure due to a better solubilization of  $\text{PbI}_2$  in DMF/DMSO solvent mixture than with  $\text{NH}_4\text{Cl}$  for instance.

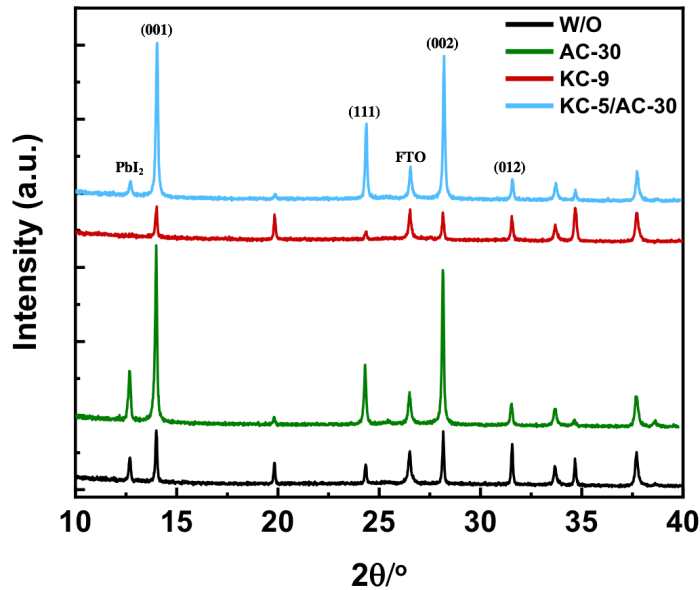


Figure IV.2 Effect of additives on the XRD patterns of the perovskite layers.

XRD results in **Figure IV.2** demonstrate both the high crystallinity of the KC-5/AC-30 sample, which is assigned to the effect of NH<sub>4</sub>Cl additive, and the lowered amount of PbI<sub>2</sub> which is due to KCl additive.

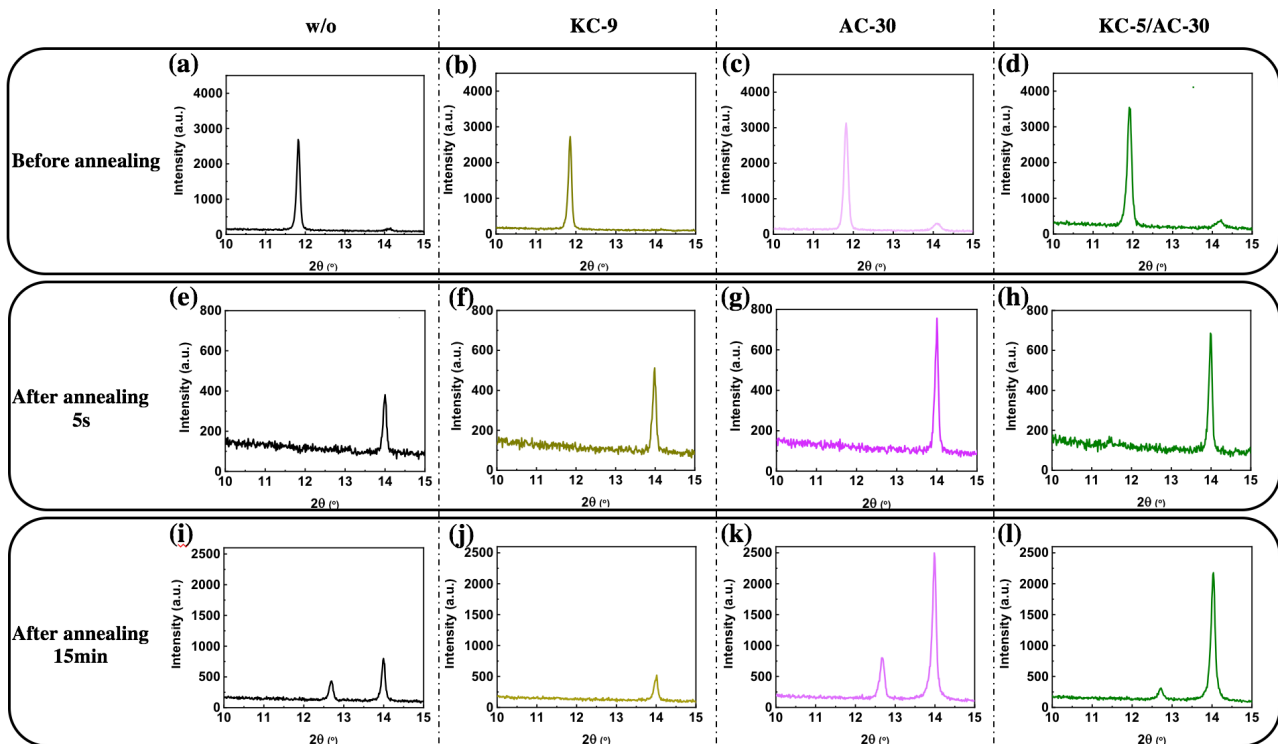


Figure IV.3 Effect of chloride additives on the XRD pattern of the films produced by spin-coating, before annealing (a-d), after 5 s of annealing (e-h) and after (i-l) full annealing.

Ammonium chloride additive, potassium chloride additive and their mixture control the perovskite film formation. To better understand the layer crystallization aspects, we compared the XRD patterns of the wet films obtained after spin-coating, after a 5 s annealing and those resulting from a full 15 min thermal annealing treatment. The former are displayed in **Figures IV.3a-d**. They all show a main diffraction peak at  $11.8^\circ$  assigned to  $\text{Cs}_{0.1}\text{FA}_{0.9}\text{PbI}_3$   $\delta$ -phase with hexagonal symmetry ((010) diffraction plane) ( $\text{P6}_3\text{mc}$  space group).[28] This phase was more intense when  $\text{NH}_4\text{Cl}$  additive was employed while  $\text{KCl}$  had no effect on the initial phase.  $\text{NH}_4\text{Cl}$  additive led also to the  $\text{Cs}_{0.1}\text{FA}_{0.9}\text{PbI}_3$   $\alpha$ -phase formation as shown by the presence of a peak at about  $14^\circ$  assigned to the (001) reflection. XRD shows that the phase change to the photoactive  $\alpha$ -phase occurred quickly, upon the first 5s of annealing at  $155^\circ\text{C}$  as highlighted in **Figures IV.3e-h**. We note that this peak was stronger when the  $\alpha$ -phase was present originally. It then favored a higher film crystallinity (**Figures IV.3i-l**).

### IV.3.3 DSC

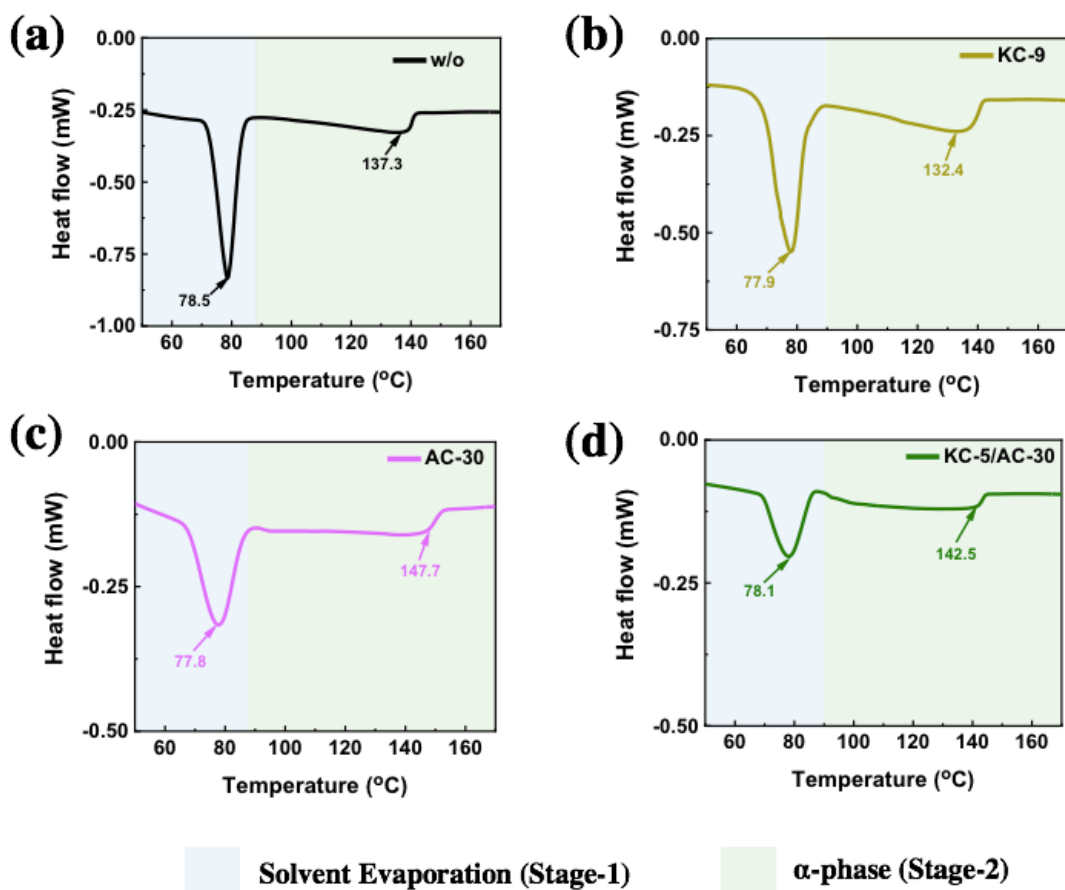
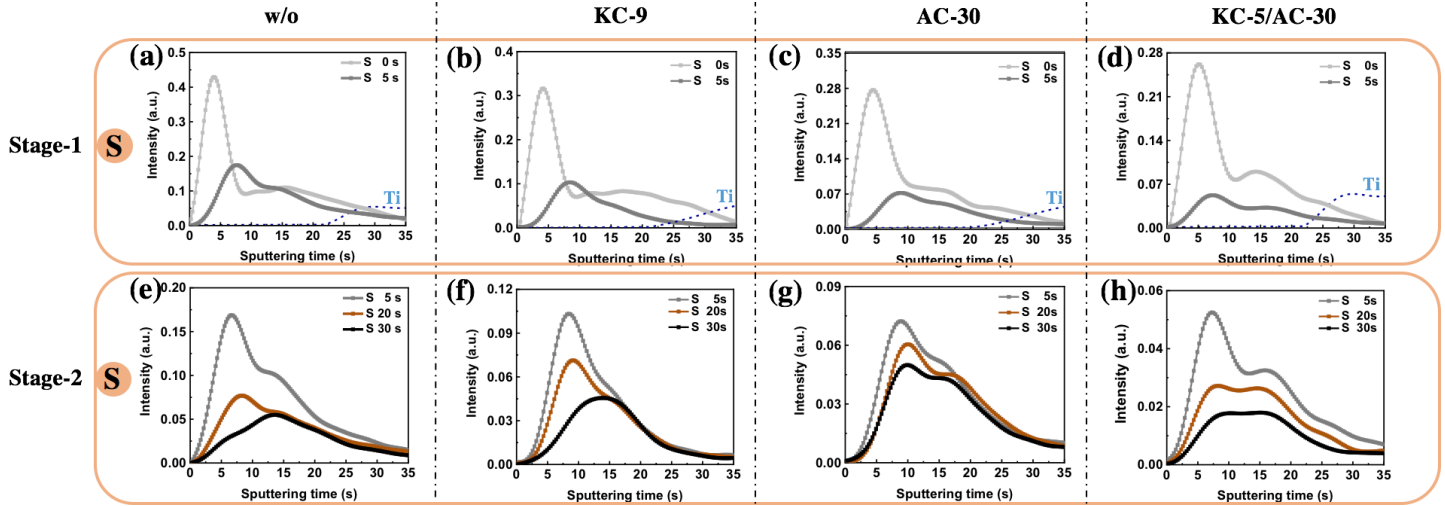


Figure IV.4 DSC curves of  $\text{Cs}_{0.1}\text{FA}_{0.9}\text{PbI}_3$  adducts prepared with various additives.

Differential Scanning Calorimetry (DSC) technique was employed to further understand the effect of Cs, ammonium and chloride ions on the formation of the crystallized perovskite. The curves were measured on the four samples prepared as powder adducts (**Figures IV.4a-d**), completed by a FAPbI<sub>3</sub> powder adduct (**Figure A.IV.7, Annex IV**). A first endothermic peak was observed at ~70°C-90°C, assigned to the evaporation of DMSO (DMF was mostly eliminated upon washing the adducts by diethyl ether)[29] since DMSO mixed with PbI<sub>2</sub> has been shown to start to evaporate at a temperature as low as 75°C.[30] First, a higher peak temperature was found for FAPbI<sub>3</sub> (82.7°C) compared to Cs<sub>0.1</sub>FA<sub>0.9</sub>PbI<sub>3</sub> (78.5°C). It suggests that the presence of CsI weakens the DMSO bonding. The evaporation temperature did not change significantly with the chloride additives (NH<sub>4</sub>Cl, KCl or both). For FAPbI<sub>3</sub> sample, an endothermic peak was observed at 101.5 °C which is attributed in the literature to the crystallization of the perovskite yellow  $\delta$ -phase.[30,31]. In the case of Cs<sub>0.1</sub>FA<sub>0.9</sub>PbI<sub>3</sub> samples, this peak was not visible. Above 100°C, an extended endothermic feature was found, assigned to the crystallization of the  $\alpha$ -phase perovskite compounds from the precursor. In the case of FAPbI<sub>3</sub>, it extended up to 162°C with a minimum at 153.5°C. This minimum can be roughly taken as the temperature at which the crystallization and growth steps end and allows a clear comparison between the samples. Adding CsI significantly reduced this temperature at 137.3 °C. Also, a low temperature was found for KCl additive (minimum at 132.4°C). Therefore, in both cases (w/o and KC-9), a fast crystallization and growth occur. On the other hand, NH<sub>4</sub>Cl delays and slows down the perovskite crystallization and crystal growth and it favors the formation of large grains. This effect of NH<sub>4</sub>Cl was also observed by *in-situ* microscopy in the case of MAPbI<sub>3</sub> perovskite by Dai et al..[32]

### IV.3.4 GD-OES



**Figure IV.5 (a-h) Evolution of GD-OES S profile in the perovskite precursor layer upon the first 30s annealing time. (The dashed line in (a-d) is the Ti profile corresponding to the *meso*-TiO<sub>2</sub>).**

The residual solvent elimination is an important aspect of the synthesis which occurs upon the film crystallization and growth. To our knowledge, the present work is the first to follow the depth profile of the solvent leaving by evaporation upon the annealing of a perovskite film using the Glow-Discharge Optical Emission Spectrometry (GD-OES) technique. The working principle of the of GD-OES technique is explained in detail in **Figure A.IV.8 (Annex IV)** and the following comment. Indeed, the solvent employed is a DMF-DMSO mixture and S element contained in DMSO can be tracked by this technique. The S element profile for the various films and various annealing times are presented in **Figures IV.5a-h**. By increasing the sputtering time, deeper part of the PVK layer is analyzed until reaching the *mp*-TiO<sub>2</sub> layer (dashed black line in **Figures IV.5a-d**). Before annealing, the DMSO profile was asymmetrical in every case and we observed that the outer part of the film was richer in solvent than the inner part. For the annealing, our results distinguish two stages. The first one occurs during the first 5 seconds of annealing on a hotplate, either with or without additive. The initial film changes from yellow translucent to brown. During this stage, the most superficial residual solvent evaporates and is almost fully eliminated at the uttermost surface while the Cs<sub>0.1</sub>FA<sub>0.9</sub>PbI<sub>3</sub> present in the wet layer is fully transformed to the  $\alpha$ -phase. We have noted that the w/o sample, is the only one for which the inner solvent is not partially eliminated but entrapped during this step. The next stage corresponds to 5s to 30s annealing times, when the film becomes dark brown. We observed a clear

effect of the additive on the solvent distribution upon annealing. In the case of the w/o sample, DMSO was eliminated fast near the surface while it remained in the deeper part of the layer. The same behavior was observed for the KC-9 sample. For these two films, the grains grow downward, from the top to the bottom. It favors the multiple and oblique grain boundaries and rather small perovskite grains.. In the presence of AC-30, the profiles are different. For AC-30, the S profile is more extended throughout the layer thickness. For the double additives, the solvent profile decreases uniformly throughout the layer thickness. In this case a bulk grain lateral growth occurs, and it results in more homogeneous films with big monolithic grains as shown by SEM cross-sectional views (**Figure IV.6**). After annealing for 2 min, the solvent in all kinds of perovskite was almost fully evaporated (**Figure A.IV.9, Annex IV**). A striking result of this study is that the additive mixture regulates the solvent elimination and then the growth of the film in its full depth. It boosts the quality of the film.

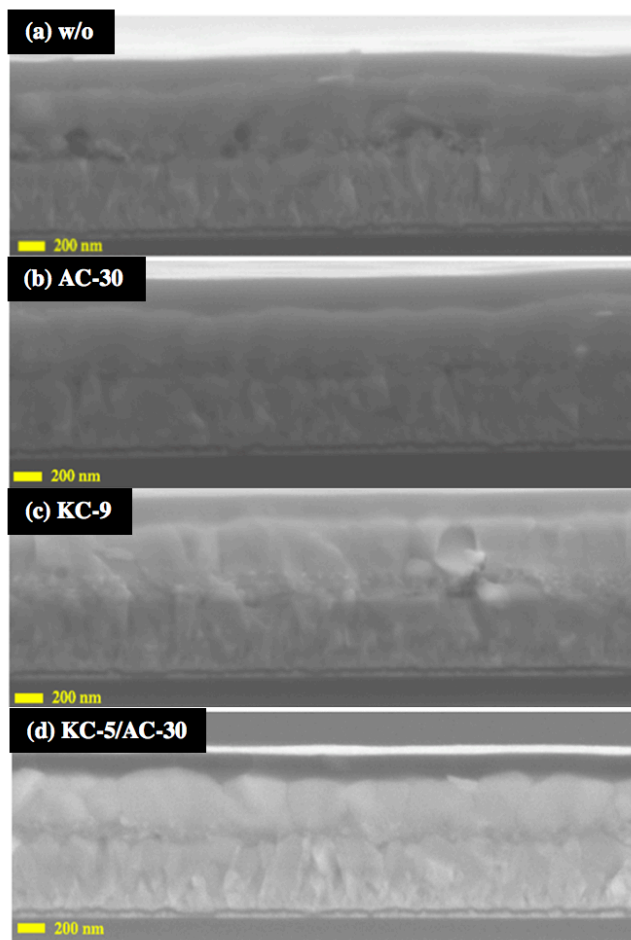


**Figure IV.6** SEM cross sectional views of (a) w/o, (b) AC-30, (c) KC-9 and (d) KC-5/AC-30  $\text{Cs}_{0.1}\text{FA}_{0.9}\text{PbI}_3$  layers deposited on glass/FTO/*c*-TiO<sub>2</sub>/*mp*-TiO<sub>2</sub> and topped with a spiroOMeTAD layer.

This study illustrates that grain growth is linked to the solvent elimination from the film. We deduce three different types of film growth as summarized in **Figure IV.7**. In **Type I**, encountered with the w/o sample, the solvent evaporation mainly occurs at the film surface. Film grows downward, multiple-boundaries perovskite grains are formed while the solvent in the inner part of the film remains entrapped and is at the origin of void formation and poor *mp*-TiO<sub>2</sub>/perovskite interface. In the **Type II**, encountered with the KC sample, the solvent is better-eliminated but the film still grows downward and the film is formed of multiple-boundaries grains. Double ammonium and potassium chloride additives (KC-5/AC-30 samples) leads to the **Type III** film formation. The solvent is homogeneously eliminated in the depth of the film which leads to the lateral growth of the grains and results in monolithic large grains with low defect density. The AC case is intermediate between **Type II** and **Type III**.

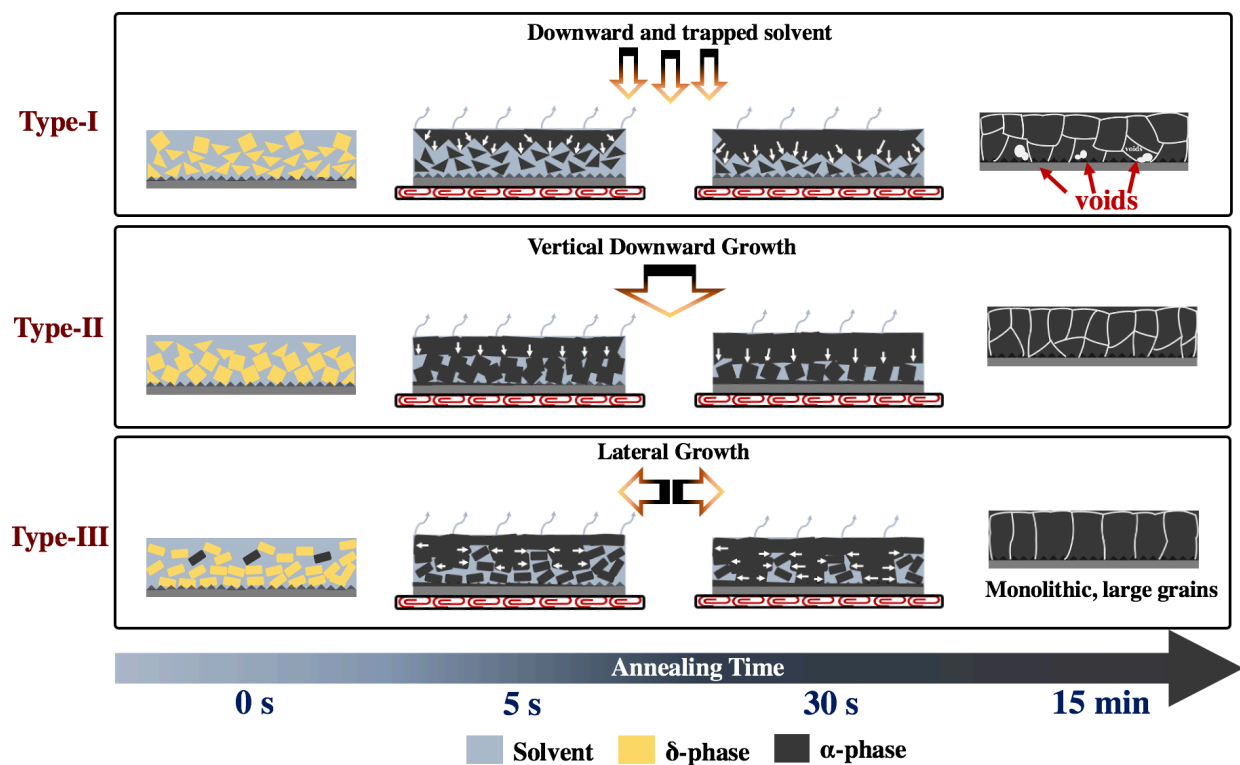


**Figure IV.7** Schematic of the different types of film formation process observed with and chloride additive(s): Grain growth direction and mechanism.

### IV.3.5 TRPL

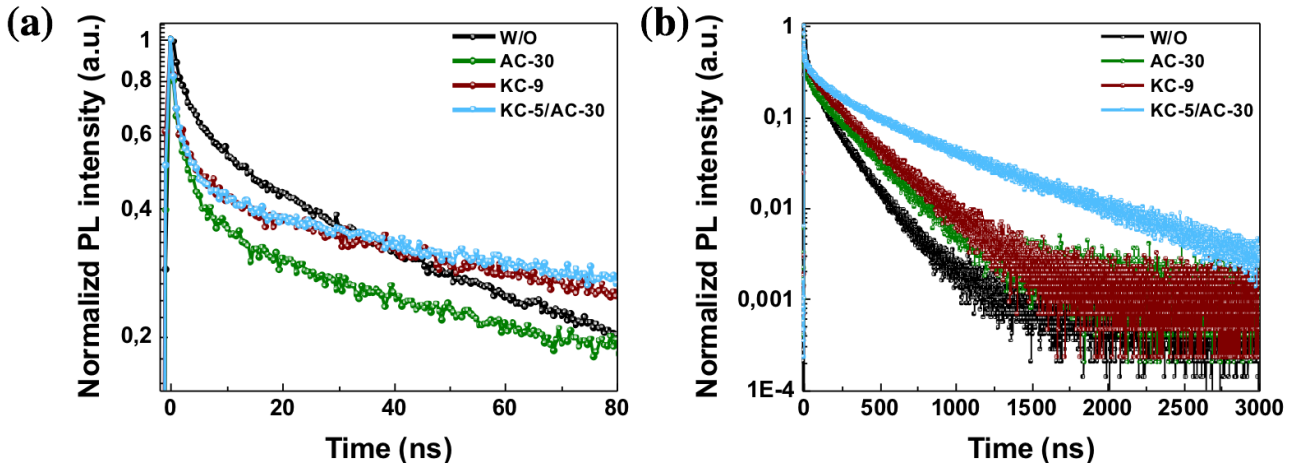


Figure IV.8 (a,b) TRPL curves of w/o, AC-30, KC-9 and KC-5/AC-30 samples.

The recorded time-resolved photoluminescence curves (TRPL) of the samples are disclosed in **Figure IV.8a** and **8b**. At short times, the PL signal decreases more rapidly for the samples grown with single or mixed chloride additives. We have quantified the decay times by modelling the decay by a tri-exponential function and the fit results are reported in **Table A.IV.2 (Annex IV)**. By fitting, the extracted emission short lifetimes ( $\tau_{fast}$ ) were measured at about 3 ns for the pristine sample and less than 1.9 ns for samples grown in the presence of chloride additives. The three latter samples exhibited a similar behavior. It suggests that, in the case of w/o sample, the electron injection is slower and more difficult. [24,33,34] The slow component,  $\tau_{slow}$ , reported in **Table A.IV.2 (Annex IV)**, is assigned to recombinations occurring in the bulk perovskite.[33,35,36] It was measured at 168 ns w/o additive and at 243 ns and 254 ns with  $\text{NH}_4\text{Cl}$  and  $\text{KCl}$  additive, respectively. It is conspicuous that both additives improve the structural quality of the methylammonium-free perovskite. By mixing  $\text{NH}_4\text{Cl}$  and  $\text{KCl}$  we achieved a remarkable 551 ns value. It demonstrates the bulk perovskite high quality that we could achieve. The KC-5/AC-30 perovskite film had a good structural quality and possessed larger numbers of carriers even after 1,500 ns, attributed to the strong suppression of non-radiative recombinations.

### IV.3.6 Absorbance

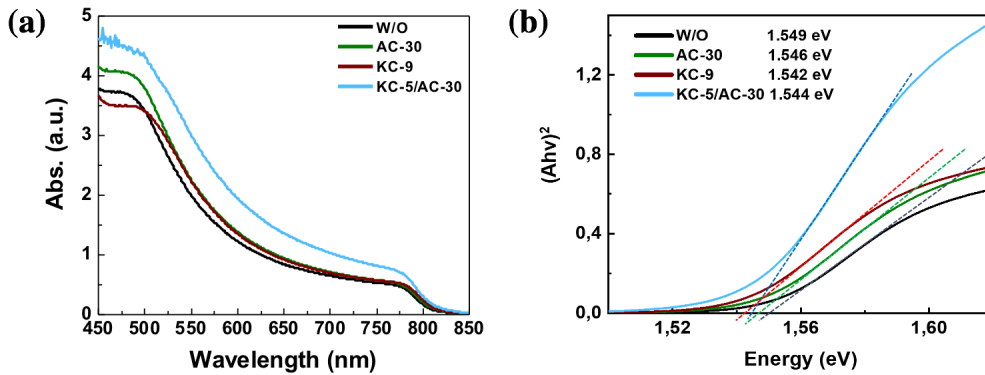


Figure IV.9 (a) Absorbance spectra and (b) corresponding Tauc plots.

Figure IV.9a compares the absorbance spectra of the optimized samples. The presence of a chloride additive increases light absorption between 500 nm and 800 nm. The mixed additive leads to a stronger absorbance which can be linked to a better control of the film growth that gives rise to thicker layers. The absorption band-edge was similar for the four samples. The Tauc plots of the absorbance spectra in Figure IV.9b provide an optical bandgap of the various PVKs measured at  $\sim 1.545$  eV, either with or without chloride additives. This value is closer to the optimum one for PV application than that of  $\text{MAPbI}_3$  or triple cation perovskites (See Chapter II).[33]

## IV.4 Characterizations of PSCs

### IV.4.1 $J$ - $V$ curves and EQE

Having improved and optimized the morphological, structural, and optical properties of the layers by employing  $\text{NH}_4\text{Cl}$  additive, KCl additive and their mixture, we now provide the characterization of the devices' performances. The device structure is presented Figure IV.10a. The  $J$ - $V$  curves of the best cells are disclosed in Figure IV.10b and the  $J$ - $V$  curves parameters are gathered in Table IV.1. The best efficiency without additive was only 16.13%. The open circuit voltage ( $V_{oc}$ ), short-circuit current density ( $J_{sc}$ ) and fill factor ( $FF$ ) parameters were low due notably to the defective morphology. These cells also exhibited a large hysteresis with a hysteresis index ( $HI$ ) measured at 28%. The statistical analysis confirmed these observations (Figure IV.10d). Adding an optimized amount of  $\text{NH}_4\text{Cl}$ , KCl or both led to a significant improvement of  $J_{sc}$ .

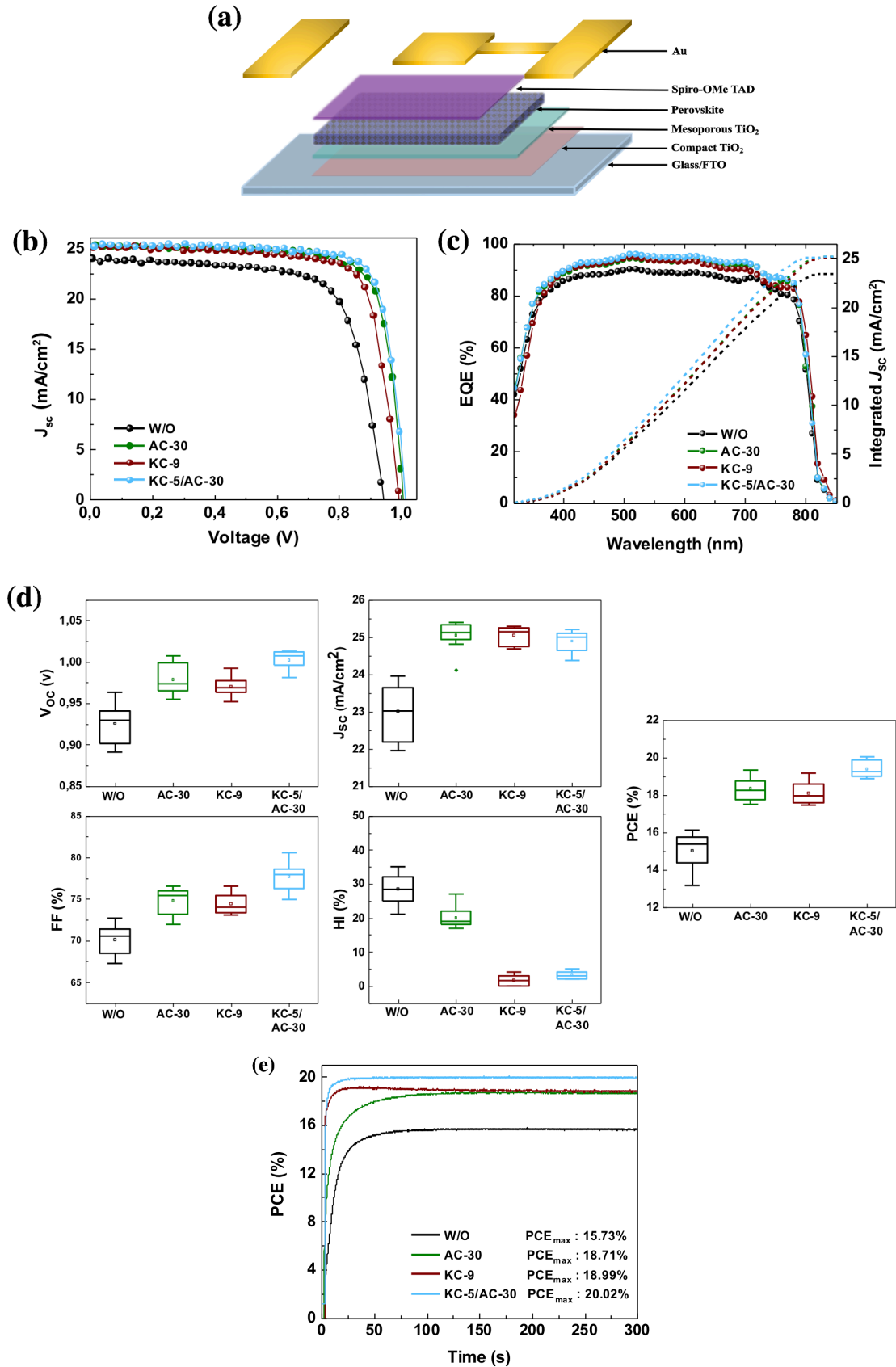


Figure IV.10 (a) Exploded schematic view of the PSC structure. Effect of chloride additives on the (b)  $J$ - $V$  curves, (c)  $EQE$  curves and integrated  $J_{sc}$  curves of the best PSCs ;(d) Statistical analysis of the optimized PSCs; (e) Tracking at the maximum power point of the best PSCs and stabilized PCEs.

**Figure IV.10c** shows the external quantum efficiency (*EQE*) spectra. It conspicuously shows the beneficial effect of chloride additive on the quantum efficiency over the whole visible spectrum. From the integration of these curves, we calculated  $J_{sc}$  of 23.42 mA/cm<sup>2</sup>, 25.13 mA/cm<sup>2</sup>, 25.08 mA/cm<sup>2</sup> and 25.11 mA/cm<sup>2</sup> for w/o, AC-30, KC-9 and KC-5/AC-30 cells, respectively. These values are in good agreement with those measured on *J-V* curves (**Table IV.1**). The other *J-V* curves parameters,  $V_{oc}$  and *FF*, were also ameliorated by additives. It is assigned to larger PVK grains in the case of NH<sub>4</sub>Cl and better structural quality and film absorbance for the two additives. A remarkable result is that adding KCl leads to almost hysteresis-free PSCs. The KC-5/AC-30 cells presented the best results with a power conversion efficiency (*PCE*) reaching a remarkable 20.05%. The latter cells combined the advantages of the two additives: NH<sub>4</sub>Cl reduces the recrystallization/crystallization growth speed upon annealing, leads to large grains, excellent layer crystallinity, while KCl increases the PbI<sub>2</sub> solubilization, suppress PbI<sub>2</sub> phase and is at the origin of the hysteresis suppression. These two additives contain chloride which stabilizes the structure before to be eliminated upon annealing.[48] These conclusions made for the best cells were confirmed by the statistical analysis disclosed in **Figure IV.10d**.

**Table IV.1 Best cells *J-V* curves parameters of Cs<sub>0.1</sub>FA<sub>0.9</sub>PbI<sub>3</sub> PSCs prepared without and with different optimized amounts of chloride additives.**

Name	Entry	$V_{oc}$ [V]	$J_{sc}$ [mA cm <sup>-2</sup> ]	FF	PCE [%]	HI <sup>a</sup> [%]
w/o	Reverse	0.941	23.82	71.92	16.13	28
	Forward	0.837	23.88	58.24	11.65	
AC-30	Reverse	1.004	25.32	76.08	19.34	18
	Forward	0.957	25.13	66.07	15.89	
KC-9	Reverse	0.992	25.24	76.54	19.16	1
	Forward	0.993	25.17	75.99	18.99	
KC-5/AC-30	Reverse	1.012	25.21	78.61	20.05	3
	Forward	1.013	24.94	76.73	19.39	

<sup>a</sup> HI=(PCE<sub>Rev</sub>-PCE<sub>For</sub>)\*100 /PCE<sub>Rev</sub>

The steady-state performances of the various cells were measured by tracking at the maximum power point (**Figure IV.10e**). The normalized curves (**Figure A.IV.10, Annex IV**) clearly indicate that w/o and AC-30 cells presented a slow time response compared to the two others. They reached their *PCE*

plateau after about 100s. The slow response of these cells is in line with their large  $HI$ . On the other hand, for devices prepared with KCl, the steady state was reached much more rapidly, that is after about 20s. It confirms the beneficial effect of  $K^+$  on the device time response. We found 15.73% and 18.71% stabilized PCEs for w/o and AC-30 cells, respectively, which must be compared to 16.13% and 19.34% PCEs measured on the reverse scan. In the presence of KCl, the discrepancy between these two values was minimum. Finally, we found a remarkable 20.02% stabilized  $PCE$  for the KC-5/AC-30 cell, very close to the 20.05% measured on the  $J-V$  curves reverse scan.

#### IV.4.2 GD-OES

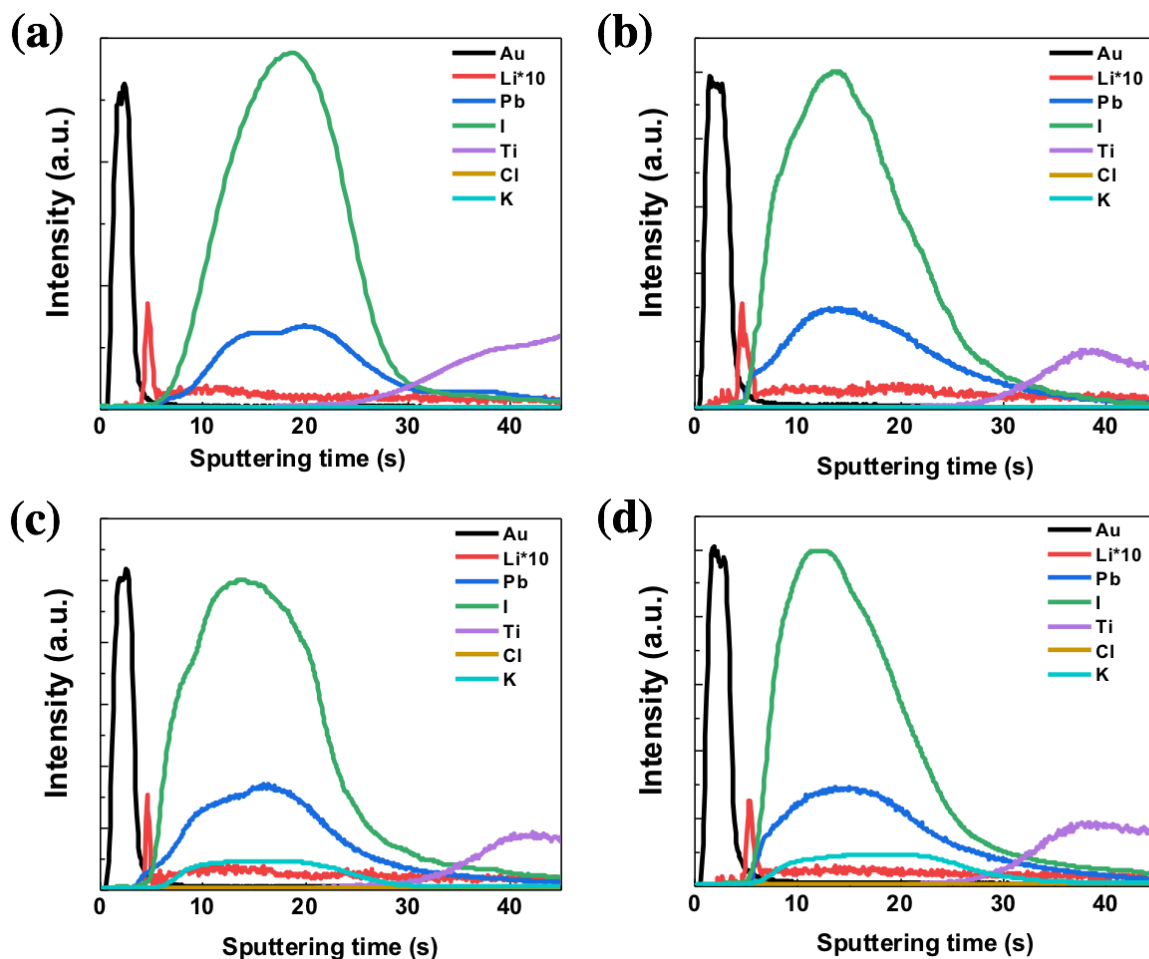


**Figure IV.11** Element distribution across the entire devices measured by GD-OES for non-polarized solar cells: (a) w/o cell, (b) AC-30 cell, (c) KC-9 cell and (d) KC-5/AC-30 cell.

To better understand the positive effect of  $K^+$ , present in the perovskite layers, on the PSC electrical response, we conducted GD-OES experiments on the full devices. Up to now, in the few papers where

this technique was employed, only  $\text{MAPbI}_{1-x}\text{Cl}_x$ -based half-cell [37] or full cells [38-40] were investigated. Our experiments consisted in directly Ar-sputtering the full devices and to detect the optical emission of the elements etched-released from the various layers. It allowed us to get a depth-profile distribution of the devices' constituent elements. In a first step we measured the compositional profile of the full cells and investigated the effect of  $\text{Cs}_{0.1}\text{FA}_{0.9}\text{PbI}_3$  growth conditions on these profiles. GD-OES allowed us to conspicuously distinguish the various layers composing the solar cells. We followed the main inorganic elements of the structure, namely Au, Li, Pb, I, Ti, Cl and K while our GD-OES system did not enable us to accurately follow N, O, C and H elements. In **Figure IV.11**, they appeared successively at increasing Ar sputtering time. One can note that the relative intensity of the various elements does not correspond directly to the relative concentrations due to the independent sputtering and emission yields for each element. First, Au of the back-electrode appeared. Then we observed a sharp Li peak corresponding to the dopant in the Spiro-OMeTAD organic hole transporting layer. This organic layer was etched rapidly. The signal of Li, present in small quantity, is multiplied by 10 in **Figure IV.11**. Then the perovskite layer appeared after 7s of sputtering time with the presence of both Pb and I. We remark that, for the AC-30, KC-9 and KC-5/AC-30 samples, the I and Pb signals extent over a longer time, with the presence of a tail. It can be explained by the fact that these films were thicker than the w/o one. After 28s-30s, Ti of  $\text{TiO}_2$  appeared (see also **Figures IV.5 a-d**). We have noted that no Cl could be detected in the perovskite layer (**Figure A.IV.11e, Annex IV**), confirming our EDX analysis (**Figures A.IV.11 a-d, Annex IV**). GD-OES is a highly sensitive technique, therefore, if Cl is present, its amount is less than 0.1 at.%. This element was also not detected by XPS technique (Collaboration with Dr Selina Olthof, Köln University, not shown). Most of it is eliminated upon annealing. On the other hand, we could clearly detect the presence of K in the KC-9 and KC-5/AC-30 samples (**Figures A.IV.11 a-d, Annex IV**). This element was homogeneously distributed over the entire perovskite layer thickness. No depletion on its top was observed, confirming that K was not, even partly, eliminated upon the annealing process.

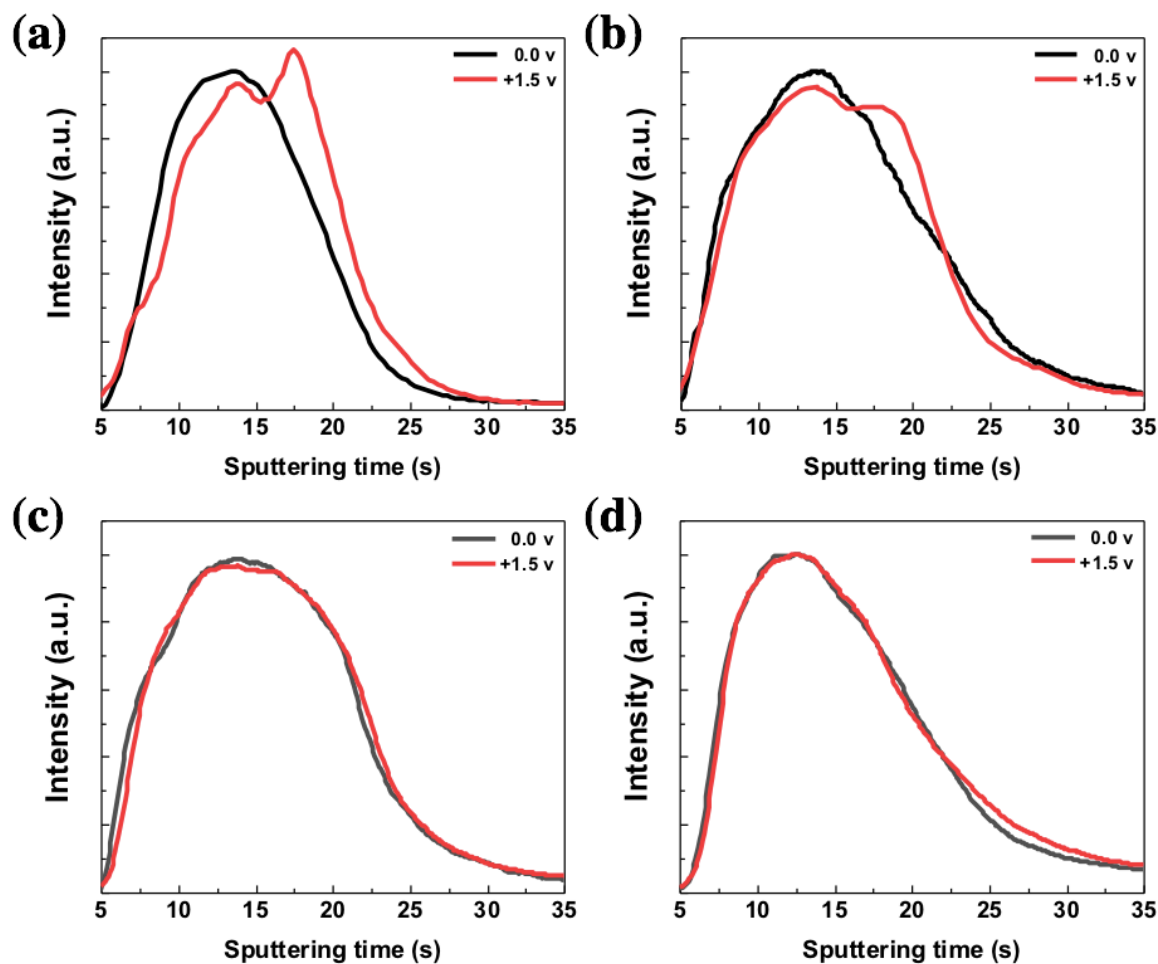


**Figure IV.12** GD-OES profile of iodine in the perovskite films after polarization at 0V (black traces) and after polarization at 1.5 V (red traces). (a) w/o, (b) AC-30, (c) KC-9 and (d) KC-5/AC-30.

Our objective was then to directly observe the effect of K doping on the mobility of iodide. To this end, we conducted GD-OES measurements on full devices after their polarization at a certain voltage. In **Figure IV.12**, we compare the I element profile for cells polarized at 0V and cells polarized at 1.5V for 30s. A profile change was clearly seen for the sample prepared without additive (**Figure IV.12a**). The initial peak (black trace) was split after applying an electric field (red trace). Two I element fractions could then be distinguished: a fixed one and a mobile one which moved toward the positively polarized  $\text{TiO}_2$  electrode. The technique visualizes that large iodide movement occurred in the layer [39]. In the case of the AC-30 cell (**Figure IV.12b**), the same phenomenon occurred but in a less extend.  $\text{NH}_4\text{Cl}$  samples were better crystallized than the w/o ones, they contained less defects. Therefore, the fraction of mobile species was reduced. On the other hand, for the two cells prepared

using KCl additive, namely KC-9 and KC-5/AC-30, the iodine profiles, measured without (black trace) and with (red trace) application of an electric field, overlapped. It shows that potassium has the remarkable property of blocking the ionic mobility. As ionic migration in halide perovskites is considered to occur through native point defects such as vacancies [41-43] and/or interstitials [43] we can conclude that K passivates these defects present in the structure. Stranks et al.,[44] who worked on the triple-cation (Cs,FA,MA)Pb(I<sub>0.85</sub>Br<sub>0.15</sub>)<sub>3</sub> perovskite prepared in the presence of KI, found passivating potassium halide layers formed at the layer interfaces and at the grain boundaries, these parts being the most defect-rich. Our characterizations have not allowed us to precisely localize the passivated defects' location, but it seems reasonable to say that the mobile I component must be more present at the grain periphery and grain boundaries. The K<sup>+</sup> action likely occurs through its ability to combine with mobile iodide. It is noteworthy that our GD-OES measurements perfectly correlate with the hysteresis phenomenon quantified on the *J-V* curves (**Figure IV.10d** and **Figure A.IV.12** in the **Annex IV**). For the w/o sample, with the largest hysteresis (HI~28%), the iodide displacement is large. For the AC-30 sample, with intermediate hysteresis (HI~18%), the displacement is present but not so important. Finally, for the KC-9 cell and KC-5/AC-30 cell, iodide is blocked while these cells are almost hysteresis-free (HI~1%-3%). It proves that hysteresis is due to the mobility of iodide in the layer. Blocking this mobility leads to hysteresis-free PSCs. We can note that this work is the first which correlates the iodide blocking, directly observed by GD-OES, and the absence of hysteresis.

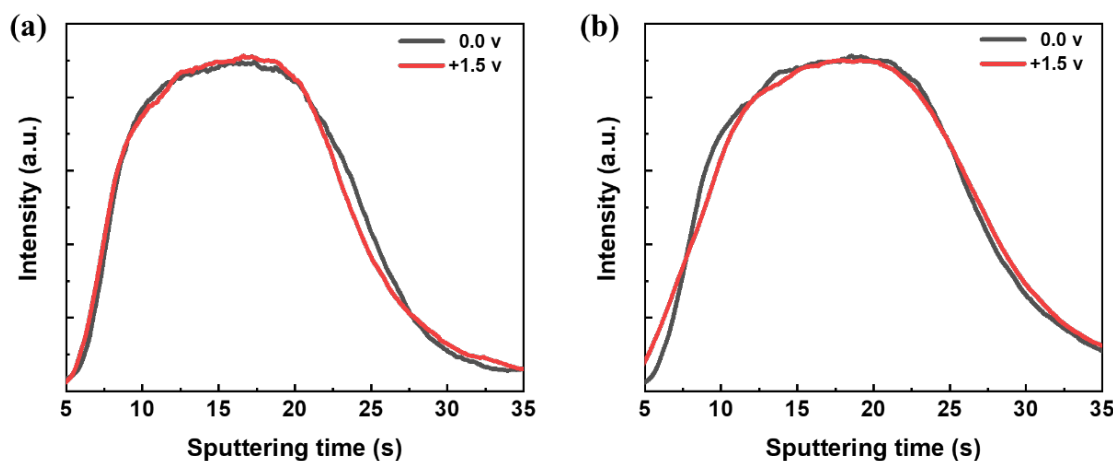


**Figure IV.13** GD-OES profile of K element in the perovskite films after polarization at 0V (black lines) and after polarization at 1.5 V (red lines). (a) KC-9 and (b) KC-5/AC-30 PSCs.

Figure IV.13 shows the K element profile without and with application of an electric field. This profile was unchanged for both KC-9 and KC-5/AC-30 cells. We can conclude that the passivation is perfectly stable, and that potassium is at the origin of a robust passivation of defects.

#### IV.4.3 Stability

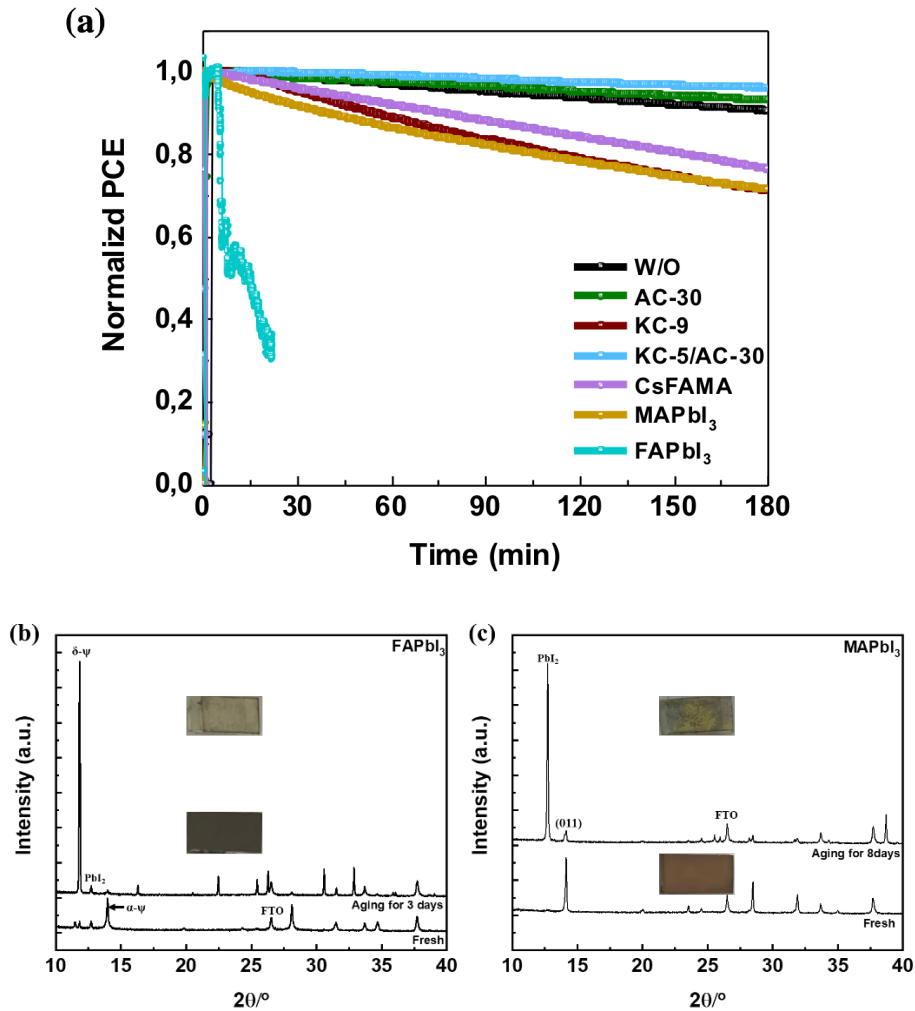
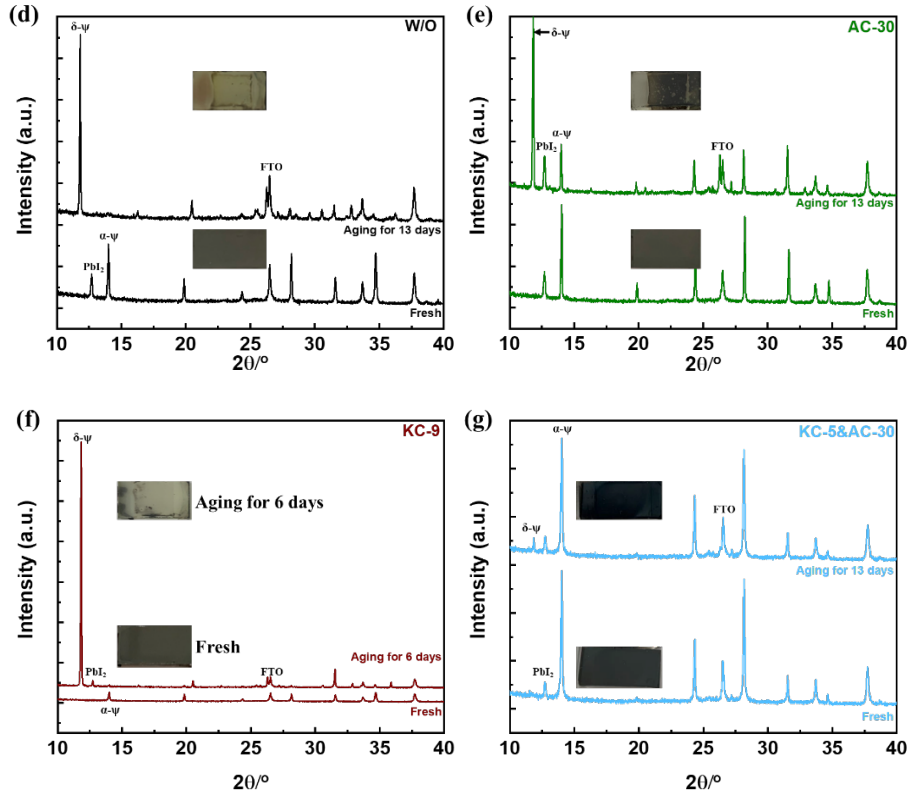


Figure IV.14 (a) Tracking of Cs<sub>0.1</sub>FA<sub>0.9</sub>PbI<sub>3</sub> cells prepared without and with NH<sub>4</sub>Cl and KCl additive, FAPbI<sub>3</sub>, MAPbI<sub>3</sub> and CsFAMA cells normalized power outputs under continuous one sun AM1.5 G illumination (unencapsulated devices, 45% RH). (b-g) XRD patterns of perovskite samples: fresh and after aging under ambient air conditions (T°=20-25°C, RH=50-60%) (b) FAPbI<sub>3</sub> (aged 3 days), (c) MAPbI<sub>3</sub> (aged 8 days), (d-g) Cs<sub>0.1</sub>FA<sub>0.9</sub>PbI<sub>3</sub>: (d) w/o (aged 13 days), (e) AC-30 (aged 13 days), (f) KC-9 (aged 6 days) and (g) KC-5/AC-30 (aged 13 days). Insets are pictures before and after aging.



**Figure IV.14** (a) Tracking of  $\text{Cs}_{0.1}\text{FA}_{0.9}\text{PbI}_3$  cells prepared without and with  $\text{NH}_4\text{Cl}$  and  $\text{KCl}$  additive,  $\text{FAPbI}_3$ ,  $\text{MAPbI}_3$  and  $\text{CsFAMA}$  cells normalized power outputs under continuous one sun AM1.5 G illumination (unencapsulated devices, 45% RH). (b-g) XRD patterns of perovskite samples: fresh and after aging under ambient air conditions ( $T^\circ=20\text{-}25^\circ\text{C}$ ,  $\text{RH}=50\text{-}60\%$ ) (b)  $\text{FAPbI}_3$  (aged 3 days), (c)  $\text{MAPbI}_3$  (aged 8 days), (d-g)  $\text{Cs}_{0.1}\text{FA}_{0.9}\text{PbI}_3$ : (d) w/o (aged 13 days), (e) AC-30 (aged 13 days), (f) KC-9 (aged 6 days) and (g) KC-5/AC-30 (aged 13 days). Insets are pictures before and after aging.

The future of the PSC technology will mainly depend on the ability in obtaining highly stable devices. Your interest in  $\text{Cs}_x\text{FA}_{1-x}\text{PbI}_3$  compounds was motivated by eliminating MA, this component being a source of instability. In **Figure IV.14**, the four unencapsulated and optimized  $\text{Cs}_{0.1}\text{FA}_{0.9}\text{PbI}_3$  cells have been continuously tracked under the solar simulator delivering 1 sun at ambient relative humidity (50-60%). Their evolutions are compared to other PSCs:  $\text{FAPbI}_3$  and two MA containing perovskites, namely  $\text{MAPbI}_3$  and  $\text{Cs}_{0.08}\text{FA}_{0.80}\text{MA}_{0.12}\text{Pb}(\text{I}_{0.88}\text{Br}_{0.12})_3$  (noted  $\text{CsFAMA}$ ) which have been studied in detail in Chapter II, Section II.1. We first confirm that  $\alpha\text{-FAPbI}_3$  is highly unstable since it is rapidly transformed into the photoinactive  $\delta\text{-FAPbI}_3$ . MAPI and KC-9 cells were poorly stable with a PCE loss of 29% after 180 min. It means that the passivation of native defect sites at the origin of the iodide mobility is insufficient to stabilize the halide perovskite material. The  $\text{CsFAMA}$  cell was also not very

stable. The stability of  $\text{Cs}_{0.1}\text{FA}_{0.9}\text{PbI}_3$  increased in the order: w/o, AC-30 and KC-5/AC-30. Mixing the two chloride additives is then a successful strategy to get high stability since the KC-5/AC-30 devices retained 97% of their initial PCE after 180 min.

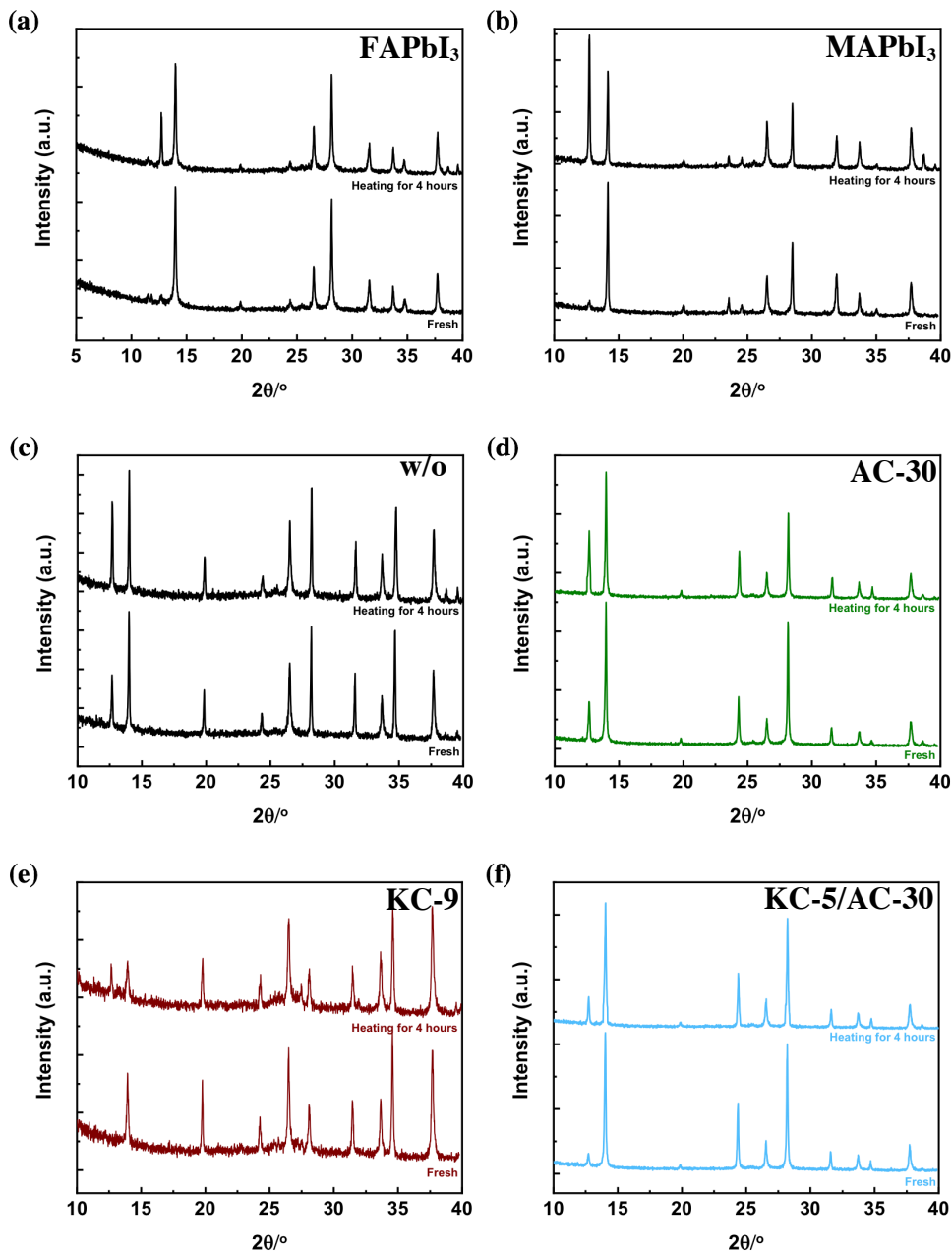


**Figure IV.15** XRD patterns of perovskite samples: fresh and after heating 4 hours at 130 °C in a  $\text{N}_2$ -filled glovebox. (a)  $\text{FAPbI}_3$ , (b)  $\text{MAPbI}_3$ , (c-f)  $\text{Cs}_{0.1}\text{FA}_{0.9}\text{PbI}_3$ : (c) w/o (d) AC-30, (e) KC-9 and (f) KC-5/AC-30.

We have also tested the resistance of the various perovskites to humidity and ambient degrading agents by following their XRD pattern and aspect after storage under the ambient atmosphere (**Figure IV.14**).

**Figure IV.14b** confirms that  $\alpha$ -FAPbI<sub>3</sub> is highly unstable. The (001) plane of the black  $\alpha$ -phase disappeared after only 3 days of aging. It was transformed into the more stable yellow  $\delta$ -phase which is photo-inactive. The change is conspicuously visualized by the sample color. MAPbI<sub>3</sub> is also poorly stable (**Figure IV.14c**). Its main (011) diffraction peak at 14.1° almost fully disappeared after 8 days of aging. It was replaced by a strong (001) PbI<sub>2</sub> peak at 12.7°. In this case the perovskite decomposes, MA is outgassed and a yellow PbI<sub>2</sub> layer is formed as shown in the inserted picture. **Figure IV.14d** shows that the w/o sample was fully degraded after 13 days of aging and was also poorly stable. The (001)  $\alpha$ -phase and (001) PbI<sub>2</sub> peaks at 14.0° and 12.7°, respectively, disappeared while a strong  $\delta$ -phase peak at 11.8° dominated the pattern. The sample color changed from dark-black to yellow. It shows that eliminating MA is not sufficient to stabilize the hybrid perovskite. In the case of the KC-9 sample (**Figure IV.14f**), PbI<sub>2</sub> was not present in the fresh sample. After only 6 days, the sample was fully degraded. The main degradation phase was the perovskite  $\delta$ -phase but some PbI<sub>2</sub> phase was also formed. Adding NH<sub>4</sub>Cl clearly stabilized the Cs<sub>0.1</sub>FA<sub>0.9</sub>PbI<sub>3</sub> sample (**Figure IV.14e**) since after 13 days the  $\alpha$ -phase is still present. However, the remarkable result is the synergistic effect of NH<sub>4</sub>Cl and KCl on the layer stability. Indeed, **Figure IV.14g** shows that after 13 days, the layers, non-protected by overlayers and encapsulation and then directly exposed to the degradation agents (moisture, UV, oxygen...) were still dark black. The small PbI<sub>2</sub> peak at 12.7° did not evolve and only a small perovskite  $\delta$ -phase peak was present. The thermal stability was tested by heating layers 4 hours at 130°C in N<sub>2</sub> atmosphere. **Figure IV.15** compares the XRD patterns of FAPbI<sub>3</sub>, MAPbI<sub>3</sub> and the four Cs<sub>0.1</sub>FA<sub>0.9</sub>PbI<sub>3</sub> samples, before and after the treatment. In all cases, a peak at 12.7° appears or grows due to the release of the organic components and formation of PbI<sub>2</sub>. The fastest degradation was found for MAPI which contains MA. For the other compounds, the perovskite phase remained the main one. We clearly observed that the KC-5/AC-30 sample was the less degraded of the series.

## IV.5 Conclusions

In summary, we have developed in this chapter a two chloride additives engineering approach for the preparation of MA-free and Br-free Cs<sub>0.1</sub>FA<sub>0.9</sub>PbI<sub>3</sub> perovskite films for PSC application. Introducing a mixture of NH<sub>4</sub>Cl and KCl additives into the PPS to assist the PVK formation has allowed us to get

films with outstanding properties. The former, employed at large mol %, led to a good film coverage, large grains, good crystallinity and reduced structural defects. The second has been shown to reduce the structural defects, reduce the  $\text{PbI}_2$  phase content and suppress the hysteresis due to the passivation of structural defects by  $\text{K}^+$ . By combining XRD, SEM, DSC and GD-OES techniques the effects of the additives on the film formation have been unveiled and three types have been distinguished. The initial yellow translucent layer formed by spin-coating contains  $\text{Cs}_{0.1}\text{FA}_{0.9}\text{PbI}_3$  in a  $\delta$ -phase,  $\alpha$ -phase combined with wetting coordinated solvent. During the first 5s of annealing time, the  $\delta$ -phase is transformed into the  $\alpha$ -phase and the surface solvent is eliminated. Then the profile of the solvent elimination has permitted us to understand the final properties of the layers. When the solvent in the deep is difficult to eliminate, the growth occurs downward, voids at the perovskite/ETL, small grains and a multiple-layer are formed (**Type I**). When the elimination speed decreases with the depth without entrapped solvent, the same morphology is obtained without voids (**Type II**). Using both  $\text{NH}_4\text{Cl}$  and  $\text{KCl}$  (and in a less extend only  $\text{NH}_4\text{Cl}$ ) allows to uniformly eliminate the solvent and then achieve a lateral growth of the perovskite grains. It results in large, monolithic and defect-poor grains with good coverage of the substrate (**Type III**). Finally, we prove that **Type III** films are highly resistant to electrical, light, moisture, and temperature external stressors.

Moreover, by using the GD-OES technique, we have shown that potassium, integrated homogeneously in the layer, passivates defects in the structure. By using this additive, hysteresis-free devices have been fabricated. Moreover, we have been able to demonstrate, by direct observation, that the hysteresis suppression is due to the ability of  $\text{K}^+$  to block iodide species migration in the PVK layer.  $\text{K}$  is insensitive to the electric field and robustly passivates native defect sites. However, blocking the ionic mobility is insufficient to fully stabilize the devices. The double chloride additive approach has permitted to prepare methylammonium-free, hysteresis-free PSCs with a stabilized PCE achieving 20.02%.

These systems will be further investigated in Chapter VI with the production of a perovskite capping layer. Beforehand, in Chapter V, we will investigate the adding of  $\text{Rb}^+$  as a supplementary monovalent cation.

## References

- [1] Turren-Cruz, S. H.; Hagfeldt, A.; Saliba, M. Methylammonium-free, high-performance, and stable perovskite solar cells on a planar architecture. *Science* **2018**, *362*, 449-453.
- [2] Park, Y. H.; Jeong, I.; Bae, S.; Son, H. J.; Lee, P.; Lee, J.; Lee, C. H.; Ko, M. J. Inorganic Rubidium Cation as an Enhancer for Photovoltaic Performance and Moisture Stability of HC(NH<sub>2</sub>)<sub>2</sub>PbI<sub>3</sub> Perovskite Solar Cells. *Adv. Funct. Mater.* **2017**, *27*, 1605988.
- [3] Li, S. D.; Liu, Z.; Qiao, Z.; Wang, X.; Cheng, L.; Zhai, Y. F.; Xu, Q. F.; Li, Z. M.; Meng, K.; Chen, G. Interfacial Structure and Composition Managements for High-Performance Methylammonium-Free Perovskite Solar Cells. *Adv. Funct. Mater.* **2020**, 2005846.
- [4] Germino, J. C.; Szostak, R.; Motti, S. G.; Moral, R. F.; Marchezi, P. E.; Seleghini, H. S.; Bonato, L. G.; de Araujo, F. L.; Atvars, T. D. Z.; Herz, L. M.; Fenning, D.; Hagfeldt, Nogueira, A. F. Postpassivation of multication perovskite with rubidium butyrate. *ACS Photonics* **2020**, *7*, 2282-2291.
- [5] Schulze, P.C.S; Bett, A.J.; Bivour, M.; Caprioglio, P.; Gerspacher, F.M.; Kabaklı, O.; Richter, A.; R., Zhang, Q.; Hermle, M.; Hillebrecht, H.; Stefan, Glunz, S.W.; Goldschmidt, J.C. 25.1% High-Efficiency Monolithic Perovskite Silicon Tandem Solar Cell with a High Bandgap Perovskite Absorber. *Sol. RRL* **2020**, *4*, 2000152
- [6] Kelly, S.; Pabitra, K.; Nayak, Alexandra, Ramadan, J.; Wenger, B.; Lin, Y.; Snaith, H. Overcoming Zinc Oxide Interface Instability with a Methylammonium-Free Perovskite for High-Performance Solar Cells. *Adv. Funct. Mater.* **2019**, *29*, 1900466
- [7] Yang, J.; Chen, Y.; Tang, W.; Wang, S.; Ma, Q.; Wu, Y.; Yuan, N.; Ding, J.; Zhang W.H. Crystallization tailoring of cesium/formamidinium double-cation perovskite for efficient and highly stable solar cells. *J. Energy Chem.* **2020**, *48*, 217-225.
- [8] Zhang, S.; Wu, S.; Chen, R.; Chen, W.; Huang, Y.; Yang, Z.; Chen, W. Formamide-assisted fast crystallization to fabricate formamidinium-based perovskite films for high-efficiency and stable solar cells. *J. Mater. Chem. C* **2020**, *8*, 1642-1648.
- [9] Lee, J. W.; Kim, D. H.; Kim, H. S.; Seo, S. W.; Cho, S. M.; Park, N. G. Formamidinium and Cesium Hybridization for Photo- and Moisture-Stable Perovskite Solar Cell. *Adv. Energy Mater.* **2015**, *5*, 1501310.
- [10] Li, Z.; Liu, N.; Liu, Z.; Wang, X.; Hu, Y.; Xu, Q. F.; Li, S. D.; Qiao, Z.; Cheng, L.; Wang, C. W.; Meng, K.; Chen, G. A Cross-Linked PCBM Interlayer for Efficient and UV-Stable Methylammonium-Free Perovskite Solar Cells. *Energy Tech.* **2020**, *8*, 2000224.
- [11] Zhao, X.; Yao, C.; Gu, K.; Liu, T.; Xia, Y.; Loo, Y.L. A hole-transport material that also passivates perovskite surface defects for solar cells with improved efficiency and stability. *Energy Environ. Sci.* **2020**, *13*, 4334-4343.
- [12] Li, N.; Luo, Y.; Chen, Z.; Niu, X.; Zhang, X.; Lu, J.; Kumar, Jiang, R. J.; Liu, H.; Guo, X.; Lai, B.; Brocks, G.; Chen, Q.; Tao, S.; Fenning, D.P.; Zhou, H. Microscopic Degradation in Formamidinium-Cesium Lead Iodide Perovskite Solar Cells under Operational Stressors. *Joule* **2020**, *4*, 1743-1758.
- [13] M. Abdelsamie; J. Xu; K. Bruening; C. J. Tassone; H.-G. Steinrück; M.F. Toney. Impact of Processing on Structural and Compositional Evolution in Mixed Metal Halide Perovskites during Film Formation. *Adv. Funct. Mater.* **2020**, 2001752
- [14] Chen, S.; Xiao, X.; Chen, B.; Kelly, L.L.; Zhao, J.; Lin, Y.; Toney, M.F.; Huang, J.; Crystallization in one-step solution deposition of perovskite films: Upward or downward? *Sci. Adv.* **2021**, *7*, eabb2412.
- [15] Son, D.-Y.; Kim, S.-G.; Seo, J.-Y.; Lee, S.-H.; Shin, H.; Lee, D.; Park, N.-G. Universal Approach toward Hysteresis-Free Perovskite Solar Cell via Defect Engineering. *J. Am. Chem. Soc.* **2018**, *140*, 1358.

- [16] Gao, L. L.; Spanopoulos, I.; Ke, W. J.; Huang, S.; Hadar, I.; Chen, L.; Li, X. L.; Yang, G. J.; Kanatzidis, M. G. Improved Environmental Stability and Solar Cell Efficiency of (MA,FA)PbI<sub>3</sub> Perovskite Using a Wide-Band-Gap 1D Thiazolium Lead Iodide Capping Layer Strategy. *ACS Energy Lett.* **2019**, *4*, 1763.
- [17] Chen, P.; Bai, Y.; Wang, S.C.; Lyu, M.Q.; Yun, J.H.; Wang L.Z. In Situ Growth of 2D Perovskite Capping Layer for Stable and Efficient Perovskite Solar Cells. *Adv. Funct. Mater.* **2018**, *28*, 1706923
- [18] Ming, W.M.; Chen, S.Y.; Du, M.H. Chemical instability leads to unusual chemical-potential-independent defect formation and diffusion in perovskite solar cell material CH<sub>3</sub>NH<sub>3</sub>PbI<sub>3</sub>. *J. Mater. Chem. A* **2016**, *4*, 16975-16981.
- [19] Lv, Y.; Ma, H.; Yin, Y.; Dong, Q.; Zhao, W.; Jin, S.; Shi, Y. [NH<sub>3</sub>(CH<sub>2</sub>)<sub>6</sub>NH<sub>3</sub>]PbI<sub>4</sub> as Dion–Jacobson phase bifunctional capping layer for 2D/3D perovskite solar cells with high efficiency and excellent UV stability. *J. Mater. Chem. A* **2020**, *8*, 10283.
- [20] Lin, Y.; Bai, Y.; Fang, Y.; Chen, Z.; Yang, S.; Zheng, X.; Tang, S.; Liu, Y.; J.; Zhao, Huang, J. Enhanced Thermal Stability in Perovskite Solar Cells by Assembling 2D/3D Stacking Structures. *J. Phys. Chem. Lett.* **2018**, *9*, 654.
- [21] Yoo, J.J.; Wieghold, S.; Sponseller, M.C.; Chua, M.R.; Bertram, S.N.; Hartono, N.T.P.; Tresback, J. S.; Hansen, E.C.; Correa-Baena, J.P.; Bulovic, V.; Buonassisi, T.; Shin, S.S.; Bawendi, M.G. An interface stabilized perovskite solar cell with high stabilized efficiency and low voltage loss. *Energy Environ. Sci.* **2019**, *12*, 2192.
- [22] Li, S.; Liu, Z.; Qiao, Z.; Wang, X.; Cheng, L.; Zhai, Y.; Xu, Q.; Li, Z.; Meng, K.; Chen, G. Interfacial Structure and Composition Managements for High-Performance Methylammonium-Free Perovskite Solar Cells. *Adv. Funct. Mater.* **2020**, *30*, 2005846.
- [23] Wei, N.; Chen, Y.; Miao, Y.; Zhang, T.; Wang, X.; Wei, H.; Zhao, Y. 5-Ammonium Valeric Acid Iodide to Stabilize MAPbI<sub>3</sub> via a Mixed-Cation Perovskite with Reduced Dimension. *J. Phys. Chem. Lett.* **2020**, *11*, 8170-8176.
- [24] Zhu, T.; Zheng, D.; Liu, J.; Coolen, L.; Pauporté, Th. PEAI-Based Interfacial Layer for High-Efficiency and Stable Solar Cells Based on a MACl-Mediated Grown FA<sub>0.94</sub>MA<sub>0.06</sub>PbI<sub>3</sub> Perovskite. *ACS Appl. Mater. Interfaces* **2020**, *12*, 37197–37207
- [25] Cho, K.T.; Grancini, G.; Lee, Y.; Oveisi, E.; Ryu, J.; Almora, O.; Tschumi, M.; Schouwink P.A.; Seo G.; Heo, S.; Park, J.; Jang, J.; Paek, S.; Garcia-Belmonte, G.; Nazeeruddin, M.K. Selective growth of layered perovskites for stable and efficient photovoltaics. *Energy Environ. Sci.* **2018**, *11*, 952.
- [26] Zhu, T.; Zheng D.; Rager, M.-N.; Pauporté, Th. Actual Organic Cations Composition Determination in Perovskite Thin Films. Application to Formamidinium Lead Iodide Stabilization for High Efficiency Solar Cell. *Sol. RRL* **2020**, *4*, 2000348.
- [27] Zhu, T., Su, J., Labat, F., Ciofini, I., and Pauporté, Th. (2020). Interfacial Engineering through Chloride-Functionalized Self-Assembled Monolayer for High Efficiency Perovskite Solar Cells. *ACS Appl. Mater. Interfaces* *12*, 744-752.
- [28] Han, Q.; Bae, S.; Sun, P.; Hsieh, Y.; Yang, Y.; Rim, Y.; Zhao, H.; Chen, Q.; Shi, W.; Li, G.; Yang, Y. Single Crystal Formamidinium Lead Iodide (FAPbI<sub>3</sub>): Insight into the Structural, Optical, and Electrical Properties. *Adv. Mater.* **2016**, *28*, 2253–2258
- [29] Grancini, G.; Roldán-Carmona; Zimmermann, C. I.; Mosconi, E.; Lee, X.; Martineau, D.; Nabey, S.; Oswald, F.; De Angelis, F.; Graetzel, M.; Nazeeruddin, M. K. One-Year stable perovskite solar cells by 2D/3D interface engineering. *Nature Commun.* **2017**, *8*, 15684;

- [30] Yang, W.S.; Noh, J.H.; Jeon, N.J.; Kim, Y.C.; Ryu, J.; Seo, S.; Seok, S.I. High-performance photovoltaic perovskite layers fabricated through intramolecular exchange. *Science* **2015**, *348*, 1234.
- [31] Lee, J.-W.; Seol, D.-J.; Cho, A.-N.; Park, N.-G. High-efficiency perovskite solar cells based on the black polymorph of  $\text{HC}(\text{NH}_2)_2\text{PbI}_3$ . *Adv. Mater.* **2014**, *26*, 4991-4998.
- [32] Dai, X.; Deng, Y.; Van Brackle C.H.; Chen, S.; Peter, N.; Rudd, X.; Xiao, Y.; Chen, B.; Huang, J. Scalable Fabrication of Efficient Perovskite Solar Modules on Flexible Glass Substrates. *Adv. Energy Mater.* **2020**, *10*, 1903108.
- [33] Zheng, D., Zhu, T., and Pauporté, Th. (2020). Using Monovalent- to Trivalent-Cation Hybrid Perovskites for Producing High-Efficiency Solar Cells: Electrical Response, Impedance, and Stability. *ACS Appl. Energy Mater.*
- [34] Yoo, H.-S, and Park, N.G. (2018). Post-Treatment of Perovskite Film with Phenylalkylammonium Iodide for Hysteresis-Less Perovskite Solar Cells. *Sol. Energy Mater. Sol. Cells* *179*, 57–65
- [35] Lee, J.W., Dai, Z., Han, T.H., Choi, C., Chang, S.Y., Lee, S.J., De Marco, N., Zhao, H., Sun, P., Huang, Y., and Yang, Y. (2018). 2D Perovskite Stabilized Phase-Pure Formamidinium Perovskite Solar Cells. *Nat. Commun.* *9*, 3021.
- [36] Zhu, H., Liu, Y., Eickemeyer, F.T., Pan, L., Ren, D., Ruiz, M., Brian Carlsen, B., Yang, B., Wang, S., Wang, Z., Liu, H., Zakeeruddin, S.M., Hagfeldt, A., Ibrahim Dar, M., Li, X., and Grätzel, M. (2020). Tailored Amphiphilic Molecular Mitigators for Stable Perovskite Solar Cells with 23.5% Efficiency. *Adv. Mater.* *32*, 1907757.
- [37] M. Kim, G. H. Kim, T. K. Lee, I. W. Choi, H. W. Choi, Y. Jo, Y. J. Yoon, J. W. Kim, J. Lee, D. Huh, S. K. Kwak, J. Y. Kim, D. S. Kim, *Joule* *2019*, *3*, 2179-2192.
- [38] Z. Ahmad, M. A. Najeeb, R. A. Shakoor, A. Alashraf, Al-Muhtaseb, S. A. Ahmed Soliman, M. K. Nazeeruddin, *Sci. Rep.* *2017*, *7*, 15406.
- [39] H. Lee, S. Gaiaschi, P. Chapon, A. Marronnier, H. Lee, J. C. Vanel, D. Tondelier, J.-E. Bourée, Y. Bonnassieux, B. Geffroy, *ACS Energy Lett.* *2017*, *2*, 943–949.
- [40] H. Lee, S. Gaiaschi, P. Chapon, D. Tondelier, J.-E. Bourée, Y. Bonnassieux, V. Derycke, B. Geffroy, *J. Phys. Chem. C* *2019*, *123*, 17728–17734.
- [41] H. Yu, H. Lu, F. Xie, S. Zhou, N. Zhao, *Adv. Functional Mater.* *2016*, *26*, 1411-1419.
- [42] C. Eames, J. M. Frost, P. R. F. Barnes, B. C. O'Regan, A. Walsh, M. S. Islam, *Nature Commun.* *2015*, *6*, 7497.
- [43] J. M. Azpiroz, E. Mosconi, J. Bisquert, F. De Angelis, *Energy Environ. Sci.* *2015*, *8*, 2118-2127.
- [44] M. Abdi-Jalebi, Z. Andaji-Garmaroudi, S. Cacovich, C. Stavrakas, B. Philippe, J. M. Richter, M. Alsari, E. P. Booker, E. M. Hutter, Pearson, A. J. Lilliu, T. J. Savenije, H. G. Rensmo, Divitini, C. Ducati, R. H. Friend, S. D. Stranks, *Nature* *2018*, *555*, 497-501.

## Chapter V. From Mono- to Tri-Alkali Metal Cations: The Mechanism of how Ammonium Chloride effect on Film Formation Process of MA-Free Halide Perovskite

### V.1 Introduction

As we all know, the composition of perovskite greatly affects the overall performance of perovskite solar cells. Different components can bring different properties, such as optical properties or structural stability. In this chapter, we design the  $ABX_3$  formula based on FA as the majority cation, due to the fact that the band gap of  $\alpha$ -FAPbI<sub>3</sub> phase (1.48 eV) is close the Shockley-Queisser limit (1.34 eV), which is the key to design the perfect PV materials. However, the extremely unstable of  $\alpha$ -FAPbI<sub>3</sub> phase made us incorporate other cation, such as MA<sup>+</sup>, Cs<sup>+</sup>, Rb<sup>+</sup> and K<sup>+</sup>, to alleviate the problem of phase instability. To achieve better performance of PSC, more and more complex perovskite materials which combined multiple cations, such as double-cation (MA-FA,[1-2] Cs-FA,[3-4] Rb-FA[5]), triple-cation (Cs-MA-FA,[6] Rb-MA-FA, [7]K-Cs-FA[8]), and quadruple-cation (Rb-Cs-MA-FA[9]) have been designed. Although MA-based perovskite solar cell can achieve very high PCE,[10-12] the presence of MA can favor the degradation since MA is a small molecular that is easy released and decomposed under heating and humid atmosphere. Lots of works have been dedicated to the enhancement of the stability of the black  $\alpha$ -FAPbI<sub>3</sub> phase, notably it its entropic stabilization by the incorporation of Cs as shown in **Chapter IV**. [6-7] Likewise, the structural engineering by introducing elemental monovalent cations into organic-inorganic halide perovskite can shed light on the long term stability of PSCs. Thereby introducing another alkali metal, Rb (same column as Cs and K), into FAPbI<sub>3</sub> perovskite led to enhanced photovoltaic performances and superior moisture stability.[5] Moreover, by using potassium halide layer to passivate the surface and grain boundaries, the nonradiative loss and photoinduced ion migration in perovskite film and interface are significantly reduced as shown in Chapter IV.[13] All these considerations led us to develop multi-metal cation KRbCsFAPbI<sub>3</sub> perovskite.

In **Chapter IV**, we proved that using ammonium chloride as additive effectively improves the efficiency of solar cells with CsFAPbI<sub>3</sub> as working layer. Although the mechanism of ammonium

chloride has been mentioned in Chapter IV. In this chapter, we explore in-depth how ammonium chloride works in each process of one-step preparation of perovskite. As far as we know, there is only a few works which tentatively explain the mechanism of action of ammonium chloride. Among them, Chen and co-workers [14] added ammonium chloride as an additive to MAPbI<sub>3</sub> by using a surface-activation chemical vapor deposition process (SA-CVD) and provided the corresponding mechanism in their paper. Another work by Qi and co-worker [15] used a two-step process to prepare Cs<sub>0.05</sub>FA<sub>0.54</sub>MA<sub>0.41</sub>Pb(I<sub>0.98</sub>Br<sub>0.02</sub>)<sub>3</sub> layers. In their work, Ammonium chloride was first combined with PbI<sub>2</sub> and spin-coated on the substrate, and then a mixed solution of FAI and CsI was dripped on the substrate to form the perovskite layer. To our knowledge, our work is the first to propose the action mechanism of ammonium chloride in the one-step preparation process of perovskite layer and to associate it with film formation process in multi-metal cation perovskite. At the same time, we are also the first ones to visually display the distribution and moving trajectory of multi metal ions. More than this, we have systematically studied how ammonium chloride and potassium iodide affect the distribution of multi-metal cations in the process of film formation by using GD-OES. GD-OES was originally used only for bulk analysis.[16] However, recent developments have shown the capability of GD-OES also for depth profile analysis within the 100 μm thickness range with detection limit around 10 μg/g, which is far below the detection limit of Auger electron spectroscopy (AES) and X-ray photoelectron spectroscopy (XPS).[17] Although there are many testing methods to detect the organic-inorganic perovskite, only few tests can analyze the structure of the whole perovskite solar cell or layer vertically. For example: Secondary Ion Mass Spectrometry (SIMS) as a typical analytical method has its main field of application on homogeneous materials, but it has poor quantification and no bulk insulators. More importantly, compared with the detection area of a ten square millimeter for GD-OES,[18] the detection area of a test is only in the square micrometer,[18] which is not enough to reflect the overall situation of perovskite and prone to errors. Grazing Incidence Wide-Angle X-ray Scattering (GIWAXS) technology can be used to detect the crystal structure and the orientation of crystal growth, and GIWAXS can be adjusted to detect the crystal structure at different depths of the film, but it cannot intuitively understand the real-time distribution of longitudinal elements, and the growth direction of the film and the situation between the interface.[19] Traditional X-ray

Photoelectron Spectroscopy (XPS) uses soft X-rays as the excitation source, usually Al K  $\alpha$  (energy of 1486.6eV) or Mg K $\alpha$  (energy of 1253.6eV), and the analytical depth is about 10nm. For the deeper range of element chemical information, it can only be obtained by ion etching. However, although the Hard X-ray Photoelectron Spectroscopy (HAXPES) technology uses upgraded energy X-ray source (such as Cr K $\alpha$ , energy 5414.9eV, synchrotron radiation source), which can obtain several times of the chemical information in the depth range of conventional XPS analysis, but it can only obtain the information about the depth of about 20 nm in the surface layer of perovskite, and the composition of the deep layer of perovskite cannot be analyzed.[20] Based on this, it is impossible to know the situation of the entire perovskite layer. GD-OES can detect the longitudinal distribution of multiple metal cations in the perovskite film and the movement trajectory of metal ions upon annealing time during the film formation process. For the comparison of the depth profiling method what we discussed above, we summarized and put it in **Table A.V.1 (Annex V)**. On one hand, the distribution of metal ions in the perovskite film can provide a good understanding of the crystallization status of the intermediate layer, thereby in-depth understanding of the importance of the intermediate layer to the perovskite solar cell. On the other hand, the distribution and trajectory of metal cations make us more intuitively understand the nature of phase separation. The addition of ammonium chloride makes the distribution of the multi-element cationic metal ions in the entire perovskite layer more uniform, so that the film quality of the perovskite layer and the intermediate layer have been significantly improved. Finally, the overall performance of perovskite solar cells has been greatly improved.

## V.2 Experimental

The preparations of substrates, compact TiO<sub>2</sub> layer and mesoporous TiO<sub>2</sub> layer were conducted as detailed in **Chapter II, Section II.1.2.1**.

### V.2.1 Preparation of Perovskite Films

*FAPbI<sub>3</sub> layers preparation:* 276.6 mg PbI<sub>2</sub> (1.2M, TCI) and 103.2 mg FAI (Greatcell) were mixed in 400  $\mu$ L DMF and 100 $\mu$ L DMSO. For the sample with NH<sub>4</sub>Cl (Alfa Aesar), we further added 9.6 mg of NH<sub>4</sub>Cl (Alfa Aesar) in the perovskite precursor solution (PPS). The PPS was stirred for 2h before use. The Spin-coating program was 1000 rpm for 10s and 4000 rpm for 30 s. 100  $\mu$ L of chlorobenzene

was dripped 20s after the starting of the spinning routine. The layers were finally annealed on a hotplate at 155 °C for 15 min. These layers are denoted FA throughout the chapter.

*Cs<sub>0.10</sub>FA<sub>0.90</sub>PbI<sub>3</sub> layers preparation:* 253.6 mg PbI<sub>2</sub> (1.1M, TCI), 77.4 mg FAI (Greatcell) and 13.0 mg CsI (TCI) were mixed in 400 μL DMF and 100μL DMSO. For the sample with NH<sub>4</sub>Cl (Alfa Aesar), we further added 8.0 mg of NH<sub>4</sub>Cl in the PPS. The PPS was stirred for 2h before use. The spin-coating program was 1000 rpm for 10s and 4000 rpm for 30 s. 100 μL of chlorobenzene was dripped 20s after the starting of the spinning routine. The layers were finally annealed on a hotplate at 155 °C for 15 min. These layers are denoted CsFA throughout the chapter.

*Rb<sub>0.05</sub>Cs<sub>0.10</sub>FA<sub>0.85</sub>PbI<sub>3</sub> layers preparation:* 73.1 mg of FAI (Greatcell), 5.3 mg of RbI (Alfa Aesar), 12.9 mg of CsI (TCI) and 253.6 mg of PbI<sub>2</sub> (1.1M, TCI) were mixed in 100 μL DMSO and 400 μL DMF. For the sample with NH<sub>4</sub>Cl (Alfa Aesar), we further added 8.0 mg of NH<sub>4</sub>Cl in the PPS. The PPS was stirred for a minimum of 2 h at room temperature in a N<sub>2</sub> filled glovebox before use. 30 μL of this solution was placed on top of the substrates. A two-step spin-coating program was employed: first spinning at 1000 rpm for 10 s and then at 4000 rpm for 30 s. 100 μL of chlorobenzene was dripped 20 s after the starting of the spinning routine. The films were then annealed at 155 °C for 15 min in glovebox with N<sub>2</sub> atmosphere. These layers are denoted RbCsFA throughout the chapter.

*K<sub>x</sub>Rb<sub>0.05</sub>Cs<sub>0.10</sub>FA<sub>0.85-x</sub>PbI<sub>3</sub> layers preparation:* A mixed metal cation PPS was prepared by mixing FAI (68.8 mg (x=0.05)/ 64.5 mg (x=0.10)/ 60.2 mg (x=0.15), Greatcell), KI (4.2 mg (x=0.05)/ 8.3 mg (x=0.10)/ 12.5 mg (x=0.15), Sigma-Aldrich), 5.3 mg RbI (Alfa Aesar), 13.0 mg CsI (TCI) and 253.6 mg of PbI<sub>2</sub> (TCI) in 400 μL DMF and 100 μL DMSO to form K<sub>x</sub>Rb<sub>0.05</sub>Cs<sub>0.10</sub>FA<sub>0.85-x</sub>PbI<sub>3</sub>. For the K<sub>0.05</sub>Rb<sub>0.05</sub>Cs<sub>0.10</sub>FA<sub>0.80</sub>PbI<sub>3</sub> sample with NH<sub>4</sub>Cl (Alfa Aesar), we further add 2.7 mg (10 mol %, noted AC-10), 5.4 mg (20 mol %, noted AC-20), 8.0 mg (30 mol %, noted AC-30) and 10.7 mg (40 mol %, noted AC-40) NH<sub>4</sub>Cl in the PPS. The solutions were stirred for a minimum of 4h at room temperature in a nitrogen filled glovebox. 30 μL of this solution was placed on top of the substrates. A two-step spin-coating program was run: first spinning at 1000 rpm for 10 s and then at 4000 rpm for 30 s. 100 μL of chlorobenzene was dripped 20 s after the starting of the spinning routine. The films were then annealed at 155 °C for 15 min.

The PAI post-deposition treatment consisted in dropping 60  $\mu\text{L}$  of a 4 mg/mL n-propylammonium iodide (PAI) solution onto the perovskite film after cooling. A one-step spin-coating program was then started without waiting: 2000 rpm/s acceleration, 3000rpm for 20s. These  $\text{K}_{0.05}\text{Rb}_{0.05}\text{Cs}_{0.10}\text{FA}_{0.80}\text{PbI}_3$  without (with)  $\text{NH}_4\text{Cl}$  layers are denoted KRbCsFA (KRbCsFA/AC) throughout the chapter.

The preparation of hole transporting material solution was conducted as detailed in **Chapter II, Section II.1.2.2**.

### V.2.2 Characterization Methods

The layers characterizations by XRD, SEM, UV-vis absorbance, steady-state PL and TRPL are described in **Chapter II, Section II.1.2.3**. The DSC and GD-OES measurements are described in **Chapter IV, Section IV.2.2**. The measurements of  $J$ - $V$  curves, maximum power point tracking and  $EQE$  spectra of the devices are described in **Chapter II, Section II.1.2.3**.

### V.3 Characterizations of perovskite Films

In this chapter, we mainly reveal the following three issues at the same time and link them together:

1. The role of ammonium chloride in perovskite containing multi-alkali metal cations.
2. How multiple metal ions move during the film formation process.
3. The effect of additives on film forming direction and distribution of multi metal cations in perovskite films.

Therefore, in order to highlight our main research content, we put part of the optimized experimental data in the **Annex V**. In Chapter IV, on the one hand, we have optimized the content of Cs and got the optimal doping ratio of 10% to form  $\text{Cs}_{0.1}\text{FA}_{0.9}\text{PbI}_3$  perovskite. On the other hand, there has been a lot of work to dope Rb into CsFAPbI<sub>3</sub>, [21, 22] and the optimal doping ratio is 5%, so we directly chose 5% Rb as the optimal doping amount to form  $\text{Rb}_{0.05}\text{Cs}_{0.1}\text{FA}_{0.9}\text{PbI}_3$  perovskite. In order to better investigate the influence of the addition of KI on the performance of the perovskite solar cell, we decided to optimize the amount of this newly metal ions and found that the best amount is 5% (the study is detailed it in **Annex V**). Moreover, we have systematically studied  $\text{NH}_4\text{Cl}$  at concentrations varying between

10 and 40 mol% of molar  $\text{PbI}_2$  content in the  $\text{K}_{0.05}\text{Rb}_{0.05}\text{Cs}_{0.10}\text{FA}_{0.80}\text{PbI}_3$  precursor solution (the study is detailed in the **Annex V**) and proved that 30% is the optimal addition amount. This result is consistent with the optimization result we got in Chapter IV.

### V.3.1 SEM

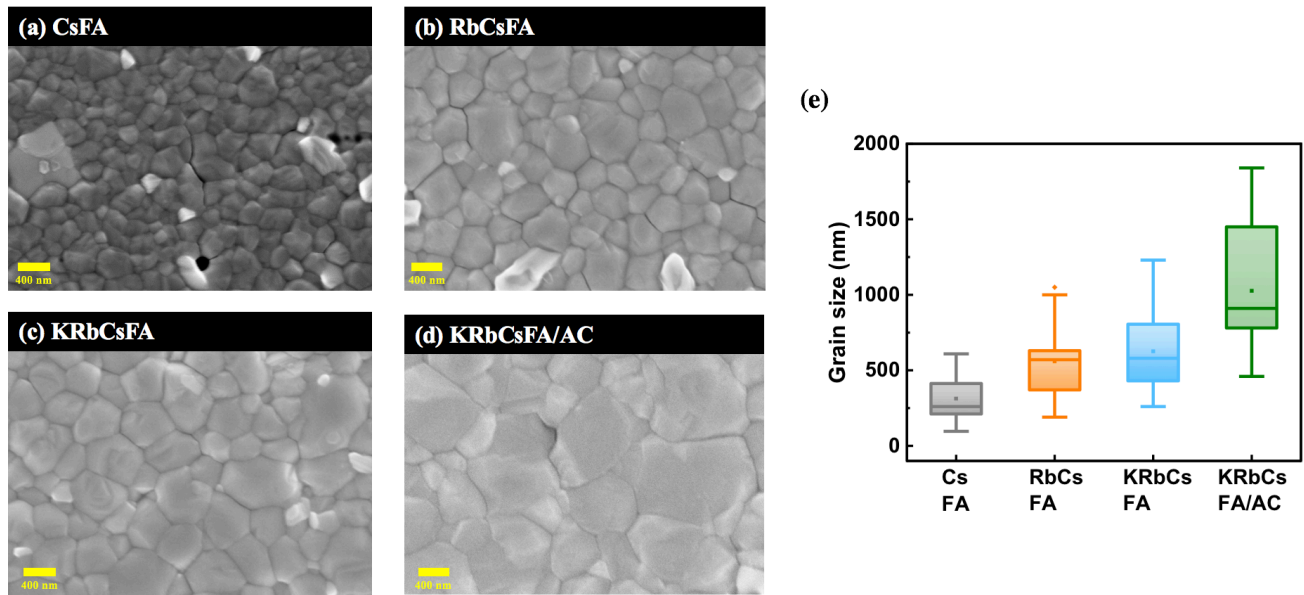


**Figure V.1** (a-d) SEM top-view images of perovskite layers prepared with different recipes: (a)  $\text{Cs}_{0.10}\text{FA}_{0.90}\text{PbI}_3$ , (b)  $\text{Rb}_{0.05}\text{Cs}_{0.10}\text{FA}_{0.85}\text{PbI}_3$ , (c)  $\text{K}_{0.05}\text{Rb}_{0.05}\text{Cs}_{0.10}\text{FA}_{0.80}\text{PbI}_3$ , (d)  $\text{K}_{0.05}\text{Rb}_{0.05}\text{Cs}_{0.10}\text{FA}_{0.80}\text{PbI}_3$  with AC additive. (the scale bar is 400 nm) (e) Statistical grain size analysis.

Firstly, we studied the effect of KI on RbCsFA system. We believe that the addition of potassium ions will form a passivating layer in RbCsFAPbI<sub>3</sub> and then improve its stabilized PCE. As we can see in **Figure A.V.1a-d** (**Annex V**), with the amount of KI increasing from 0 to 5 mol%, the morphology of perovskite layer became compact. Compared to the w/o one, the grain size also increased with less  $\text{PbI}_2$  crystal on the surface, which indicated that 5 molar% of KI can improve the crystallization of RbCsFAPbI<sub>3</sub> system. With more KI added, the  $\text{PbI}_2$  crystal were present again and spread on the surface everywhere. Next, the effect of  $\text{NH}_4\text{Cl}$  on the KRbCsFAPbI<sub>3</sub> system was explored. In **Figure A.V.2** (**Annex V**), the w/o sample presented small grains and some bright grains dispersed onto the surface corresponding to  $\text{PbI}_2$ . There was still  $\text{PbI}_2$  present on the surface after adding 10 mol% of  $\text{NH}_4\text{Cl}$ , but the increase of grain size of perovskite could be seen clearly (**Figure A.V.2b**, **Annex V**). Increasing  $\text{NH}_4\text{Cl}$  up to 30 mol% led to a continuous enlargement of the perovskite grain size (**Figure A.V.2b-d**,

**Annex V**), which means that 30 mol% can greatly improve the quality of KRbCsFAPI system. However, when the percentage up to 40 mol%, the size keep same as with 30 mol% sample, but the appearance of  $\text{PbI}_2$  indicated a decrease of the crystalline quality (**Figure A.V.2e, Annex V**).

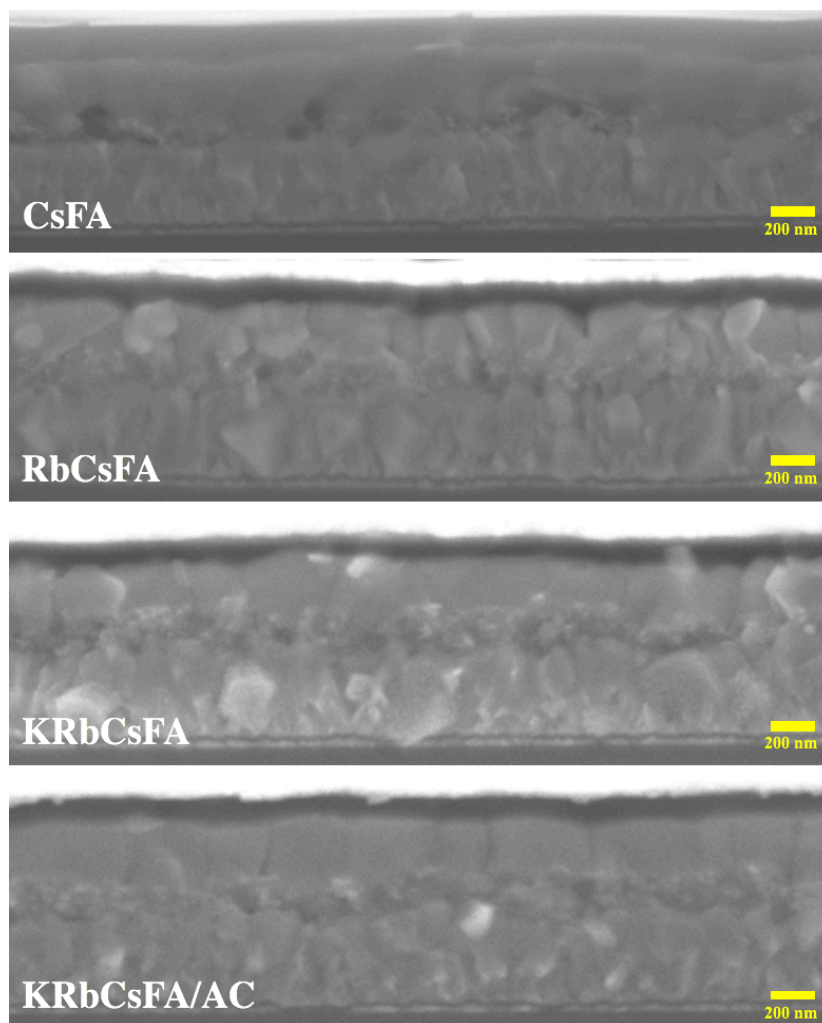


**Figure V.2** SEM cross-sectional views of perovskite layers deposited on glass/FTO/*c*-TiO<sub>2</sub>/*m*p-TiO<sub>2</sub> and topped with a SpiroOMeTAD layer.

We have focused our attention on the effect of alkali metal on the morphology of these four kinds of perovskite layers. From **Figure V.1a** to **1c** we can see that, with the incorporation of more kinds of alkali metal cations, the morphology of the film is improved, which is manifested in the increase in the grain size (**Figure V.1e**), elimination of the pinholes and the decrease of lead iodide crystals (bright grains) especially present on the surface. The mean grain size of RbCsFA and KRbCsFA were very close, around 730 nm, much larger than 327 nm for the Cs sample (**Figure V.1e**). In addition, compared

to samples without additives, the morphology of the sample with AC as the additive was better. It can be seen from the comparison between **Figure V.1c** and **1d** that the grain size increased. The addition of ammonium chloride greatly increased the grain size, from 730 nm to 1100 nm.

In **Figure V.2**, we also can get the same conclusion as from top-surface morphology. Compared to CsFA sample with voids and RbCsFA sample with disordered crystals, the quality of KRbCsFA perovskite film is improved obviously, as it is composed of large and homogeneous grains. In addition, the quality of perovskite was further enhanced by using AC as additive and it resulted in more homogeneous films with big monolithic grains as observed on SEM cross-sectional views.

### V.3.2 XRD

XRD patterns allowed us to detect the quality of perovskite layer and to check the purity of perovskite phase. In **Figure A.V.1e to g** (**Annex V**), the result showed that 5 mol% of KI gave the best crystallinity compare to other mol%. The addition of excessive K (more than 10%) led to phase separation. A small peak at around  $10^\circ$  was present in K10 and K15 films XRD patterns showed that the phase separation started when 10 mol% KI or more was added to the RbCsFA system. From the XRD result of KRbCsFA with varying the amount of AC (**Figure A.V.2f**, **Annex V**), we got the same conclusion as in Chapter IV:  $\text{NH}_4\text{Cl}$  can increase the precursors solubility in solvent and then favor the  $\alpha$ -phase formation.

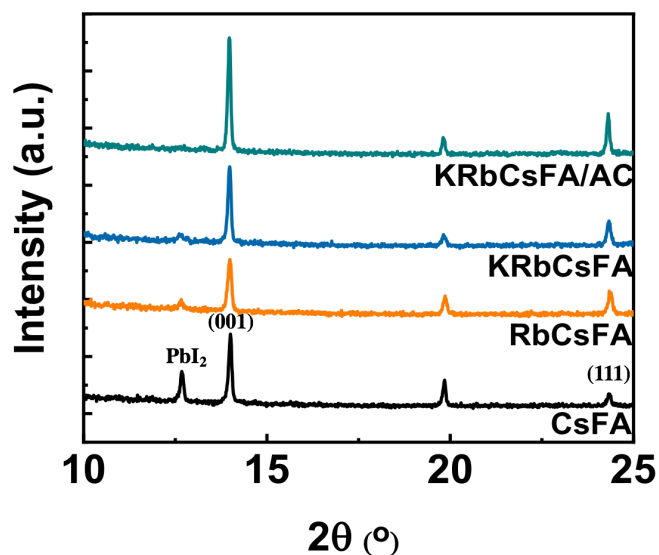


**Figure V.3** XRD patterns of four kinds of perovskite layers.

From the XRD results in **Figure V.3**, we can also draw the same conclusion as from SEM measurements. With the increasing kinds of metal cations incorporated, the (001) peak of perovskite gradually increased, while the intensity of  $\text{PbI}_2$  at 12.6 degree gradually declined. In addition, compared to samples without additives, the morphology of the sample with AC as the additive was better. XRD results show that it went along with an increase in the material crystallinity (**Figure V.3**). While increasing the crystal size with increase in metal cations, we found from the XRD results that the peaks at (001) and (002) moved to the left, which means that the perovskite lattice is also expanding (**Figure A.V.3, Annex V**). The displacement amplitude of (002) is larger than (001) in **Figure A.V.3b (Annex V)**, which can be explained as peak shift is usually more apparent at larger angles.[23] The shift of the perovskite peak to the left may suggest that iodine takes up interstitial position causing lower angle shift due to small ionic radii of Rb (152 pm) and K (133 pm).[24] Moreover, the peak shifts also suggest that metal cation may be assisting iodine to take up the interstitial position. KRbCsFA/AC sample shows a more substantial shift compared to KRbCsFA sample in **Figure V.3b**, may indicating an even larger lattice constant resultant in the film.

### V.3.2.1 Spin-coating process

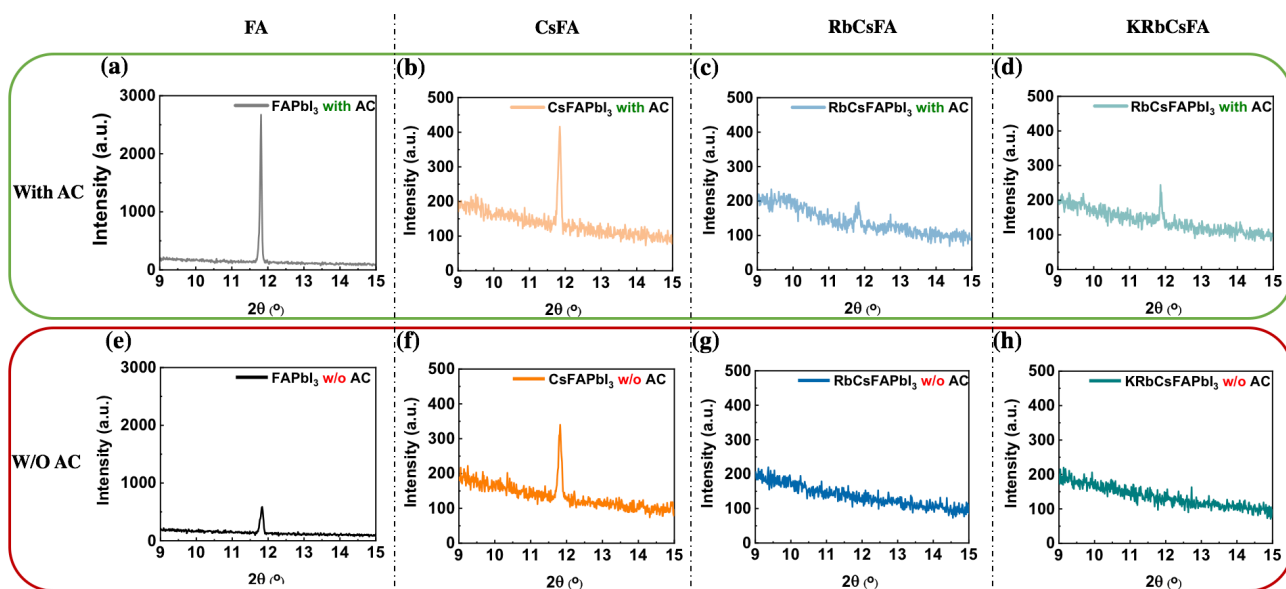


**Figure V.4** Effect of Ammonium Chloride on the XRD pattern of the films produced by spin-coating only, (a-d) with AC and (e-h) without AC (FA= $\text{FAPbI}_3$ , CsFA= $\text{Cs}_{0.10}\text{FA}_{0.90}\text{PbI}_3$ , RbCsFA= $\text{Rb}_{0.05}\text{Cs}_{0.10}\text{FA}_{0.85}\text{PbI}_3$ , KRbCsFA= $\text{K}_{0.05}\text{Rb}_{0.05}\text{Cs}_{0.10}\text{FA}_{0.80}\text{PbI}_3$ )

In order to gain a deep understanding of the effect of different metal cations and ammonium chloride on film formation process. We used XRD to track and analyze each stage of the one-step preparation of perovskite film. **Figure V.4e-h** compares the XRD patterns of the samples with and without AC as additive. XRD peaks were more intense for the FA and CsFA samples, their patterns were dominated by the (010) peak of the yellow  $\delta$ -phase (**Figures V.4a-b, Figures V.4e-f**). After adding AC the  $\delta$ -phase, absent of the pristine layers, appeared in the sample of RbCs and KRbCs (**Figures V.4c-d, Figures V.4g-f**). To explain this phenomenon, we can assume that the addition of AC helps the formation of the  $\delta$ -phase during the spin-coating process. On the one hand, the  $\delta$ -phase peak of CsFA sample was much weaker than that of FA sample. It is explained by the incorporation of Cs in the A-site of  $ABX_3$  which is effective in suppressing the formation of hexagonal polytypes.[25] This result is in good agreement with thermodynamic calculations, which showed that Cs incorporation into  $\delta$ -FAPbI<sub>3</sub> is thermodynamically favorable.[26] On the other hand, we can see that the intensity of the  $\delta$ -phase peak decreased greatly or even did not exist when more than two kinds of metal cations were added. This is probably because the addition of two or three metal cations expands the degree of inhibition of the formation of hexagonal polytypes.

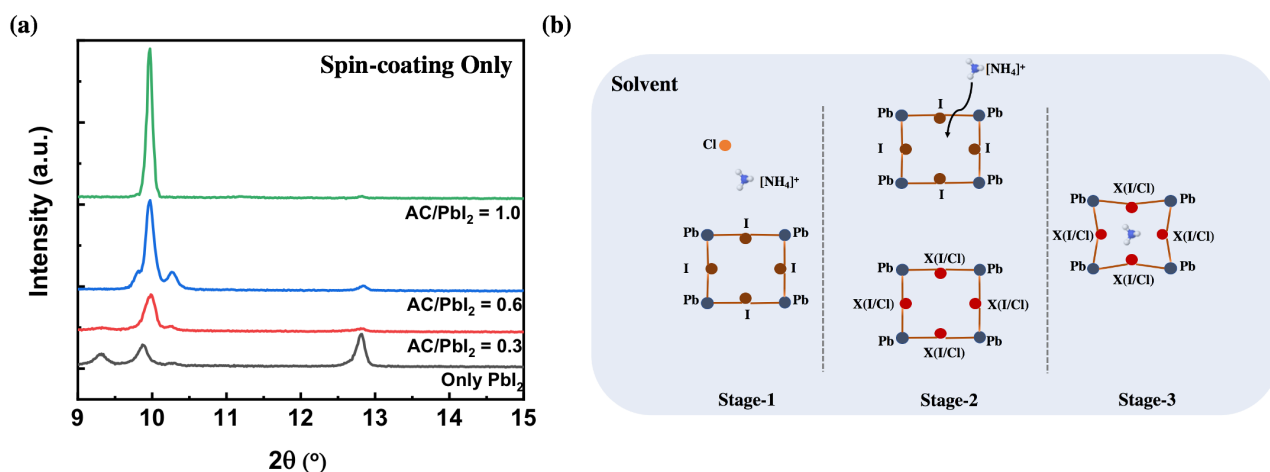


**Figure V.5 (a) XRD patterns of the result of different amounts of ammonium chloride on PbI<sub>2</sub>, (b) Intermediate  $x[\text{NH}_4]^+ [\text{PbI}_2\text{Cl}_x]^{x-}$  formation process.**

In order to confirm our conjecture and exclude the interference of other cations, we studied the effect of AC on PbI<sub>2</sub> by XRD. According to **Table A.V.3 (Annex V)** and our previous work [8], we know that the best amount of AC to get the highest PCE is 30 mol %. Therefore, we investigated three

different amounts of AC, namely 30 mol%, 60 mol% and 100 mol% of PbI<sub>2</sub>. In the **Figure V.5a**, we can see the PbI<sub>2</sub> peak at 12.6 degree and three peaks between 9 degree and 10.5 degree, which belong to the PbI<sub>2</sub>-solvent system [27]. The intensity of crystal PbI<sub>2</sub> peak was strong in the sample without AC. It means that PbI<sub>2</sub> did not dissolve completely in this case. With the increasing amount of AC added into PbI<sub>2</sub> solution, the peaks at 9.32 degree and 10.28 degree and 12.6 gradually disappeared. It means that AC can increase the solubility of PbI<sub>2</sub> and that all PbI<sub>2</sub> is dissolved when 100 mol % of AC is added. However, adding a large amount of AC makes PbI<sub>2</sub> better dissolved, but leads to excessive growth of PbI<sub>2</sub> due to the dissolving competition between PbI<sub>2</sub> and NH<sub>4</sub>Cl.[14] Among them, the NH<sub>4</sub>Cl ligand matrix is similar to that of metal chalcogenide complex (MCC) acting on nanocrystals, which helps to connect neighboring particles better.[28] We can clearly see from SEM in **Figure A.V.4 (Annex V)** that excessive AC led to crystal overlap. This kind of crystal overlap produces more pinholes (**Figures A.V.4d and A.V.4e, Annex V**). Among these three peaks of PbI<sub>2</sub> of the sample without AC, the main peak at 9.86 degree was moving to 9.97 degree after we added AC into PbI<sub>2</sub> solution, which represents that the lattice is shrunk due to NH<sub>4</sub><sup>+</sup> with small ionic radius preferentially diffuses into the [PbI<sub>2</sub>Cl<sub>x</sub>]<sup>x-</sup> octahedral layer and form x[NH<sub>4</sub>]<sup>+</sup> [PbI<sub>2</sub>Cl<sub>x</sub>]<sup>x-</sup> intermediate phase. Since we did not detect the existence of this intermediates in the XRD results after spin-coating (**Figure V.4**), we believe that this intermediate was formed before δ-phase and as a bridge to better transform into δ-phase. Another reason is that the reaction of AC and PbI<sub>2</sub> can be reflected in the solid state, indicating that the energy required for the reaction is very low. In **Figure V.5b**, we detail the process of forming this intermediate phase.

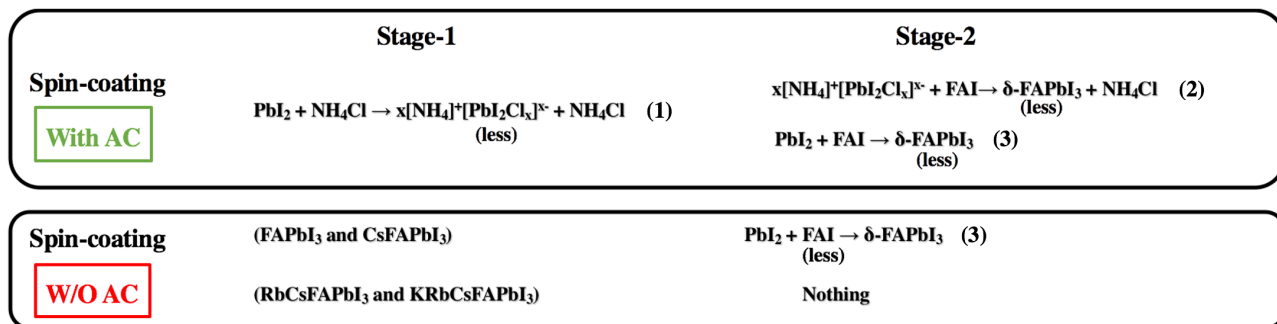


**Figure V.6** Reactions occurring upon the precursor solutions spin-coating process.

Through the above analysis, we propose in **Figure V.6** the film formation mechanisms upon spin-coating for these four kinds of precursor solution, with and without AC. On one hand, FA and CsFA had the binding of FAI with  $\text{PbI}_2$  for the samples without AC as additive (**Equation 3, Figure V.6**). This reaction did not occur significantly for  $\text{RbCsFAPbI}_3$  and  $\text{KRbCsFAPbI}_3$  samples. On the other hand, in the recipe with AC as additive,  $\text{PbI}_2$  firstly combines with AC to form  $x[\text{NH}_4]^+ [\text{PbI}_2\text{Cl}_x]^-$  intermediate in the stage-1 (**Equation 1, Figure V.6**), and then this intermediate combines with FAI to form  $\delta\text{-FAPbI}_3$  (**Equation 2, Figure V.6**) in the stage-2.

### V.3.2.2 Anti-solvent process

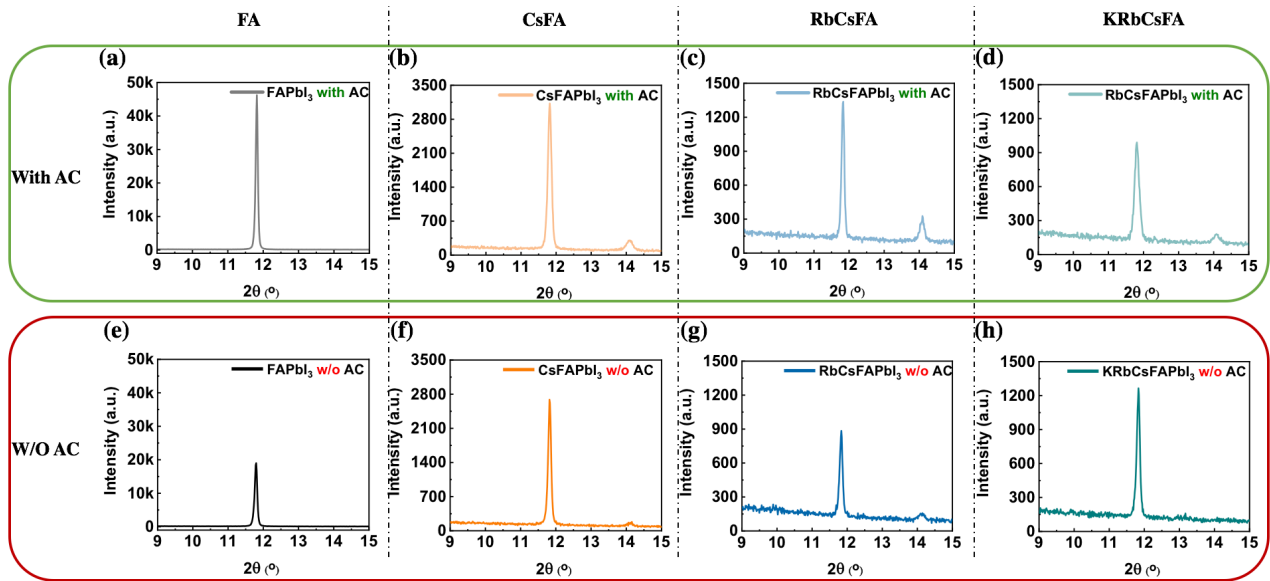


**Figure V.7** Effect of Ammonium Chloride on the XRD pattern of the films produced by spin-coating and then anti-solvent. (a-d) with AC and (e-h) without AC (FA:  $\text{FAPbI}_3$ , CsFA:  $\text{Cs}_{0.10}\text{FA}_{0.90}\text{PbI}_3$ , RbCsFA:  $\text{Rb}_{0.05}\text{Cs}_{0.10}\text{FA}_{0.85}\text{PbI}_3$ , KRbCsFA:  $\text{K}_{0.05}\text{Rb}_{0.05}\text{Cs}_{0.10}\text{FA}_{0.80}\text{PbI}_3$ )

We now focus on the effect of dripping chlorobenzene anti-solvent upon spin-coating. We tracked the anti-solvent process by measuring the XRD pattern of the various samples. Compared to without additive (**Figures V.7e-h**), the four kinds of perovskite with AC (**Figures V.7a-d**) exhibited the following changes: (1) In all cases, the peak of  $\delta$ -phase of FA sample was greatly enhanced, which indicates that more  $\text{PbI}_2$  was converted into (010) peak of  $\delta$ -phase. (2) The enhancement amplitude of  $\alpha$ -phase in CsFA sample and RbCsFA sample is much larger than that of  $\delta$ -phase. We can then assume that the intermediate can be directly converted into  $\alpha$ -phase with FAI in the presence of multi-metal cations. Because both intermediate and  $\alpha$ -phase are cubic, the conversion is rather easy to occur. To

confirm our conjecture, we added FAI-IPA solution to the substrate covered with  $\text{NH}_4\text{Cl}$ - $\text{PbI}_2$  intermediate and then check if only  $\alpha$ -phase can be formed directly and we compared to the behavior of a  $\text{PbI}_2$  layer (**Figure A.V.5, Annex V**). Compared to the substrate without intermediate compound (**Figure A.V.5a, Annex V**), the  $\alpha$ -phase can be only directly formed by dropping FAI-IPA solution onto the substrate with intermediate compound layer (**Figure A.V.5b, Annex V**). Many miscellaneous peaks appear when FAI-IPA is added dropwise to the substrate covered by the  $\text{PbI}_2$  solution without AC (**Figure A.V.5a, Annex V**). (3) In the KRbCsFA sample after AC was added, the intensity of the  $\delta$ -phase peak decreased compared with the sample without AC, but a new  $\alpha$ -phase peak appeared. This means that after the addition of AC to sample KRbCsFA, the reduced  $\delta$ -phase is transformed into  $\alpha$ -phase.

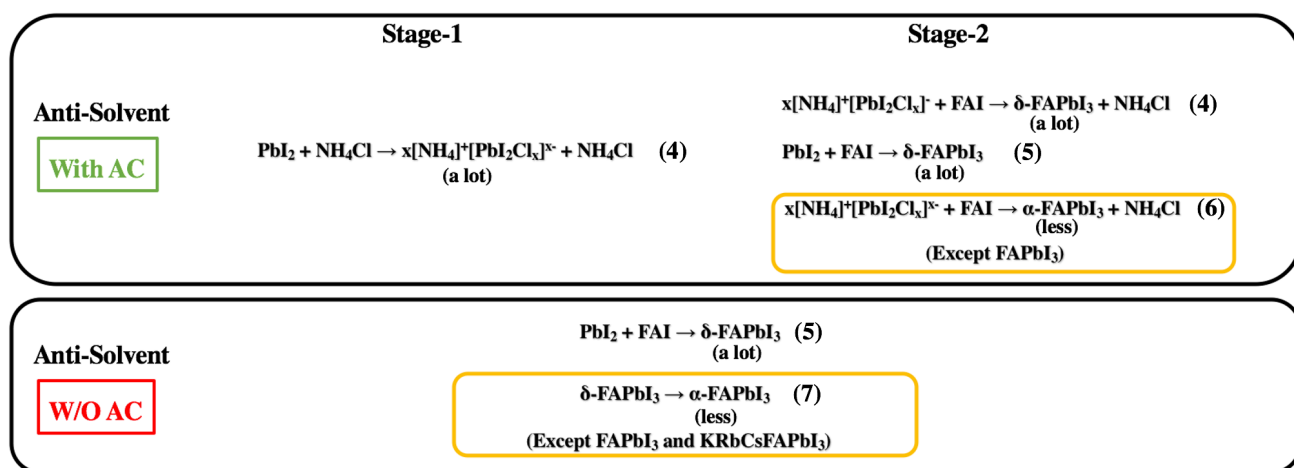


**Figure V.8 Summarized mechanism of anti-solvent process.**

Our analysis of anti-solvent effect, has allowed us to propose a mechanism of anti-solvent action which is summarized in **Figure V.8**. We first divide the mechanism of adding AC samples into two stages. The massive formation of intermediates occurs first at stage-1 (**Equation 4, Figure V.8**), and then the intermediates and  $\text{PbI}_2$  combine with FAI at the same time at stage-2 to form  $\delta$ -phase (**Equations 4 and 5, Figure V.8**). It should be noted that, except for the FA sample, the rest of the samples all have **Equation 6 (Figure V.8)**. For samples without AC, the main reaction is **Equation 5**.  $\alpha$ -phase is formed except for FA and KRbCsFA and in much less extend than with AC (**Equation 7, Figure V.8**).

### V.3.2.3 Annealing process

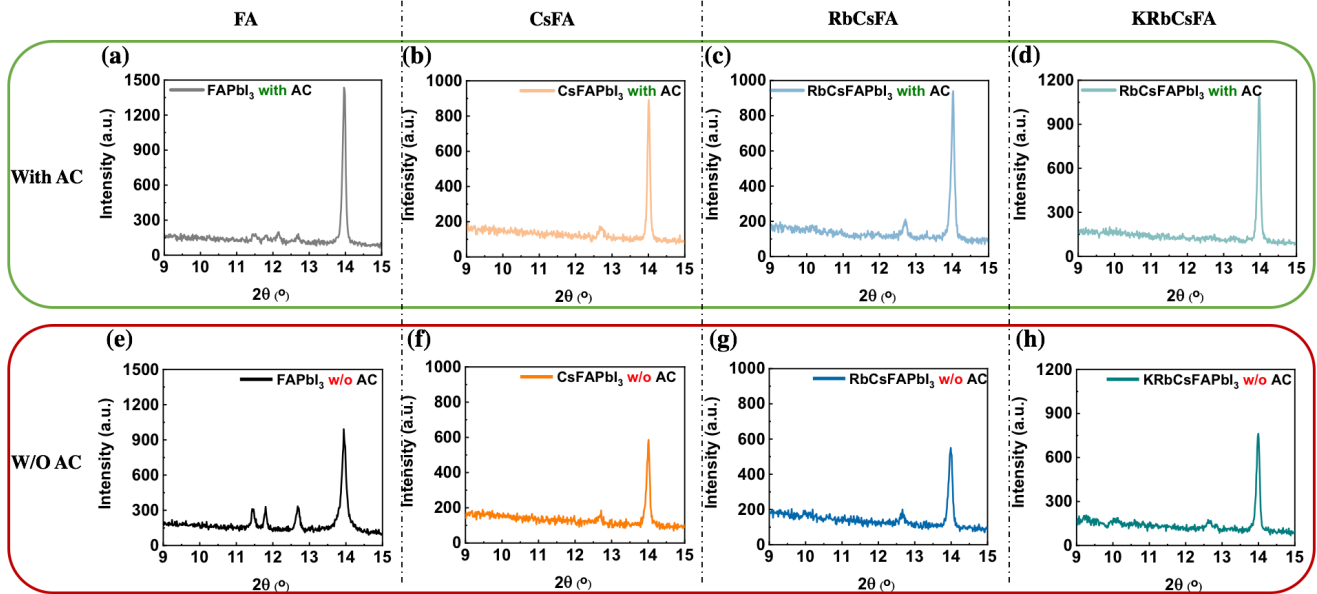


**Figure V.9** Effect of Ammonium Chloride on the XRD pattern of the films produced finally by annealing at 155°C for 15 min. (a-d) with AC and (e-h) without AC (FA: FAPbI<sub>3</sub>, CsFA: Cs<sub>0.10</sub>FA<sub>0.90</sub>PbI<sub>3</sub>, RbCsFA: Rb<sub>0.05</sub>Cs<sub>0.10</sub>FA<sub>0.85</sub>PbI<sub>3</sub>, KRbCsFA: K<sub>0.05</sub>Rb<sub>0.05</sub>Cs<sub>0.10</sub>FA<sub>0.80</sub>PbI<sub>3</sub>)

We finally investigated the effect of the annealing step. In order to be consistent with the previous process, we used XRD to verify the effect of AC in the final film (**Figures V.9a-h**). By comparison, we found that the samples with AC added exhibited lower PbI<sub>2</sub> peak intensity and a better crystallized  $\alpha$ -phase after 15 minutes of annealing. These results are perfectly in agreement with those from our cross-sectional SEM studies described above (**Figure V.2**).

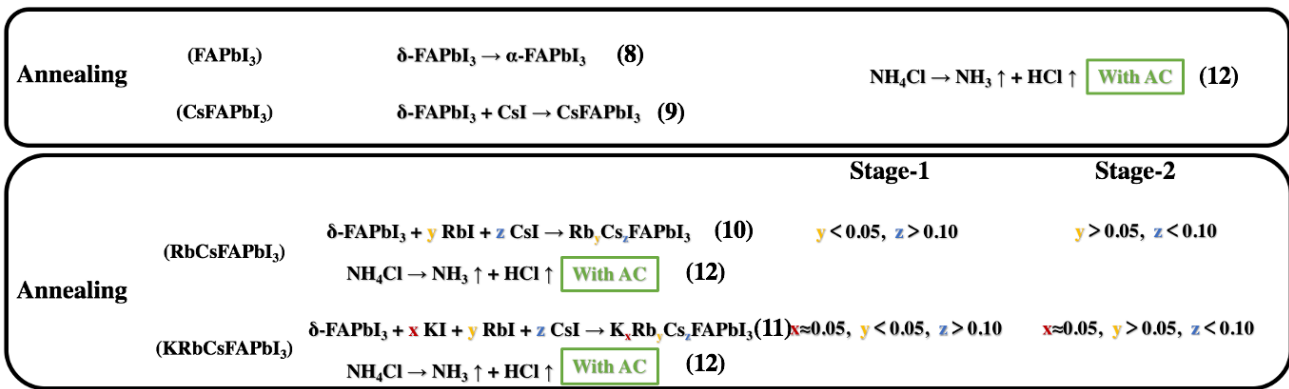


**Figure V.10** Summarized mechanism of Annealing process.

Finally, the deduced mechanisms of the annealing process for the various samples are summarized in **Figure V.10**. For the sample with AC, the intermediate-product ammonium chloride will continue to

decompose into volatile ammonia and hydrogen chloride gas at 155 °C and will be eliminated. It is worth emphasizing that, combined with the results obtained from GD-OES discussed below, we subdivided the annealing step of RbCsFA and KRbCsFA samples containing multiple metal cations into two stages. Since the crystal growth direction is from top to bottom, the Cs dominant  $\alpha$ -phase will form in stage-1, and then Rb dominant  $\alpha$ -phase will formed in stage-2. For the KI added samples, because potassium ions are uniformly distributed throughout the perovskite layer thickness, we assume that its atomic ratio remains constant (around 0.05).

### V.3.3 DSC

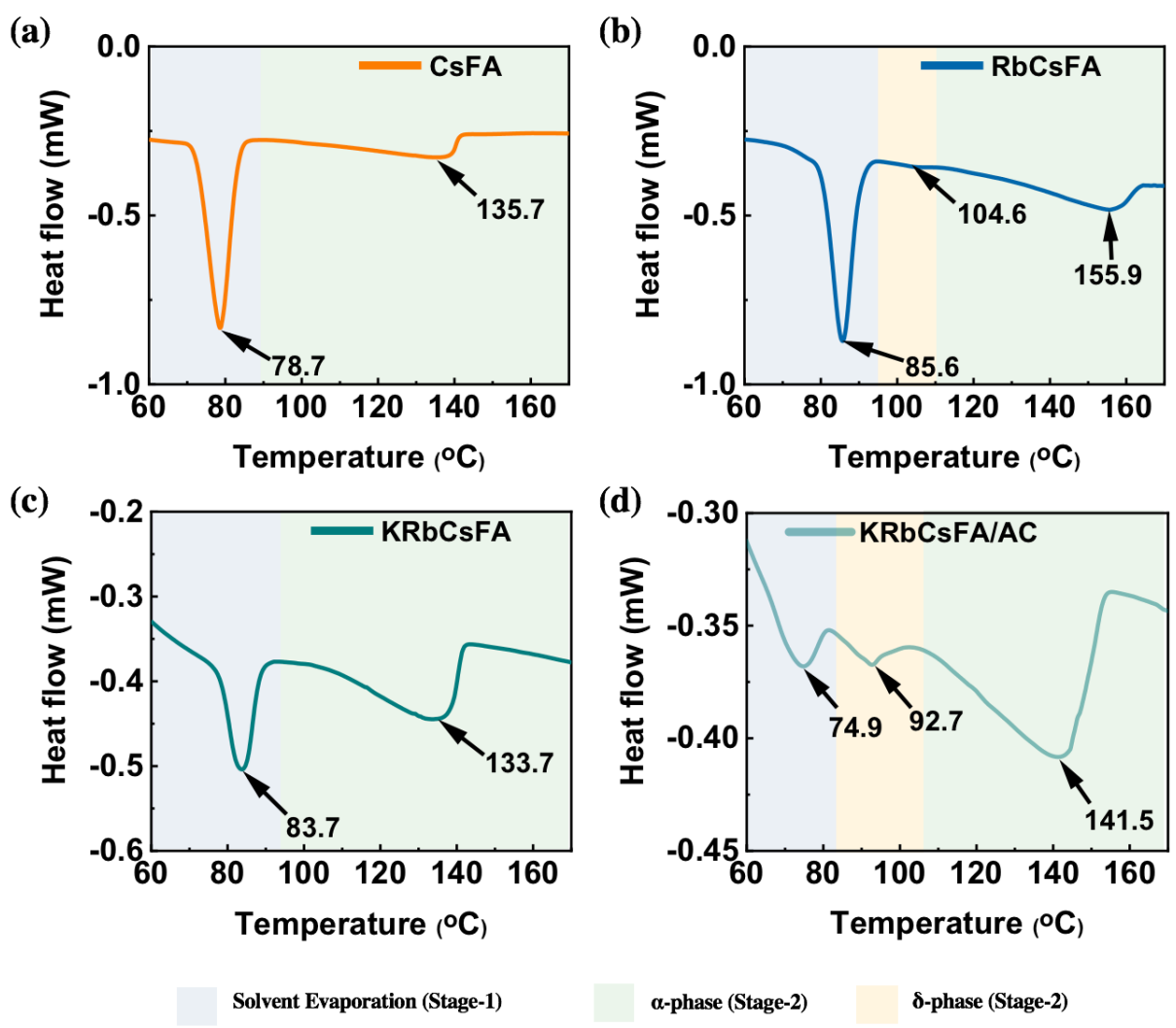


Figure V.11 DSC curves of (a)CsFA, (b)RbCsFA, (c)KRbCsFA and (d)KRbCsFA/AC.

Differential Scanning Calorimetry (DSC) was then employed to further understand the effect of K, Cs, Rb, ammonia and chloride ions on the formation of the crystallized perovskite. The curves were

measured on the four samples prepared as powders adducts (**Figures V.11a-d**), completed by a FAPbI<sub>3</sub> powder adduct (**Figure A.IV.7, Annex IV**). A first endothermic peak was observed at ~70°C-90°C, assigned to the evaporation of DMSO (DMF was eliminated upon washing the adducts by diethyl ether)[30] since DMSO mixed with PbI<sub>2</sub> has been shown to start to evaporate at a temperature as low as 75°C.[31] First, a higher peak temperature was found for FAPbI<sub>3</sub> (82.7°C) compared to Cs sample (78.5°C). It suggests that the presence of CsI weakens the DMSO bonding. The evaporation temperature increased by around 6°C with the Rb and K introduced into the PPS. However, the temperature corresponding to the first endothermic peak of sample with AC has reduced to 74.9°C, which shows that the formation of the intermediate weakens the bonding between solvent and adduct, making the solvent evaporation easier. For FAPbI<sub>3</sub> sample, an endothermic peak was observed at 101.5 °C which is attributed in the literature to the crystallization of the perovskite yellow  $\delta$ -phase.[31,32]. We can also see this peak in RbCsFA and KRbCsFA/AC samples, at 104.6 °C and 92.7 °C, respectively. In the case of CsFA and KRbCsFA samples, this peak was not visible. Above 105°C, an extended endothermic feature was found, assigned to the crystallization of the  $\alpha$ -phase perovskite compounds. In the case of FAPbI<sub>3</sub>, it extended up to 162°C with a minimum at 153.5°C (**Figure A.IV.7, Annex IV**). This minimum can be roughly taken as the temperature at which the crystallization and growth steps end and allows a clear comparison between the samples. Adding different metal cations and additive can greatly affect the temperature corresponding to this step. Adding CsI significantly reduced this temperature at 137.3 °C. Through thermodynamic calculation, we can also see that the Gibbs free energy becomes lower after doping small amount of Cs into FAPbI<sub>3</sub>. [29] Also, a low temperature was found for KRbCsFA sample (minimum at 133.7°C). For the reason why CsFA and KRbCsFA samples do not have peak related to the  $\delta$ -phase may be due to the period of process of crystallization of the  $\delta$ -phase is short, and then this peak was hidden by process of crystallization of the  $\alpha$ -phase. Therefore, in both cases (CsFA and KRbCsFA), a fast crystallization and growth occur. On the other hand, both RbI (in RbCsFA sample) and NH<sub>4</sub>Cl (in KRbCsFA sample) can delay and slow down the perovskite crystal growth and it favors the formation of large grains. This effect of NH<sub>4</sub>Cl was also observed by *in-situ* microscopy in the case of MAPbI<sub>3</sub> perovskite by Dai et al..[33]

### V.3.4 GD-OES

#### a- Cations distribution upon annealing

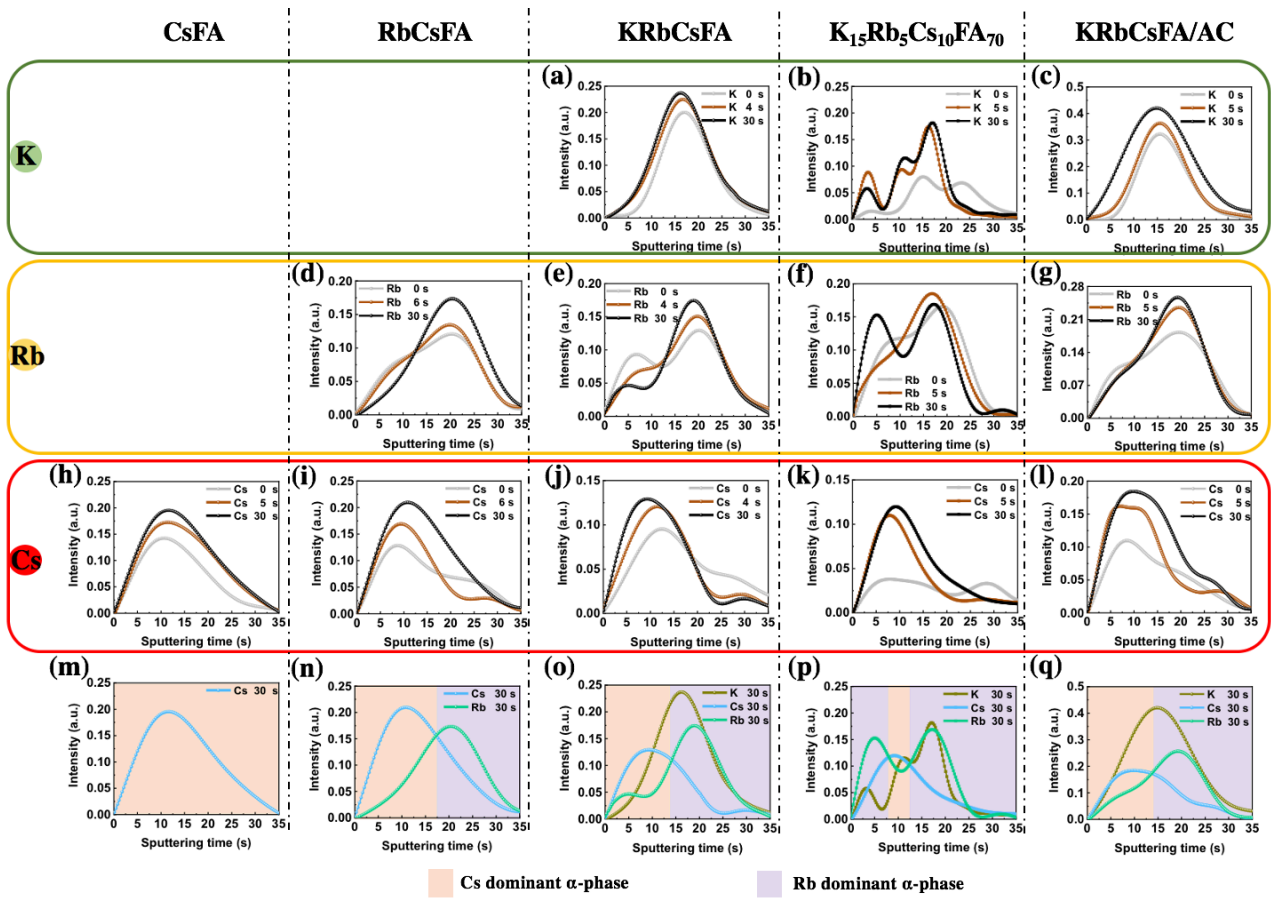


**Figure V.12** Distribution of different metal cations upon annealing by using GD-OES. (a-c) Distribution of potassium ions. (d-g) Distribution of rubidium ions. (h-l) Distribution of cesium ions. (m-q) All metal ion fractions after annealing for 30s, (m) CsFA, (n) RbCsFA, (o) KRbCsFA, (p)  $K_{15}RbCsFA$ , (q) KRbCsFA/AC.

In order to get a deeper understanding of the film formation mechanism, we followed the movement of the metal ions during the film annealing and the influence of AC on the film formation process. We introduced GD-OES as the main measurement technique to gain a deep understanding of these processes. It allowed us to follow the depth-profile distribution of the perovskite layers constituent elements. As far as we know, this is the first work reporting the real-time moving track of polymetallic cations upon the film-formation process. Using this detection method, we have been able to make the results more visual and easier to understand by everyone. At the same time, our results show that potassium ion rich perovskite composition can cause phase separation.

In **Figure V.12**, we present the movement of all metal ions for five kinds of perovskites upon annealing. Let us first explore the results from the GD-OES test, from only containing a single cesium metal cation to simultaneously containing three metal cations (K, Cs and Rb). When only cesium ions were present in CsFA samples, we can see that the curve strength of cesium ions increased and became boarder with the increase of annealing time (**Figure V.12h**). This means that with the increase of annealing time, phase transition and solvent continuous evaporation occurred, the Cs gradually entered  $\delta$ -FAPbI<sub>3</sub> lattice and then corresponding crystallinity of the film became higher, which made the distribution of Cs in the perovskite film more uniform from top to bottom. For RbCsFA, that contains two metal cations, we found that, before annealing, the distribution of Rb and Cs was not uniform in the perovskite layer and showed two peaks. When the annealing time increased from 0 to 30s, Rb curve gradually moved in the direction of the TiO<sub>2</sub> layer (**Figure V.12d**), while Cs moved in the opposite direction (**Figure V.12i**). The reason for the upward movement of Cs may be due to the large amount of solvent evaporation on the surface of the perovskite layer accompanied by the annealing, which first causes the crystallization on the surface, and the energy required for the formation of Cs dominant  $\alpha$ -phase is lower than formation of Rb dominant  $\alpha$ -phase, so the moving direction of Cs is upwards. From the perspective of the energy required for phase transformation, the temperature required for all-inorganic perovskite CsPbI<sub>3</sub> to transform from orthorhombic ( $\delta$ -phase) into a cubic ( $\alpha$ -phase) structure is 300 °C,[34, 36] but RbPbI<sub>3</sub> cannot transform from yellow phase to black phase at its melting point.[36] In **Figure V.12n**, on the one hand, we can see that the intensity of Rb is very low from 0 to 10 seconds (sputtering time), but after 10 seconds, the intensity of Rb gradually increases. We can also see from **Figure A.V.6 (Annex V)** that until the end of the annealing process, the peak of Rb do not move much, which is due to the fact that the Rb mainly concentrates in the bulk perovskite rather than on the surface of perovskite.[29] On the other hand, from the beginning to the end, the curves of Cs and Rb always have overlapping areas, which shows it is not just superposition of CsFA and RbFA, but perfect integration into the perovskite. For sample KRbCsFA containing three metal cations, potassium ions are homogeneous distributed throughout the perovskite layer thickness as potassium has a small atomic radius (**Figure V.12a**). From 0 s to 30 s, there are always two peaks of Cs and Rb, which means that these two elements are non-uniformly distributed in the perovskite layer. For the Rb,

the concentration is lower in the upper layer of the perovskite, compared to the lower part of the layer (**Figure V.12e**). The distribution of cesium is opposite to that of rubidium (**Figure V.12j**). It should be noted that the position of the first peak and the second peak of the Cs curve in **Figure V.12j** are discontinuous, which indicates that the Cs element fault appears at the interface between perovskite and TiO<sub>2</sub> layer, but is enriched in the TiO<sub>2</sub> layer. By comparing the recipe with or without potassium metal ion, we can find that, after adding potassium ion in the perovskite precursor solution (PPS), the peak intensity of Rb and Cs changes little in the same time after ~5 s of annealing. This also shows that the addition of potassium ions accelerates the movement of ions during annealing, which means that the energy required for film formation is reduced (**Figure V.13**). Regarding this point, we will verify it in the DSC results. Compared to RbCsFA sample showed in **Figure V.12n**, the distribution of Cs and Rb in **Figure V.12o** (KRbCsFA) is less uniform, and the peak of Cs shifts to the left by 4s. Although the Rb curve has a small peak at 5s, the curve is still continuous and does not fluctuate much. The presence of potassium ions seems to enable Cs and Rb to be better integrated in the upper part of perovskite layer. What we need to mention here is that the three metal cations will not move significantly during the annealing period from 30 s to 15 min (**Figure A.V.6, Annex V**). For this reason, the graph we show in the text is only 30 seconds (**Figure V.12**).

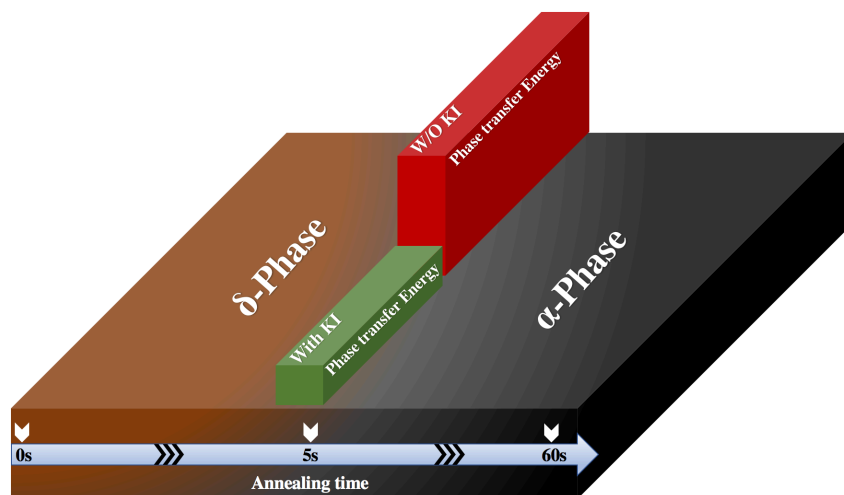


**Figure V.13 Schematic of phase transfer of recipe with and without KI upon annealing time.**

As for the recipe with adding AC as additive, all the metal cations distribution became more even compared with no AC samples. On the one hand, all cations show broader peaks (**Figures V.12c, V.12g and V.12i**). On the other hand, compared to the double peaks of Rb and Cs in the sample without

AC (Figures V.12e and V.12j), there is no obvious double peaks in the samples prepared with AC additive. It shows that AC can slow down the movement of different metal cations so that they can be better evenly distributed into the perovskite lattice and may favor the film formation process.

We also explored the phase separation phenomenon in the potassium-rich  $K_{15}RbCsFA$  sample. Compared with potassium poor  $K_5RbCsFA$  sample, the curve of the potassium-rich one shows a multi-peak distribution, especially for the curves of K and Rb (Figures V.12c and V.12g). This uneven cation distribution in Figure V.12p explains well the (002) peak of  $\delta$ -CsPbI<sub>3</sub> at around 10 degree found in Figure A.V.1e (Annex V).[37] The excessive potassium causes an extremely uneven distribution of other metal cations in the perovskite layer during film formation process, and finally leads to phase separation as we showed in Figure A.V.1e (Annex V). The results obtained by GD-OES can intuitively show the distribution of different metal ions in the perovskite layer under phase separation. In addition, we can assume that the atomic ratios corresponding to different depths of the perovskite layer are not the same, that is, they change with the depth.

**b- Solvent elimination upon annealing**

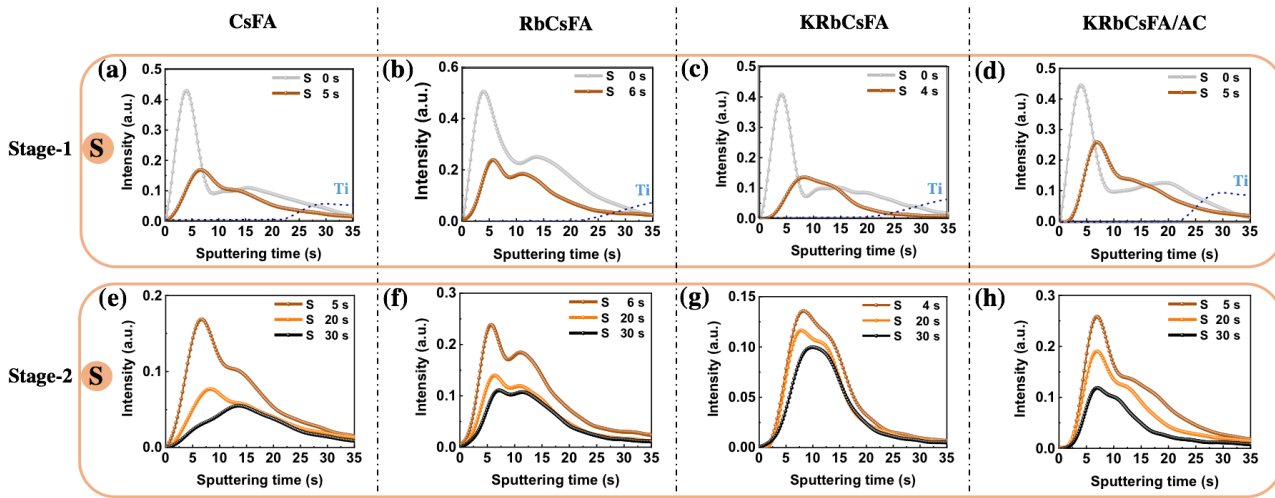


**Figure V.14 Evolution of GD-OES S profile in the perovskite precursor layer upon annealing. (Dashed line in (a-d): Ti profile corresponding to the *meso*-TiO<sub>2</sub>).**

The residual solvent elimination is an important aspect of the synthesis which occurs upon the film crystallization and growth. To our knowledge, our work is the first to use the GD-OES technique to

follow the depth profile of the solvent elimination by evaporation upon the annealing of a perovskite films. Indeed, the solvent employed was a DMF-DMSO mixture and S element contained in DMSO can be tracked by this technique. The S element profile for the various films and various annealing times are presented in **Figures V.14e-l**. By increasing the sputtering time, deeper part of the PVK layer was analyzed until reaching the *meso*-TiO<sub>2</sub> layer (dashed black line in **Figures V.14e-h**). Before annealing, the DMSO profile was asymmetrical in every case and we observed that the outer part of the film was richer in solvent than the inner part.

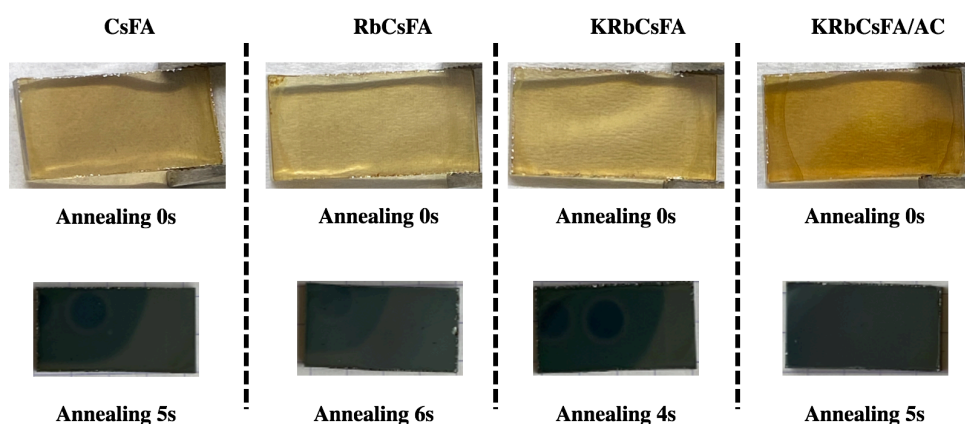


**Figure V.15** Change of perovskite film color with annealing for a few seconds.

For the annealing, our results distinguish two stages. The first one occurred during the first 4 s~7 s of annealing on a hotplate. The initial film changed from yellow translucent to brown (**Figure V.15**). It is worth noting that the sample with AC added had the darkest color before annealing (**Figure V.15**), which also shows that the intermediate will make the phase change easier. During this stage (stage-1), the most superficial residual solvent evaporates and is almost fully eliminated at the uttermost surface while these four kinds of perovskite present in the wet layer is fully transformed into the  $\alpha$ -phase (**Figure A.V.7, Annex V**). The next stage (stage-2) corresponds to 4-6s to 30s annealing times, when the film became dark-brown. We observed a clear effect of multi-metal cation and additive on the solvent distribution upon annealing. In the case of sample without AC, DMSO was eliminated fast near the surface, especially in sample CsFA and KRbCsFA (**Figures V.14e** and **V.14g**). This result is in good agreement with DSC result that both CsFA and KRbCsFA samples have fast crystallization process. However, less solvent remained in the deeper part of the layer. For these three films, the same point is that overall grains grow downward, from the top to the bottom. It favors the multiple and

oblique grain boundaries and rather small perovskite grains. The difference among these three samples is that the rate of solvent evaporation from bottom to the top. In the presence of RbI and KI in PPS, the S profiles are different compared to CsFA. For CsFA, the rate of first peak, which represent the layer near the surface, is faster than the second peak that represent the layer near the TiO<sub>2</sub> layer (**Figure V.14i**). This velocity difference will make it difficult for the inner solvent to evaporate, so that voids will appear when the film formation process is completed (**Figure V.2**). If the perovskite grains in the upper layer are tightly bonded, it will be difficult for the solvent in the bottom part of the layer to pass through the perovskite in the upper layer and then evaporate through the surface. Therefore, the remaining solvent will evaporate through pinholes and lateral diffusion. I believe this is the essential reason for the formation of the voids. As for RbCsFA and KRbCsFA samples, the intensity of the sulfur curve at about 20s for these two samples becomes very weak compared to the curve when annealed for 5s. Looking back at CsFA sample, we can clearly see that the sulfur curve still maintains high strength at the position of around 20s after annealing for 30s.

In the presence of AC, the profiles are different. For KRbCsFA/AC, the S profile is more extended throughout the layer thickness. Upon annealing, the solvent profile decreases uniformly throughout the layer thickness. In this case a bulk grain lateral growth occurs, and it results in more homogeneous films with big monolithic grains as shown in the cross-section SEM view (**Figure V.2**). For all the investigated samples, **Figure A.V.8 (Annex V)** shows that the solvent was fully eliminated after 2 min of annealing. A striking result of this study is that the additive regulates the solvent elimination and then the growth of the film in its full depth. It boosts the quality of the film. In **Figure V.16**, we have summarized the grain growth mechanism which is linked to the solvent elimination and the trajectories of metal ions in the film formation process obtained by GD-OES and DSC. In CsFA and KRbCsFA samples, metal cations are moving fast upon annealing time (**Figures V.16a and c**). For CsFA, however, the solvent in the inner part of the film remains entrapped and is at the origin of void formation and poor *meso*-TiO<sub>2</sub>/perovskite interface. In the case of RbCs sample, the slow movement of metal cation will generally cause better gains growth with the continuous elimination of the bottom solvent (**Figure V.16b**). The best grain growth was achieved in KRbCsFA/AC samples with a slow diffusion of polymetallic cations and a continuous elimination of the solvent in the full deep of the

film which led to the lateral growth of the grains and resulted in monolithic large grains with low defect density (Figure V.16d).

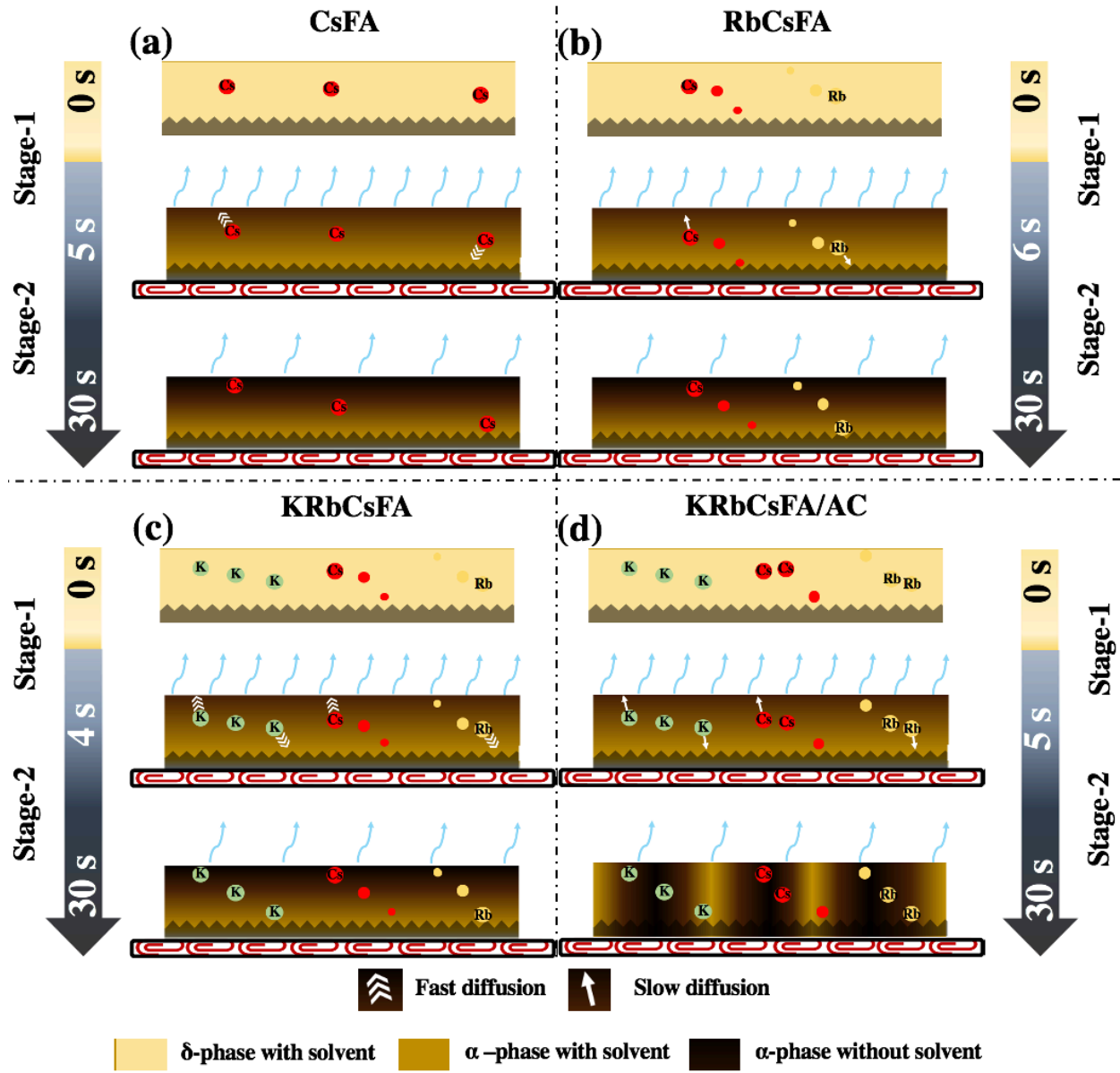
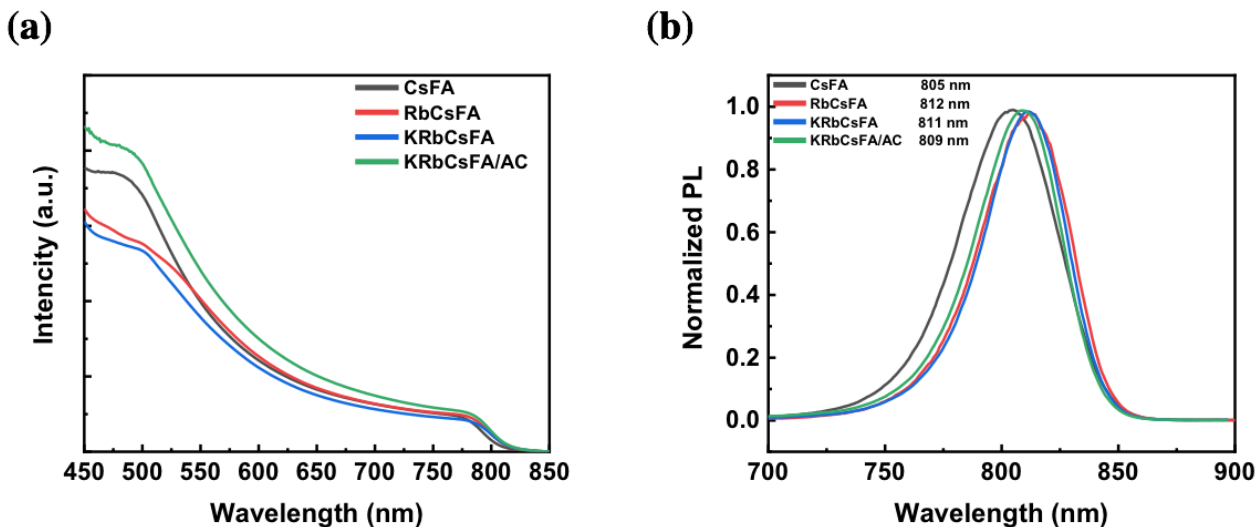


Figure V.16 Schematic of the distribution of multi-cation in four kinds of perovskite layer and corresponding film formation process.

### V.3.5 Absorbance and Steady PL



**Figure V.17** Effects of PVK cation composition and AC additive on the layer absorbance and PL spectra.

The optical property of the perovskite films was characterized by UV-VIS spectrophotometry and photoluminescence (PL) spectroscopy. The absorbance spectra in **Figure V.17a** show that absorption onset of RbCsFA and KRbCsFA sample are red-shifted compared to the CsFA sample. The bandgap of CsFA, RbCsFA and KRbCsFA samples are estimated to be 1.550 eV, 1.540 eV and 1.535 eV, respectively (**Figure A.V.9, Annex V**). The band gap reduction was also confirmed by the steady-state PL spectra of these films (**Figure V.17b**). There is also a small red-shift in the emission peak of KRbCsFA sample (811 nm) compared to the RbCsFA sample (812 nm) and the CsFA sample (805 nm). In addition, the detailed result of steady PL, UV-VIS and corresponding bandgap for  $K_xRb_{0.05}Cs_{0.10}FA_{0.85-x}$  system and KRbCsFA with different molar% of  $NH_4Cl$  are showed in **Figure A.V.10-13 (Annex V)**.

## V.4 Characterizations of PSCs

### V.4.1 $J$ - $V$ curves and EQE

**Table V.1 Best cells  $J$ - $V$  curves parameters of solar cells. (Cs: Cs<sub>0.10</sub>FA<sub>0.90</sub>PbI<sub>3</sub>, RbCs: Rb<sub>0.05</sub>Cs<sub>0.10</sub>FA<sub>0.85</sub>PbI<sub>3</sub>, KRbCsFA: K<sub>0.05</sub>Rb<sub>0.05</sub>Cs<sub>0.10</sub>FA<sub>0.80</sub>PbI<sub>3</sub>)**

Name	Additive	Scan direction	$V_{oc}$ [V]	$J_{sc}$ [mA. cm <sup>-2</sup> ]	$FF$	PCE [%]	$HI^a$ [%]
CsFA	NO	Reverse	0.943	23.91	72.13	16.26	26
		Forward	0.846	23.83	59.36	11.96	
RbCsFA	NO	Reverse	1.017	24.49	76.12	18.96	24
		Forward	1.006	24.36	58.89	14.43	
KRbCsFA	NO	Reverse	1.031	23.96	78.08	19.29	3
		Forward	1.034	23.79	76.17	18.74	
KRbCsFA /AC	NH <sub>4</sub> Cl 30 mol%	Reverse	1.083	24.79	78.61	21.10	4
		Forward	1.072	24.66	76.74	20.29	

<sup>a)</sup>  $HI=(PCE_{Rev}-PCE_{For})*100/PCE_{Rev}$

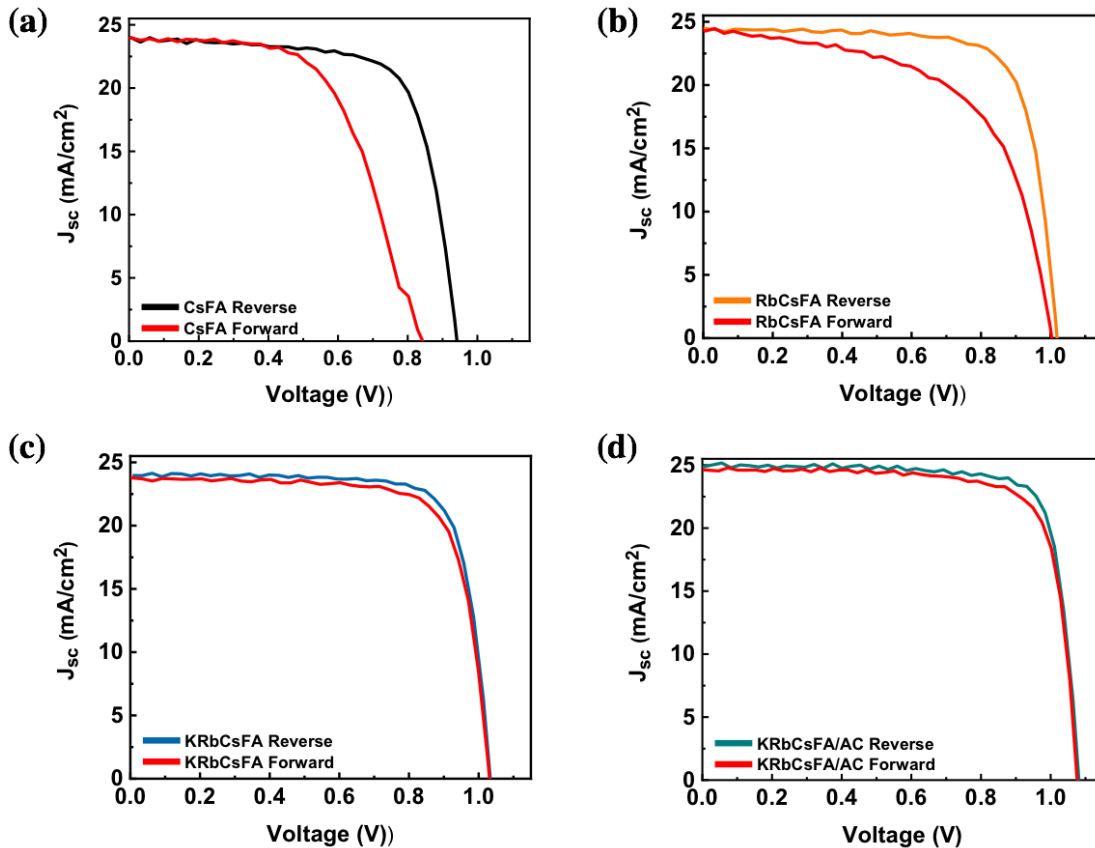


**Figure V.18 Reverse and forward  $J$ - $V$  curves of the best cells listed in Table 1.**

**Table V.1** and **Figure V.18** summarizes the best cells results for different recipes of perovskites. The CsFA cells exhibited poor performances with a *PCE* at 16.2 % on the reverse scan (**Figure V.18a**) and a large hysteresis. After the introduction of Rb ions, all the parameters of the solar cell was enhanced, especially morphology and crystallinity. However, better quality of RbCsFA perovskite still had a large *HI*, which directly caused the low stabilized *PCE*. In order to decrease the *HI* and increase the stabilized *PCE*, we further introduced  $K^+$  in the recipe. In our Chapter IV, we have confirmed that potassium ion (from KCl) can block the movement of iodine ions in perovskite solar cells by passivating native defects, and that it results in a reduction of the *HI* parameter[8]. The actual results are indeed the same as our predictions. By incorporating KI in PPS, the *HI* is decrease from 26% to 3%. In this Chapter, we have done a lot of experiments and measurements on  $NH_4Cl$  added sample and give its detailed action mechanism. From the obtained mechanism, we can see that the formation of  $NH_4Cl$  related intermediates can not only greatly improve the quality of the perovskite film, but also make the distribution of metal cations more uniform. Based on the various benefits given by the additives, the final *PCE* of KRbCsFA/AC sample can achieve 21.1% with a small *HI*.

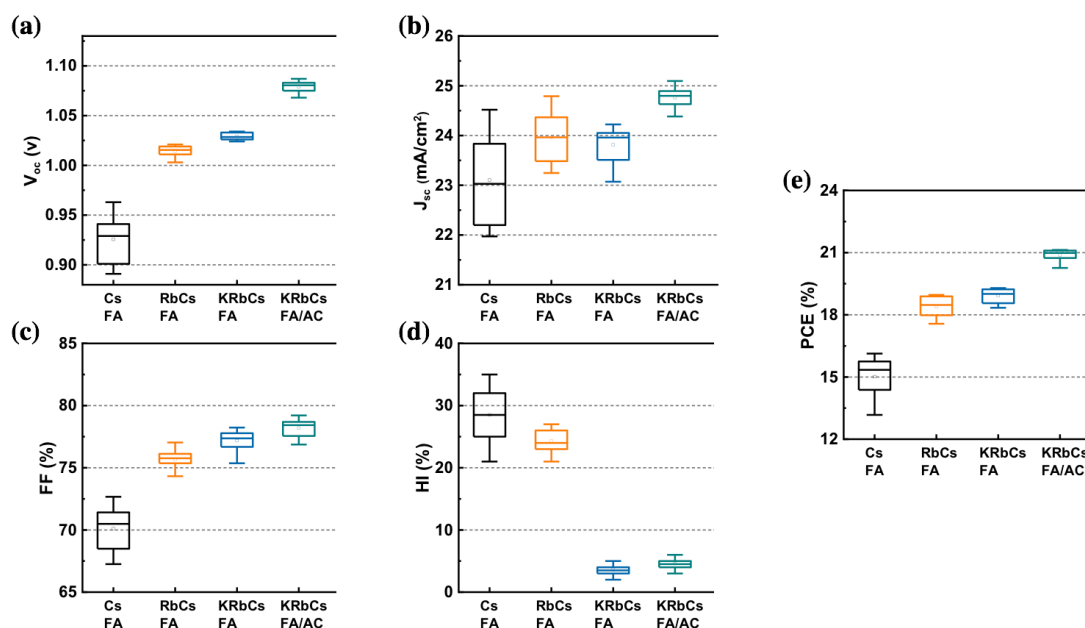


**Figure V.19** Statistical analysis of the optimized PSCs *J-V* curve parameters and *PCE*.

In order to better compare the overall situation of different *J-V* curves parameters of various formulations, their statistical analysis is displayed in **Figure V.19**. We can clearly see that the addition

of Rb mainly improves the  $FF$  and  $V_{oc}$  parameters. The addition of K, compared with the RbCsFA sample, mainly reduces the  $HI$ . Moreover, the addition of  $NH_4Cl$  improved all parameters. It can be seen that the appropriate amount of additives can greatly enhance the performance of the solar cells.

The  $EQE$  spectra are reported in **Figure V.20** and the results are in good agree with the superior  $J_{sc}$  for these devices. In **Figure V.21**, we present the  $PCE$  trackings at the maximum power and corresponding steady-state  $PCEs$ . We first notice that the KRbCsFA devices with potassium have better  $PCE$  compared to RbCsFA, although the results of the reverse scan  $PCE$  are almost the same (**Table V.1**). From the **Figure V.19**, we confirm the conclusion that  $NH_4Cl$  can enhance all the performance parameters of solar cells. Therefore, the best steady-state  $PCE$  was reached for the KRbCsFA/AC PSC due to the synergistic action of potassium ion and ammonium chloride.

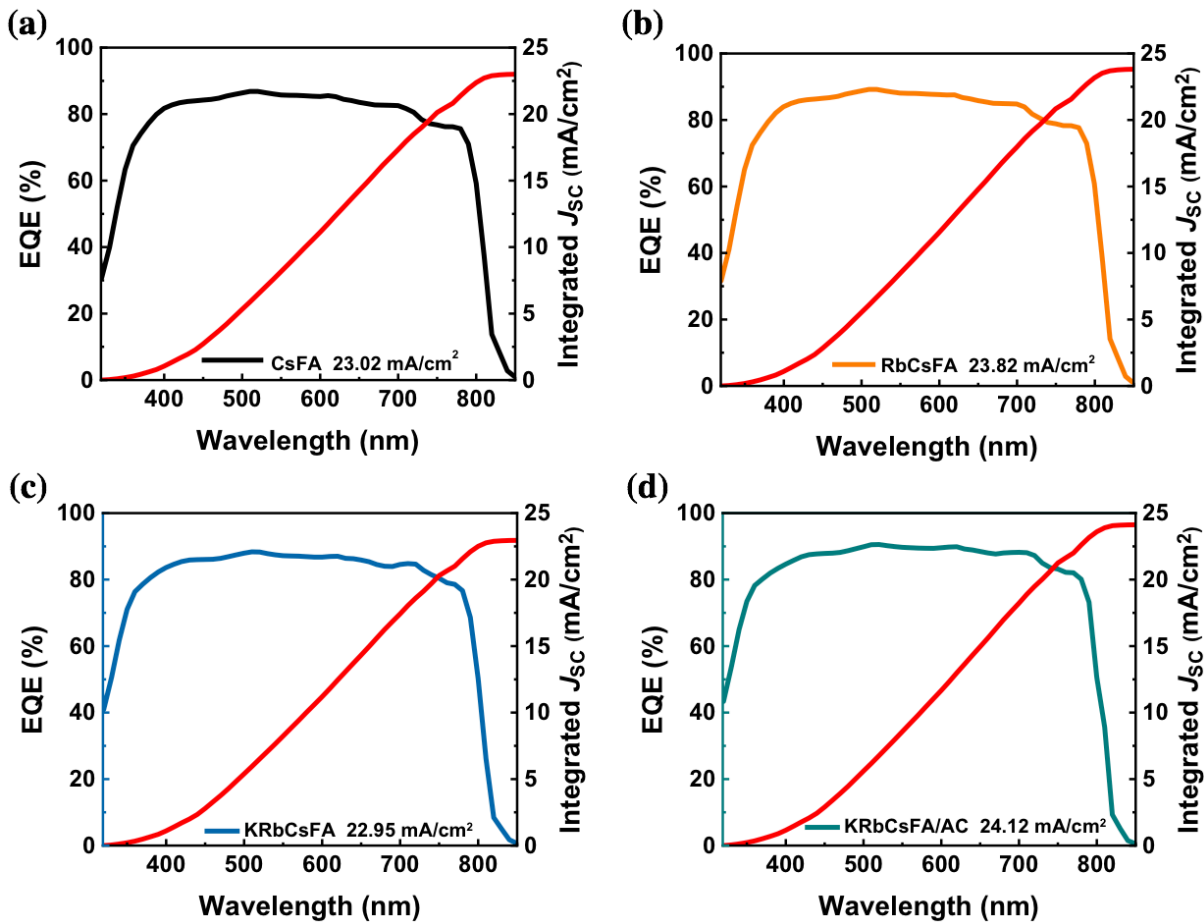


**Figure V.20** Effect of PVK composition on the EQE and  $J_{sc}$  integration curves

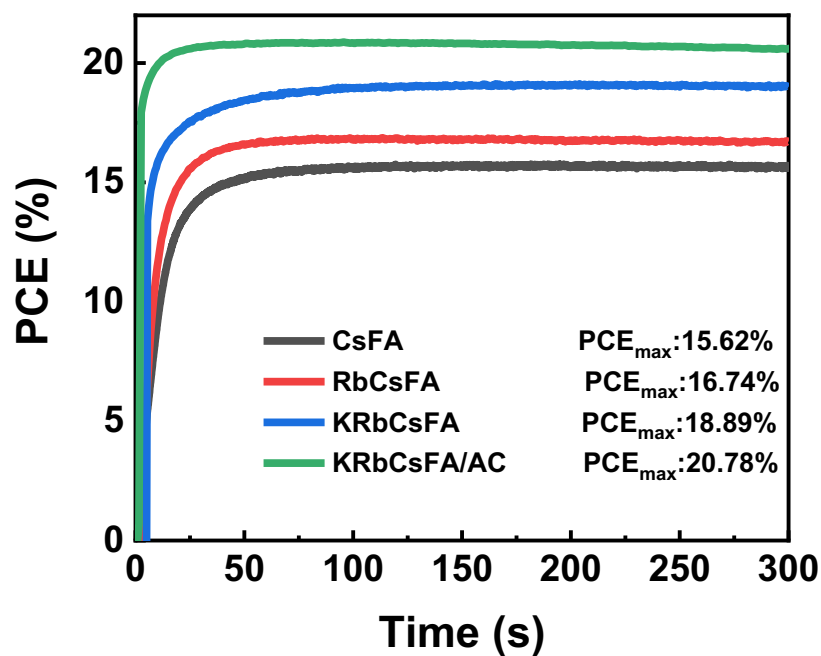


Figure V.21 PCE tracking at the maximum power and steady-state PCE.

#### V.4.2 Stability

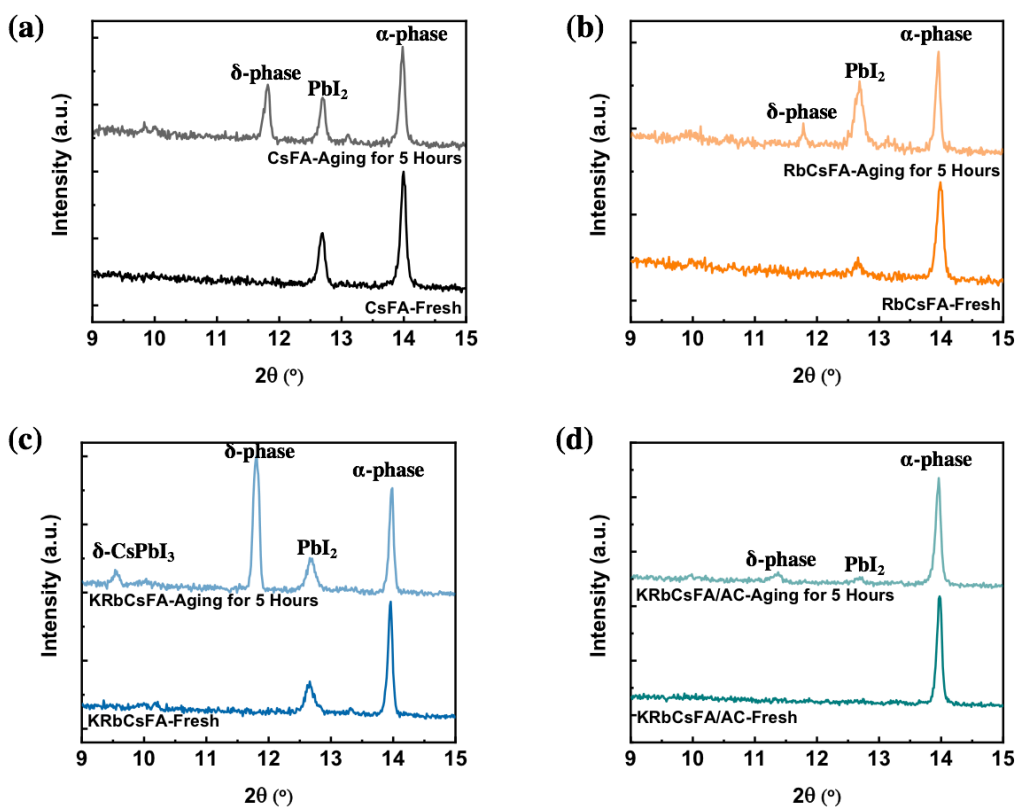


Figure V.22 (a-d) XRD patterns of the (a) CsFA, (b) RbCsFA, (c) KRbCsFA and (d) KRbCsFA/AC layers under harsh condition (unencapsulated, 20°C, 90±5% RH).

**Figure V.22** shows the stability of these four kinds of perovskite layer after ageing for 5 hours under high humidity condition ( $90\pm 5\%$  RH). Although the aging time was only five hours, the results clearly reflect the stability of these four compositions and recipes under high humidity. Compared with RbCsFA sample, CsFA present a better stability as the peak of  $\text{PbI}_2$  appears faster and stronger. Another point worth noting is that RbCsFA aging is more likely to be directly transformed into  $\text{PbI}_2$  than yellow  $\delta$ -phase. The case of CsFA sample is just the opposite to that of RbCsFA sample, as being easier to be transformed into yellow  $\delta$ -phase. For aging, a phase transition is preferable rather than the decomposition of perovskite crystals. However, for a sample doped with potassium ion, accompanied by the decrease in the intensity of the (001) peak is the enhancement of the  $\delta$ -phase peak. At the same time, the new peak around 9.4 degree appear which belong to the  $\delta$ - $\text{CsPbI}_3$ . [38] It indicates that the phase separation is more likely to occur for KRbCsFA sample under high humidity. The incredible thing is that the KRbCsFA/AC sample presents a very high stability compared to other samples and no phase separation happened. The reason for this can be explained by a better crystallization with more uniform distribution of metal cations.

## V.5 Conclusions

In this chapter, we first explored the mechanism of ammonium chloride action in multi-metal cation perovskites and refined it to each preparation process. Through a large number of experiments and tests, we found that ammonium chloride mainly leads to the formation of intermediates which can increase the solubility of  $\text{PbI}_2$  and then favor the formation of a large amount of  $\delta$ -phase which is the phase before transfer to black phase. Secondly, we explored the movement of multi-metal cation in perovskite layer during the film formation process by using GD-OES and presented the intuitive evidence of phase separation caused by potassium. Furthermore, we further confirmed that the targeted growth direction of the film is the lateral growth. Finally, we combined this additive with GD-OES detection technology and found how the additive influence the distribution of multi-metal cation film formation and the formation of intersection layer between perovskite and  $\text{TiO}_2$ . Based on the above research results, we have successfully prepared high-efficiency solar cells, which had a 21.1% PCE (stabilized at 20.8%).

In the Chapter VI, we will use post-treatment technique to greater enhance the performance of perovskite and use a variety of testing methods to prove that post-processing is indispensable for the preparation of perovskite solar cells.

## References

- [1] Pellet, N.; Gao, P.; Gregori, G.; Yang, T. Y.; Nazeeruddin, M. K.; Maier, J.; Gratzel, M. *Angew. Chem. Int. Ed.* **2014**, *53*, 3151–3157.
- [2] Li, X.; Bi, D. Q.; Yi, C. Y.; Decoppet, J. D.; Luo, J. S.; Zakeeruddin, S. M.; Hagfeldt, A.; Gratzel, M. *Science* **2016**, *353*, 58–62.
- [3] Li, Z.; Yang, M. J.; Park, J. S.; Wei, S. H.; Berry, J. J.; Zhu, K. *Chem. Mater.* **2016**, *28*, 284–292.
- [4] Lee, J. W.; Kim, D. H.; Kim, H. S.; Seo, S. W.; Cho, S. M.; Park, N. G. *Adv. Energy Mater.* **2015**, *5*, 1501310–1501318.
- [5] Park, Y. H.; Jeong, I.; Bae, S.; Son, H. J.; Lee, P.; Lee, J.; Lee, C. H.; Ko, M. J. *Adv. Funct. Mater.* **2017**, *27*, 1605988–16059815.
- [6] Saliba, M.; Matsui, T.; Seo, J. Y.; Domanski, K.; Correa-Baena, J. P.; Nazeeruddin, M. K.; Zakeeruddin, S. M.; Tress, W.; Abate, A.; Hagfeldt, A.; Gratzel, M. *Energy Environ. Sci.* **2016**, *9*, 1989–1997.
- [7] Duong, T.; Mulmudi, H. K.; Shen, H. P.; Wu, Y. L.; Barugkin, C.; Mayon, Y. O.; Nguyen, H. T.; Macdonald, D.; Peng, J.; Lockrey, M.; Li, W.; Cheng, Y. B.; White, T. P.; Weber, K.; Catchpole, K. *Nano Energy* **2016**, *30*, 330–340.
- [8] Daming, Z.; Zhu, T.; Pauporte, Th. *Solar RRL* **2021**, 2100010.
- [9] Saliba, M.; Matsui, T.; Domanski, K.; Seo, J. Y.; Ummadisingu, A.; Zakeeruddin, S. M.; Correa-Baena, J. P.; Tress, W. R.; Abate, A.; Hagfeldt, A.; Gratzel, M. *Science* **2016**, *354* (6309), 206–209.
- [10] Yang, W. S.; Noh, J. H.; Jeon, N. J.; Kim, Y. C.; Ryu, S.; Seo, J.; Seok, S. I.; *Science* **2015**, *348*, 1234–1237.
- [11] Shin, S.S.; Yeom, E.J.; Yang, W.S.; Hur, S.; Kim, M.G.; Im, J.; Seo, J.; Noh, J.H.; Seok, S.I.; *Science* **2017**, *356*, 167–171.
- [12] Yang, W. S.; Park, B.-W.; Jung, E. H.; Jeon, N. J.; Kim, Y. C.; Lee, D. U.; Shin, S. S.; Seo, J.; Kim, E. K.; Noh, J. H.; Seok, S. I. *Science* **2017**, *356*, 1376–1379.
- [13] Abdi-Jalebi, M.; Andaji-Garmaroudi, Z.; Cacovich, S. et al. *Nature* **2018**, *555*, 497–501.
- [14] Guoqing, T.; Xinzhang, L.; Zihang, S.; Guopeng, L.; Huan, L.; Linwei, Y.; Jun, X.; Yang, J.; Yun, S.; Yi, S.; Kunji, C. Surface-activation modified perovskite crystallization for improving photovoltaic performance. *Mater. Today Energy* **2017**, *5*, 173–180.
- [15] Guoqing, T.; Dae, S.; Luis K. O.; Yuqiang, L.; Yanqiang, H.; Hui, Z.; Afshan, J.; Longbin, Q.; Zonghao, L.; Yabing, Q. *Adv. Energy Mater.* **2021**, 2003712.
- [16] R. Payling, *Mater. Forum* **1994**, *18*, 195.
- [17] Oswald, S.; Baunack, S. *Thin Solid Films* **2003**, *425*, 9–19.
- [18] Harvey, S.; Zhen, L.; Christians, J.; Kai, Z.; Luther, J.; Berry, J. *ACS Appl. Mater. Interfaces*, **2018**, *10*, 28541–28552.
- [19] Zheng, G.; Zhu, C.; Ma, J. et al. *Nat. Commun.* **2018**, *9*, 2793.

- [20] Philippe, B.; Saliba, M.; Correa-Baena, J.; Cappel, U.; Turren-Cruz, S.; Grätzel, M.; Hagfeldt, A.; Rensmo, H.; *Chem. Mater.* **2017**, *29*, 3589–3596.
- [21] Turren-Cruz, S.; Hagfeldt, A.; Saliba, M.; *Science* **2018**, *362*, 449-453.
- [22] Shunde, L.; Zhou, L.; Zhi, Q.; Xiao, W.; Lei, C.; Yufeng, Z.; Qiaofei, X.; Zhimin, L.; Ke, M.; Gang, Chen.; *Adv. Funt. Mat.* **2020**, *30*, 2005846.
- [23] Meng, Z.; Jueming, B.; Yongyoon, C.; Yong, L.; Jianhui, Z.; Lau, C. F. J.; Green, M. A.; Shujuan, H.; Ho, A. W.Y. *Nano Energy*, **2019**, *63*, 2211-2855.
- [24] Abdi-Jalebi, M.; Andaji-Garmaroudi, Z.; Cacovich, S.; Stavrakas, C.; Philippe, B.; Richter, J.M.; Alsari, M.; Booker, E.P.; Hutter, E.M., Pearson, A.J.; Lilliu, S.; Savenije, T.J.; Rensmo, H.; Divitini, G.; Ducati, C.; Friend, R.H.; Stranks, S.D.; *Nature*, **2018**, *555*, 497.
- [25] Qin, M.; Tse, K.; Lau, T.-K.; Li, Y.; Su, C.-J.; Yang, G.; Chen, J.; Zhu, J.; Jeng, U.-S.; Li, G.; Chen, H.; Lu, X. *Adv. Mater.* **2019**, *31*, 1901284.
- [26] Schelhas, L. T.; Li, Z.; Christians, J. A.; Goyal, A.; Kairys, P.; Harvey, S. P.; Kim, D. Hoe; Stone, K. H.; Luther, J. M.; Zhu, Stevanovic, K. V.; Berry, J. J. *Energy Environ. Sci.* **2019**, *12*, 1341.
- [27] Guo, Y.; Shoyama, K.; Sato, W.; Matsuo, Y.; Inoue, K.; Harano, K.; Liu, C.; Tanaka, H.; Nakamura, E. *J. Am. Chem. Soc.* **2015**, *137*, 15907–15914.
- [28] Dolzhenkov, D. S.; Zhang, H.; Jang, J.; Son, J.; Panthani, M. G.; Shibata, T.; Chattopadhyay, S.; Talapin, D.V. *Science* **2015**, *347*, 425-428.
- [29] Philippe, B.; Saliba, M.; Correa-Baena, J.; Cappel, B.; Cruz, S.; Grätzel, M. HakanRensmo, A. *Chem. Mater.* **2017**, *29*, 3589–3596
- [30] Grancini, G.; Roldán-Carmona; Zimmermann, C. I.; Mosconi, E.; Lee, X.; Martineau, D.; Nabey, S.; Oswald, F.; De Angelis, F.; Graetzel, M.; Nazeeruddin, M. K. One-Year stable perovskite solar cells by 2D/3D interface engineering. *Nature Commun.* **2017**, *8*, 15684;
- [31] Yang, W.S.; Noh, J.H.; Jeon, N.J.; Kim, Y.C.; Ryu, J.; Seo, S.; Seok, S.I. High-performance photovoltaic perovskite layers fabricated through intramolecular exchange. *Science* **2015**, *348*, 1234.
- [32] Lee, J.-W.; Seol, D.-J.; Cho, A.-N.; Park, N.-G. *Adv. Mater.* **2014**, *26*, 4991-4998.
- [33] Dai, X.; Deng, Y.; Van Brackle C.H.; Chen, S.; Peter, N.; Rudd, X.; Xiao, Y.; Chen, B.; Huang, J. *Adv. Energy Mater.* **2020**, *10*, 1903108.
- [34] Eperon, G. E.; Paterno, G. M.; Sutton, R. J.; Zampetti, A.; Haghighirad, A. A.; Cacialli, F.; Snaith, H. J. *J. Mater. Chem. A* **2015**, *3*, 19688.
- [35] Sutton, R. J.; Eperon, G. E.; Miranda, L.; Parrott, E. S.; Kamino, B. A.; Patel, J. B.; Hörantner, M. T.; Johnston, M. B.; Haghighirad, A. A.; Moore, D. T.; Snaith, H. J. *Adv. Energy Mater.* **2016**, *6*, 1502458.
- [36] Trots, D. M. ; Myagkota, S. V. *J. Phys. Chem. Solids* **2008**, *69*, 2520.
- [37] Ge, J.; Ma, Z.; Chen, W.; Cao, X.; Yan, J.; Fang, H.; Qin, J.; Liu, Z.; Pan, S. *Nanoscale* **2020**, *12*, 13558-13566
- [48] Nengxu, L.; Yanqi, L.; Zehua, C.; Xiuxiu, N.; Xiao, Z.; Jiuzhou, L.; Rishi, K.; Junke, J.; Huifen, L.; Xiao, G.; Barry, L.; Geert, B.; Qi, C.; Shuxia, T.; David, P.; Fen, N.; Huanping, Z. *Joule*, **2020**, *4*, 1743-1758.

## Chapter VI. The Effect of PAI post-treatment on Perovskite layer

### VI.1 Introduction

2D halide perovskites have recently been recognized as a promising avenue in perovskite solar cells (PSCs) in terms of encouraging stability and defect passivation effect. However, the efficiency of ultrastable 2D Ruddlesden–Popper PSCs still lag far behind their 3D perovskite counterparts. However, the formation of a 2D capping layer on PVK by its surface treatment is classically employed to boost the PSC performances. The strategy of using a variety of ammonium compounds which react with the 3D perovskite and form a 2D perovskite layer appears as especially promising. For example, solutions of n-butylammonium iodide,[1] 2-phenylethylammonium iodide (PEAI), (See Refs[2, 3, 4] and **Chapter II, Section II.1.3**) n-hexylammonium bromide, [5] n-propylammonium iodide [6], propane-1,3-diammonium (PDA) iodide [6] and 1,6-diaminohexane ammonium iodide [7] can be spin-coated on the 3D perovskite layer and then form 2D perovskite layer with wide bandgap. The 2D capping layers form a barrier that protect the underneath 3D perovskite films and constitute an intermediate energy band mitigating exciton recombination.[8] What we need to explain in advance is that the PEAi post-treatment used in **Section II.1 (Chapter II)** has no effect on the MA-free perovskite system (**Table VI.1, Annex VI**). Consequently, in this chapter, we have only focused our attention on PAI (n-propylamine hydroiodide or n-propyl ammonium iodide). Through the application of PAI post-treatment to  $\text{Cs}_{0.1}\text{FA}_{0.9}\text{PbI}_3$  (developed in **Chapter IV**) and  $\text{K}_{0.05}\text{Rb}_{0.05}\text{Cs}_{0.10}\text{FA}_{0.80}\text{PbI}_3$  (developed in **Chapter V**) systems, we found a great improvement of the performance of the solar cells, not only in their efficiency, but also in their stability. To better present the effect of PAI post-treatment, we will mainly show the result of  $\text{Cs}_{0.1}\text{FA}_{0.9}\text{PbI}_3$  system in the main body of **Chapter VI** while most of the  $\text{K}_{0.05}\text{Rb}_{0.05}\text{Cs}_{0.10}\text{FA}_{0.80}\text{PbI}_3$  system case is treated in the **Annex VI, Chapter VI**.

### VI.2 Experimental

The preparation of substrates, compact  $\text{TiO}_2$  layer and mesoporous  $\text{TiO}_2$  layer were conducted as detailed in **Chapter II, Section II.1.2.1**.

### VI.2.1 Preparation of Perovskite Films

The *KC-5/AC-30* (here after AKC) and *KRbCsFA/AC* layers, were prepared as described in **Section IV.2.1 (Chapter IV)** and **Section V.2.1 (Chapter V)** respectively.

### VI.2.2 Post-treatment Method

The PAI post-treatment consisted of dropping 60  $\mu\text{L}$  of a 4 mg/mL propylamine hydroiodide (also called n-propylammonium iodide and noted PAI) solution onto the perovskite film after its cooling. A one-step spin-coating program was employed just after the solution deposition (2000 rpm/s acceleration, 3000 rpm for 20s). Thenafter, the samples were not heated. The optimized treated films are noted AKC-PAI and KRbCsFA/AC-PAI, hereafter.

### VI.2.3 Characterizations Method

The characterizations of the layers by XRD, SEM, UV-vis absorbance, steady-state PL and TRPL were done as described in **Chapter II, Section II.1.2.3**. The measurements of *J-V* curves, maximum power point tracking and *EQE* spectra of the devices are described in **Chapter II, Section II.1.2.3**.

## VI.3 Characterizations of perovskite Films

### VI.3.1 SEM

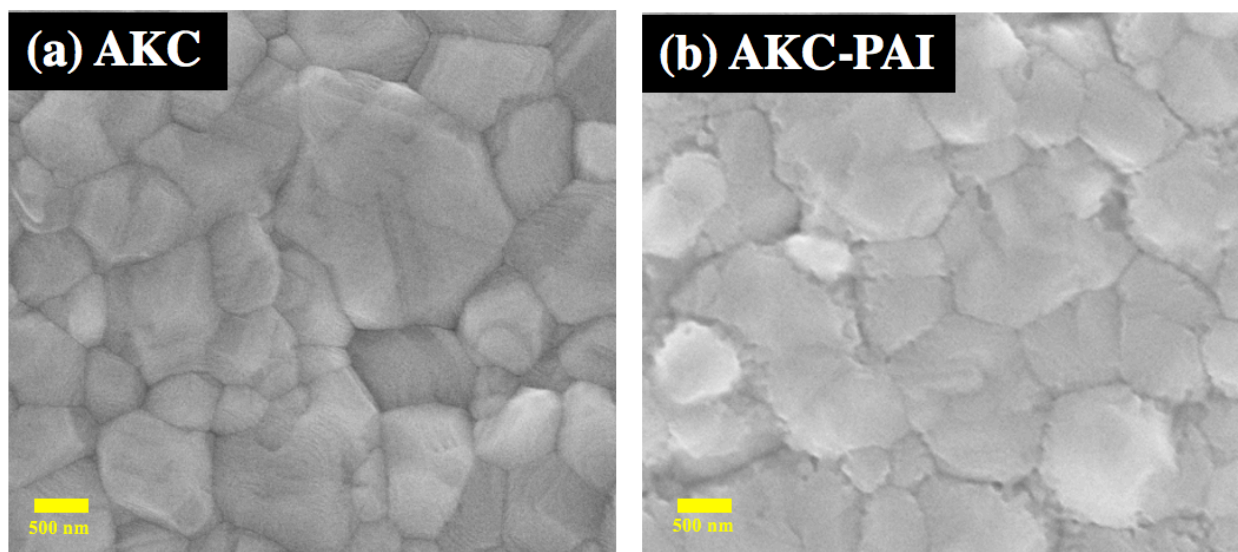


**Figure VI.1 SEM  $\text{Cs}_{0.1}\text{FA}_{0.9}\text{PbI}_3$  layer top views before (a) and after (b) PAI treatment.**

In **Figure VI.1**, the PVK layer surface was altered after the PAI post-growth treatment with the formation of the capping layer. This change was clearly visible at the grain boundaries with the presence of an extra-phase. The appearance of this extra-phase reduced the height difference between the grains, so that the surface roughness was reduced, which is more conducive to the close combination of the perovskite layer and the HTM layer. To prove this, we performed AFM imaging measurements of the KRbCsFA/AC sample surface and found that the average roughness decreased from 29.7 nm (before post-treatment) to 22.12 nm (after post-treatment) (**Figure A.VI.1, Annex VI**). We also obtained the same roughness reduction with the MAPI system. (**Figure III.3, Chapter III**). the effect of the treatment on the PSC performance is discussed in **Section VI.4.1**.

### VI.3.2 XRD

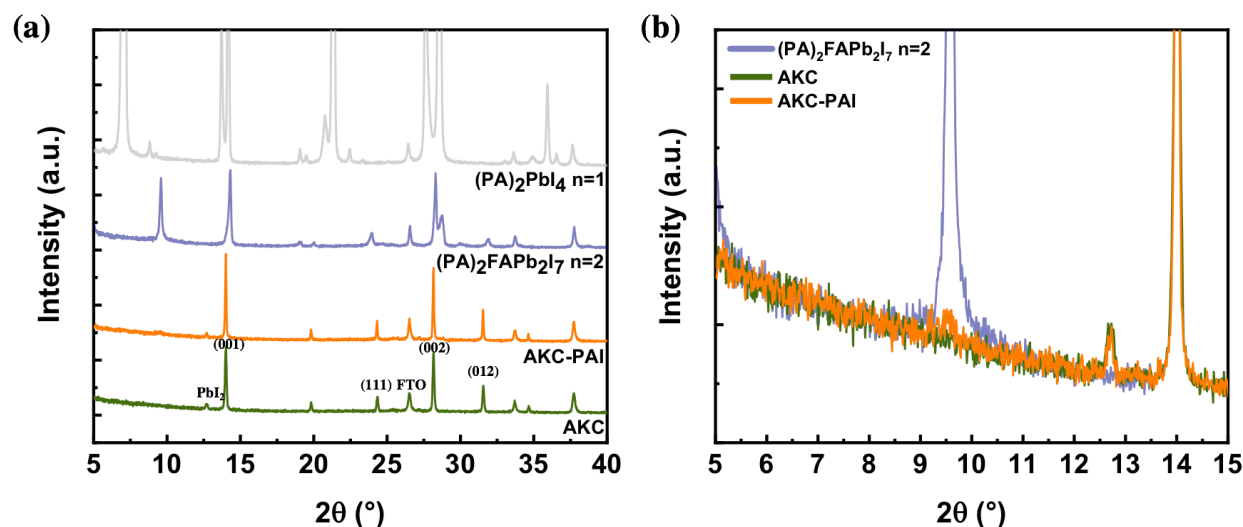


**Figure VI.2 (a)** XRD patterns of Cs<sub>0.1</sub>FA<sub>0.9</sub>PbI<sub>3</sub> layers. The same sample was measured before and after the PAI treatment. **(b)** Enlarged XRD pattern . Comparison with (PA)<sub>2</sub>PbI<sub>4</sub> (n=1) and (PA)<sub>2</sub>FAPbI<sub>7</sub> (n=2) reference 2D layers.

The XRD patterns of a AKC sample before and after the PAI treatment are compared in **Figure VI.2a** and **b**. PAI did not react with PbI<sub>2</sub> since the PbI<sub>2</sub> peak at 12.7° was unchanged. On the other hand, the PVK peaks intensity increased. The treatment resulted in a recrystallization and quality improvement of the PVK. It also caused the appearance of a small extra-XRD peak at 9.53° (**Figure VI.2b**). Based on the reference XRD patterns displayed in **Figure VI.2a**, this peak is assigned to the (040) reflection of the 2D (PA)<sub>2</sub>FAPbI<sub>7</sub> (n=2) compound.

### VI.3.3 Absorbance and Steady-state PL

We measured the absorbance spectra of the films before and after the treatment. In **Figure VI.3a**, the absorbance of the latter is slightly reduced. To reveal the absorbance contribution of the capping layer, we plotted the curve derivative (**Figure VI.3b**). The differential absorbance presented a peak at 580 nm. This peak was indexed based on the absorbance curve of reference 2D layers prepared with  $n=1$  and  $n=2$  stoichiometries. Their absorbance curve presented a main peak at 500 nm for  $n=1$  and 580 nm for  $n=2$ . The absorbance differential peak at 580 nm of AKC-PAI film fit then with  $n=2$  (**Figure VI.2b**). We have also measured the PL spectra of the AKC-PAI films. Above the main emission at 806 nm due to the 3D  $\text{Cs}_{0.1}\text{FA}_{0.9}\text{PbI}_3$  phase of AKC, the spectrum of the treated sample presented an extra-emission at 570-580 nm (**Figure VI.2c**) which agrees with the absorbance observation and confirms that the produced capping layer is mainly made of 2D  $(\text{PA})_2\text{FAPb}_2\text{I}_7$ . Its formation can be described as follows: the surface 3D perovskite is partly dissolved by isopropyl alcohol (IPA) and PAI reacts with the release compounds to form the 2D layer.[9] It is at the origin of recombination suppression at the PVK/HTL interface and then to the increased  $V_{oc}$  and  $FF$  parameters.

### VI.3.4 TRPL

In **Figure A.VI.2 (Annex VI)**, we present the time-resolved photoluminescence (TRPL) decay curves for KRbCsFA/AC and KRbCsFA/AC-PAI samples. The curves were analyzed by using three exponential decay components and the fitting parameters are gathered in **Table A.IV.2 (Annex VI)**. We can clearly see that the fast component is much longer for the sample without PAI post-treatment ( $\tau_{\text{fast}} = 19.97$  ns) compared to the PAI post-treated sample ( $\tau_{\text{fast}} = 1.55$  ns). Moreover, the faster decay is analyzed as an efficient quenching of the radiative recombination by the fast transfer of the hole toward the 2D capping layer. The slower decay time is related to the structural quality of the perovskite layers. The longer is this value, the better is the structural quality of the material. Depending on this, we measured  $\tau_{\text{slow}}$  at 252.69 ns and 454.65 ns for KRbCsFA/AC and KRbCsFA/AC-PAI samples, respectively. It can be explained by the fact that using PAI post-treatment improves of the crystal quality at the perovskite layer near surface and defect passivation. This result agrees with our conclusion on the perovskite XRD peak intensity enhancement in **Figure VI.2a**.

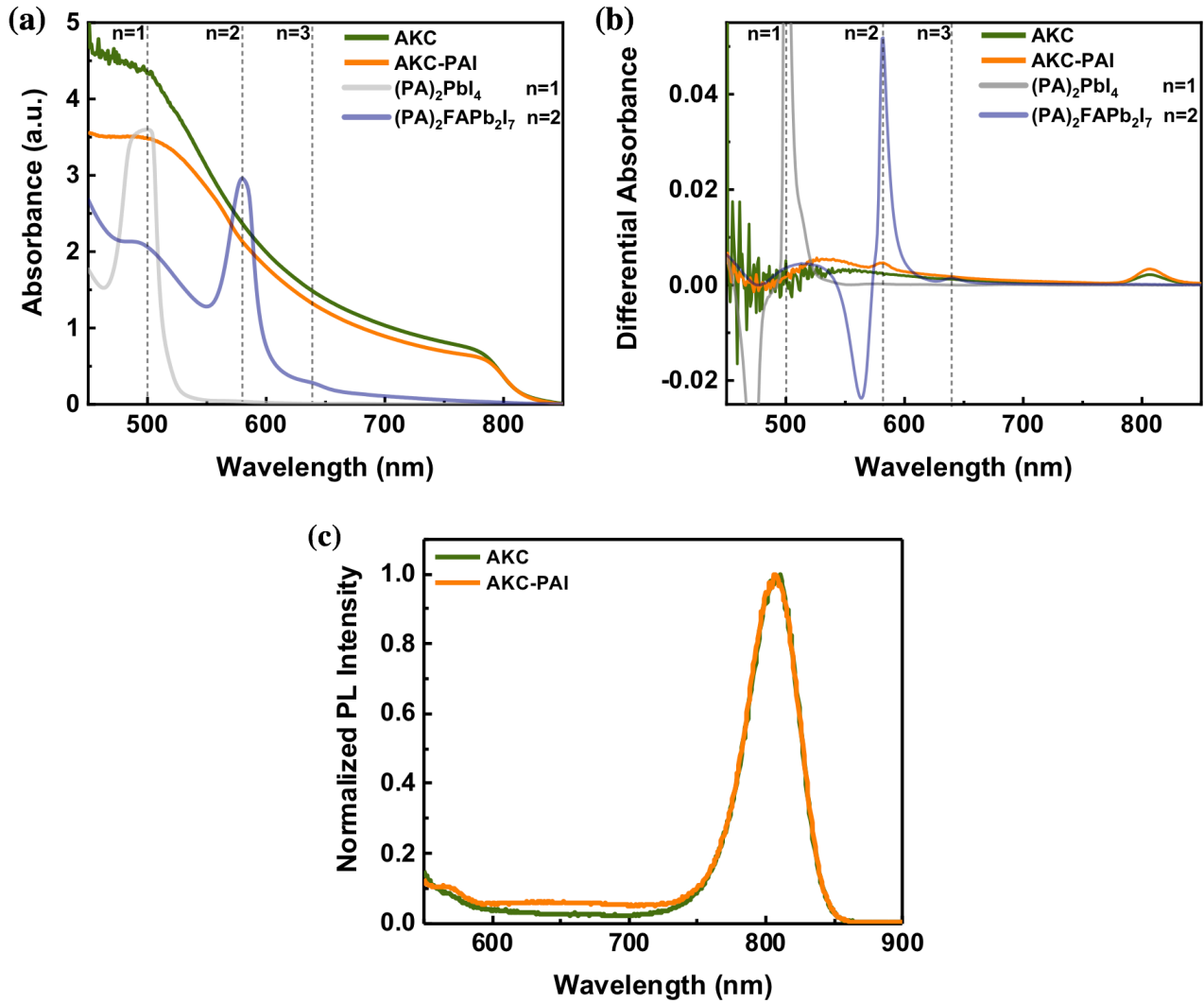


Figure VI.3 Optical properties of  $\text{Cs}_{0.1}\text{FA}_{0.9}\text{PbI}_3$  layers. The same sample was measured before and after the treatment. (a) absorbance spectra and (b) absorbance differential spectra of AKC layers before and after the PAI treatment. Comparison with  $(\text{PA})_2\text{PbI}_4$  (n=1) and  $(\text{PA})_2\text{FAPbI}_7$  (n=2) reference 2D layers. (c) photoluminescence spectrum of AKC sample before and after PAI post-treatment.

## VI.4 Characterizations of PSCs

### VI.4.1 *J-V* curves and EQE

**Table VI.1 Effect of PAI concentration in IPA solvent on the *J-V* curves parameters of AKC(-PAI) cells.**

Name	Scan direction	V <sub>oc</sub> [V]	J <sub>sc</sub> [mA.cm <sup>-2</sup> ]	FF [%]	PCE [%]	HI <sup>a)</sup> [%]
AKC	Reverse	1.014	25.23	78.69	20.13	4
	Forward	1.012	24.96	76.84	19.41	
AKC-PAI (2 mg/mL)	Reverse	1.034	25.12	78.88	20.48	4
	Forward	1.035	24.98	76.07	19.67	
AKC-PAI (3 mg/mL)	Reverse	1.045	25.24	78.54	20.72	1
	Forward	1.046	25.17	77.03	20.28	
AKC-PAI (4 mg/mL)	Reverse	1.051	25.31	79.23	21.08	3
	Forward	1.049	25.02	77.91	20.45	
AKC-PAI (5 mg/mL)	Reverse	1.043	24.89	77.61	20.15	2
	Forward	1.042	24.74	76.73	19.78	

<sup>a)</sup>  $HI = (PCE_{Rev} - PCE_{For}) * 100 / PCE_{Rev}$

**Table VI.2 Effect of PAI concentration in IPA solvent on the *J-V* curves parameters of KRbCsFA/AC cells.**

Name	Scan direction	V <sub>oc</sub> [V]	J <sub>sc</sub> [mA.cm <sup>-2</sup> ]	FF [%]	PCE [%]	HI <sup>a)</sup> [%]
KRbCsFA/AC	Reverse	1.083	24.79	78.69	21.13	4
	Forward	1.072	24.66	76.84	20.32	
KRbCsFA/AC- PAI (2 mg/mL)	Reverse	1.093	24.67	78.72	21.23	2
	Forward	1.095	24.41	77.89	20.82	
KRbCsFA/AC- PAI (3 mg/mL)	Reverse	1.109	24.73	79.03	21.67	3
	Forward	1.107	24.59	77.38	21.06	
KRbCsFA/AC- PAI (4 mg/mL)	Reverse	1.121	24.86	80.83	22.53	4
	Forward	1.116	24.71	78.84	21.74	
KRbCsFA/AC- PAI (5 mg/mL)	Reverse	1.102	24.08	76.36	20.26	3
	Forward	1.095	24.12	74.82	19.76	

<sup>a)</sup>  $HI = (PCE_{Rev} - PCE_{For}) * 100 / PCE_{Rev}$

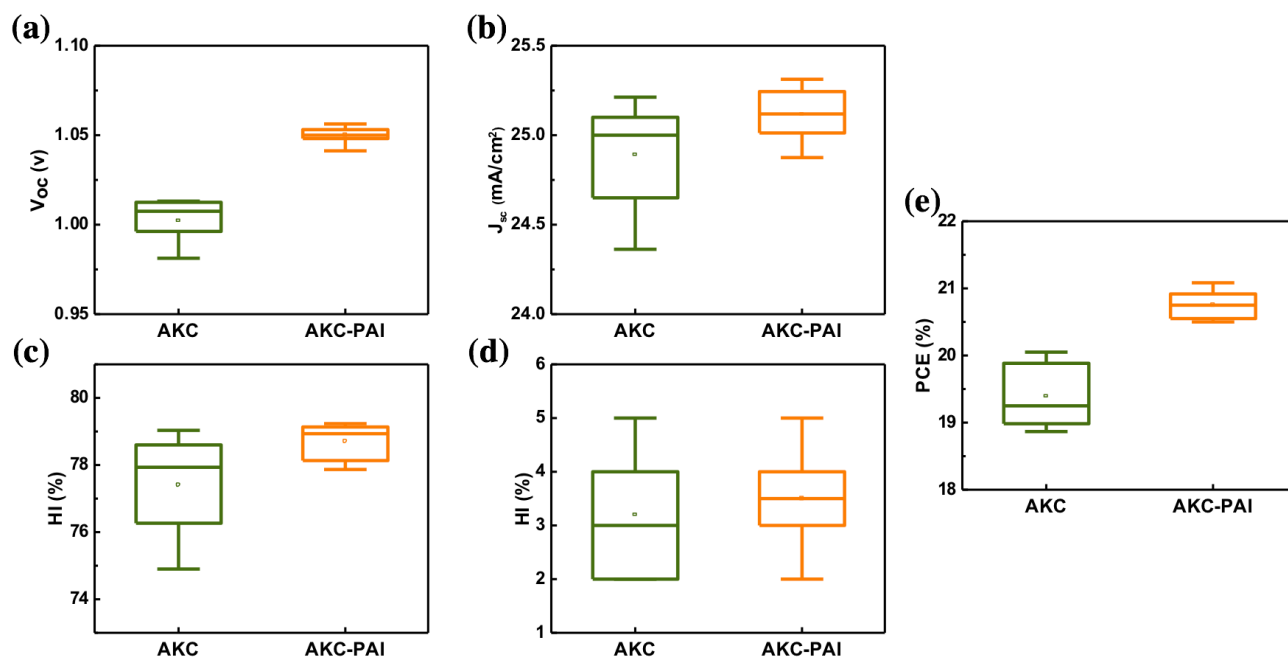


**Figure VI.4** Statistical analysis of the  $J$ - $V$  curve parameters with (AKC-PAI) and without (AKC) PAI post-treatment. ( $4\text{mg}\cdot\text{mL}^{-1}$  PAI concentration in IPA).

The effect of spin-coating a solution of PAI at various concentration in isopropyl alcohol (IPA) solvent on the  $J$ - $V$  curves is disclosed in **Table VI.1** for the CsFAPbI<sub>3</sub> system and in **Table VI.2** for the KRBcCsFA/AC system. An improvement of the performances was found for all the investigated concentrations and the best efficiencies for these two systems were obtained for  $4\text{mg}\cdot\text{mL}^{-1}$  with a  $PCE$  that reached 21.08% (**Figure VI.4**, **Table VI.1**) and 22.53% (**Table VI.2**), respectively. The statistical analysis (**Figure VI.4**) figures out that this treatment mainly improved the cell  $V_{oc}$  and the  $FF$ , while the  $J_{sc}$  was unchanged at a high value. It is concluded that the PAI treatment reduces the charge recombination at the PVK/HTL interface.

The external quantum efficiency ( $EQE$ ) spectra and integrated current density of the AKC and AKC-PAI cells are plotted as a function of the wavelength in **Figure VI.5b**. Both  $J_{sc}$ , calculated and measured on the  $J$ - $V$  curves, are in good agreement. In **Figure VI.5b**, the  $EQE$  of the latter is slightly reduced in agreement with the slight reduction of the absorbance showed in **Figure VI.3a**. The  $EQE$  result of KRBcCsFA/AC system, is presented in **Figure A.VI.3c** and **d** (**Annex VI**). We also found that the integrated current increased slightly and its increase is consistent with  $J_{sc}$  (**Table A.VI.3**, **Figure A.VI.3a** and **b** in the **Annex VI**). The significant improvement was confirmed by measuring the

steady-state *PCE* which achieved 21.03% for AKC-PAI (**Figure VI.5c**) and 22.04% for KRbCsFA/AC-PAI (**Figure VI.6**). Both values are very close to the ones measured on the *J-V* curves and gained around 1% absolute compared to the untreated AKC and KRbCsFA/AC cells.

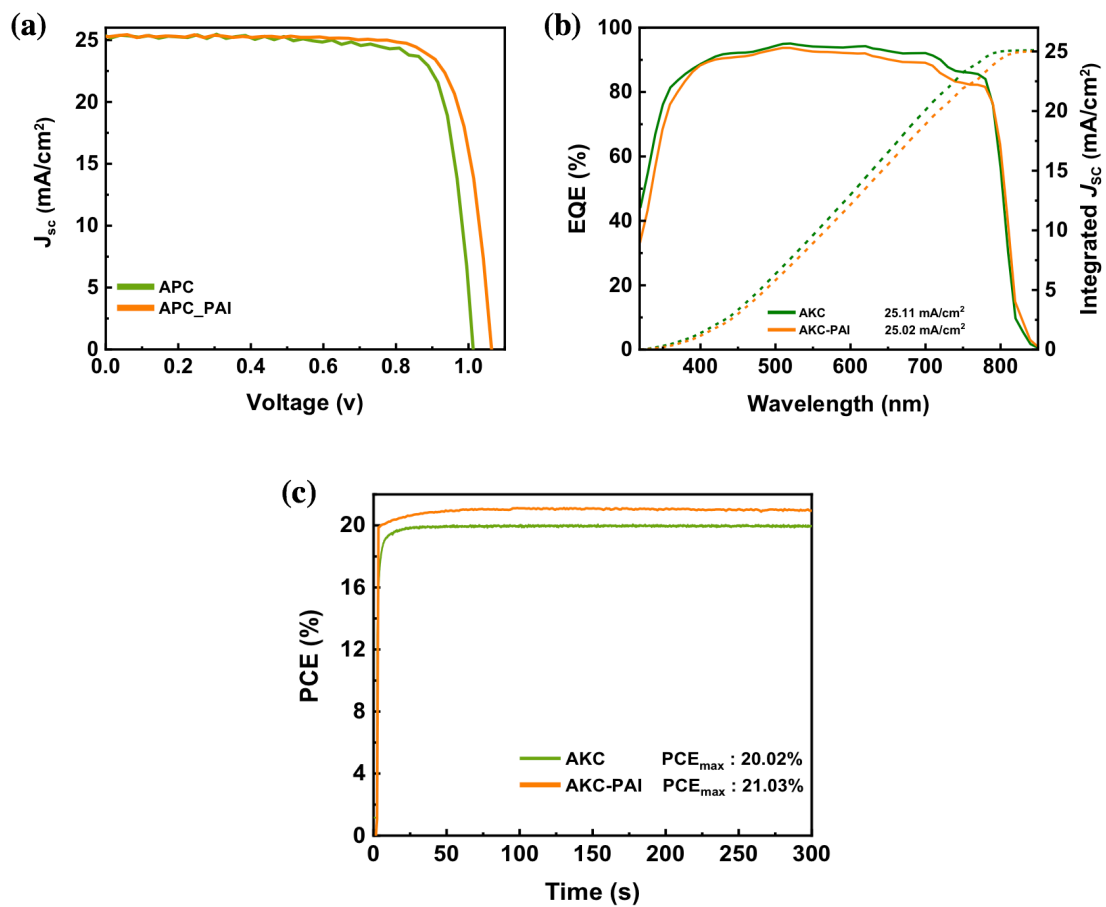
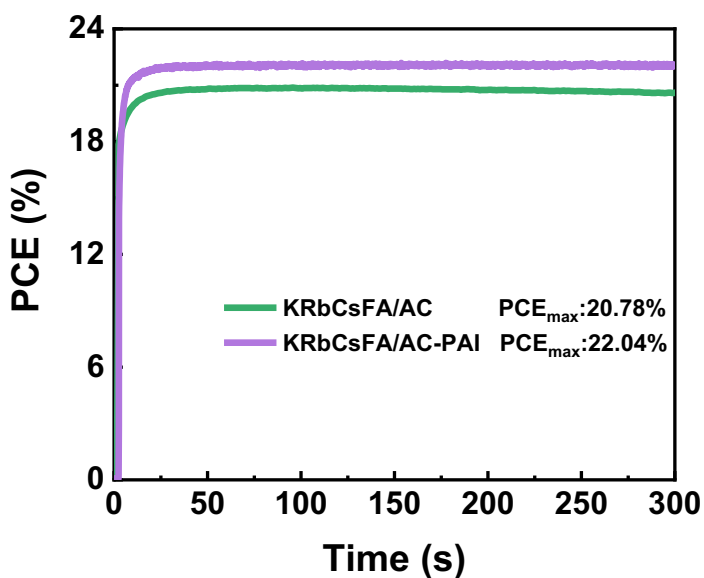


Figure VI.5 Effects of capping layer on (a) the reverse scan *J-V* curves, (b) *EQE* spectra and integrated *Jsc* curves of AKC cells. (c) Steady-state *PCE* at the maximum power point.



**Figure VI.6** steady-state PCE at the maximum power point.

#### VI.4.2 Stability

The future of the PSC technology will depend on the ability of scientists to develop devices highly resistant to heat, moisture, and light and which stand long-term operation. This led us to evaluate the effect of our double engineering approach on the stability toward various degradation agents. First, the stability of unencapsulated cells under one sun illumination was followed by tracking at their maximum power point (MPP). **Figure VI.7a** shows that the PAI-treated cell was the most efficient and stable. After a small *PCE* decrease during the first 70 min, the *PCE* increased slowly for the next hours. It suggests some initial interfacial reorganization before stabilization and improvement. Getting PSCs highly stable under high moisture is the trickiest issue because PVKs form hydrate compounds in the presence of humidity.[9,10] We performed a highly demanding test by following unencapsulated cells aged under high humidity environment ( $RH \geq 90\%$ , the other conditions being ambient) for several days. In **Figure VI.7b** follows the normalized *PCE* of AKC and AKC-PAI cells. The remarkable result is that coupling the mixed chloride additives (AKC) and the surface treatment (AKC-PAI) even further improved the stability of the cells. The unencapsulated AKC-PAI cells retained about 80% of their initial *PCE* after 40 h of aging in this case. This test, performed under highly demanding conditions,

is an accelerated one, and one can expect a much better stability for devices after their *ad hoc* encapsulation.

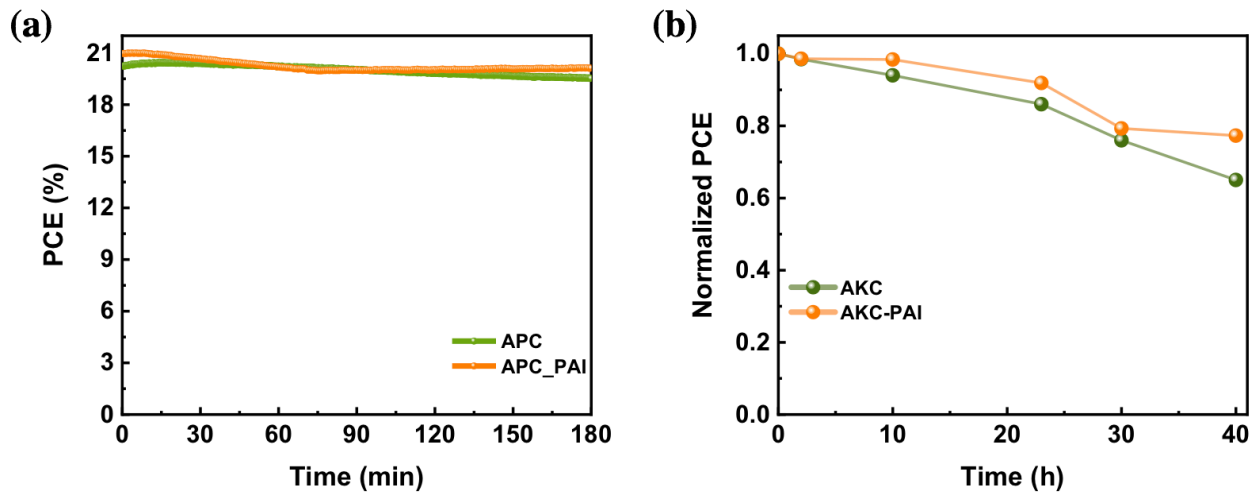


Figure VI.7 (a) Tracking of the AKC and AKC-PAI cells at their maximum power point; (b) Normalized PCE evolution of cells stored under ambient condition and very high humidity (RH $\geq$ 90%).

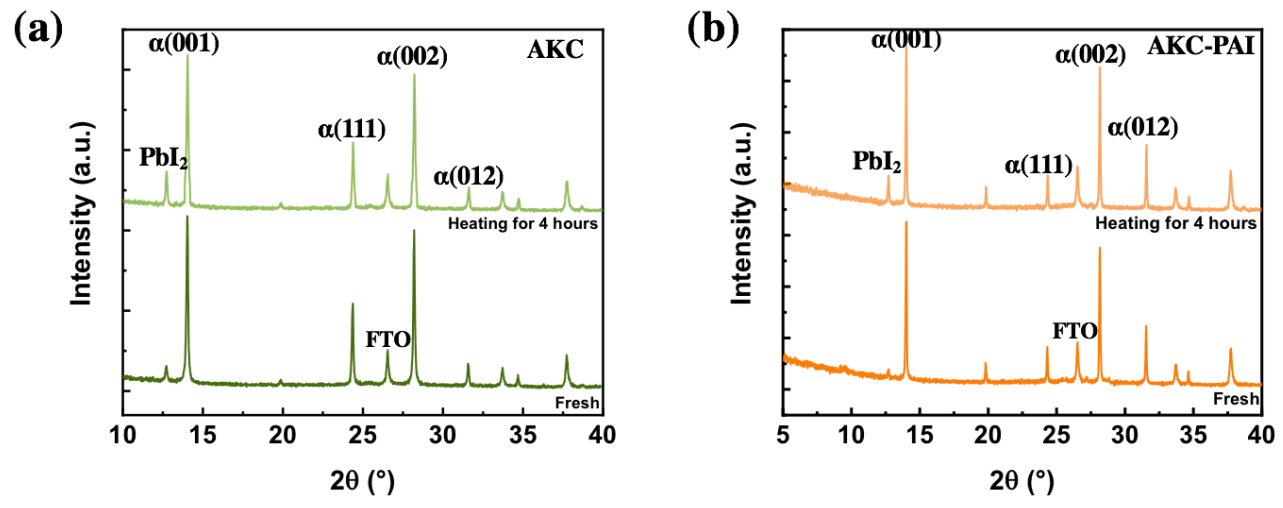
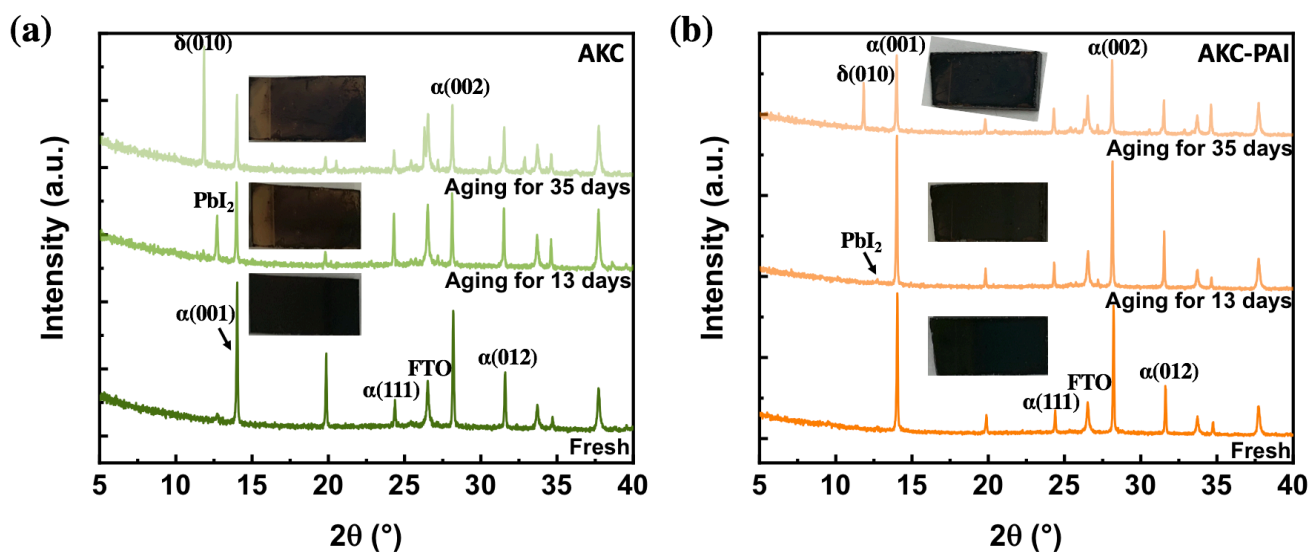


Figure VI.8 Effect of layer heating at 130°C for 4h on the XRD pattern of (a) AKC and (b) AKC-PAI layers.

We also implemented accelerated aging tests. The thermal stability was investigated by heating the layers at 130°C for 4h in a N<sub>2</sub>-filled glovebox. The results, disclosed in **Figure VI.8**, show that PbI<sub>2</sub> is the heating degradation product of α-Cs<sub>0.1</sub>FA<sub>0.9</sub>PbI<sub>3</sub>. Using the chloride mixed-additives (AKC sample) led to films with less initial PbI<sub>2</sub>, to a decrease of the PbI<sub>2</sub> formation by heating and then slowed down the thermal degradation. The capping layer further suppressed the degradation and the AKC-PAI layer

was more stable than the AKC one. After 4 hours, the PVK/PbI<sub>2</sub> peak ratio (at 13.9° and 12.7°) was 3.4 for AKC sample and 4.6 for the AKC-PAI sample. The aging of the layers stored under ambient air (20°C, 55±10% relative humidity (RH)) was followed by XRD. **Figure VI.9** shows that the employment of the chloride additives was of great effectiveness since the  $\alpha$ -phase was still present after 35 days in the AKC sample even if the  $\delta$ -phase (010) peak was more intense than the  $\alpha$ -phase (001) one. The interesting point is that the capping layer further increased the stability. After 13 days of aging, the XRD pattern was unchanged. After 35 days, the sample was still black colored and the most intense diffraction peaks were those of the  $\alpha$ -phase.



**Figure VI.9** XRD patterns of the (a) AKC and (b) AKC-PAI layers under ambient condition (20°C, 55±10% RH). The insets are layers pictures.

## VI.5 Conclusions

In summary, we have fabricated highly efficient and stable MA-free PSCs by constructing the interfacial capping layers at the perovskite and HTL interfaces. Treating the film surface with *n*-propylammonium iodide (PAI) resulted in a record stabilized PCE of 21.03% for the CsFAPI system and 22.04% for the KRbCsFA/AC system. Moreover, we have proved that the optimized films are highly resistant to electrical, light, moisture, and temperature external stressors and that this resistance is reinforced by the capping interfacial layer.

## References

- [1] Lin, Y.; Bai, Y.; Fang, Y.; Chen, Z.; Yang, S.; Zheng, X.; Tang, S.; Liu, Y.; Zhao, J.; Huang, J. *Phys. Chem. Lett.* **2018**, *9*, 654.
- [2] Cho, K. T.; Grancini, G.; Lee, Y.; Oveisi, E. J.; Ryu, Almora, O.; Tschumi, M.; Schouwink, P. A.; Seo, G.; Heo, S.; Park, J.; Jang, J.; Paek, S.; Garcia-Belmonte, G.; Nazeeruddin, M. K. *Energy Environ.Sci.* **2018**, *11*, 952.
- [3] X. Wang, Y. Wang, T. Zhang, X. Liu, Y. Zhao, *Angew. Chem., Int. Ed.* **2020**, *59*, 1469.
- [4] Zhu, T.; Zheng, D.; Rager, M.-N.; Pauporté, Th. *Sol. RRL*, **2020**, *4*, 2000348.
- [5] Yoo, J. J.; Wieghold, S.; Sponseller, M. C.; Chua, M. R.; Bertram, S. N.; Hartono, N. T. P.; Tresback, J. S.; Hansen, E. C.; Correa-Baena, J. P.; Bulovic, V.; Buonassisi, T.; Shin, S. S.; Bawendi, M. G. *Energy Environ. Sci.* **2019**, *12*, 2192.
- [6] Shunde, L.; Zhou, L.; Zhi, Q.; Xiao, W.; Lei, C.; Yufeng, Z.; Qiaofei, X.; Zhimin, L.; Ke, M.; Gang, Chen.; *Adv. Funt. Mat.* **2020**, *30*, 2005846.
- [7] Lv, Y.; Ma, H.; Yin, Y.; Dong, Q.; Zhao, W.; Jin, S.; Shi, Y. *J. Mater. Chem. A* **2020**, *8*, 10283.
- [8] Luo, D.; Su, R.; Zhang, W.; Gong, Q.; Zhu, R. *Nat. Rev. Mater.* **2019**, *5*, 44.
- [9] Leguy, A.; Hu, Y.; Campoy-Quiles, M.; Alonso, M. I.; Weber, O. J.; Azarhoosh, P.; van Schilfgaarde, M.; Weller, M. T.; Bein, T.; Nelson, J.; Piers Barnes, R.F. *Chem. Mater.*, **2015**, *27*, 3397–3407.
- [10] Zheng, D.; Tong, C.; Zhu, T.; Rong, Y.; Pauporté, Th. *Nanomaterials*, **2020**, *10*, 2512.

## General Conclusion and Perspectives

During the past decade, organo-metal halide perovskites (PVKs) have risen as the most promising semiconductor family for photovoltaic solar cells due to a broad range of unique properties. In this thesis, we have performed a comprehensive exploration of different compositions of hybrid perovskites and of the controllability of their structure.

In Chapter I, we have presented the context of our research from application of solar energy to current research status of solar cells. Among them, we have highlighted that perovskite solar cells have become one of the most interesting and promising emerging technology. Moreover, the working principle of photovoltaic devices and a bibliographic review were described in this chapter.

In Chapter II, we fully have explored perovskite solar cells (PSCs) from the point of view of cation composition and cell structure. In the first part, we have fully investigated the electrical response of solar cells prepared with perovskites ranging from a mono-cation to a triple-cation composition. The best results have been found with the double MA/FA lead iodide compound ( $\text{FA}_{0.94}\text{MA}_{0.06}\text{PbI}_3$ ) which was prepared using MAI additive in the precursor solution. This strategy has been found the most accurate to achieve high efficiency and stability. It is more efficient than to the more complicated Cs, FA, MA, I and Br-based perovskite. FAMA presented the best morphology, crystallinity and optical properties for the application. The ideality factor decreased from MAPI, CsFAMA and FAMA. For the later SRH recombination with the less intensity was found. In the second part, we investigated the effect of AVA additive and of the cell structure on PSCs. In the presence of AVA, no 2D-perovskite phase was detected. AVA is deleterious for the PVK film morphology when *1mp* substrate was used while it was beneficial in reducing PVK bulk defects. Using a *3mp* scaffold led to a significant improvement of the PVK structural quality as shown by TRPL measurements and solved the potential problems of pinhole and related electrical shunt pathways. *1mp*-AVA cells achieved a PCE of 16.9%, stabilized at 15.9%. This efficiency was significantly lower with higher hysteresis compared to *1mp*-MAPI cells. We have also unveiled that MAPI is degraded by moisture with the formation of a monohydrate MAPI intermediate phase prior to  $\text{PbI}_2$  formation and MA release. The mechanism has been shown irrespective of the PVK environment. AVA has been shown beneficial for the stability of

the MAPI layer. Moreover, a slower degradation has also been found when MAPI-AVA PVK is embedded in the triple mesoscopic scaffold. The high stability of TiO<sub>2</sub>/ZrO<sub>2</sub>/Carbon/PVK cells is due to the protection by the all-inorganic scaffold.

In Chapter III, we successfully prepared a MAPI perovskite solar cell with an outstanding efficiency of 19.01% through the addition of Au\_NPs, and further improved the efficiency of the cell to 20.44% (reverse) through PAI post-treatment. Based on the above good results, we conducted a detailed analysis and demonstrated the mechanism of Au\_NPs in MAPbI<sub>3</sub> perovskite through a combination of simulation and experiments. Simulation and analysis of the Au\_NPs in both qualitative and quantitative aspects have been performed. From the final simulation results, we found that the optical effect of Au\_NPs on MAPI system can only be very weak. Moreover, by many experiments and different characterization methods (GD-OES, XRD, DSC, etc.), we have shown that Au\_NPs govern the growth direction of perovskite layer and the quality of the formed film. Therefore, we have concluded that the addition of Au\_NPs improves the perovskite efficiency significantly by playing a positive role on the final quality of the film. Only a very small part of the enhancement can be assigned to the effect of the gold nanoparticles themselves.

In Chapter IV, we have developed a two chloride additives engineering approach for the preparation of MA-free and Br-free Cs<sub>0.1</sub>FA<sub>0.9</sub>PbI<sub>3</sub> perovskite films for PSC application. Introducing a mixture of NH<sub>4</sub>Cl and KCl additives into the PPS to assist the PVK formation has allowed us to get films with outstanding properties. The former, employed at large mol %, led to a good film coverage, large grains, good crystallinity and reduced structural defects. The second has been shown to reduce the structural defects, reduce the PbI<sub>2</sub> phase content and suppress the hysteresis due to the passivation of structural defects by K<sup>+</sup>. Moreover, we have been able to demonstrate, by direct observation, that the hysteresis suppression is due to the ability of K<sup>+</sup> to block iodide species migration in the PVK layer. K is insensitive to the electric field and robustly passivates native defect sites. However, blocking the ionic mobility is insufficient to fully stabilize the devices. The double chloride additive approach has permitted to prepare methylammonium-free, hysteresis-free PSCs with a stabilized PCE achieving 20.02%.

In Chapter V, we first explored the mechanism of ammonium chloride action in multi-metal cation perovskites and refined it to each preparation process. Through a large number of experiments and tests, we found that ammonium chloride mainly leads to the formation of intermediates which can increase the solubility of  $\text{PbI}_2$  and then favor the formation of a large amount of  $\delta$ -phase which is the phase before transfer to black phase. Secondly, by using GD-OES, we explored the movement of multi-metal cation in perovskite layer during the film formation process and presented the intuitive evidence of phase separation caused by potassium. Furthermore, we further confirmed that the targeted growth direction of the film is the lateral growth. Finally, we combined this additive with GD-OES detection technology and found how the additive influence the distribution of multi-metal cation film formation and the formation of intersection layer between perovskite and  $\text{TiO}_2$ . Based on the above research results, we have successfully prepared high-efficiency solar cells, which had a 21.1% PCE (stabilized at 20.8%).

In Chapter VI, we fabricated highly efficient and stable MA-free PSCs by constructing interfacial capping layers at the perovskite and HTL interfaces. Treating the film surface with *n*-propylammonium iodide (PAI) resulted in a record stabilized PCE of 21.03% for the CsFAPI system and 22.04% for the KRbCsFA/AC system. Moreover, we have proved that the optimized films are highly resistant to electrical, light, moisture, and temperature external stressors and that this resistance is reinforced by the capping interfacial layer.

## Perspectives

### 1. Application of GD-OES

Glow Discharge Optical Emission Spectrometry (GD-OES) is one of the few detection technologies that have not been widely used in the field of perovskite solar cell. Therefore, this detection technology has great development space which can help researcher to detect film formation mechanism and

element distribution, especially facing complex composition of perovskite. Moreover, GD-OES can be also used to detect the cell with biased treated, which can help us to figure out the hysteresis caused by anion migration. Although in this work, we have developed three main functions of using GD-OES in perovskite solar cell, we firmly believe that GD-OES technique must be further explored.

## 2. Application of Additives

In this thesis, the improvement of the overall performance of various perovskites has been achieved through additives. We have especially explored two chloride additives, KCl and NH<sub>4</sub>Cl. An important result is that mixing these additives has resulted in a synergistic effect. This approach that we have developed for various 3D perovskites could be also fruitful for the quasi-2D ones.

## 3. Application of 2D capping layer

Unlike small cations in 3D perovskites (e.g., MA<sup>+</sup>, formamidinium (FA<sup>+</sup>), and Cs<sup>+</sup>), the bulky organic cations in 2D perovskites provide a steric barrier for surface water adsorption. Moreover, the large hydrophobic cation in the 2D perovskite crystal lattice can effectively suppress moisture intrusion. The strategy of formation of a 2D capping layer on 3D PVK by its surface treatment became more and more popular. Not only that, the emergence of a variety of bulky organic cations also gives researchers a variety of choices. We firmly believe that good choice is very important, due to different bulky organic cations has different effect on perovskite with different composition.

## 4. Stability test and encapsulation

Finally, to strengthen our discoveries, standardized aging tests should be implemented on the perovskites developed in this thesis. The objective could be to meet stability standards of IEC61215:2016 qualification tests, for instance. It would necessitate to tightly and efficiently encapsulate our solar cells.

## Annex I-Chapter I

From the perspective of energy strategy, fossil energies (coal, oil, natural gas...) as non-renewable energy sources, are quickly exhausting with reserves which significantly reduce with time and costs which go up sharply. Moreover, fossil fuels cause the increase of the earth average temperature due released of CO<sub>2</sub> gas which produces greenhouse effect.

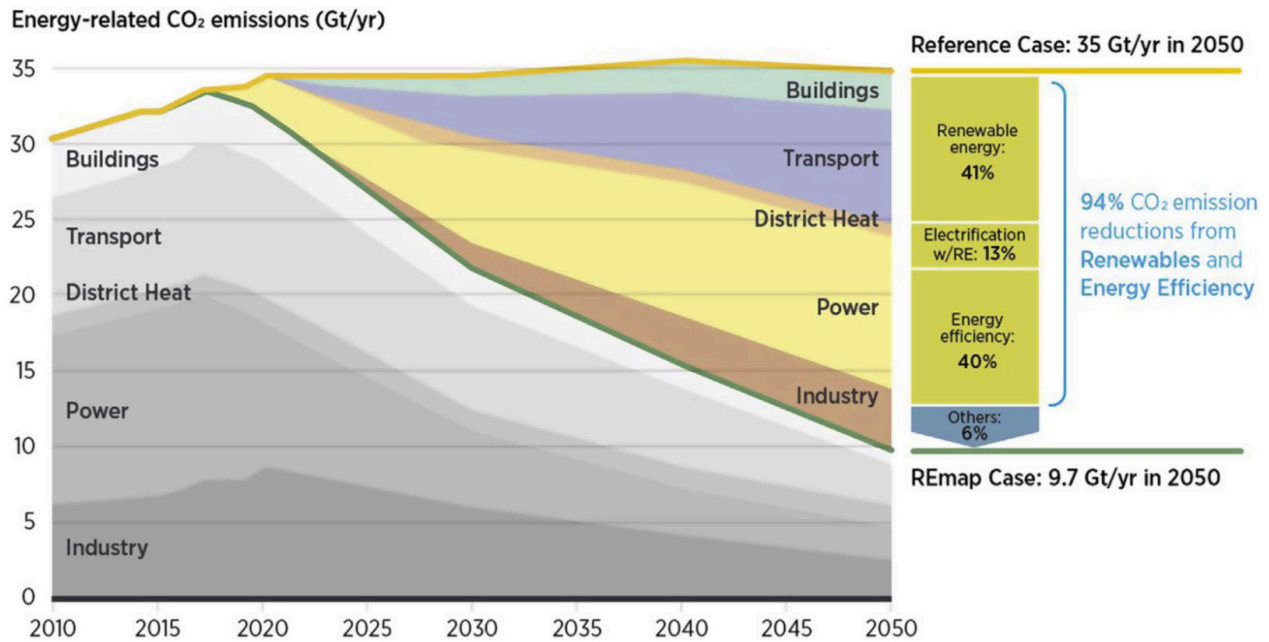


**Figure A.I.1 CO<sub>2</sub> emission reduction potential by technology in the Reference Case and REmap, 2010–2050. Note: Figure shows the breakdown of energy-related CO<sub>2</sub> emissions by technology in the REmap Case compared to the Reference Case. The figure excludes emissions from non-energy use (feedstocks). [1]**

To slow down this effect, the use of renewable energy will reduce CO<sub>2</sub> emissions, which will play a key role in many ways as showed in **Figure A.I.1**. It will improve the quality of economic development, build a better environment for humankind, achieve global climate goals, and improve energy efficiency.

## REmap 2050: 222 EJ

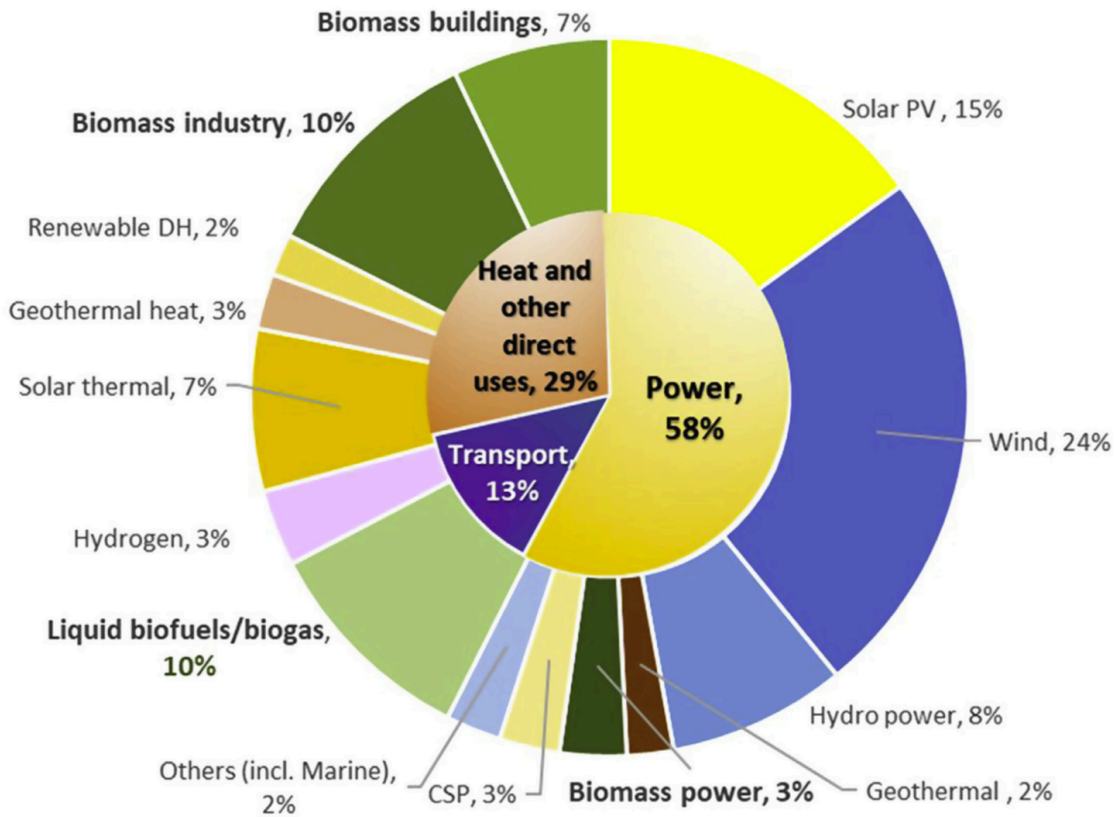


**Figure A.I.2 Global total primary energy supply in the Reference Case and Remap between 2015 and 2050. Note: includes non-energy use (feedstock).[1]**

Simultaneously, driven by both technological progress and model innovation, energy storage may become an important driving force for the development of renewable energy. **Figure A.I.2** provides a breakdown of renewables deployment. In total 222 EJ (1 EJ =  $10^{18}$  J) renewable energy is deployed in final energy terms. The power sector accounts for 58%. This includes growth of renewable power consumption related to electrification (notably electric vehicles and heat pumps). This type of renewables deployment could also be attributed to the end use sectors. In terms of total renewables deployment, the key role of bioenergy (32% incl. district heating), wind (24%) and solar PV (15%) deserves special attention. However, There is still a long way to go until replacing fossil energy.

[1] IRENA, Global Energy Transformation. A Roadmap to 2050, IRENA, Abu Dhabi, 2018.

## Annex II-Chapter II

### A.II.1. Mono- to Triple-Cation Hybrid Perovskites for High Efficiency Solar Cells

#### A.II.1.1 Impedance spectroscopy study of the three different PVKs

To get further insights into the effect of the perovskite on the cell electrical response, the PSCs were investigated by electrical impedance spectroscopy (EIS). This technique provides *in operando* characterizations of the cells and is safe for the devices.[1-19] By sweeping the frequency over a wide range, the various electrical phenomena occurring in the PSCs at various time scales can be discriminated. To have a comprehensive overview of the electrical response and well-understand the  $J-V$  curves,  $V_{appl}$  was varied from the short circuit to the open circuit. This technique provides a deep understanding of the devices functioning.

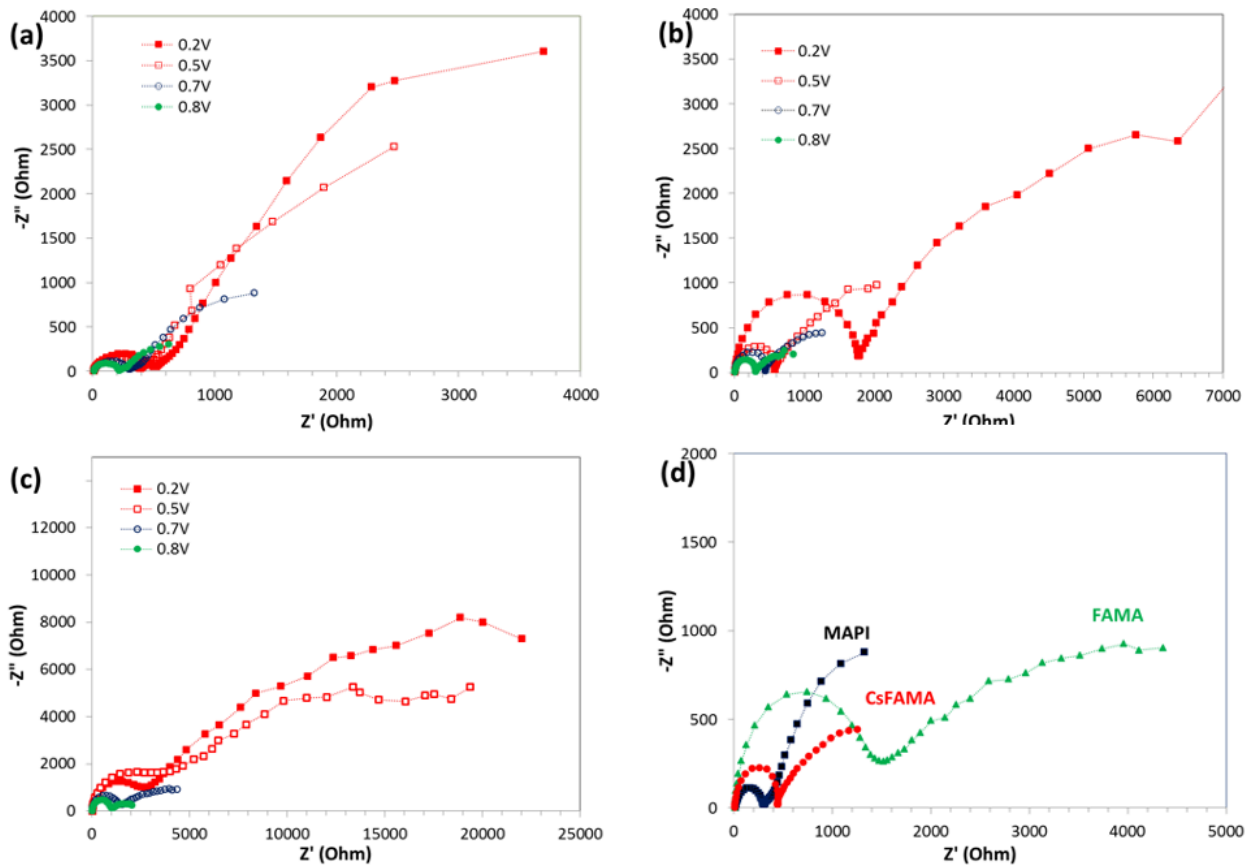


Figure A.II.1 Impedance spectra of the investigated PSCs. Effect of the applied voltage for (a) MAPI, (b) CsFAMA and (c) FAMA. (d) Comparison of the EIS at 0.7V for the three cells.

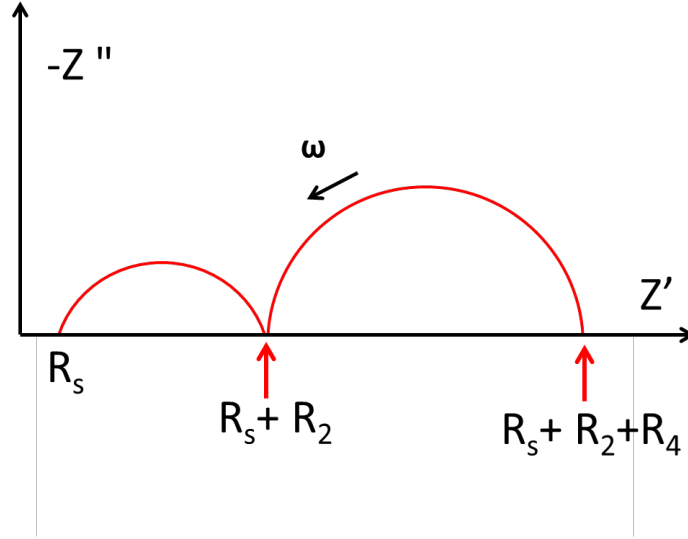
The electrical impedance spectra of the PSCs were measured at room temperature, between 1 MHz and 20 MHz, with a 20 mV ac signal, using a PGSTAT 12 apparatus from Autolab. All the measured cells had the same contact geometries. The impedance spectra were measured at room temperature, over a large applied voltage ( $V_{\text{appl}}$ ) range, under a  $\sim 0.9$  sun light power density supplied by a halogen Schott lamp. The cell illuminated area was delimited by a  $0.16 \text{ cm}^2$  mask. The spectra were analyzed using the Z-view software from National Instrument.

**Figure A.II.1** shows the effect of  $V_{\text{appl}}$  and perovskite on the spectra Nyquist plots (imaginary versus real part plots). We can note that, for all these high efficiency cells, no inductive loop at intermediate frequency was observed, confirming our previous observation that it is the electric response due to parasitic reactions that is the signature of not optimized devices.[4]

#### **A.II.1.2 Analysis of the impedance spectra.**

They have been analyzed by using equivalent electrical circuits (EEC). The most general one, established a previous work of my research group,[5] is presented in **Figure A.II.2a** and we have kept the same notations. For each potential, the electrical elements have been extracted by fitting the spectra. For CsFAMA and FAMA, two arcs of circle were observed on the spectra (**Figure A.II.1b** and **Figure A.II.1c**). They have been analyzed by using the type III EEC presented in **Figure A.II.2b** which contains three resistances and two constant phase elements (CPE). The various R and CPE electrical elements have been determined from the fits for each applied voltage.

The experimental impedance spectra have been fitted using simplified electrical equivalent circuits derived from the general one shown in **Figure A.II.2a**. The various R and CPE electrical elements have been determined from the fits for each applied voltage. The resistances can also be read on the spectra from the intersection of the circle arcs with the x-axis as shown in the Figure:



We have used CPE elements and not capacitances for the fits because the circle arcs are not semi-circles but are flattened. We have then determined the  $C_2$  and  $C_4$  capacitances from the  $CPE_2$  and  $CPE_4$  parameters. The CPE impedance is defined by  $Z_{CPE} = \frac{1}{T(i\omega)^p}$  where  $\omega$  is the angular frequency related to the frequency by  $f = \frac{\omega}{2\pi}$ ,  $i$  is the square root of  $-1$ , and  $p$  is lower than 1. The exact formulae to get  $C_2$  and  $C_4$  for one or two relaxations are:

$$C_2 = \left[ \left( \frac{1}{R_s} + \frac{1}{R_2} \right)^{p_2-1} T_2 \right]^{1/p_2} \quad (\text{A.II.1})$$

$$C_4 = \left[ \left( \frac{1}{R_s+R_2} + \frac{1}{R_4} \right)^{p_4-1} T_4 \right]^{1/p_4} \quad (\text{A.II.2})$$

The  $C_2$ ,  $1/C_4$ ,  $R_2$  and  $R_4$  have been then plotted for the various cells as a function of the applied voltage in **Figure A.II.3**, **Figure A.II.4** and **Figure A.II.5**.

$R_s$  is the series resistance due to the contacts and external wires electrical contributions. It is determined by extrapolating the real part of the spectra at high frequencies to the X-axis. Capacitances have been extracted from the CPE elements using the Brug's protocole[20] as explained in Pauporté et al. previous works.[3-7]  $CPE_2$  and  $CPE_4$  have given  $C_2$  and  $C_4$ , respectively as explained above. The type IV EEC shown in **Figure A.II.2c** was employed for fitting of the MAPI spectra (**Figure A.II.1a**). For these cells, a shoulder was found at intermediate frequencies for most of the  $V_{appl}$  which led us to employ an EEC with three relaxations, a  $R_3//CPE_3$  element being added.

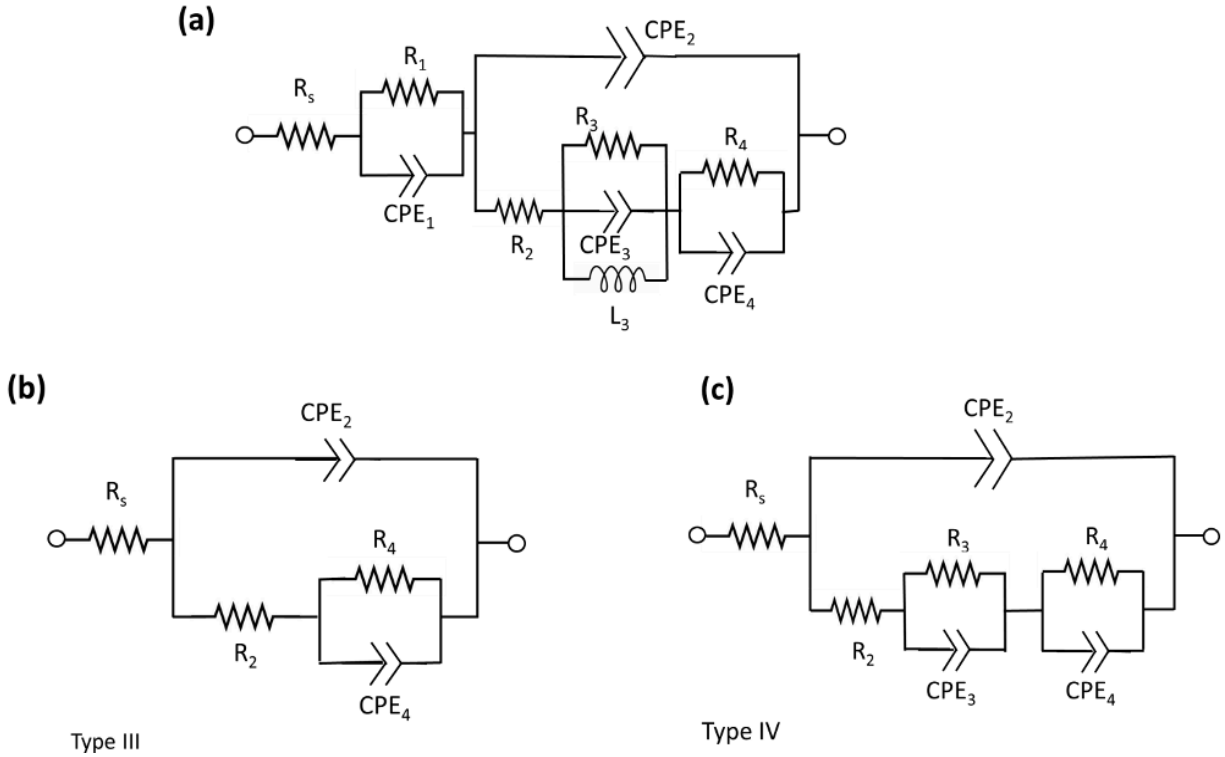


**Figure A.II.2** General equivalent electrical circuit (a). EECs employed for fitting the FAMA and CsFAMA spectra (b) and the MAPI spectra (c).

The  $C_2$  element is a light insensitive parameter[4] which values were well-reproducible for each perovskite. **Figure A.II.3** displays the variation of  $C_2$  with the applied voltage ( $V_{\text{appl}}$ ) for the three investigated perovskites.  $C_2$  was almost constant below 0.6V while, above this value, it increased and formed a S-shaped curve. In the case of FAMA cells, a fast  $C_2$  increase was observed at large  $V_{\text{appl}}$ . Below 0.6V,  $C_2$  is assigned to the bulk dielectric relaxation of the perovskite material. It is related to the relative permittivity of the perovskite,  $\epsilon_r$ , according to:

$$C_2 = \epsilon_r \epsilon_0 \rho / d \quad (\text{A.II.3})$$

with  $d$  the perovskite layer thickness,  $\rho$  the layer roughness factor and  $\epsilon_0$  the vacuum permittivity ( $8.85 \times 10^{-12} \text{ F.m}^{-1}$ ). The  $C_2$  average values for MAPI is  $1.6 \cdot 10^{-7} \text{ F.cm}^{-2}$  with  $d$  measured on SEM cross-sectional views at circa 370 nm (**Figure II.2a, Chapter II**). Assuming  $\rho=1$ ,  $\epsilon_r$  is calculated at  $\sim 66$  for MAPI. This value is in good agreement with our previous study.<sup>19</sup> The same calculation gives  $\epsilon_r \sim 41$  ( $C_2 \sim 0.77 \cdot 10^{-7} \text{ F.cm}^{-2}$ ) for CsFAMA and  $\epsilon_r \sim 41$  ( $C_2 \sim 0.89 \cdot 10^{-7} \text{ F.cm}^{-2}$ ) for MAPI. These values are overestimated since they neglect any roughness of the layer.

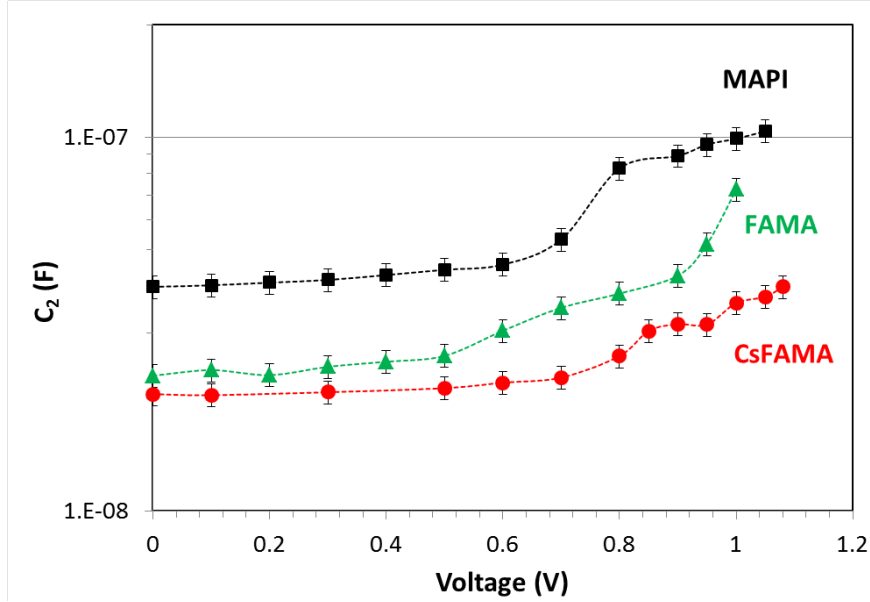


**Figure A.II.3**  $C_2$  parameter versus the applied voltage. Comparison of the three perovskites.

$R_2$ ,  $R_4$  and  $C_4$  elements are light sensitive and are related to the charges photogenerated in the devices.[4]  $R_2$  versus  $V_{appl}$  curves for the various perovskites are shown in **Figure A.II.4a**. For  $V_{appl} < 0.9$  V, this parameter varies in a large extent with the perovskite. It increases in the order MAPI, CsFAMA and FAMA cells. Above 0.9V, this parameter drops quickly for the FAMA cell and cross the other cells curves. This behavior can be linked to the lower  $V_{oc}$  measured for these devices and identify  $R_2$  as a recombination resistance. At this point, it is interesting to analyze more precisely the TRPL curves presented in **Figure II.6 (Chapter II)**. They have been fitted by a tri-exponentials function and the slow decay time (noted  $\tau_{slow}$ ) is found to vary with the perovskite.  $\tau_{slow}$  is measured at 59 ns, 93 ns and 117 ns for MAPI, CsFAMA and FAMA, respectively (**Table II.1, Chapter II**).  $\tau_{slow}$  is classically assigned to the bulk recombination of the photogenerated charges in the perovskite. It scales with the crystal quality and it mitigates with the density of recombination sites in the bulk and at the grain boundaries. We find in **Figure A.II.4** an exponential relationship between  $R_2$  and  $\tau_{slow}$ .

$$R_2 = 1/k_2 = A \exp(\tau_{slow}) \quad (\text{A.II.4})$$

A is a constant and the fit is excellent ( $R^2=0.999$ ). This relationship between  $R_2$  and  $\tau_{slow}$  has been assessed by completing the series with a FAMA cell that did not undergo the PEAI treatment (FAMA\* dot in **Figure A.II.4b**). It allows us to assign the  $R_2$  component to the recombination occurring in the

perovskite layer, especially at the grain boundaries. Recombination resistance  $R_2$  is inversely related to the recombination rate ( $k_2$ ) and it provides a direct quantitative view of the recombination rate. The higher is this resistance, the lower is the recombination rate.

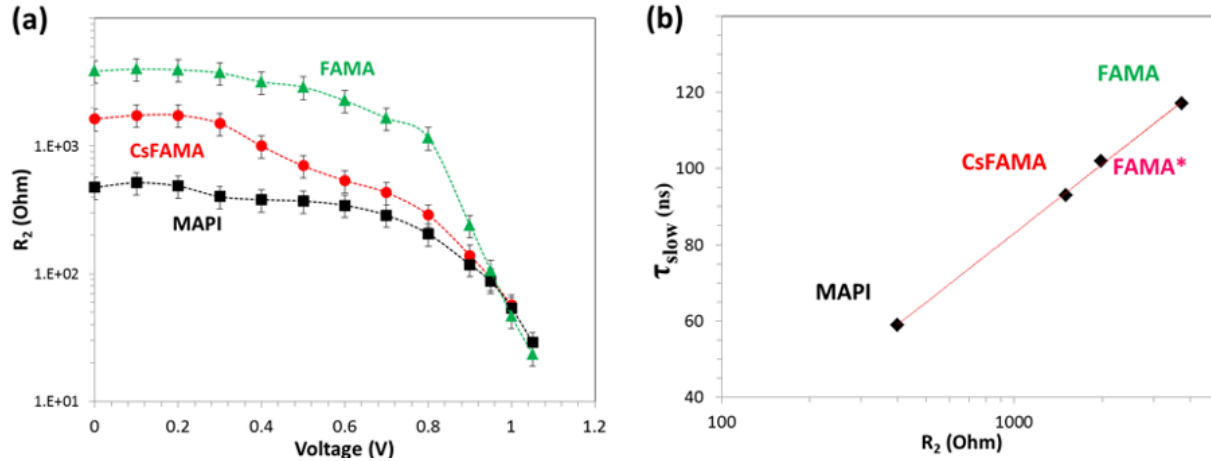


**Figure A.II.4** (a)  $R_2$  parameters as a function of  $V_{app}$  for the three perovskites. (b)  $R_2$  (measured at 0.3V) versus  $\tau_{slow}$  of TRPL (FAMA\* is a FAMA cell without PEAI treatment).

$R_4$  is also a recombination resistance but originates from recombinations occurring at or near the interfaces hereafter called interfacial recombinations. In **Figure A.II.5**, for  $V_{app} < 0.8V$ , MAPI and CsFAMA have about the same  $R_4$  value while FAMA has the highest  $R_4$ . This cell presents the best interfaces. Above 0.9V,  $R_4$  of CsFAMA is shifted to higher potential compared to MAPI and FAMA. This agrees with the higher  $V_{oc}$  for CsFAMA cells. The fact of shifting  $R_2$  and  $R_4$  curves toward higher voltage is favorable for the cell performances since it increases the cell  $V_{oc}$ .

**Table A.II.1.**  $R_2$  and  $R_4$  measured at the  $V_{oc}$  for the three PSCs.

At the $V_{oc}$	$R_2$	$R_4$	$R_2/R_4$
<b>MAPI</b>	29 $\Omega$	4 $\Omega$	7.3
<b>CsFAMA</b>	26 $\Omega$	6 $\Omega$	4.3
<b>FAMA</b>	24 $\Omega$	8 $\Omega$	3.0

In **Table A.II.1** we report typical values of  $R_2$  and  $R_4$  at the  $V_{oc}$  for the three kinds of cells. The  $R_2/R_4$  ratio quantifies the relative interfacial versus bulk recombination rates ( $k_4/k_2$ ). We observed that in all

cases the interfacial recombination rate is dominant. It increases in the order FAMA (3.0), CsFAMA (4.3) and MAPI (7.25). Extracting the resistance values at the  $V_{oc}$  therefore provide a finer view of the recombination phenomena than steady state measurements.

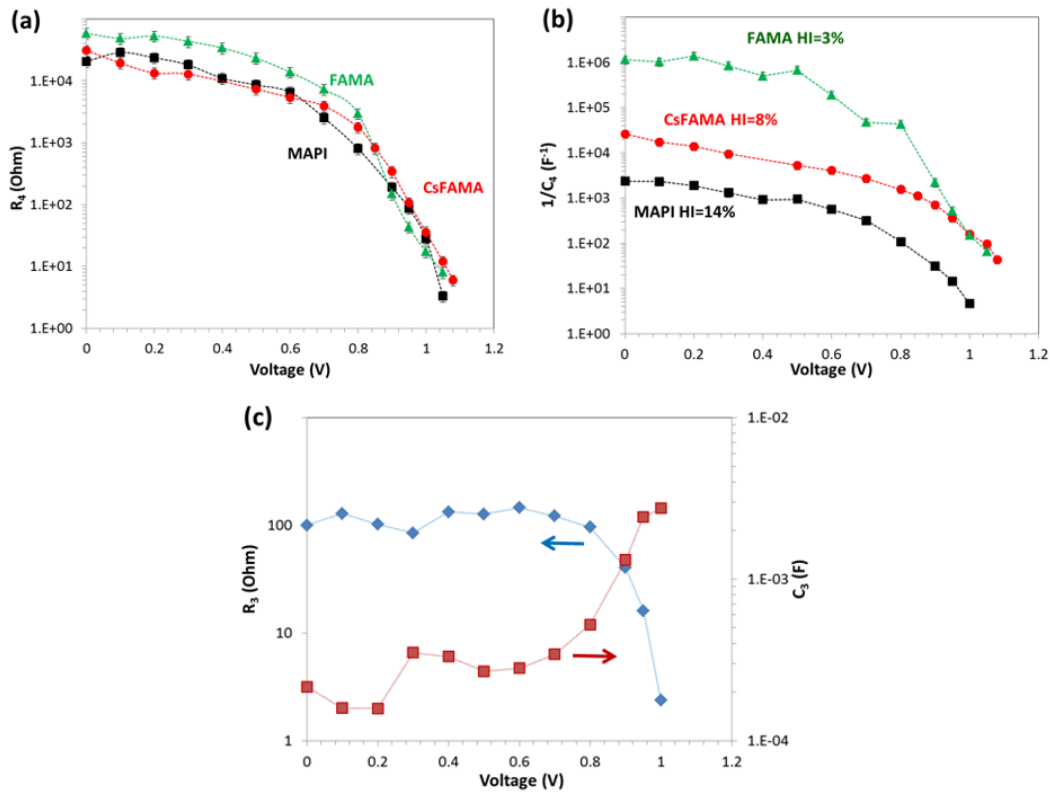


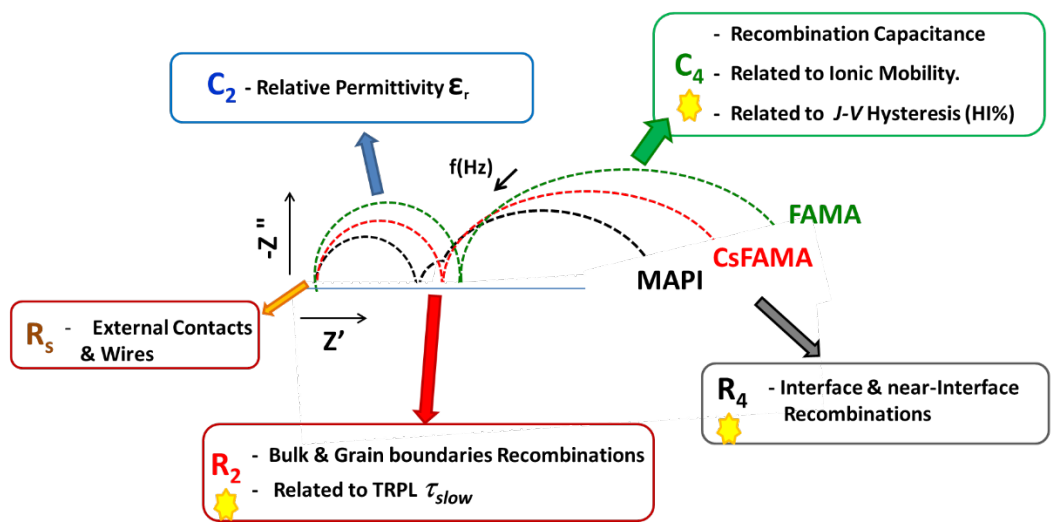
**Figure A.II.5 (a)  $R_4$  and (b)  $1/C_4$  parameters versus  $V_{appl}$  for the three perovskites. (c) Variation of  $R_3$  and  $C_3$  of MAPI cells with  $V_{appl}$ .**

$C_4$  is a light sensitive parameter which value dramatically increases with the light irradiation and can reach very high values.[4] In our case,  $C_4$  attained more than  $1.10^{-1} F.cm^{-2}$  at high  $V_{appl}$ . Jacobs et al.[4] have shown that such high values cannot be explained by a charge accumulation layer and cannot be the result of photogenerated charges separated across an interface. There is little doubt that  $C_4$  is related to the recombination of charges. Because charge recombination in PSC is a phase delayed phenomenon, in addition to the real component, an imaginary component is also introduced. This imaginary component is analyzed here as a capacitance in the equivalent electrical circuits used to fit our data (Figure A.II.2). It is the main contribution of  $C_4$ . This delayed recombination process is a special behavior occurring in PSCs due to the ionic conductivity of the perovskite. The movements of ions introduce defects that act as recombination centers and affect the dynamics of the charges. To better

follow the effect of  $V_{\text{appl}}$  and perovskite material, we have plotted the  $1/C_4$  parameter in **Figure A.II.5**. This parameter can be directly compared with the recombination resistances. As expected, it dramatically increases from MAPI to CsFAMA and FAMA. Recombinations are suppressed in the latter device. We can also note that the low frequency capacitance  $C_4$  modulates the electrical response of the cells under voltage scan at rather low rate in the  $J-V$  curve. A consequence is that  $C_4$  is related to the  $J-V$  curve hysteresis. It increases from FAMA, CsFAMA and MAPI which exhibit HI at  $\sim 3\%$ ,  $\sim 8\%$  and  $\sim 14\%$ , respectively (see **Figure A.II.5b**). We confirm here Pauporté's group previous discovery in Ref.[4] that  $C_4$  is closely related to the hysteresis index: the higher is  $C_4$ , the higher is the hysteresis amplitude.

In the case of the MAPI cells, we have introduced an intermediate frequency relaxation to well-fit the spectra. The variations of the  $R_3$  and  $C_3$  parameters with  $V_{\text{appl}}$  are presented in **Figure A.II.5c**. They were batch-dependent but we reproducibly observed rather flat curves for  $R_3$  and  $C_3$  between 0.0V and 0.6V. It reminds the behavior of  $C_2$  and may be related to bulk properties rather than interfacial ones. However, with the actual knowledges on the EIS response of PSCs, it is difficult to clearly state which physical process occurring in the cells is at the origin of these parameters.

The dependency of the various elements to light and their assignment are summarized in the **Schematic A.II.1**.



**Schematic A.II.1. Main information extracted from the electrical impedance spectroscopy data and their correlations with other measurements. ⚡ Light sensitive element.**

### A.II.1.3 Conclusions

The cells have been thoroughly investigated by impedance spectroscopy over a wide applied potential range. We have proposed two EECs based on our general EEC for analyzing the electrical response of the three kinds of solar cells. For all these optimized devices, with high efficiency for their category, no inductive loop at intermediate frequency due to parasitic reaction was found. The main information extracted from the electrical impedance spectroscopy data and their correlations with other measurements are summarized in **Schematic A.II.1**. We have extracted the dielectric permittivity of the three perovskites from the high frequency capacitance  $C_2$  and measured them at 66, 41 and 41 for MAPI, CsFAMA and FAMA, respectively. We have found a fair relationship between the high frequency resistance  $R_2$  and the slow decay time  $\tau_{\text{slow}}$  of the OIHP TRPL. This has led us to assign  $R_2$  to recombination occurring in the perovskite bulk and grain boundaries. The low frequency resistance  $R_4$  has been assigned to the recombination at and near the interfaces. The low frequency capacitance  $C_4$  which modulates the electrical response of the cells under voltage scan at rather low rate has been assigned to a phase delayed recombination phenomenon, the delay being a consequence of the ionic mobility and defect formation. For these three recombination-related electrical elements, the best values have been found for our highly efficient FAMA cell which is almost hysteresis-free. Finally, under electrical and light irradiation stresses, the investigated FAMA cell was highly stable while MAPI was more stable than CsFAMA. Finally, the strategy of mediating the growth of  $\text{FA}_{1-x}\text{MA}_x\text{PbI}_3$  perovskite double cation by MACl additive is found the best to suppress recombinations, suppress ion mobility, reach high efficiency with low hysteresis and stabilize the perovskite compound.

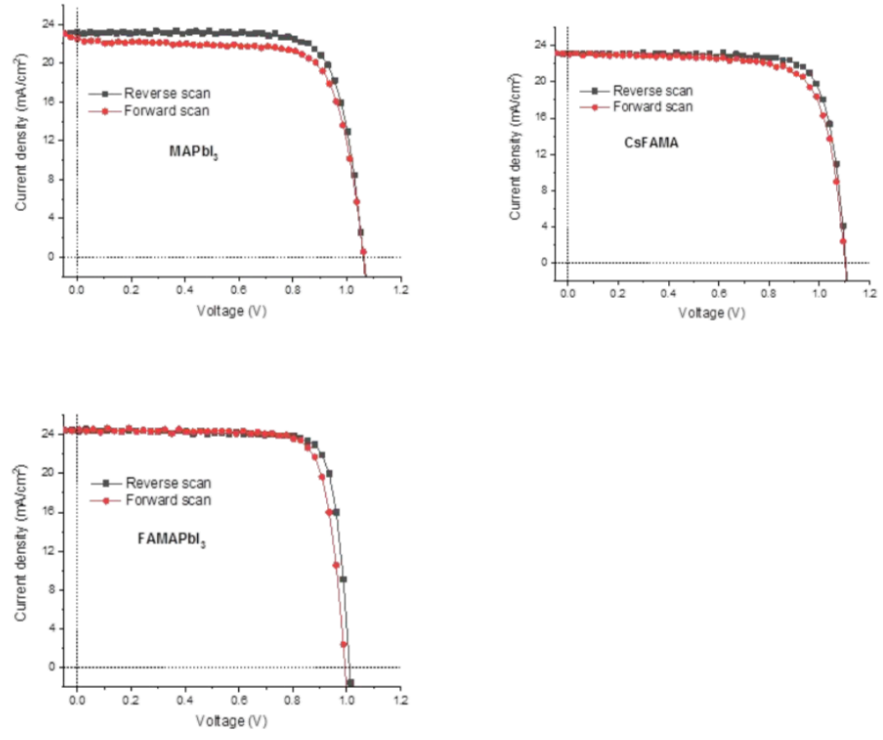


Figure A.II.6 Typical  $J-V$  curves reverse/forward scans for (a) MAPI, (b) CsFAMA and (c) FAMA cells.

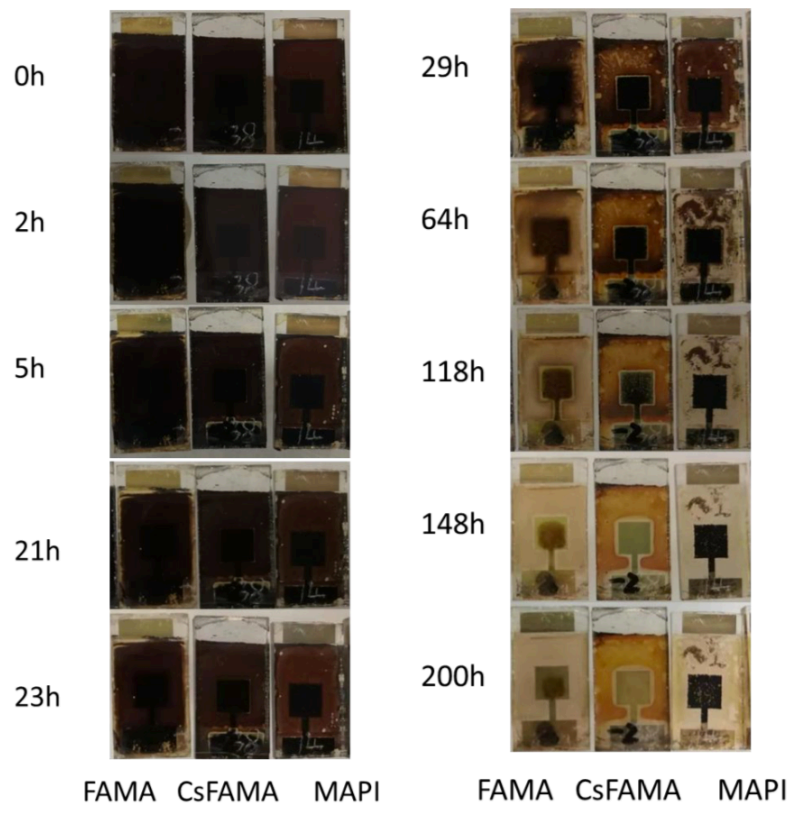


Figure A.II.7 Images of the solar cells degradation in a high humidity environment of 90% RH, at 20°C and under ambient light.

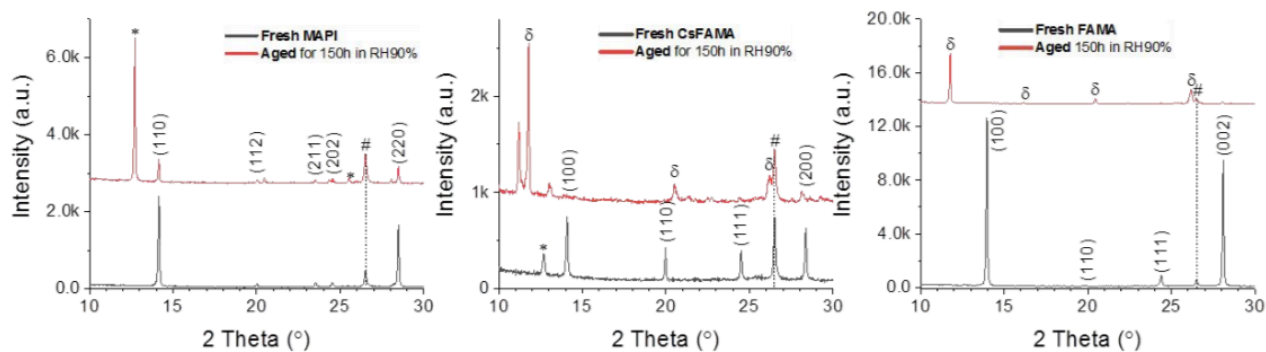


Figure A.II.8 XRD patterns before and after 150h of stability test at 90% RH. \*marks the  $\text{PbI}_2$  phase.

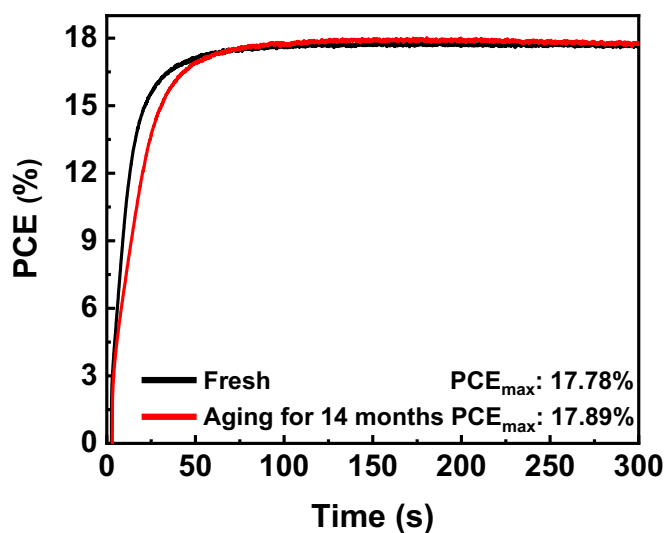


Figure A.II.9 Tracking curves of *Fresh* and *14 months  $\text{N}_2$  stored MAPI cell*.

Table A.II.2 *J-V* curves parameters of fresh and aged MAPI PSC that stored in a glovebox filled with nitrogen for 14 months. (same cell)

Name	Entry	$V_{oc}$ [V]	$J_{sc}$ [ $\text{mA cm}^{-2}$ ]	FF	PCE [%]	HI <sup>a</sup> [%]
Fresh	Reverse	1.056	23.37	78.36	19.33	16
	Forward	1.024	23.19	68.13	16.18	
Aged cell	Reverse	1.061	23.62	78.88	19.77	18
	Forward	1.025	23.49	67.67	16.29	

<sup>a</sup>  $HI = (PCE_{Rev} - PCE_{For}) * 100 / PCE_{Rev}$

**A.II.2. Effects of 5-Ammonium Valeric Acid Iodide as Additive on two different structure of Perovskite solar cells**

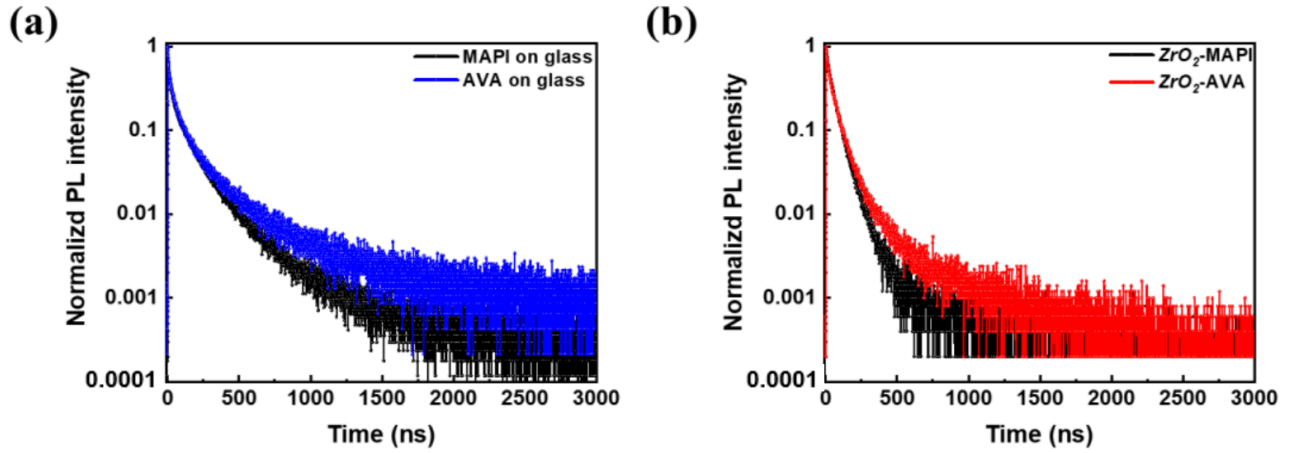


Figure A.II.10 (a) TRPL of 1mp-MAPI and 1mp-AVA layers deposited on glass. (b) TRPL of 3mp-MAPI and 3mp-AVA layers deposited on mesoporous ZrO<sub>2</sub>/glass.

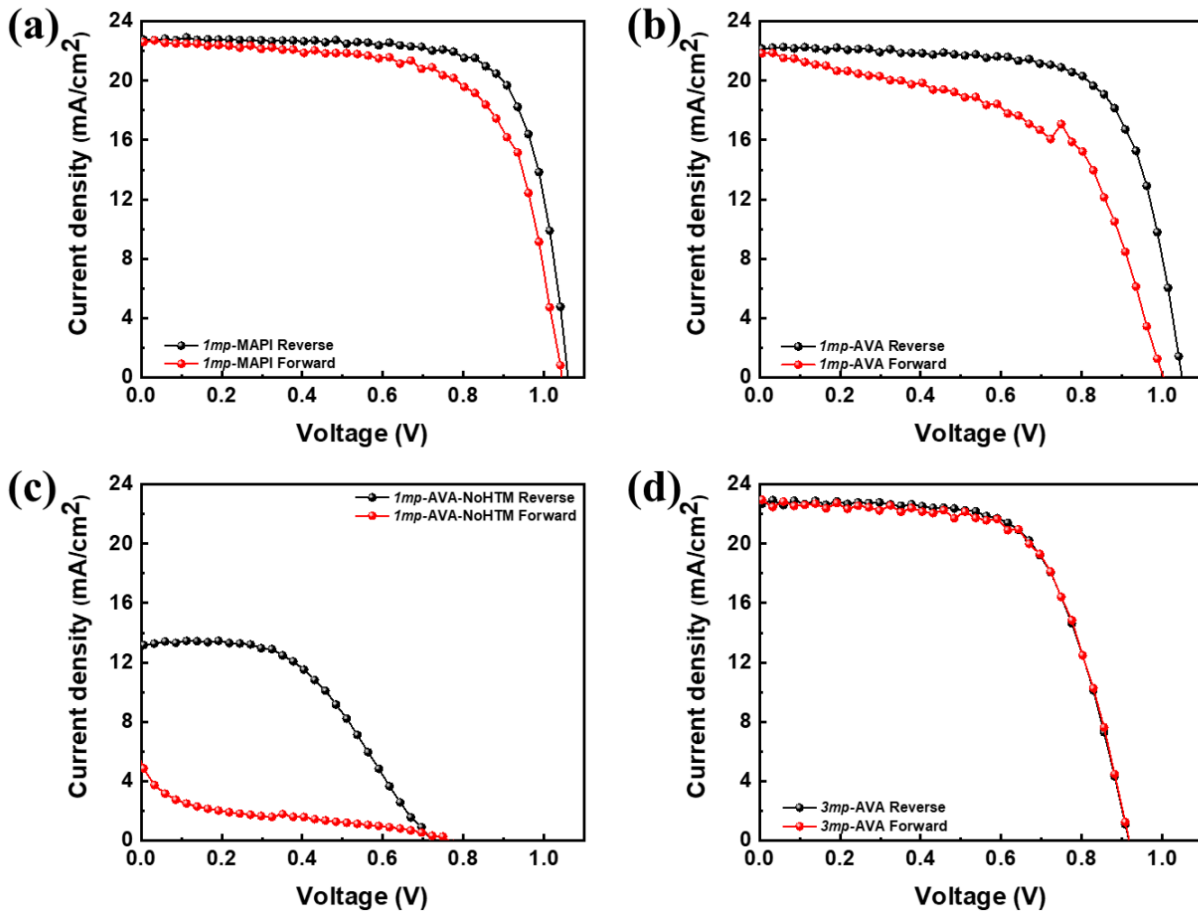
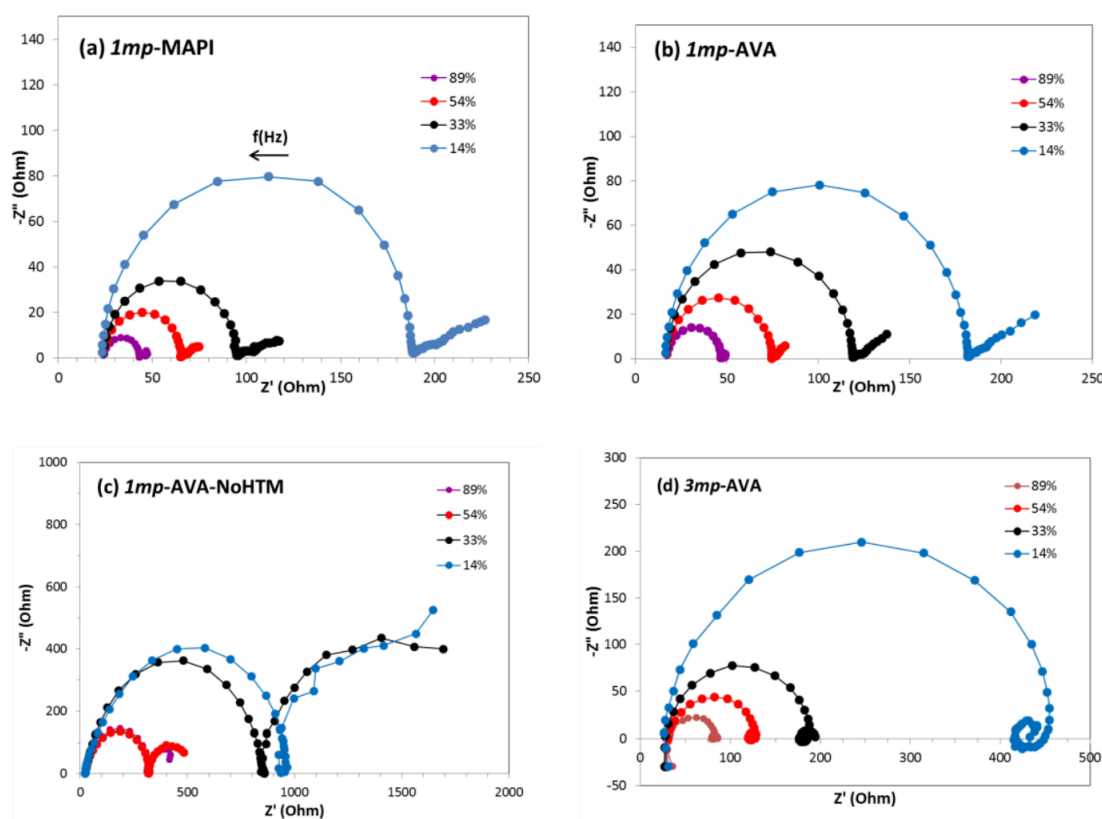


Figure A.II.11 Forward and reverse  $J-V$  curves of (a) 1mp-MAPI, (b) 1mp-AVA, (c) 1mp-MAPI-NoHTM and (d) 3mp-AVA best cells.

### A.II.2.1 Effect of light intensity at $V_{oc}$ on impedance spectra.

The effects of 5-ammonium valeric acid iodide (5-AVAI) as additive on two different structures of Perovskite solar cells were further investigated by electrical impedance spectroscopy (EIS). The impedance spectra were measured between 600 kHz and 20 mHz with a PGSTAT 12 system from Autolab. The ac signal was 20 mV. The cells were unencapsulated and illuminated with a halogen Schott lamp equipped with an optical fiber light guide. Experiments were conducted by either changing the power of the lamp to vary the light intensity from 8 sun% to 90 sun% or by applying a constant voltage ( $V_{app}$ ) between 0V and the  $V_{oc}$  under 90 sun% illumination. The cell illuminated area was delimited by a 0.16 cm<sup>2</sup> mask. The full EIS characterization measurements of a PSC lasted typically 1h. The spectra were analyzed using the Z-view software from National Instrument.



**Figure A.II.12** Effect of the light intensity in sun% on the impedance spectra measured at the  $V_{oc}$ . (a) *1mp*-MAPI, (b) *1mp*-AVA, (c) *1mp*-AVA-NoHTM and (d) *3mp*-AVA.

The effect of light intensity on the impedance spectra at  $V_{oc}$  is displayed in **Figure A.II.12**. For the *1mp* cells with a HTL, the spectra and the behaviour were close. They presented a large semi-circle at

high frequency and a second relaxation at low frequency. The former, which dominated the spectra, expanded continuously with reducing the light intensity. The two other samples presented a different behaviour. The *Imp*-AVA-NoHTM cells, without Spiro-OMeTAD HTM layer, exhibited an additional relaxation at very high frequency, an inductive loop at intermediate frequency and a second circle arc at low frequency. The *3mp*-AVA cells presented a spiral like aspect at low frequency.

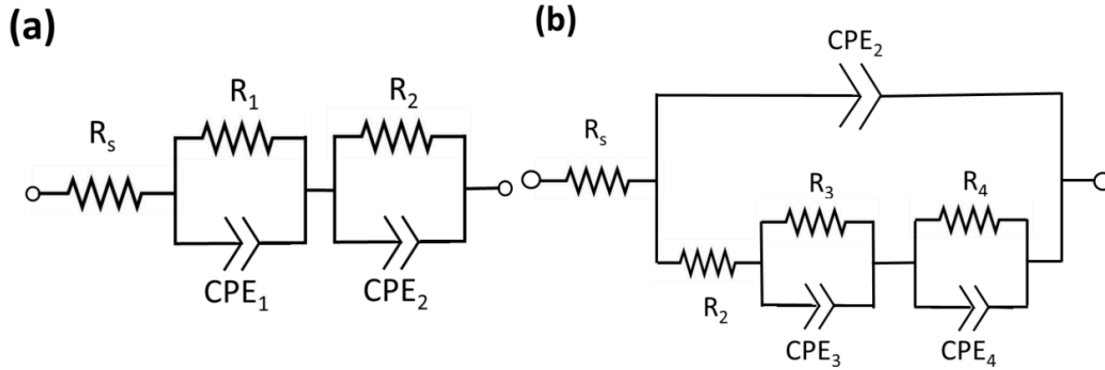


**Figure A.II.13 (a,b) Equivalent electrical circuits employed to fit impedance spectra of PSCs. See the core text for explanation.  $R_s$ ,  $R_1$ ,  $R_2$ ,  $R_3$  and  $R_4$  are resistances.  $CPE_1$ ,  $CPE_2$ ,  $CPE_3$  and  $CPE_4$  are constant phase elements.**

In all cases, we focused the analysis on the high frequency circle arc. It was fitted by a  $R_2//CPE_2$  circuit, except for the badly functioning *Imp*-AVA-NoHTM device for which a  $R_1//CPE_1$  circuit in series with the  $R_2//CPE_2$  one was employed to better fit the deviation from a circle arc (**Figure A.II.12a**). The former additional elements ( $R_1$  and  $CPE_1$ ) are discussed in the next section. CPE is a *constant phase element* from which a capacitance is extracted as described above (**Section A.II.1.2**).[23,24] The reader can refer to the previous works by Pauporté et al. for details on the analysis of impedance spectra of perovskite solar cells.[23,25-28] We must precise that, due to a different cell geometry and perovskite loading, in this section and in the next one (**Section A.II.2.2**), the values of the extracted electrical elements cannot be compared between *Imp* and *3mp* cells.

$R_2$  is plotted as a function of the  $V_{oc}$  in **Figure A.II.14a**. The curves fitted an exponential function, from which we have determined an ideality factor, noted  $n'_{ID}$ . In **Table II.7 (Chapter II)**, we compare  $n_{ID}$ , determined from the  $V_{oc}$ , and  $n'_{ID}$  extracted from the  $R_2$  curves. The two parameters are in good agreement and, importantly, they vary in a similar manner with the cell type. We can conclude that  $R_2$

is a recombination resistance which measures the recombination in the bulk perovskite. We have also extracted the high frequency capacitance  $C_2$  from the impedance spectra and reported this parameter in **Figure A.II.14b**. For *1mp* cells with a HTM, they are similar and do not significantly vary with  $V_{oc}$ . This capacitance is assigned to the bulk perovskite dielectric properties. AVA does not significantly change this parameter. On the other hand, the deviation observed for *1mp*-AVA-NoHTM can be assigned to the presence of the inductive loop on the EIS spectra and to the additional  $R_1//CPE_1$  circuit that render the accurate determination of  $C_2$  more difficult. In the case of *3mp*-AVA cells, the lower value of  $C_2$  for the *3mp*-AVA cell is related to a different architecture and device size.

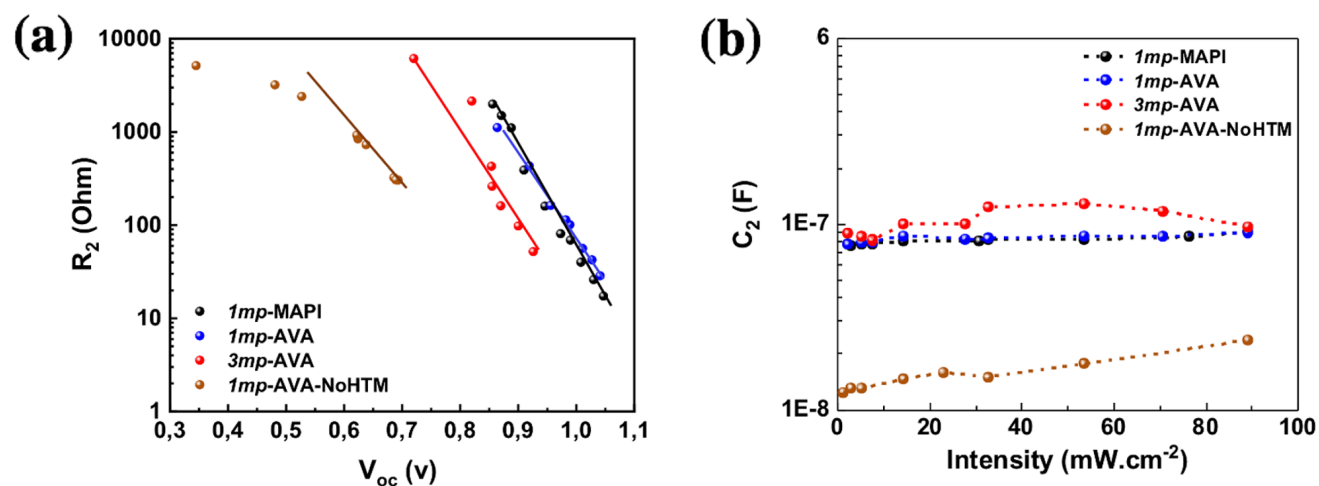


**Figure A.II.14** (a) Variation of  $R_2$  versus  $V_{oc}$ . (b)  $C_2$  versus light intensity.

### A.II.2.2 Effect of Applied Potential on Impedance Spectra.

We have further investigated the effect of AVA additive and cell architecture by studying the cells electrical responses at various applied voltage ( $V_{appl}$ ). **Figure A.II.15** shows the spectra. The two *1mp* cells with HTM (**Figures A.II.15a** and **A.II.15b**) presented similar spectral features: a circle arc at high frequency, a second circle arc at low frequency and, at its foot, a shoulder that has been taken into account by using a  $R_3//CPE_3$  electrical element in the equivalent electrical circuit. This circuit, already used above, is presented in **Figure A.II.13b**.

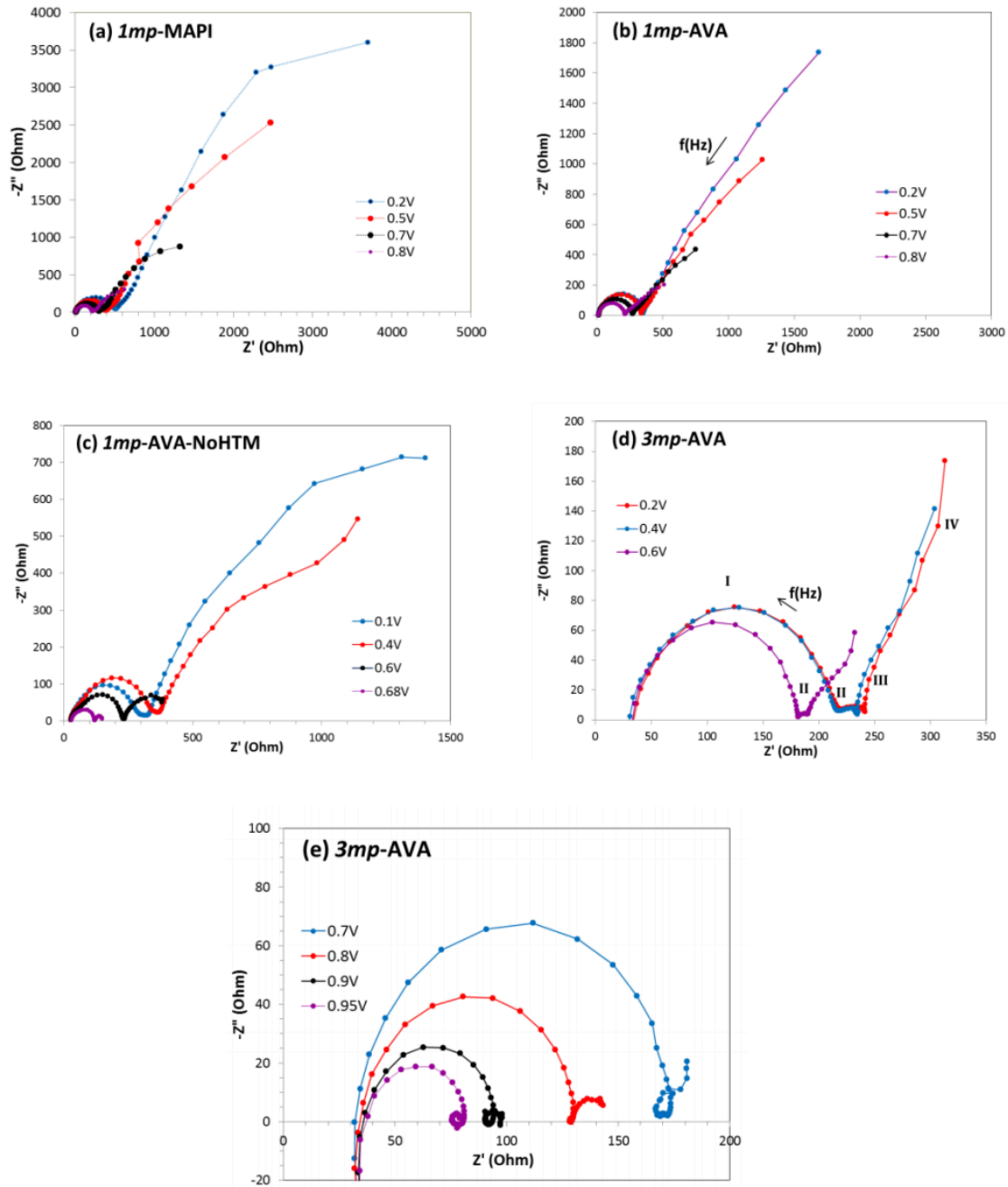


**Figure A.II.15** Effect of the applied voltage on the impedance spectra of the investigated cells. (a) *1mp*-MAPI, (b) *1mp*-AVA (c) *1mp*-AVA-NoHTM, (d) *3mp*-AVA low voltage and (e) *3mp*-AVA high voltage.

The *1mp*-AVA-NoHTM impedance spectra exhibited at high frequency the two relaxations described above (**Figure A.II.15c**). At intermediate frequency a flat intermediate feature was found while a circle arc was present at low frequency. For the *3mp*-AVA cell, one could distinguish at low  $V_{appl}$  at least four relaxations noted I, II, III and IV in **Figure A.II.15d**. At higher  $V_{appl}$ , the shape described in the previous section with the spiral at low frequency was found. The analysis of the intermediate and low

frequency electrical response of the  $3mp$  cell is not straightforward and we have focused our analysis on the high frequency arc of circle.

$R_s$  element values were determined from the extrapolation of the spectra at very high frequencies on the x-axis (impedance real part). It is due to the contacts and wires resistances. The higher  $R_s$  for the  $3mp$ -AVA cell is assigned to the larger size of the cell and to the carbon back-contact which is less conducting than the gold one. The  $1mp$ -AVA-NoHTM presented also a rather high  $R_s$  and a high frequency  $R_1//CPE_1$  component in spite of the use of a gold back-contact. We suggest that a layer is formed at the interface between PVK and gold which introduces an additional resistance and capacitance. The gold evaporation process provokes damages on the PVK layer at the origin of defects which act as recombination centers. This phenomenon is deleterious for photovoltaic properties.

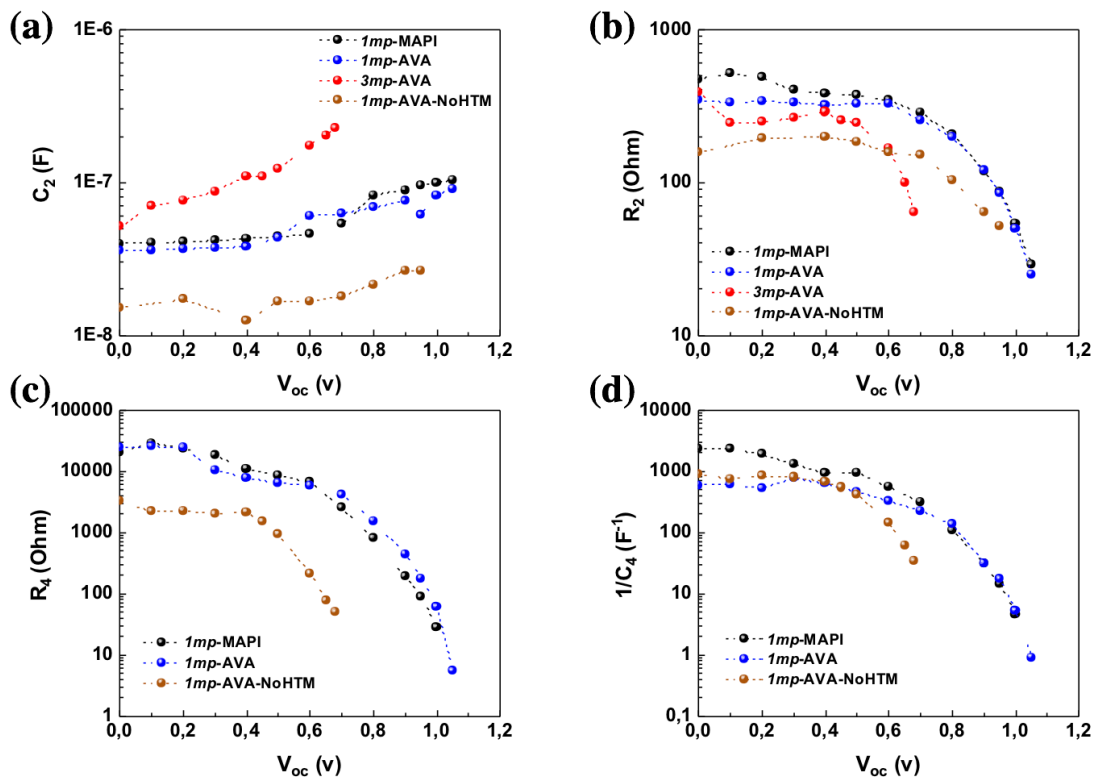


**Figure A.II.16** Effect of  $V_{appl}$  on the solar cells electrical parameters.

$C_2$  is presented in **Figure A.II.16a**.  $1mp$ -MAPI and  $1mp$ -AVA cells have similar behavior. At low applied voltage,  $C_2$  is assigned to the dielectric intrinsic capacitance of the PVK layer. Introducing AVA does not change the permittivity of the layer significantly. The fact that  $C_2$  is unchanged over a large  $V_{appl}$  in  $3mp$  device suggests that  $C_2$  is a dielectric intrinsic capacitance of MAPI-AVA material

filling the pores. Higher and increasing  $C_2$  are found for *Imp*-AVA-NoHTM cell that suggest several contributions for this electrical component.

$R_2$  and  $R_4$  are analyzed as recombination resistances. The higher these resistances, the lower the charge recombinations and the best is the cell.[23,28] In general, AVA seems detrimental for these resistances. XRD has shown a slightly worse crystallinity and SEM views (**Figure II.13b, Chapter II**) has revealed the presence of pinholes in *Imp*-AVA layers which are detrimental for the performances. The lower resistances values reflect these features. The voltage at which  $R_2$  and  $R_4$  parameters drop is linked to the cells  $V_{oc}$ . It is quite close for *Imp*-MAPI and *Imp*-AVA cells. However, when HTM is absent in the *Imp* cell, these parameters drop at low  $V_{appl}$ , showing a recombination acceleration which results in the low  $V_{oc}$  recorded. In a recent investigation of my group [20] and in Section A.II.1.2, the origin of  $C_4$  is discussed. It is analyzed as a recombination capacitance related to the ion mobility that delays de charges recombination.  $C_4$  reflects thus charge recombinations. **Figure A.II.16d** shows that this parameter varies like  $R_2$  and  $R_4$  confirming this analysis. The *Imp*-AVA-NoHTM cell presents low  $1/C_4$  above 0.5V in good agreement with the large hysteresis of these cells and the low  $V_{oc}$ .

We can also note that, when an inductive loop is present, the total resistance, measured at low frequency, decreases more quickly than in the absence of this feature. A quick decrease of the total resistance leads to smaller FF on the  $J$ - $V$  curves and then is detrimental for the device performances. It is the case of *Imp*-AVA-NoHTM and *3mp* cells.

At this stage, based on the present knowledges of the scientific community on the impedance response of PSCs, we are unable to assign an origin and discuss the inductive loop as well as  $C_3$  and  $R_3$  elements.

### **A.II.2.2 Conclusions**

Our EIS study has stated that  $R_2$  element also varies with the  $V_{oc}$  like a recombination resistance from which we have extracted an ideality factor comparable to the ones determined from the  $V_{oc}$ . The EIS study at various applied voltages has allowed us to extract two other parameters,  $R_4$  and  $C_4$ , that have been shown related to recombinations. Higher recombinations have been found in the case of the *Imp*-AVA cells that are linked to the presence of pinholes in the PVK layer. We have shown that the mesoporous carbon back-electrode function differently to the gold one in the case of HTL-free devices.

The PVK/gold interface presents defects and likely a damaged interlayer at the origin of poor performances. In the case of *3mp*-AVA cells, the intermediate frequency EIS features, especially an inductive loop, is at the origin of a fast decrease of the total cell resistance with  $V_{appl}$  and then to a low FF and  $V_{oc}$  compared to the *Imp* cells with HTM.

## References

- [1] Zhang, J.; Juárez-Pérez, E.J.; Mora-Seró, I.; Viana, B.; Pauporté, Th. Fast and low temperature growth of electron transport layers for efficient perovskite solar cells. *J. Mater. Chem. A* **2015**, *3*, 4909–4915.
- [2] Pitarch-Tena, D.; Ngo, T.T.; Vallés-Pelarda, M.; Pauporté, Th.; Mora-Seró, I. Impedance Spectroscopy Measurements in Perovskite Solar Cells. Device Stability During the Measurement and Noise Reduction. *ACS Energy Lett.* **2018**, *3*, 1044–1048.
- [3] Wang, P.; Shao, Z.; Ulfa, M.; Pauporté, T. Insights into the Hole Blocking Layer Effect on the Perovskite Solar Cell Performance and Impedance Response. *J. Phys. Chem. C* **2017**, *121*, 9131–9141.
- [4] Wang, P. J.; Ulfa, M.; Pauporté, T. Effects of Perovskite Monovalent Cation Composition on the High and Low Frequency Impedance Response of Efficient Solar Cells. *J. Phys. Chem. C* **2018**, *122*, 1973–1981.
- [5] Ulfa, M.; Zhu, T.; Goubard, F.; Pauporté, T. Molecular versus polymeric hole transporting materials for perovskite solar cell application. *J. Mater. Chem. A* **2018**, *6*, 13350–13358.
- [6] Ulfa, M.; Wang, P.J.; Zhang, J.; Liu, W.; Marcillac, D.; Coolen, L.; Peralta, S.; Pauporté, T. Charge Injection and Electrical Response in Low-Temperature SnO<sub>2</sub>-Based Efficient Perovskite Solar Cells. *ACS Appl. Mater. Interfaces* **2018**, *10*, 35118–35128.
- [7] Ulfa, M.; Pauporté, T.; Bui, T.T.; Goubard, F. Impact of Organic Hole Transporting Material and Doping on the Electrical Response of Perovskite Solar Cells. *J. Phys. Chem. C* **2018**, *122*, 11651–11658.
- [8] Almora, O.; Aranda, C.; Mas-Marzá, E.; Garcia-Belmonte, G. On Mott-Schottky analysis interpretation of capacitance measurements in organometal perovskite solar cells. *Appl. Phys. Lett.* **2016**, *109*, 173903.
- [9] Pascoe, A.R.; Duffy, N.W.; Scully, A.D.; Huang, F.; Cheng, Y.B. Insights into Planar CH<sub>3</sub>NH<sub>3</sub>PbI<sub>3</sub> Perovskite Solar Cells using Impedance Spectroscopy. *J. Phys. Chem. C* **2015**, *119*, 4444–4453
- [10] Juarez-Perez, E.J.; Wußler, M.; Fabregat-Santiago, F.; Lakus-Wollny, K.; Mankel, E.; Mayer, T.; Jaegermann, W.; Mora-Sero, I. Role of the Selective Contacts in the Performance of Lead Halide Perovskite Solar Cells. *J. Phys. Chem. Lett.* **2014**, *5*, 680–685.
- [11] Juarez-Perez, E.J.; Sanchez, R.S.; Badia, L.; Garcia-Belmonte, G.; Kang, Y.S.; Mora-Sero, I.; Bisquert, J. Photoinduced Giant Dielectric Constant in Lead Halide Perovskite Solar Cells. *J. Phys. Chem. Lett.* **2014**, *5*, 2390–2394.
- [12] Dualeh, A.; Moehl, T.; Tétreault, N.; Teuscher, J.; Gao, P.; Nazeeruddin, M.K.; Grätzel, M. Impedance Spectroscopic Analysis of Lead Iodide Perovskite-Sensitized Solid-State Solar Cells. *Sci. Rep.* **2014**, *8*, 362–373.
- [13] Gonzalez-Pedro, V.; Juarez-Perez, E.J.; Arsyad, W.S.; Barea, E.M.; Fabregat-Santiago, F.; Mora-Sero, I.; Bisquert, J. General Working Principles of CH<sub>3</sub>NH<sub>3</sub>PbX<sub>3</sub> Perovskite Solar Cells. *Nano Lett.* **2014**, *14*, 888–893.
- [14] Almora, O.; Zarazua, I.; Mas-Marza, E.; Mora-Sero, I.; Bisquert, J.; Garcia-Belmonte, G. Capacitive Dark Currents, Hysteresis, and Electrode Polarization in Lead Halide Perovskite Solar Cells. *J. Phys. Chem. Lett.* **2015**, *6*, 1645–1652.

- [15] Guerrero, A.; Juarez-Perez, E.J.; Bisquert, J.; Mora-Sero, I.; Garcia-Belmonte, G. Electrical Field Profile and Doping in Planar Lead Halide Perovskite Solar Cells. *Appl. Phys. Lett.* **2014**, *105*, 133902.
- [16] Kim, H.-S.; Mora-Sero, I.; Gonzalez-Pedro, V.; Fabregat-Santiago, F.; Juarez-Perez, E. J.; Park, N.-G.; Bisquert, J. Mechanism of Carrier Accumulation in Perovskite Thin-Absorber Solar Cells. *Nat. Commun.* **2013**, *4*, 2242.
- [17] Zarazua, I.; Han, G.F.; Boix, P.P.; Mhaisalkar, S.; Fabregat-Santiago, F.; Mora-Sero, I.; Bisquert, J.; Garcia-Belmonte, G. Surface Recombination and Collection Efficiency in Perovskite Solar Cells from Impedance Analysis. *J. Phys. Chem. Lett.*, **2016**, *7*, 5105-5113.
- [18] Yang, T.-Y.; Gregori, G.; Pellet, N.; Grätzel, M.; Maier, J. The Significance of Ion Conduction in a Hybrid Organic-Inorganic Lead Iodide-Based Perovskite Photosensitizer. *Angew. Chem., Int. Ed.* **2015**, *54*, 7905–7910.
- [19] Anaya M.; Zhang, W.; Clasen Hames, B.; Li, Y.; Fabregat-Santiago, F.; Calvo, M.E.; Snaith, H.J.; Miguez, H.; Mora-Sero I. Electron Injection and Scaffold Effects in Perovskite Solar Cells. *J. Mater. Chem. C* **2017**, *5*, 634-644.
- [20] Brug, G.J.; Van Der Eeden, A.L.G.; Sluyters-Rehbach, M.; Sluyters, J.H. The Analysis of Electrode Impedance Complicated by the Presence of a Constant Phase Element. *J. Electroanal. Chem.* **1984**, *176*, 275-295.
- [21] Zhu, T.; Zheng, D.; M.-N. Rager, M.N.; Pauporté, T. Actual Organic Cations Composition Determination in Perovskite Thin Films. Application to Formamidinium Lead Iodide Stabilization for High Efficiency Solar Cell. *Sol. RRL* **2020**, 2000348.
- [22] Tress, W.; Yavari, M.; Domanski, K.; Yadav, P.; Niesen, B.; Baena, J.P.C.; Hagfeldt, A.; Graetzel, M. Interpretation and evolution of open-circuit voltage, recombination, ideality factor and subgap defect states during reversible light-soaking and irreversible degradation of perovskite solar cells. *Energy Environ. Sci.* **2018**, *11*, 151–165.
- [23] Zhu, T.; Zheng, D.; Liu, J.; Coolen, L.; Pauporté, Th. Electrical response of high efficiency and stable solar cells based on MA<sub>0.94</sub>Cl mediated grown FA<sub>0.94</sub>MA<sub>0.06</sub>PbI<sub>3</sub> perovskite. *ACS Appl. Mater. Interfaces* **2020**, *12*, 37197–37207.
- [24] Zheng, D.; Zhu, T.; Pauporté, Th. Using Monovalent- to Trivalent-Cation Hybrid Perovskites for Producing High-Efficiency Solar Cells: Electrical Response, Impedance, and Stability. *ACS Appl. Energy Mater.* **2020**, *3*, 10349–10361.
- [25] Wang, P.; Ulfa, M.; Pauporté, T. Effects of perovskite monovalent cation composition on the high and low frequency impedance response of efficient solar cells. *J. Phys. Chem. C* **2018**, *122*, 1973–1981.
- [26] Ulfa, M.; Wang, P.; Zhang, J.; Liu, J.; Daney de Marcillac, W.; Coolen, L.; Peralta, S.; Pauporté, T. Charge injection and electrical response in low temperature SnO<sub>2</sub>-based efficient perovskite solar cells. *ACS Appl. Mater. Interfaces* **2018**, *10*, 35118–35128.
- [27] Ulfa, M.; Zhu, T.; Goubard, F.; Pauporté, Th. Molecular versus polymeric hole transporting materials for perovskite solar cell application. *J. Mater. Chem. A* **2018**, *6*, 13350–13358.
- [28] Zheng, D.; Zhu, T.; Pauporté, Th. Using Monovalent- to Trivalent-Cation Hybrid Perovskites for Producing High-Efficiency Solar Cells: Electrical Response, Impedance, and Stability. *ACS Appl. Energy Mater.* **2020**, *3*, 10349–10361.

### Annex III-Chapter III

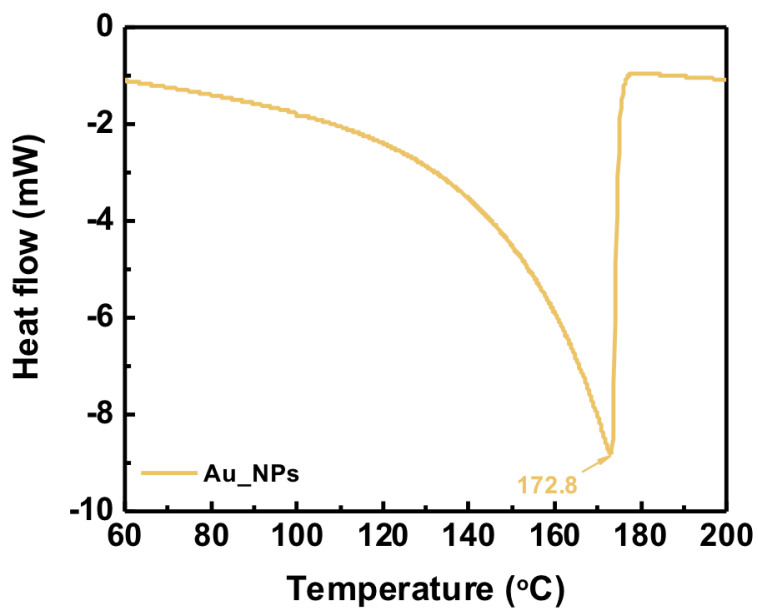


Figure A.III.1 DSC curves of Au\_NPs.

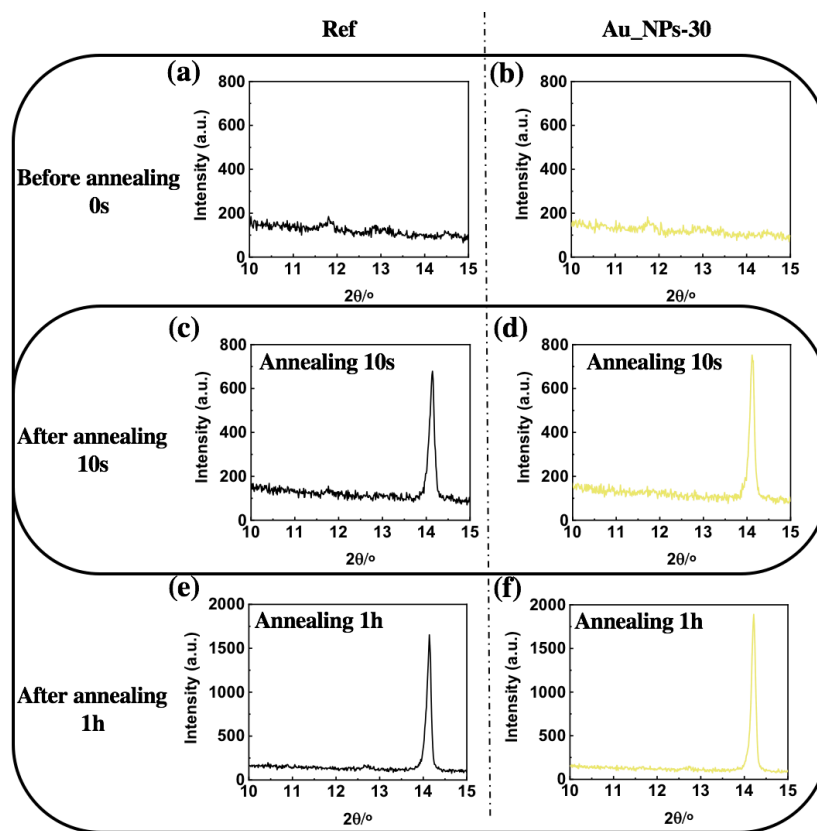


Figure A.III.2 Effect of Au\_NPs on the XRD pattern of the films produced before annealing (a-b), after 10 s of annealing (c-d) and after full annealing (e-f).

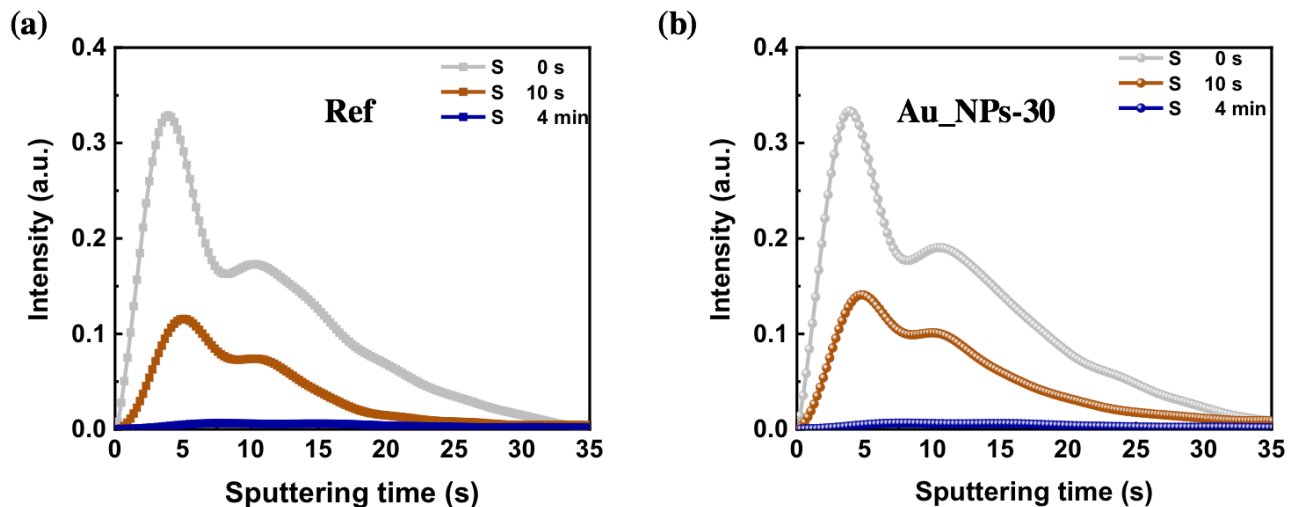


Figure A.III.3 Effect of additives on the GD-OES S profile between 0 s and 4 min.

Table A.III.1 **ExpDec 3** function fitting parameters of the TRPL decay curves measured at 472 nm on the MAPbI<sub>3</sub> films with different volume of Au\_NPs deposited on Glass.

ExpDec 3 : $y = A_1 \exp(-x/\tau_1) + A_2 \exp(-x/\tau_2) + A_3 \exp(-x/\tau_3) + y_0$										
Name	$y_0$	$A_1$	$\tau_{\text{fast}}$ [ns]	$RC_{\text{fast}}^a$	$A_2$	$\tau_{\text{int}}$ [ns]	$RC_{\text{int}}^a$	$A_3$	$\tau_{\text{slow}}$ [ns]	$RC_{\text{slow}}^a$
Ref	9.96E-4	0.37	4.39	0.12	0.57	15.06	0.62	0.06	61.97	0.26
Au_NPs-15	4.93E-4	0.43	3.92	0.08	0.53	14.44	0.37	0.04	287.47	0.55
Au_NPs-30	9.12E-4	0.46	2.37	0.02	0.31	15.07	0.06	0.23	323.26	0.92
Au_NPs-45	29.2E-4	0.47	2.29	0.03	0.22	17.64	0.12	0.31	90.51	0.85

**Formula A.III.1:**

$$0.06 M = \frac{n_{Au}}{V_{Au}}$$

$$n_{Au} = 0.06 M \times 30 \times 10^{-3} \times 10^{-3} L = 1.8 \times 10^{-6} mol = 1.8 \times 10^{-3} mmol$$

(  $30 \times 10^{-3} \times 10^{-3} L$  imized volume of Au\_NPs.)

$$\frac{n_{Au}}{n_{PbI_2}} = \frac{1.8 \times 10^{-3} mmol}{1.35 mmol} = 0.001333 \dots (\sim 0.13\%)$$

$$\frac{n_{Au}}{n_{MAPbI_3}} = \frac{V_{Au} \times \frac{19.32}{196}}{V_{MAPbI_3} \times \frac{3.947}{158.97 + 461}} = 15.483 \times \frac{V_{Au}}{V_{MAPbI_3}} = 0.001333 \dots$$

$$\frac{V_{Au}}{V_{PbI}} = 0.000086 (\sim 0.009\%)$$

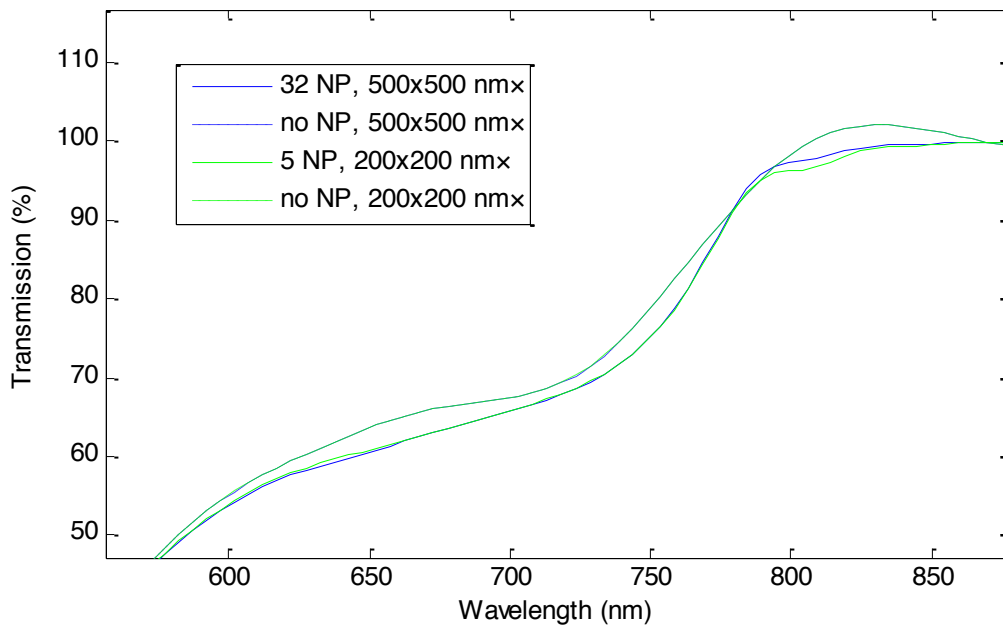


**Figure A.III.4 Effect of the number of Au\_NPs on different MAPI cell area.**

**Formula A.III.2:**

The curve is well fitted by a linear curve  $A = 0.0036 \times N + 0,0031$  corresponding to **Beer-Lambert's law** :  $A = \mathbf{l}\epsilon c$  where  $l = 100$  nm is the propagation length,  $c$  is the concentration and  $\epsilon$  is the molar extinction coefficient.

From this fit, we find  $\epsilon = 8.8.10^8$  L.mol<sup>-1</sup>cm<sup>-1</sup>. The **attenuation cross section** is then given by  $\sigma = \frac{\ln 10}{N_A} \epsilon$  so that  $\sigma = \mathbf{340}$  nm<sup>2</sup>. It is of quite similar order of magnitude than the Mie value (670 nm<sup>2</sup>), but lower probably because the losses in MAPI (quality factor of the LSP resonance) were not included in the Mie calculation.

**Formula A.III.3:**

The light absorption within a given volume is given by:

$$Abs = \iiint_V \|\vec{E}\| \epsilon'' dV \quad (\epsilon'' \text{ is the imaginary component of the relative permittivity}).$$

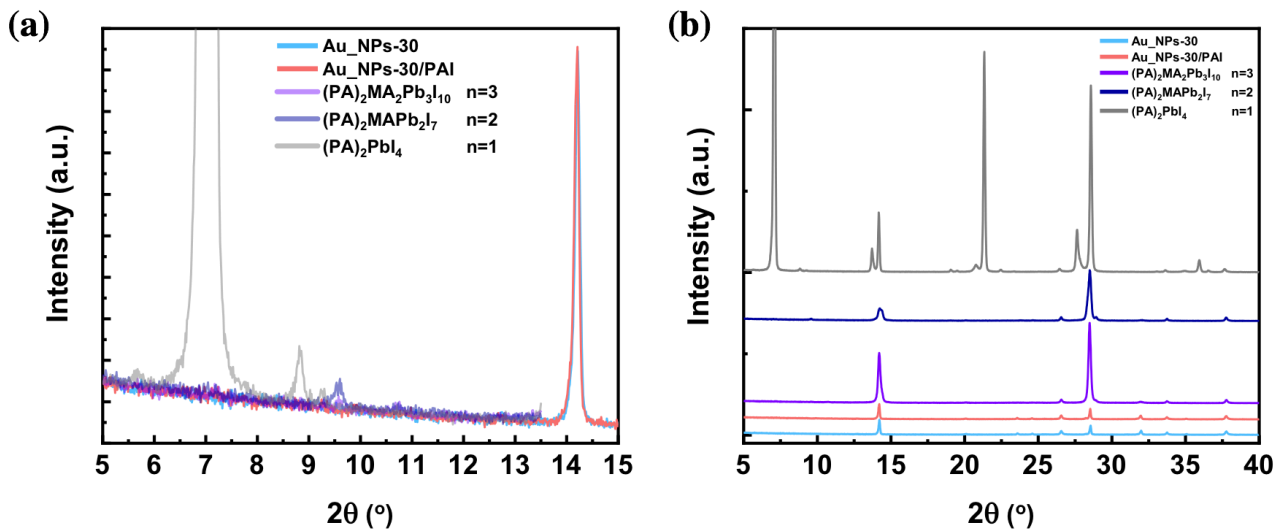


**Figure A.III.5** The same sample was measured before and after the treatment. Comparison with (PA)<sub>2</sub>PbI<sub>4</sub> (n=1), (PA)<sub>2</sub>MAPbI<sub>7</sub> (n=2) and (PA)<sub>2</sub>MA<sub>2</sub>PbI<sub>10</sub> (n=3) reference 2D layers.

**Table A.III.2 Effect of PAI concentration in IPA on the  $J$ - $V$  curves parameters of Au\_NPs-30 cells.**

Name	Entry	$V_{oc}$ [V]	$J_{sc}$ [ $\text{mA cm}^{-2}$ ]	FF [%]	PCE [%]	HI <sup>a)</sup> [%]
Ref	Reverse	1.059	23.37	76.81	19.01	16
	Forward	1.047	23.11	66.12	16.02	
2 mg/mL	Reverse	1.067	23.07	77.62	19.10	13
	Forward	1.052	22.93	68.73	16.57	
3 mg/mL	Reverse	1.089	23.17	79.81	20.13	14
	Forward	1.077	23.01	70.12	17.37	
4 mg/mL	Reverse	1.103	23.26	79.68	20.44	13
	Forward	1.091	23.14	70.42	17.78	
5 mg/mL	Reverse	1.069	22.19	73.45	17.42	13
	Forward	1.048	21.98	65.89	15.18	

a)  $HI = (PCE_{Rev} - PCE_{For}) * 100 / PCE_{Rev}$

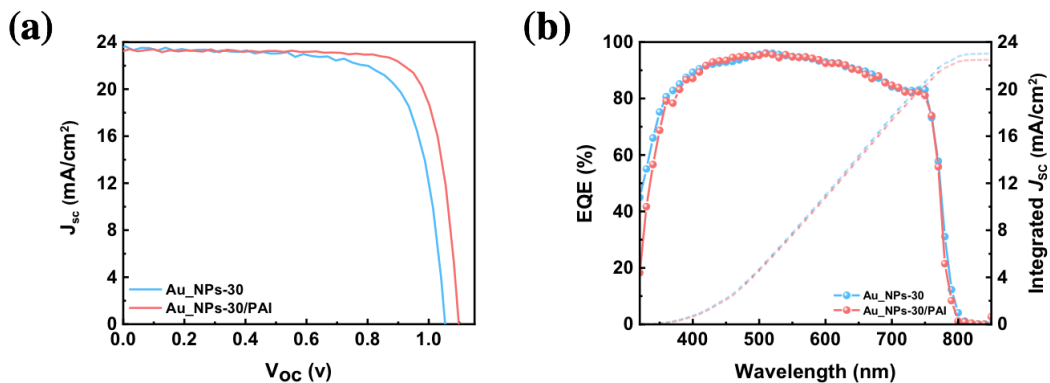


**Figure A.III.6 Effects of capping layer on (a) the reverse scan  $J$ - $V$  curves, (b)  $EQE$  spectra and integrated  $J_{sc}$  curves.**

## Annex IV-Chapter IV

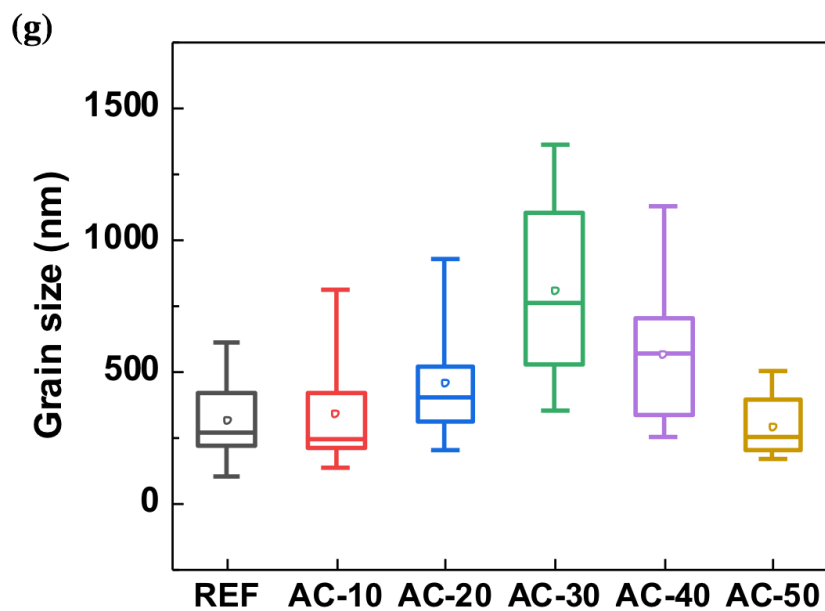
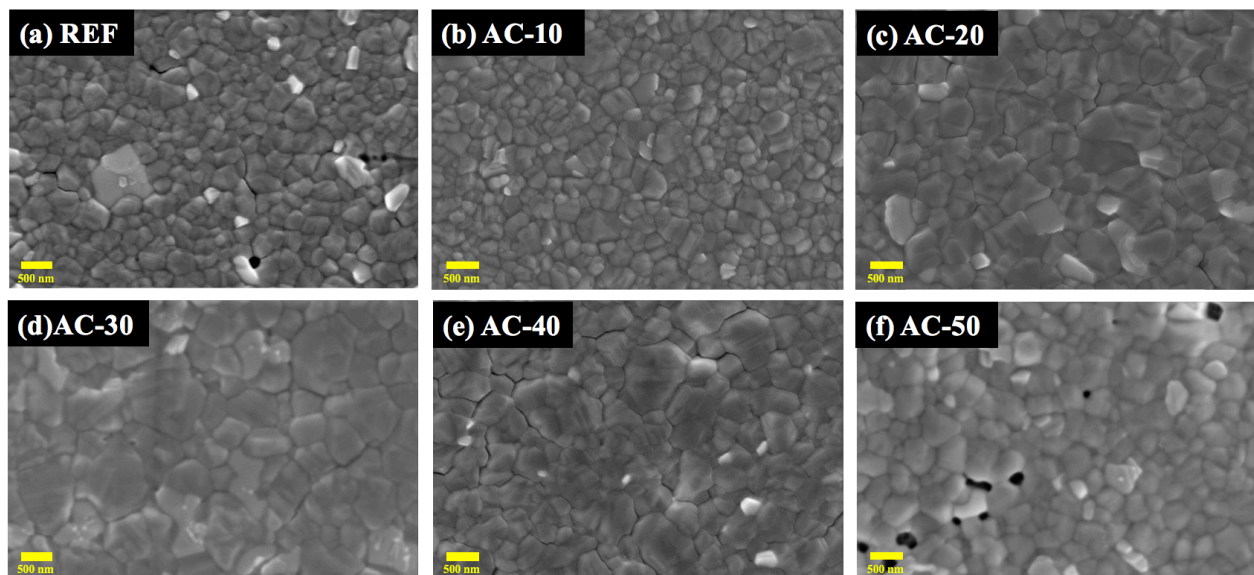


Figure A.IV.1 SEM top-view images of  $\text{Cs}_{0.1}\text{FA}_{0.9}\text{PbI}_3$  layers prepared with increasing amount of ammonium chloride (AC) additive: (a) w/o, (b) AC-10, (c) AC-20, (d) AC-30, (e) AC-40 and (f) AC-50. The scale bar is 500 nm. (g) Statistical analysis of the grain size.

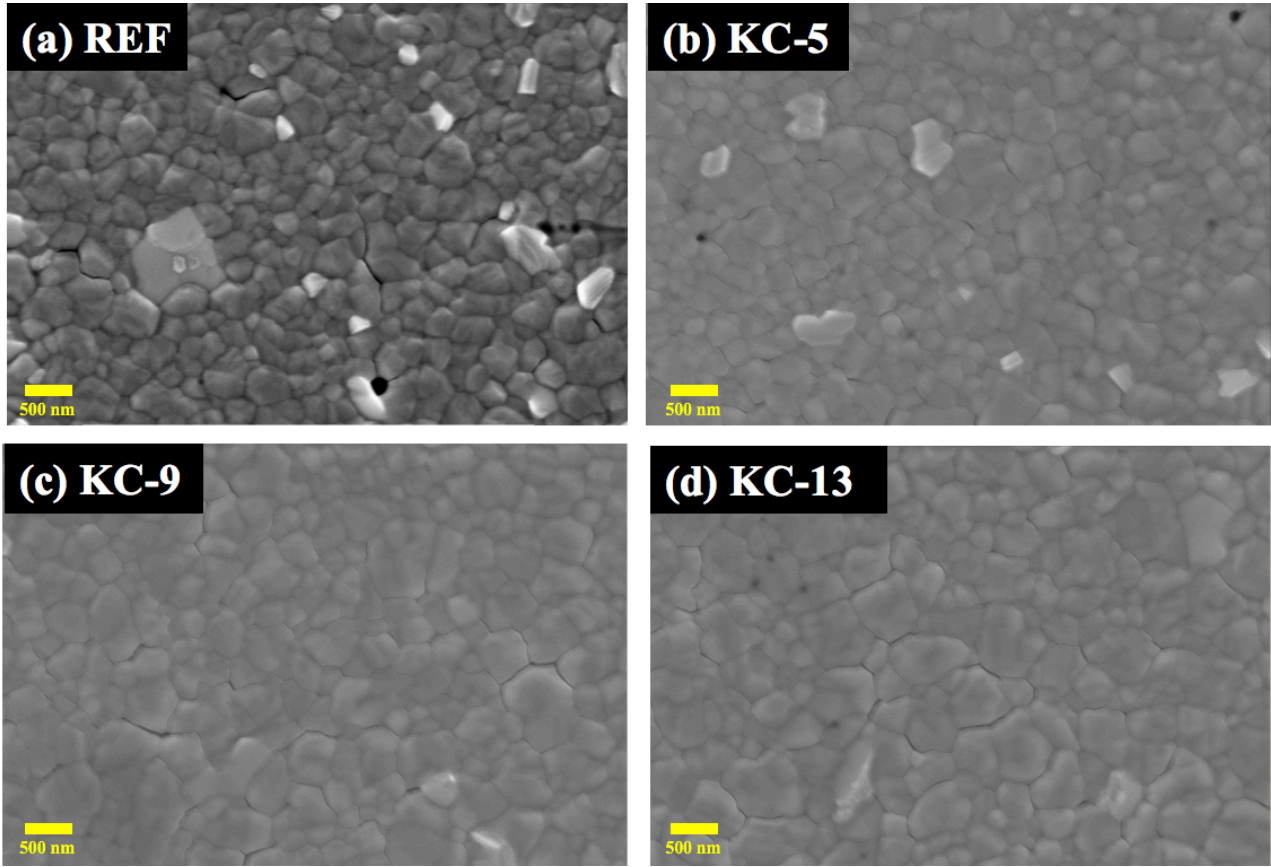


Figure A.IV.2 SEM top view images of  $\text{Cs}_{0.1}\text{FA}_{0.9}\text{PbI}_3$  layers prepared with increasing amount of potassium chloride additive: (a) w/o, (b) KC-5, (c) KC-9 and (d) KC-13.

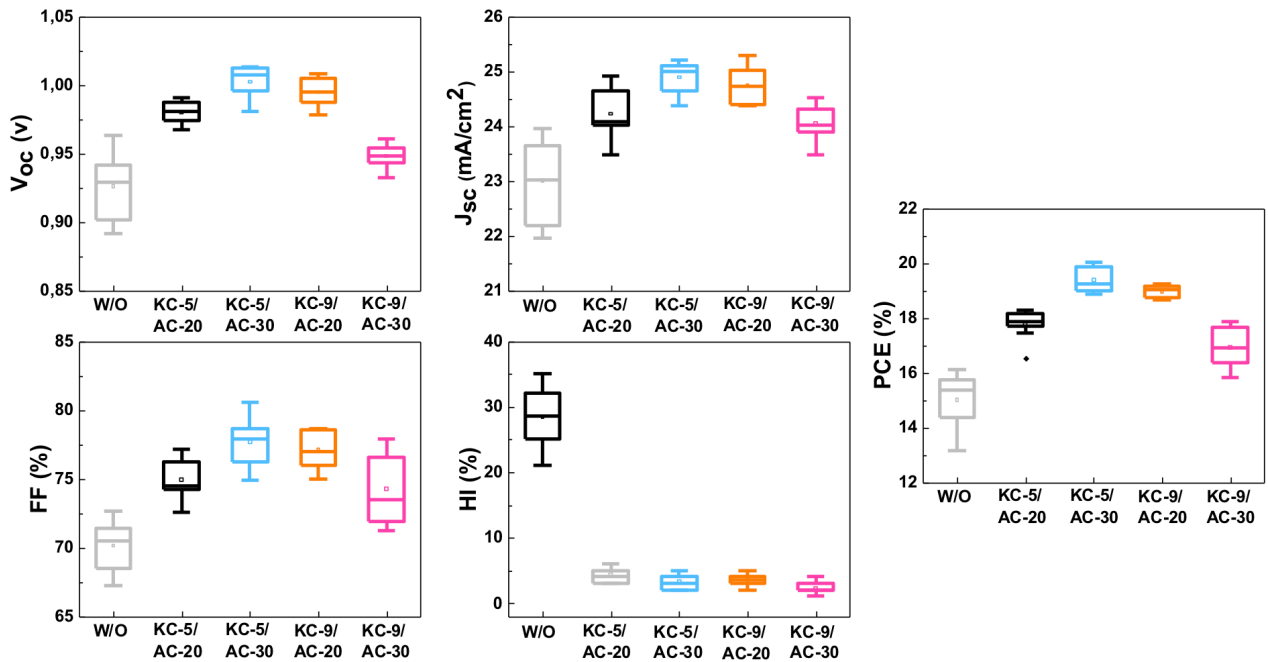


Figure A.IV.3 Statistical analysis of the effect of combining AC and KC additives on the  $J-V$  curve parameters of PSCs.

**Table A.IV.1  $J$ - $V$  curves parameters,  $PCE$  and  $HI$  of  $Cs_{0.1}FA_{0.9}PbI_3$  PSCs prepared with different amount of AC and KC additives**

No.	Entry	$V_{oc}$ [V]	$J_{sc}$ [ $mA\ cm^{-2}$ ]	FF [%]	PCE [%]	HI <sup>a</sup> [%]
<b>w/o</b>	Revers e	0.941	23.82	71.92	16.13	28
	Forwa rd	0.837	23.88	58.24	11.65	
<b>KC-5/AC- 20</b>	Revers e	0.984	24.65	75.34	18.27	4
	Forwa rd	0.976	24.34	75.14	17.58	
<b>KC-5/AC- 30</b>	Revers e	1.012	25.21	78.61	20.05	3
	Forwa rd	1.013	24.94	76.73	19.39	
<b>KC-9/AC- 20</b>	Revers e	1.005	24.39	78.53	19.24	2
	Forwa rd	1.004	24.17	77.84	18.89	
<b>KC-9/AC- 30</b>	Revers e	0.947	24.31	77.69	17.88	2
	Forwa rd	0.951	24.19	76.64	17.63	

<sup>a</sup>  $HI = (PCE_{Rev} - PCE_{For}) * 100 / PCE_{Rev}$

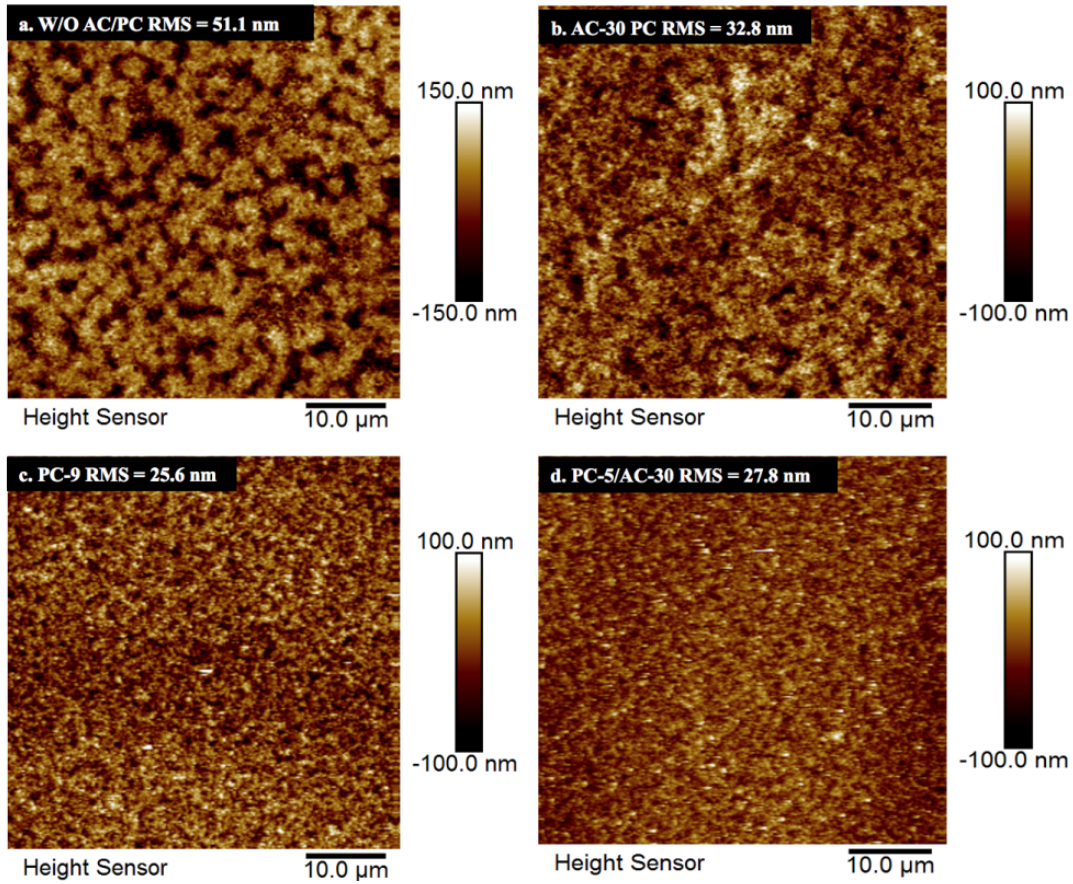


Figure A.IV.4 AFM image of  $\text{Cs}_{0.1}\text{FA}_{0.9}\text{PbI}_3$  perovskite layer surfaces. Effect of additives: (a) w/o, (b) AC-30, (c) PC-9 and (d) PC-9/AC-30 respectively.

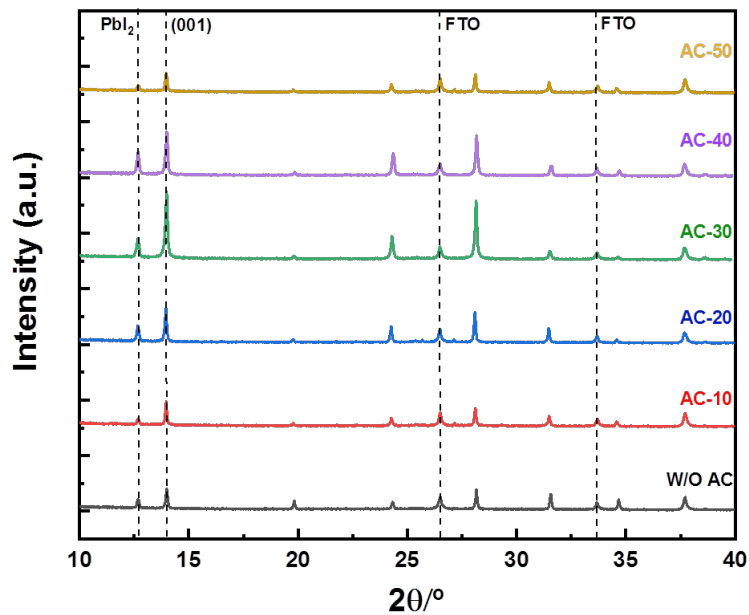


Figure A.IV.5 XRD patterns of pristine  $\text{Cs}_{0.1}\text{FA}_{0.9}\text{PbI}_3$  layer and  $\text{Cs}_{0.1}\text{FA}_{0.9}\text{PbI}_3$  layers prepared with various AC additive amount.

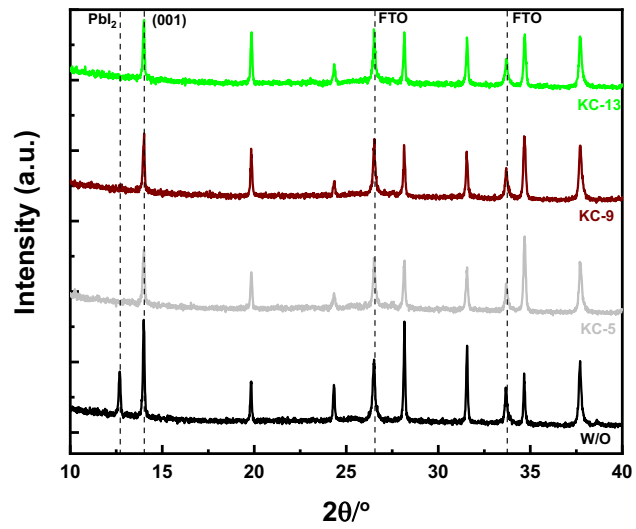


Figure A.IV.6 XRD patterns of pristine  $\text{Cs}_{0.1}\text{FA}_{0.9}\text{PbI}_3$  layer and  $\text{Cs}_{0.1}\text{FA}_{0.9}\text{PbI}_3$  layers prepared with various KC additive amount.

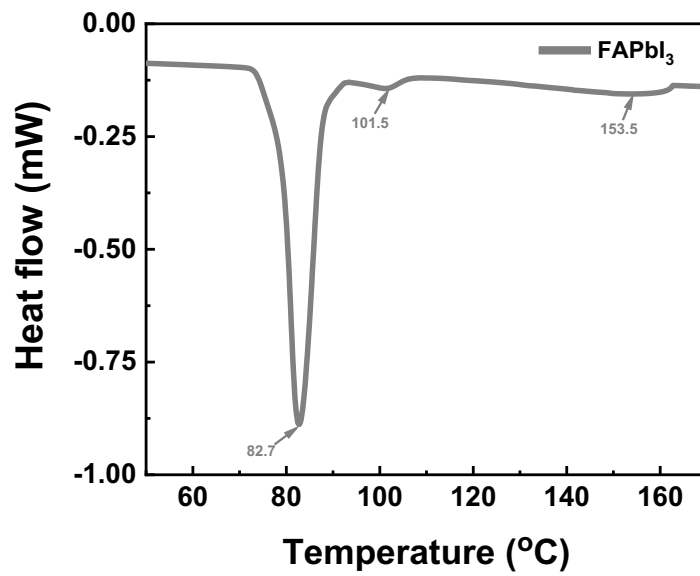
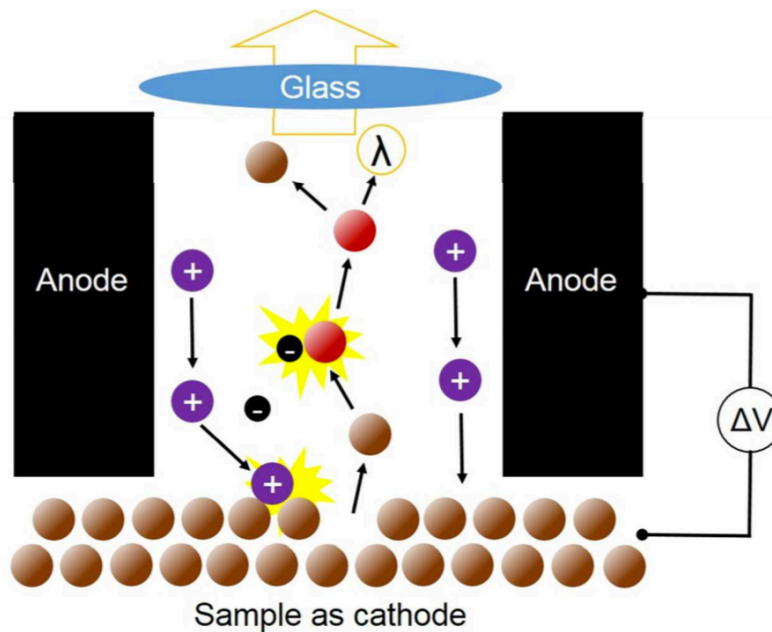


Figure A.IV.7 DSC curve of  $\text{FAPbI}_3$  adduct.



**Figure A.IV.8 Schematic illustration of GD-OES measurement set-up.[1]**

The glow-discharge (GD) plasma, generated in an anode tube, sputters the surface of the analyzed sample (perovskite layer, precursor layer, perovskite solar cell...) layer by layer and excites the sputtered atoms. The photons emitted from excited atoms, are collected and analyzed to obtain the depth-resolved elemental analysis, with nanometric depth resolution. In GD-OES a radio frequency (RF) plasma is used to obtain the elemental profile of conductive, insulating or hybrid materials. The GD plasma has a double role: firstly it sputters the surface of the sample and by optimizing the plasma conditions layer-by-layer erosion can be achieved; secondly, it excites the sputtered atoms. More in details, by applying a RF-power to the sample, an Ar-plasma is created in the tubular anode in our case. The inner diameter of the anode defines the analyzed spot size, as the plasma is restricted to this area. When the discharge gas breaks down electrically, forming electrons and positively charged ions, the latter are accelerated towards the sample by the electric field and the ion bombardment of the surface of the sample causes the sputtering of the material to be analyzed. When entering the gas phase environment of the glow discharge, the sputtered atoms are excited by collisions with high-energy electrons, metastable argon atoms and ions. The de-excitation of the excited species causes the emission of photons characteristic of the different elements composing the material, which are collected using an optical spectrometer. As the sample is continuously sputtered, the collected light

reflects the temporal evolution of the sputtered species, therefore it is possible to obtain the depth-resolved elemental analysis, with nanometric depth resolution.

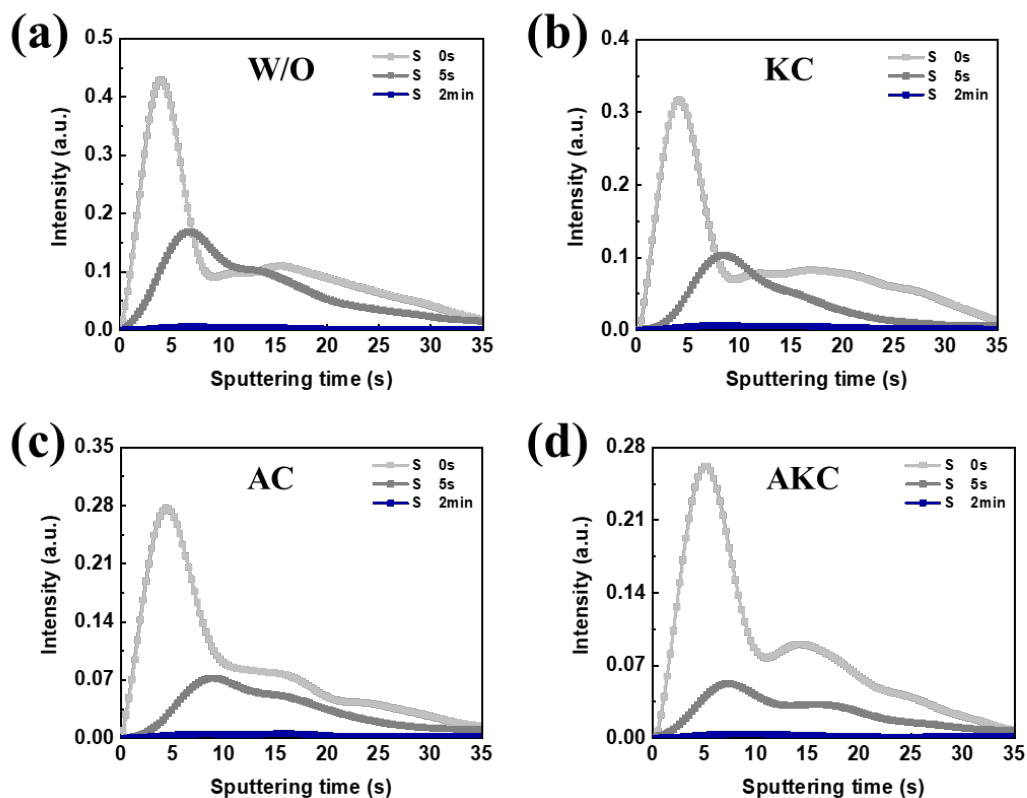


Figure A.IV.9 Effect of additives on the GD-OES S profile between 0 s and 2 min.

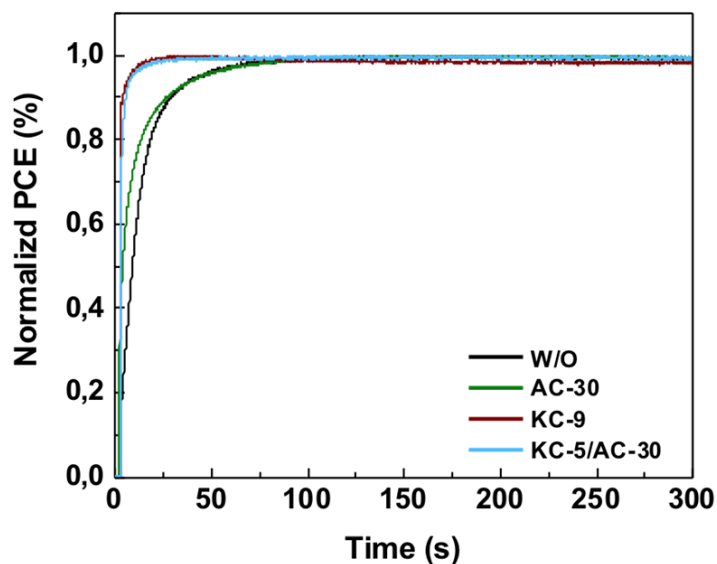


Figure IV.10 Effect of additive on the tracking of the best  $\text{Cs}_{0.1}\text{FA}_{0.9}\text{PbI}_3$  cells normalized PCE.

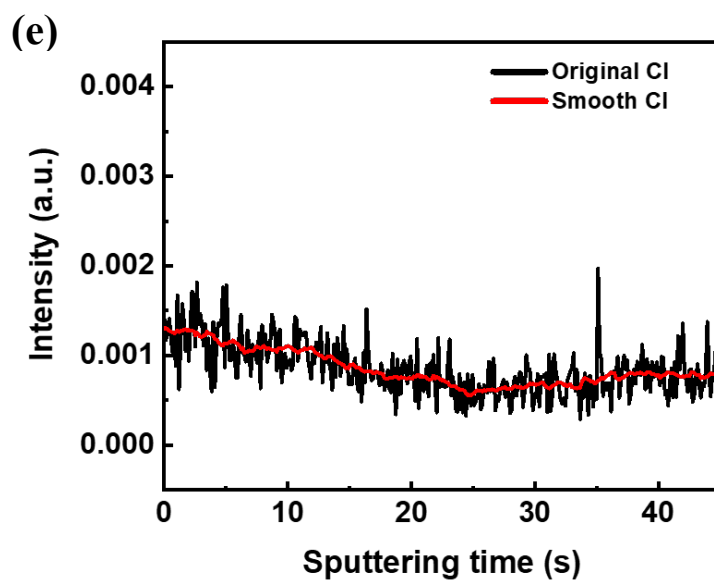
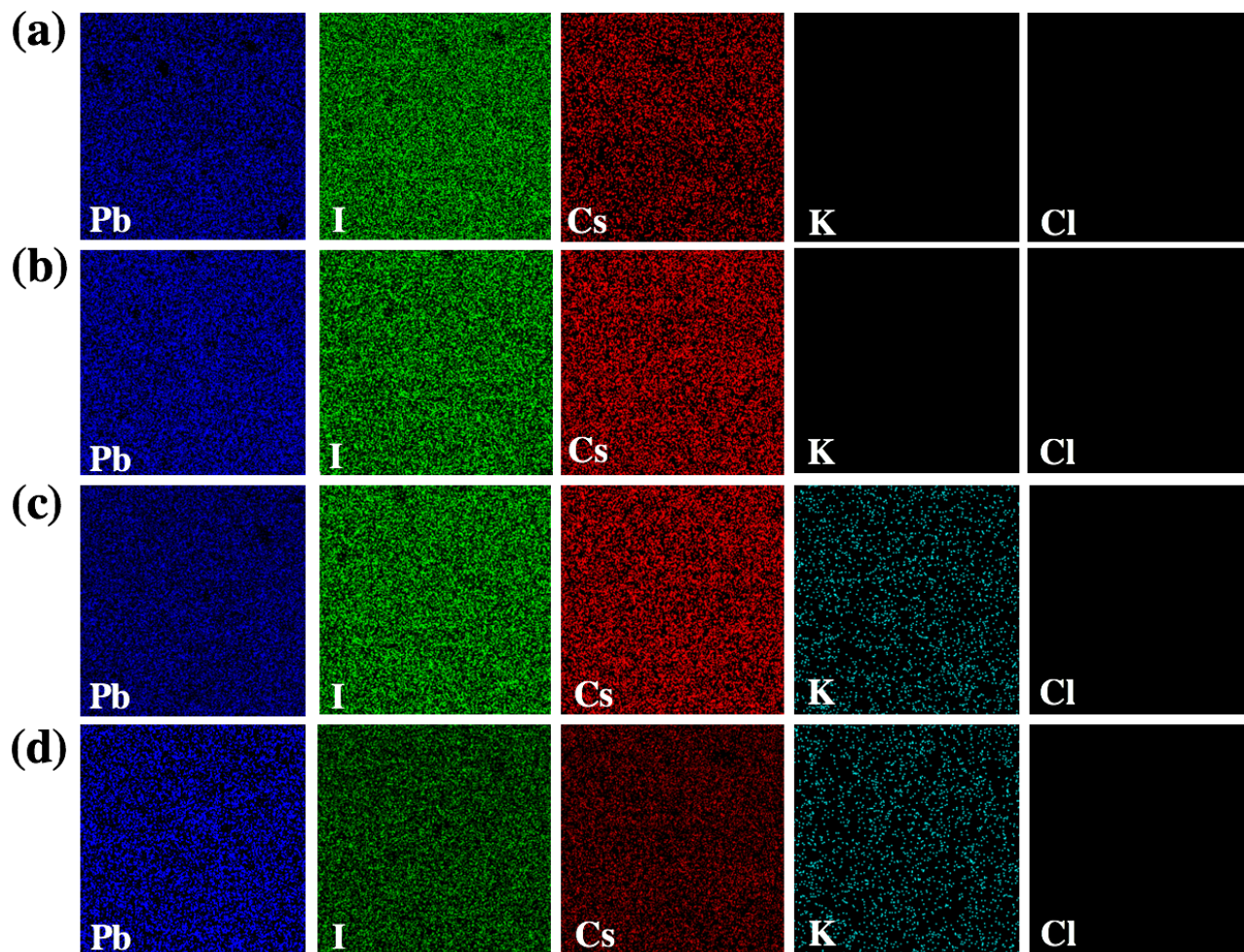


Figure A.IV.11 EDX elements mapping results of the perovskite layers. (a) w/o, (b) AC-30, (c) KC-9 and (d) KC-5/AC-30. Size: 8  $\mu\text{m}$   $\times$  8  $\mu\text{m}$ . (e) GD-OES profile of Cl element in the KC-5/AC-30 PSC. The red trace is the smoothed curve.

**Table A.IV.2 ExpDec 3** function fitting parameters of the TRPL decay curves measured at 472 nm on the series of optimized  $\text{Cs}_{0.1}\text{FA}_{0.9}\text{PbI}_3$  films deposited on  $\text{TiO}_2$ .

$$\text{ExpDec 3 : } y = A_1 \exp(-x/\tau_1) + A_2 \exp(-x/\tau_2) + A_3 \exp(-x/\tau_3) + y_0$$

	$y_0$	$A_1$	$\tau_{\text{fast}}$ [ns]	$\text{RC}_{\text{fast}}^{\text{a}}$	$A_2$	$\tau_{\text{int}}$ [ns]	$\text{RC}_{\text{int}}^{\text{a}}$	$A_3$	$\tau_{\text{slow}}$ [ns]	$\text{RC}_{\text{slow}}^{\text{a}}$
<b>w/o</b>	7.8E-4	0.38	3.0	0.019	0.35	32.5	0.191	0.28	168	0.790
<b>AC-30</b>	1.59E-3	0.54	1.5	0.012	0.19	22.3	0.064	0.25	243	0.923
<b>KC-9</b>	13.7E-4	0.49	1.6	0.009	0.16	36.2	0.066	0.32	254	0.925
<b>KC-5/AC-30</b>	29.1E-4	0.52	1.9	0.007	0.19	76.8	0.099	0.24	551	0.895

<sup>a</sup> $\text{RC}_{\text{xx}}$ : fast, intermediate and slow relative contributions.

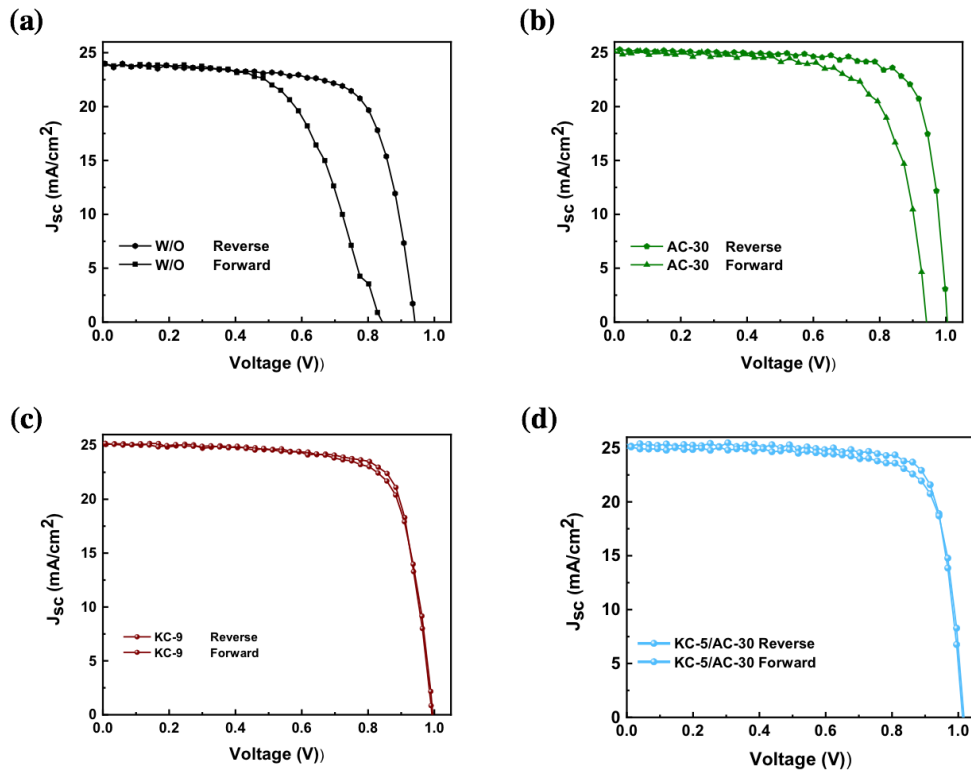


**Figure A.IV.12** Forward and reverse  $J$ - $V$  curves of (a)w/o, (b) KC-9, (c) AC-30 and (d) KC-5/AC-30 solar cells.

References

[1] H. Lee, S. Gaiaschi, P. Chapon, A. Marronnier, H. Lee, J. C. Vanel, D. Tondelier, J.-E. Bourée, Y. Bonnassieux, B. Geffroy, ACS Energy Lett. 2017, 2, 943–949.

## Annex V-Chapter V

**Table A.V.1 Comparison of the depth profile measuring methods**

Analytical method	Detection limit	Minimum area	Detection depth	Insulator analysis
AES	0.1 at. %	100 nm	1 $\mu\text{m}$	NO
XPS	0.1 at. %	100 $\mu\text{m}$	$\sim 10$ nm (Al K $\alpha$ , energy of 1486.6eV)	YES
HAXPES	0.1 at. %	100 $\mu\text{m}$	$\sim 20$ nm (Cr K $\alpha$ , energy of 5414.9eV)	YES
<b>GD-OES</b>	<b>10 <math>\mu\text{g/g}</math></b>	<b>5 mm</b>	<b>100 <math>\mu\text{m}</math></b>	<b>YES</b>
SIMS	0.1 $\mu\text{g/g}$	1 $\mu\text{m}$	1 $\mu\text{m}$	NO

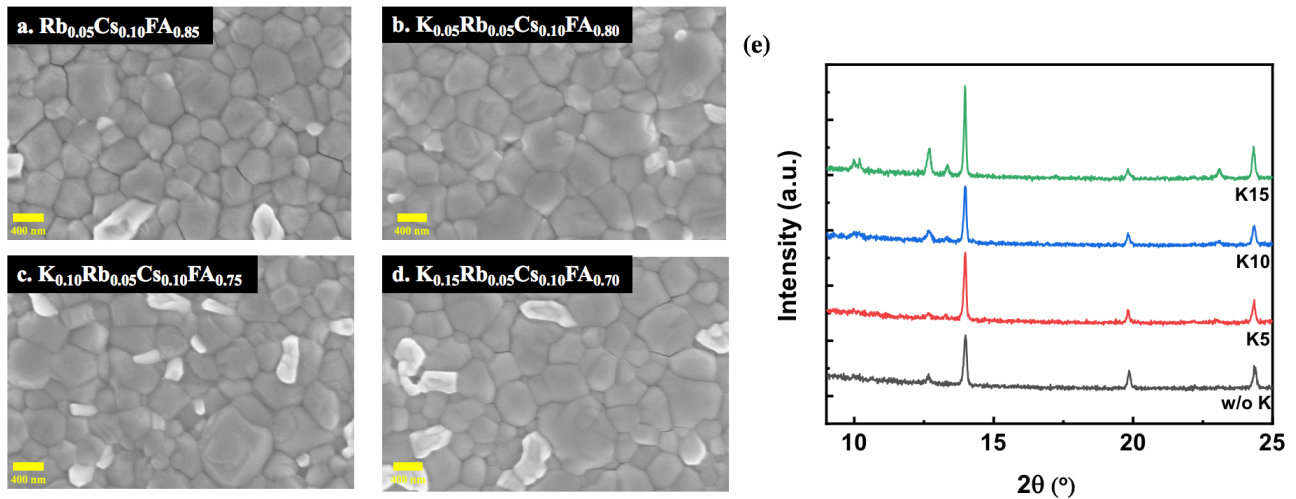


**Figure A.V.1 (a-d) SEM top-view images of  $\text{K}_x\text{Rb}_{0.05}\text{Cs}_{0.1}\text{FA}_{0.85-x}\text{PbI}_3$  layers prepared with increasing amount of KI : (a) w/o K, (b) K5 ( $x=0.05$ ), (c) K10 ( $x=0.10$ ), (d) K15 ( $x=0.15$ ); (e) XRD pattern of  $\text{K}_x\text{Rb}_{0.05}\text{Cs}_{0.1}\text{FA}_{0.85-x}\text{PbI}_3$ .**

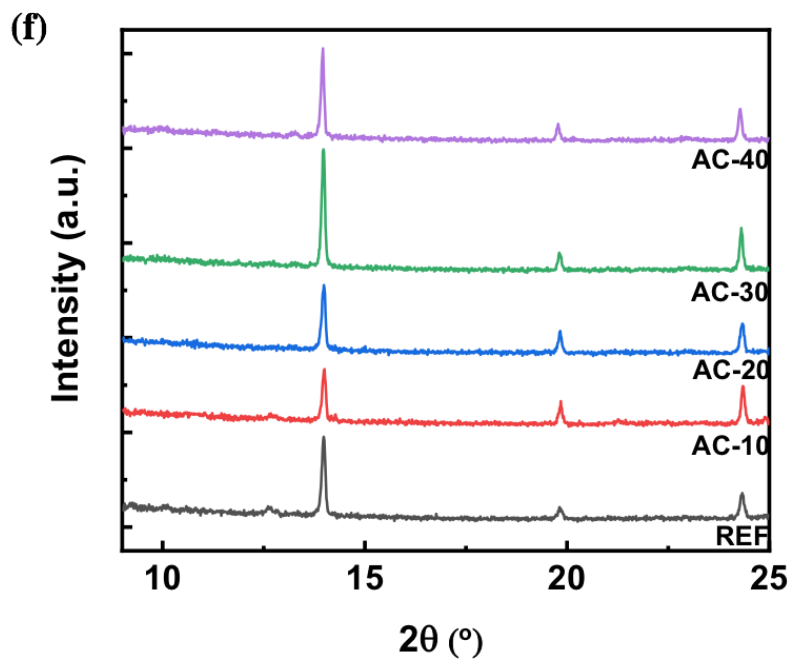
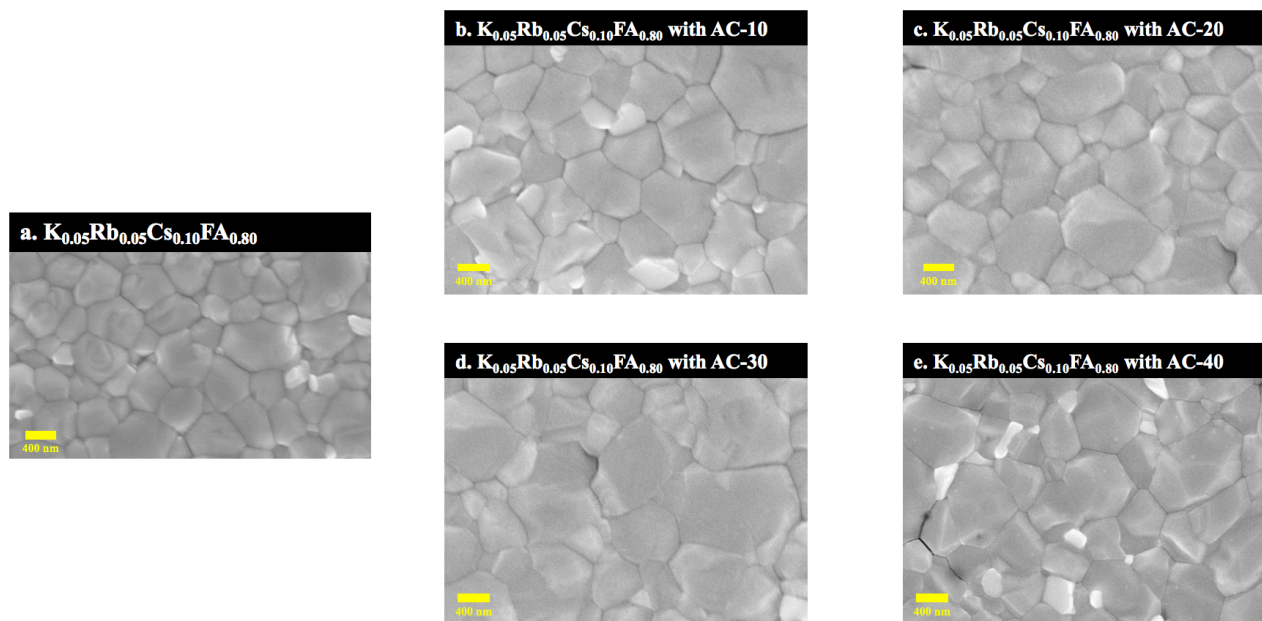


Figure A.V.2 (a-d) SEM top-view images of  $K_{0.05}Rb_{0.05}Cs_{0.1}FA_{0.80}PbI_3$  layers prepared with increasing amount of  $NH_4Cl$  (AC): (a) w/o AC, (b) AC-10, (c) AC-20, (d) AC-30, (e) AC-40; (f) XRD pattern of  $K_{0.05}Rb_{0.05}Cs_{0.1}FA_{0.80}PbI_3$  with different amount of AC.

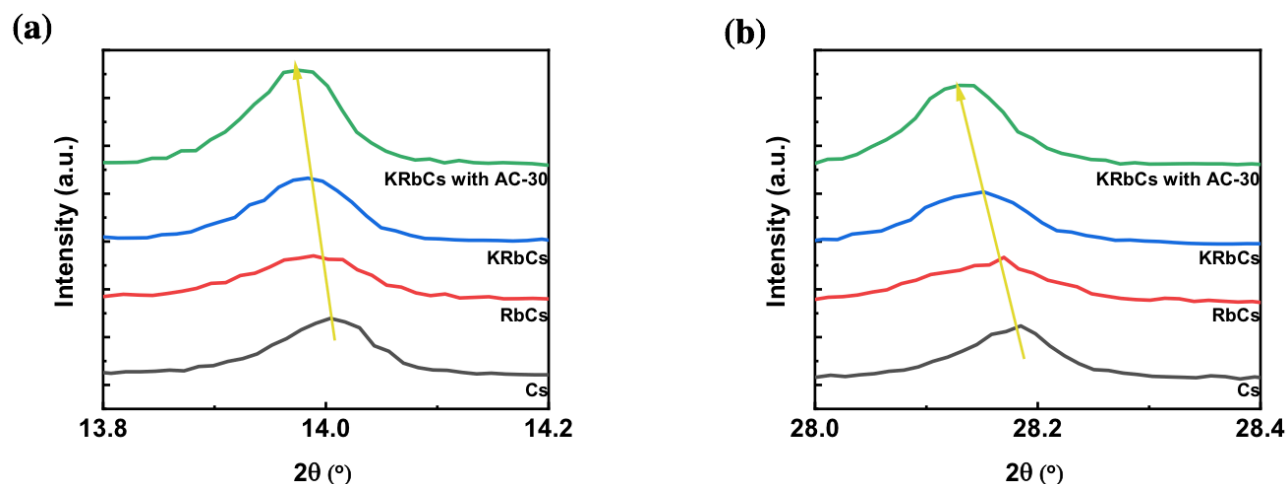


Figure A.V.3 XRD patterns of four kinds of perovskite layers. (a) (001) peak and (b) (002) peak.

Table A.V.2 The performance of RbCsFA Solar cell with different amount of KI.

Name	Scan direction	$V_{oc}$ [V]	$J_{sc}$ [mA. cm <sup>-2</sup> ]	$FF$	PCE [%]	$HI^{(a)}$ [%]
Rb <sub>0.05</sub> Cs <sub>0.10</sub>	Reverse	1.017	24.49	76.12	18.96	24
	Forward	1.006	24.36	58.89	14.43	
K <sub>0.05</sub> Rb <sub>0.05</sub> Cs <sub>0.10</sub>	Reverse	1.031	23.96	78.08	19.29	3
	Forward	1.034	23.79	76.17	18.74	
K <sub>0.10</sub> Rb <sub>0.05</sub> Cs <sub>0.10</sub>	Reverse	1.044	23.48	75.08	18.40	5
	Forward	1.043	23.32	72.17	17.55	
K <sub>0.15</sub> Rb <sub>0.05</sub> Cs <sub>0.10</sub>	Reverse	1.021	23.17	71.69	16.96	3
	Forward	1.017	23.06	69.84	16.38	

<sup>a)</sup>  $HI = (PCE_{Rev} - PCE_{For}) * 100 / PCE_{Rev}$

**Table A.V.3 The performance of KRbCsFA Solar cell with different amount of AC.**

Name	Scan direction	$V_{oc}$ [V]	$J_{sc}$ [mA. cm <sup>-2</sup> ]	$FF$	PCE [%]	$HI^{(a)}$ [%]
K <sub>0.05</sub> Rb <sub>0.05</sub> Cs <sub>0.10</sub>	Reverse	1.031	23.96	78.08	19.29	3
	Forward	1.034	23.79	76.17	18.74	
K <sub>0.05</sub> Rb <sub>0.05</sub> Cs <sub>0.10</sub> With AC-10	Reverse	1.043	24.13	77.12	19.41	2
	Forward	1.045	24.06	75.57	19.00	
K <sub>0.05</sub> Rb <sub>0.05</sub> Cs <sub>0.10</sub> With AC-20	Reverse	1.064	24.35	78.38	20.31	4
	Forward	1.061	24.29	75.77	19.53	
K <sub>0.05</sub> Rb <sub>0.05</sub> Cs <sub>0.10</sub> With AC-30	Reverse	1.083	24.79	78.69	21.13	4
	Forward	1.072	24.66	76.84	20.32	
K <sub>0.05</sub> Rb <sub>0.05</sub> Cs <sub>0.10</sub> With AC-40	Reverse	1.052	23.89	73.43	18.45	5
	Forward	1.048	23.73	70.84	17.62	

<sup>a)</sup>  $HI = (PCE_{Rev} - PCE_{For}) * 100 / PCE_{Rev}$

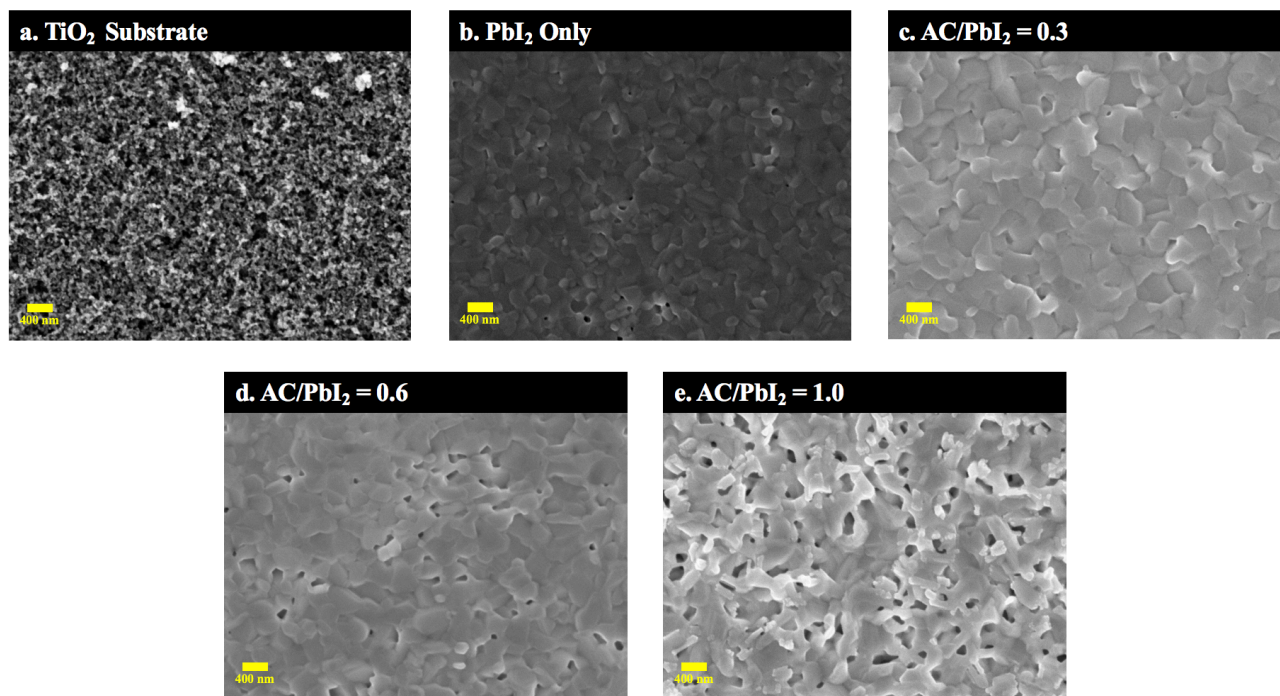


**Figure A.V.4 SEM top-views of (a) TiO<sub>2</sub> substrate, (b) PbI<sub>2</sub> (c) PbI<sub>2</sub> with 30 mol% AC (d) PbI<sub>2</sub> with 60 mol% AC (e) PbI<sub>2</sub> with 100 mol% AC.**

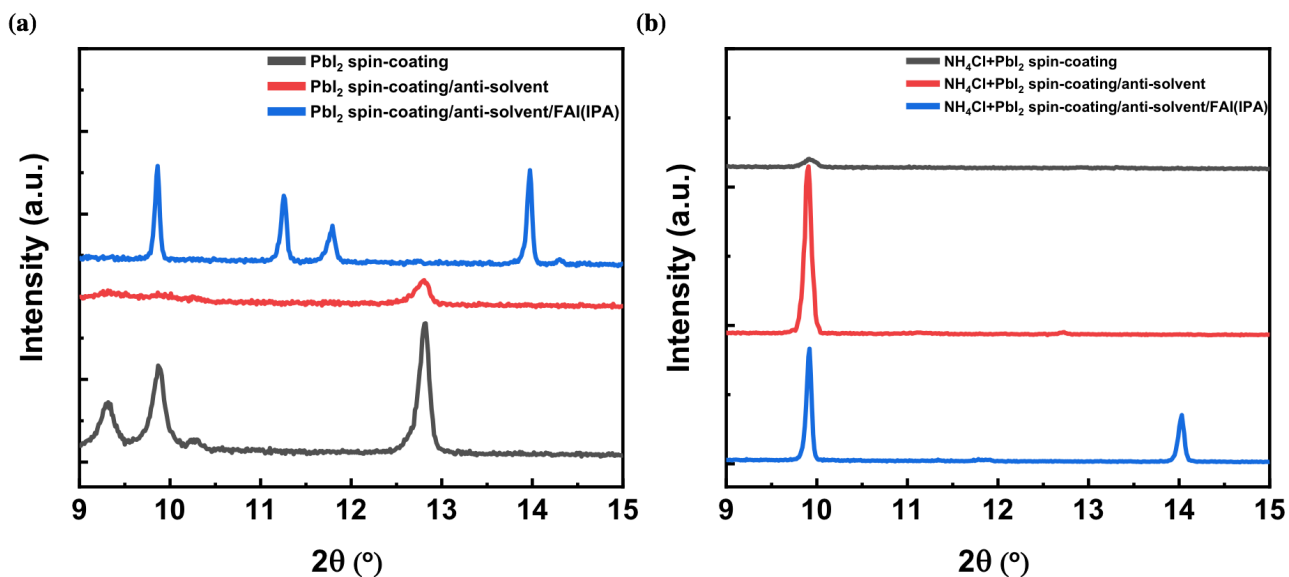


Figure A.V.5 XRD patterns of different preparation stages of (a) without AC and (b) with AC to show the effect of  $\text{NH}_4\text{Cl}$ - $\text{PbI}_2$  intermediate on  $\alpha$ -phase formation.

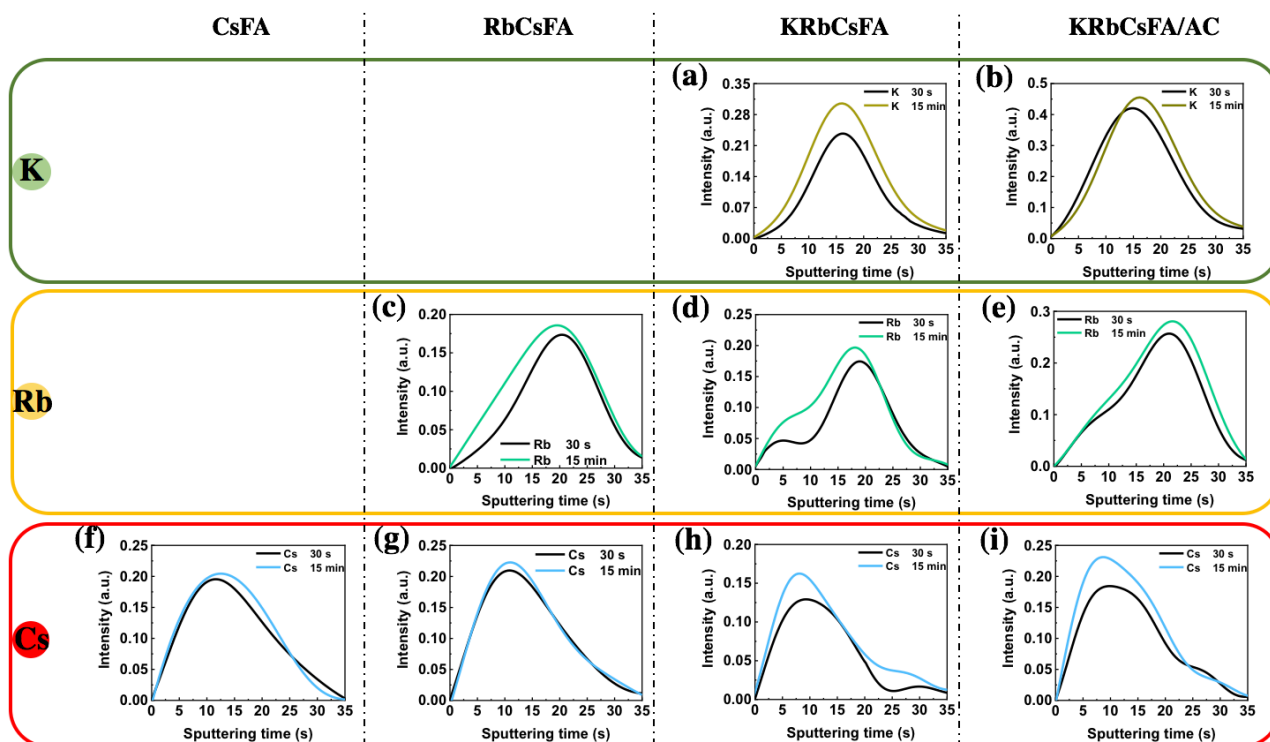


Figure A.V.6 GD-OES curve of distribution of metal cations distribution at increasing annealing times up to full annealing.

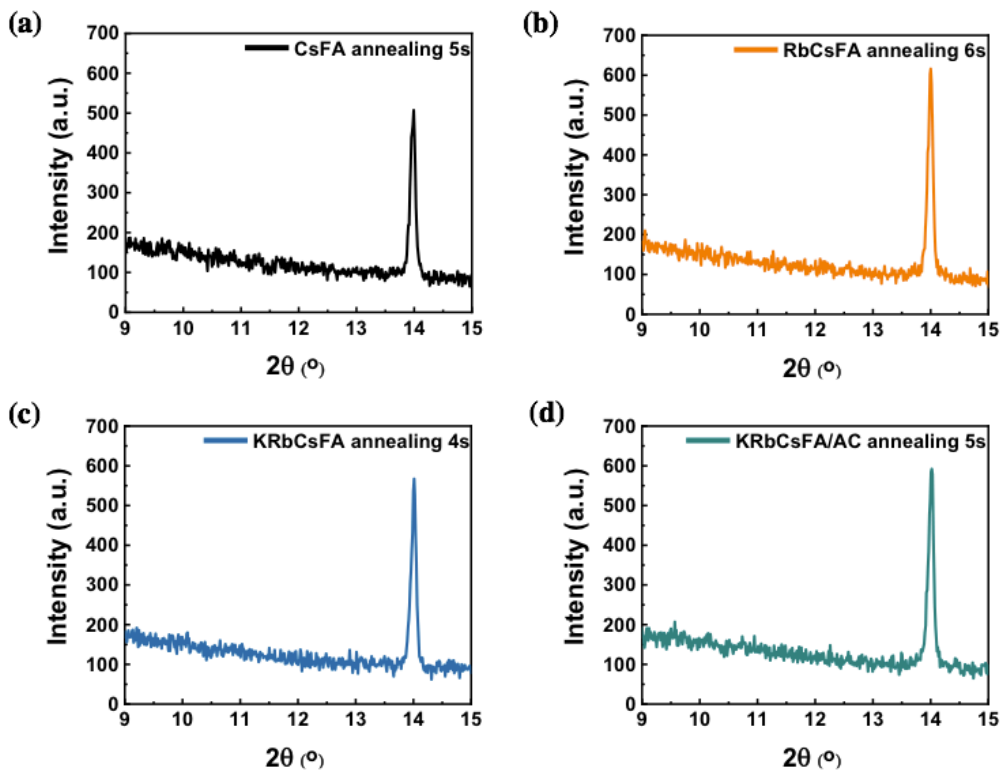


Figure A.V.7 XRD patterns of the PVK samples with various compositions at the annealing color changing times.

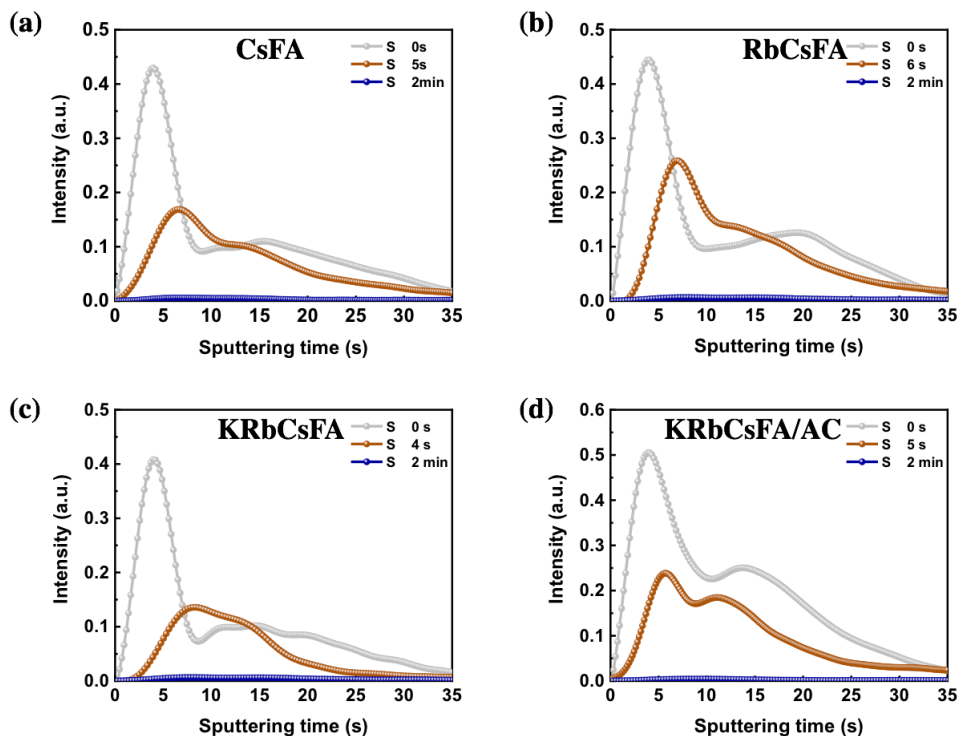


Figure A.V.8 (a-d) Evolution of GD-OES S (DMSO solvent) profile in the perovskite precursor layer upon annealing.

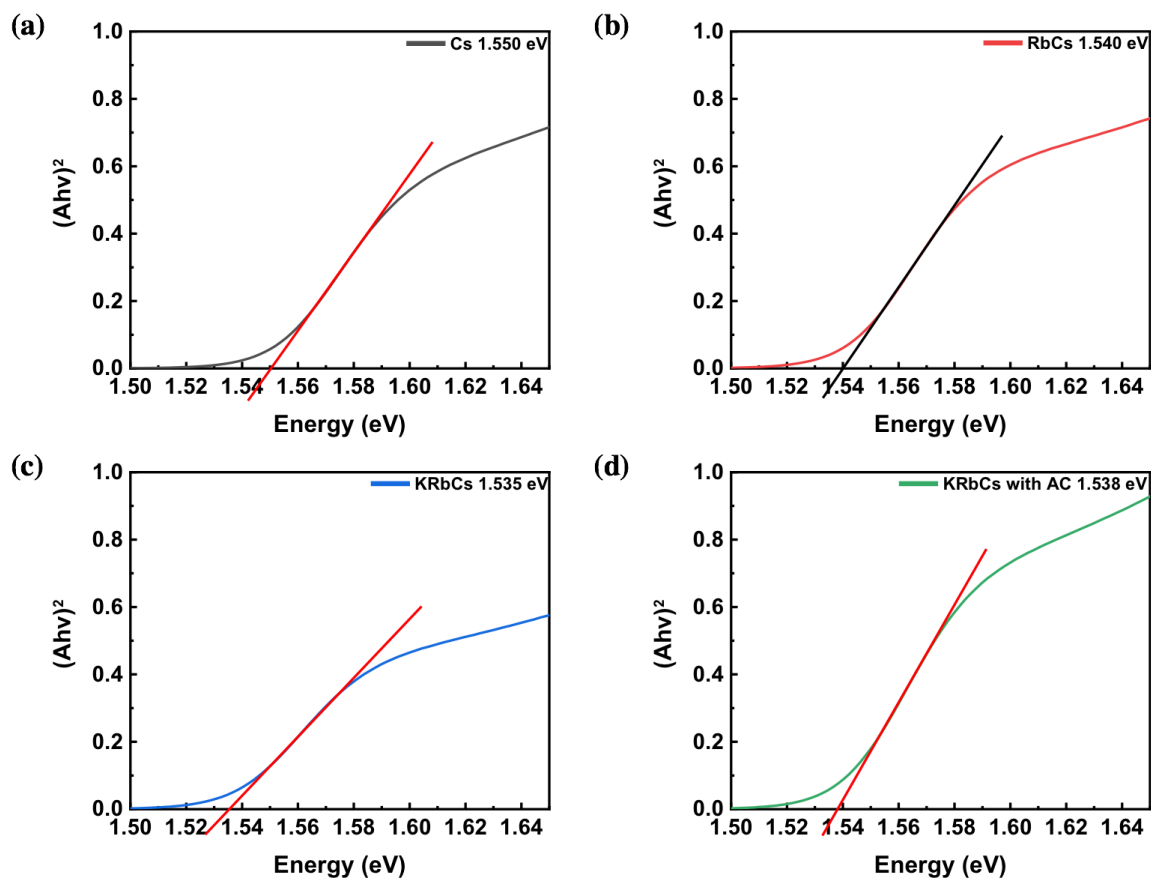


Figure A.V.9 Tauc plots of the absorbance curves and optical direct bandgap determination .

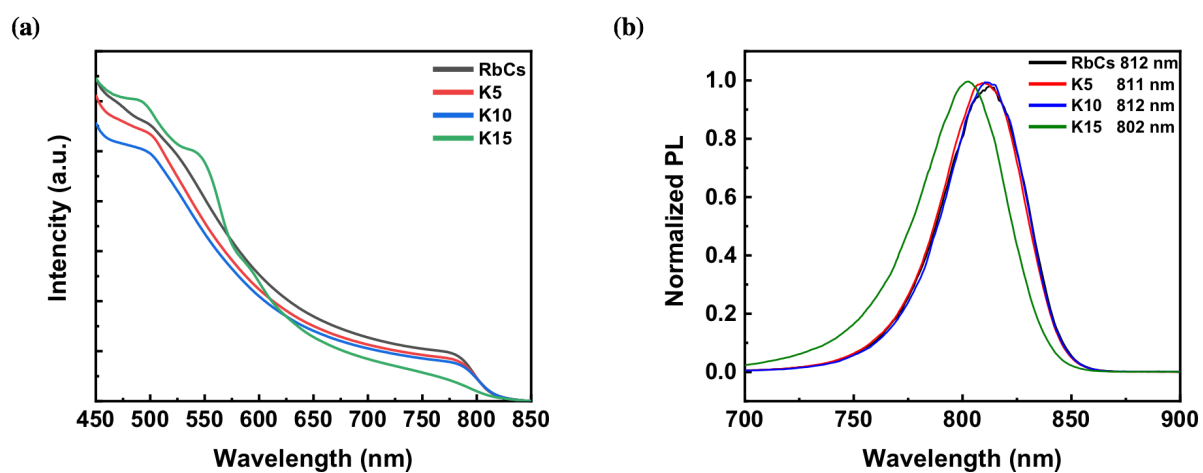


Figure A.V.10 Effect of KI on the (a) absorbance and (b) steady-state photoluminescence of the  $K_xRb_{0.05}Cs_{0.10}FA_{0.85-x}$  layers deposited on the FTO/c-TiO<sub>2</sub>/mp-TiO<sub>2</sub> layers' substrate.

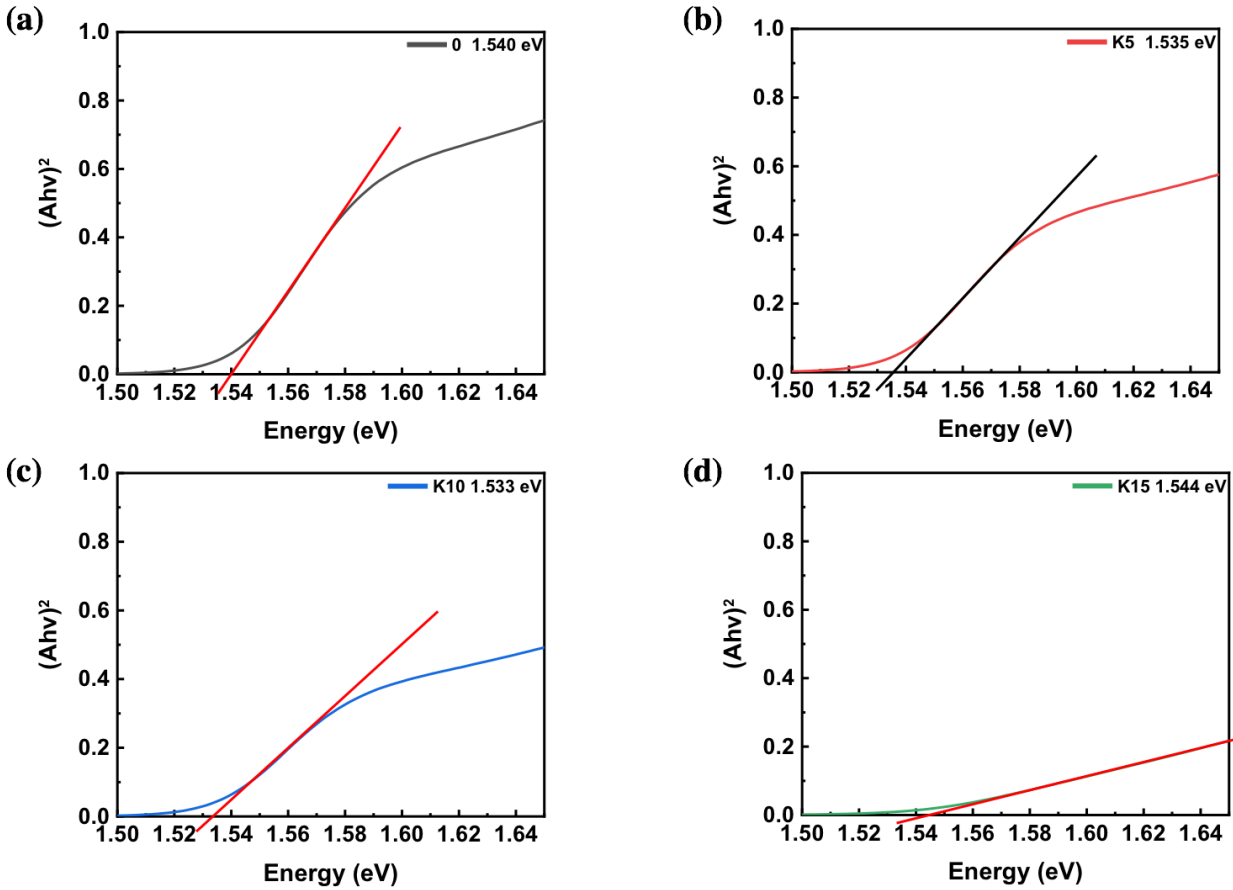


Figure A.V.11 Effect of KI content for  $K_xRb_{0.05}Cs_{0.10}FA_{0.85-x}$  system. Tauc plot and bandgap determination.

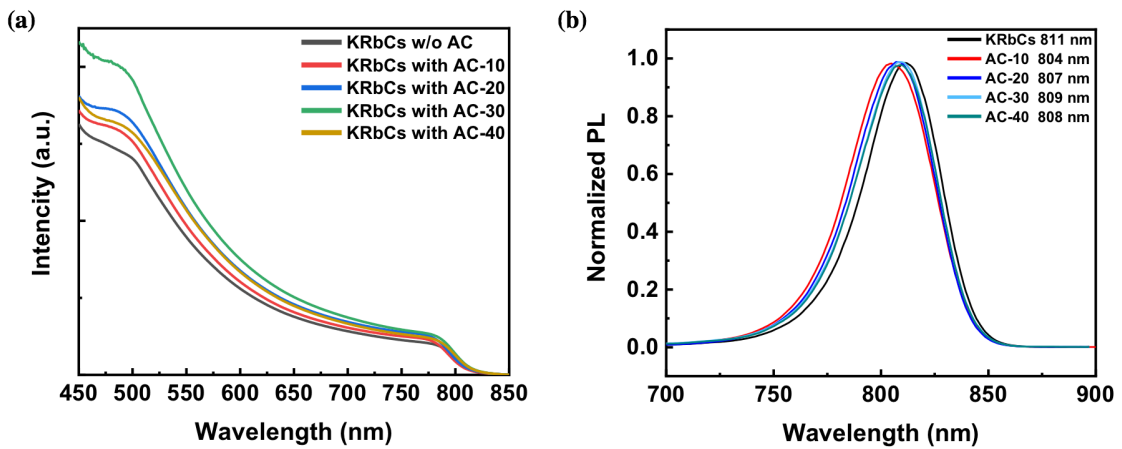


Figure A.V.12 Effect of AC on the (a) absorbance and (b) steady-state photoluminescence of the KRbCsFA layers deposited on the FTO/c-TiO<sub>2</sub>/mp-TiO<sub>2</sub> layers' substrate.

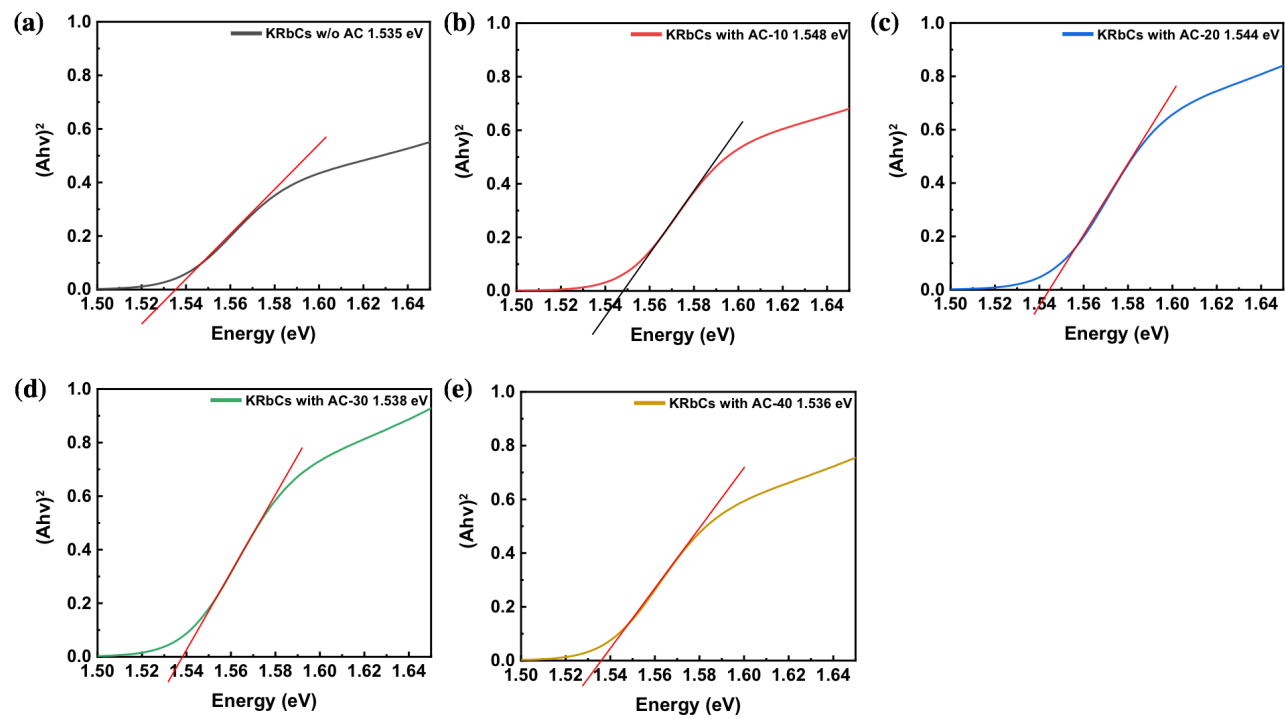


Figure A.V.13 Effect of AC on the Tauc plot and bandgap determination of the KRbCsFA films.

## Annex VI-Chapter VI

**Table A.VI.1 Comparison the effect of different post-treatment solutions on  $J$ - $V$  curve parameters based on CsFAPbI<sub>3</sub>/AC cell.**

Post-treatment solution	Scan direction	$V_{oc}$ [V]	$J_{sc}$ [mA. cm <sup>-2</sup> ]	$FF$	PCE [%]	$HI^a$ [%]
\	Reverse	1.010	25.12	77.31	19.61	4
	Forward	1.011	24.81	75.33	18.89	
PEAI	Reverse	1.003	24.34	68.84	16.81	15
	Forward	0.989	24.05	59.98	14.27	
PAI	Reverse	1.047	24.89	78.82	20.54	5
	Forward	1.049	24.46	76.37	19.59	

<sup>a)</sup>  $HI = (PCE_{Rev} - PCE_{For}) * 100 / PCE_{Rev}$

**Table A.VI.2 ExpDec 3 function fitting parameters of the TRPL decay curves measured at 472 nm on KRbCsFA/AC films deposited on TiO<sub>2</sub>, before and after PAI post-treatment.**

<b>ExpDec 3 : <math>y = A_1 \exp(-x/\tau_1) + A_2 \exp(-x/\tau_2) + A_3 \exp(-x/\tau_3) + y_0</math></b>										
NAME	$y_0$	$A_1$	$\tau_{fast}$ [ns]	$RC_{fast}^a$	$A_2$	$\tau_{int}$ [ns]	$RC_{int}^a$	$A_3$	$\tau_{slow}$ [ns]	$RC_{slow}^a$
KRbCsFA /AC	1.0E-3	0.30	19.97	0.06	0.36	58.67	0.21	0.29	252.69	0.73
KRbCsFA /AC-PAI	1.8E-3	0.63	1.55	0.02	0.28	16.02	0.10	0.09	454.65	0.88

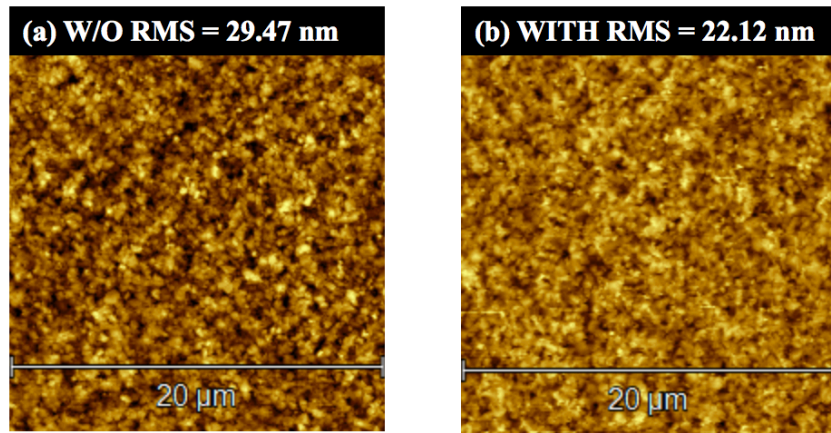


**Figure A.VI.1 AFM image of KRbCsFA/AC perovskite layer surfaces: (a) before and (b) after PAI post-treatment. Size : 20μm \* 20μm**

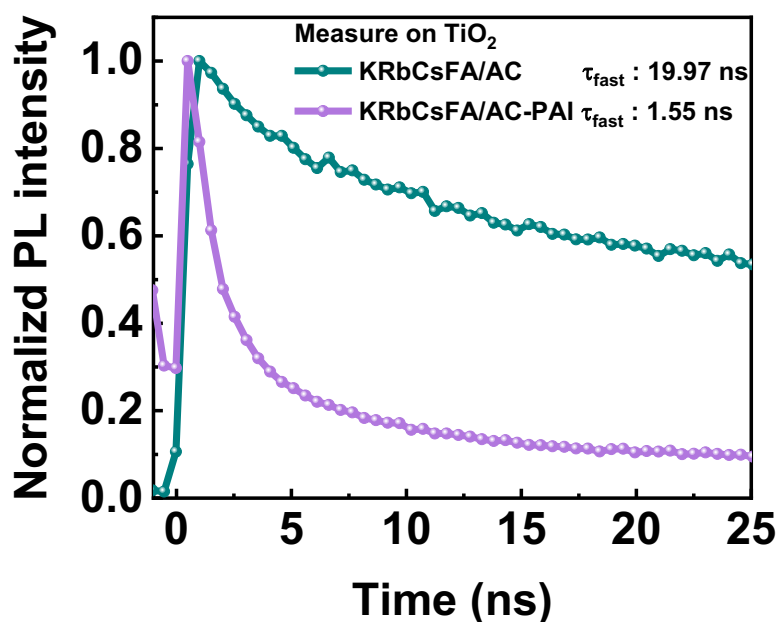


Figure A.VI.2 TRPL curves of KRbCsFA/AC PVK layers without and with PAI post-treatment.

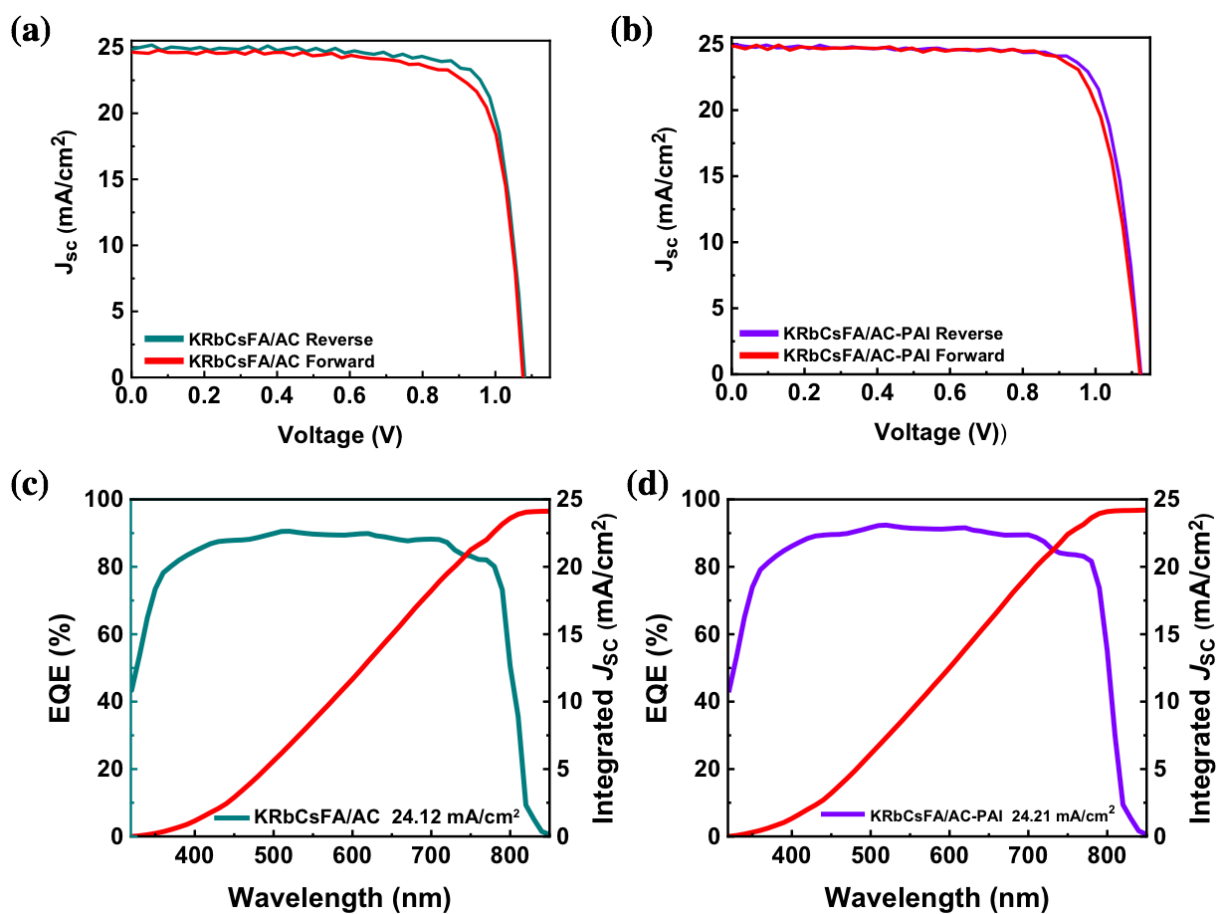


Figure A.VI.3 Effects of capping layer on (a,b) the reverse scan of  $J$ - $V$  curves, (c,b) EQE spectra and integrated  $J_{sc}$  curves.

## List of publications

### Papers published in peer-reviewed journals

- [1] **Daming, Z.**; Changheng, T.; Tao, Z.; Yaoguang, R.; Pauporté, Th. Effects of 5-Ammonium Valeric Acid Iodide as Additive on Methyl Ammonium Lead Iodide Perovskite Solar Cells. *Nanomaterials*, **2020**, *10*, 2512.
- [2] **Daming, Z.**; Tao, Z.; Pauporté, Th. From Mono- to Triple-Cation Hybrid Perovskites for High-Efficiency Solar Cells: Electrical Response, Impedance, and Stability. *ACS Appl. Energy Mater.* **2020**, *3*, 10349–10361.
- [3] **Daming, Z.**; Tao, Z.; Pauporté, Th. A Coadditive Strategy for Blocking Ionic Mobility in Methylammonium-Free Perovskite Solar Cells and High-Stability Achievement. *Sol. RRL* **2021**, 2100010.
- [4] **Daming, ZHENG**; Pauporté, Th. Control by Mixed-Chloride Additives of the Quality and Homogeneity of Bulk Halide Perovskite upon Film Formation Process. *J. Mat. Chem. A* **2021**, *9*, 17801-17811.
- [5] **Daming, ZHENG**; Schwob, C., Prado, Y.; Zakarya, O.; Coolen, L.; Pauporte, Th. How Do Gold Nanoparticles Boost the Performance of Perovskite Solar Cells? **2021**, submit to *Nano Energy*, under review.
- [6] **Daming, ZHENG**; Tao Z.; Yanfa, Y.; Pauporte, Th. Controlling the formation process of Methylammonium-Free Halide Perovskite films for a homogeneous incorporation of alkali metal cations beneficial to solar cell performances. **2021**, submit to *Advanced Energy Materials*
- [7] **Daming, ZHENG**; Raffin, F.; Volovitch, P.; Pauporte, Th. Control of Perovskite Film Crystallization and Growth Direction to Target Homogeneous Monolithic Structures for High Efficiency Solar Cells. **2021**, submit to *Energy & Environmental Science*, under review.

- [8] Tao, Z.; **Daming, ZHENG**; Jiawen, L.; Coolen, L.; Pauporté, Th. PEAI-Based Interfacial Layer for High-Efficiency and Stable Solar Cells Based on a MACl-Mediated Grown  $\text{FA}_{0.94}\text{MA}_{0.06}\text{PbI}_3$  Perovskite. *ACS Appl. Mater. Interfaces* **2020**, *12*, 37197–37207.
- [9] Tao, Z.; **Daming, ZHENG**; Rager, M.; Pauporté, Th. The Stabilization of Formamidinium Lead Tri-Iodide Perovskite through a Methylammonium-Based Additive for High-Efficiency Solar Cells. *Sol. RRL* **2020**, *4*, 2000348.
- [10] Chenxi, M.; **Daming, ZHENG**; Demaille, D.; Gallas, B.; Schwob, C.; Pauporté, Th. Coolen, L. Light management in highly-textured perovskite solar cells: From full-device ellipsometry characterization to optical modelling for quantum efficiency optimization. *Sol. Energ. Mat. and Sol. C.* **2021**, *230*, 111144.